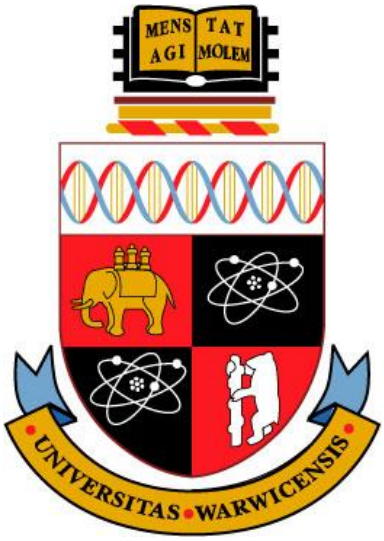

Musculo-Skeletal Modelling and Parameterisation in Vivo

by

Yu, Tung Fai MEng (Hons)

余東徽

Thesis

Submitted to the University of Warwick
for the degree of

Doctor of Philosophy

Department of Physics

March 2014

THE UNIVERSITY OF WARWICK

Contents

List of Tables

List of Figures

Acknowledgements

This work was supported by the Engineering and Physical Sciences Research Council (EPSRC) through a Doctoral Training Award. The whole Gait Laboratory was obtained through Birmingham Science City – Translational Medicine, Clinical Research Infrastructure and Trials Platform, with support from Advantage West Midland.

I would like to acknowledge my supervisor Professor Adrian Wilson, who kindly provided me the opportunity to study for a PhD degree. I would like to thank him for his academic guidance and support. I would like to thank my 2nd supervisor Dr Michael Chappell and Professor Keith Godfrey for their academic support.

I would like to thank my fiancée Natalie Ellis, my parents Mabel Cheng and Raymond Yu and my sister Sarah Yu, who endlessly encouraged and supported me through my life, and through my post graduate research.

I would like to thank my colleagues in the University of Warwick: Sakil Zuberi, Roland Wong, Oliver Alderman and all members of the medical physics group between 2008 and 2013, for their help and company.

Finally I would like to thank the Department of Physics mechanical workshop and electronics workshop for the technical supports, and I would like to thank the Physics administration team for their administration support.

Declarations

I, the author, declare that the work presented in this thesis is of my own work. The work was performed in the Department of Physics and School of Engineering (Gait Laboratory), University of Warwick, under the supervision of Professor Adrian J Wilson and Dr Michael J Chappell.

I declare that this thesis has only been submitted to the University of Warwick for the degree of Doctor of Philosophy and has not been submitted for a degree at another university.

The experimental methods and handling of measured data from human subjects were approved by the University of Warwick Biomedical and Scientific Research Ethics Committee (BSREC). BSREC reference: REGO-2013-104

Details of the work presented in this thesis are/ will be published in the following articles:

YU, T. F. & WILSON, A. J. 2012. Structural Identifiability Analysis and Preliminary Parameter Estimation for an Arm Model Incorporating the Hill Muscle Model. *In: 5th European Conference of the International Federation for Medical and Biological Engineering*, 37, 864-867.

YU, T. F. & WILSON, A. J. 2012. A Novel Passive Movement Method for Parameter Estimation of a Musculo-Skeletal Arm Model Incorporating a Modified Hill Muscle Model. *In: Proc. 8th IFAC Symposium on Biological and Medical Systems (IFAC BMS'12).*

YU, T. F. & WILSON, A. J. In press, Corrected Proof, 2013. A Passive Movement Method for Parameter Estimation of a Musculo-Skeletal Arm Model Incorporating a Modified Hill Muscle Model. *Computer Methods and Programs in Biomedicine Special Issue: 8th IFAC Symposium on Biological and Medical Systems.*

Abstract

This thesis describes the development of an anatomically meaningful musculo-skeletal model of the human arm, incorporating two modified Hill muscle models representing the elbow flexor and extensor muscles. In vivo experimental methods to determine parameter values are presented. The stimulus for this work was to enable the prediction of movement, to support development of prostheses and orthoses such as Functional Electrical Stimulation (FES).

A key problem in model based movement studies is that the passive parameter values in the Hill muscle models and the joint had not been experimentally determined in vivo. The result has been an inability for predictive models to generate realistic predictions of human movement dynamics.

In the model, movement dynamics of the forearm was described using the Newton-Euler method, which was validated from analysis of physical pendulum. Structural identifiability analyses of the muscle models ensured that values for the model parameters could be uniquely determined from perfect noise free data.

A novel experimental procedure termed the passive movement method is described, which exclusively parameterised the model's passive components. Simulated model dynamics were fitted to measured movements of the freely swinging forearm under gravity. Model values were obtained on an individual subject basis. The average muscle model spring and damping constants for four healthy subjects were 143N/m and 1.73Ns/m respectively.

Separately, the force/length characteristics of the muscles' active component, the contractile element (CE), were obtained from measurements of isometric maximum voluntary contraction (MVC) at different elbow angles. The results for the five healthy subjects showed good agreement with results reported in the literature.

A preliminary experiment was performed to predict elbow flexion movement under FES. An electrical stimulus that generated a specified isometric elbow flexion moment (10% of MVC) was applied to generate elbow flexion movement. Simulated FES arm movement was compared with the measured results. The simulated change in elbow angle did not agree with the measured data. A major cause for this was believed to be skin movement causing a change in the current path across the muscle fibres, thus affecting the force generated.

The passive movement method described in this thesis filled an important chapter to fully parameterise musculo-skeletal models in vivo. Although in the FES movement experiment, simulated change in elbow angle generated by FES did not agree with measured data, the shape of the dynamic response in the fitted simulated movement showed good agreement with the measured FES movement.

Abbreviations

2D	Two dimensional
3D	Three dimensional
ADC	Analogue to digital converter
ADL	Activities of daily living
Ag/AgCl	Silver/silver chloride
CE	Contractile element
CoP	Centre of pressure
csv or .csv	Comma separated variables (file)
EMG	Electromyogram, electromyography
FES	Functional electrical stimulation
F/V	Force/velocity
g	Gravitational constant, 9.81ms^{-2}
IACR	Isometric arm contraction rig (section 6.2.3)
MAE	Mean absolute error
MVC	Maximum voluntary contraction
ODE	Ordinary differential equation
PC	Personal computer
PID	Proportional-integral-derivative
S.d.	Standard deviation
sEMG	Surface electromyogram, surface electromyography

Chapter 1 Introduction

1.1 Motivation

3D models of individual joints or groups of joints within the musculo-skeletal system have allowed the positional changes of parts of the body to be visualised (kinematic analysis (Winter, 2005)) and the muscle forces determined (inverse dynamics analysis, e.g. (Nagano et al., 2004, Delp et al., 2007, John et al., 2012)). Those forces, once determined, can then be used in forward dynamic simulations to predict movement (Thelen et al., 2003, John et al., 2012). While these studies have focused on the movement of healthy human subjects, e.g. pedalling (Thelen et al., 2003) and walking (John et al., 2012), one of the main stimuli of musculo-skeletal modelling and movement analysis is to generate predictive models for the development of control strategies associated with orthoses or prostheses in movement rehabilitation (Yamaguchi and Zajac, 1990, Piazza and Delp, 2001).

Recent computational studies, e.g. (Davoodi and Andrews, 1999), which incorporated mathematical predictive models of human movement in the development and optimisation of functional electrical stimulation (FES) control strategies (Rushton, 1997, Peckham and Knutson, 2005) have identified patterns of stimulation, which were not only capable to control complex movement such as balance and moving from a sit to stand position, but also in addressing physiological effects such as decreasing muscle force from fatigue (Bajd et al., 1999, Braz et al., 2007).

However, muscle injuries and disease differ widely between patients, and there is evidence that the dynamic characteristics of the muscles may become very different after a long period of muscle disease, e.g. after spinal cord injury (SCI)

(Shields and Dudley-Javoroski, 2003), in comparison to muscles in a healthy person. Therefore predictive models derived using anthropometric data from a population of healthy subjects cannot correctly predict the movement dynamics for all patients. In order to optimise rehabilitation for an individual patient using model based techniques, parameter values must be specific to an individual patient. From this, the ability to obtain subject specific model parameter values so that movement can be predicted accurately, has become a key part in musculo-skeletal modelling.

From a clinical point of view, if these computational predictive models are to be adopted, then the predicted movement must be realistic. To validate this, the predicted dynamics must be demonstrated to be in agreement with measured data.

Much of the focus for musculo-skeletal modelling has either been on multi-body segment motion e.g. (Nagano et al., 2004) or on the analysis of individual joint movements e.g. (Hof, 1998, Venture et al., 2005, Mohammed et al., 2012).

Whole body models use theories in mechanics, such as the Newton-Euler method or the Lagrange-Euler method, to describe the dynamics of multiple interacting body segments. Inverse dynamic simulation, and parameter estimation techniques have been used to determine muscle forces of individual muscle groups within the body from kinematic measurements e.g. (Davoodi and Andrews, 1999, Zhang and Zhu, 2004, Winter, 2005, John et al., 2012). However, limited anatomical and physiological data on individual joints and muscles were incorporated into these models, and muscles are often modelled as pure force generators, and therefore the mechanisms that gave rise to or modulate the force characteristics were not described. The main problem with such approaches is that they cannot be used to explore anatomical and physiological processes and the impact of changes in an underlying disease process. An example of such changes is in the mechanical characteristic of tendons after a long period of disuse and aging (Narici and Maganaris, 2007).

The majority of the modelling work on individual joints has been aimed at understanding the motion around the joint, e.g. (Leedham and Dowling, 1995, Hof, 1998). Commonly the classical Hill muscle model (Hill, 1938) and variations of Hill muscle models (modified Hill muscle models) have been used to describe the muscle as mechanistic models, which use mechanical components to represent the passive components of the dynamics and a pure force generator, the contractile element (CE), to represent the active component. These muscle models are commonly incorporated into joint models which also incorporate models of the soft tissues surrounding the joint (e.g. ligaments) as passive components. These components form musculo-skeletal models that are anatomically and physiologically meaningful. As well as having an application in the control of orthoses and prostheses, such predictive models also have value in gaining an improved understanding of neuro-muscular disease processes and how changes in the dynamics of individual components affect movement and the control of movement.

Interestingly, studies which parameterised the musculo-skeletal models through inverse dynamics analysis, and successfully predicted movement that agreed with measured kinematic data (Thelen et al., 2003, John et al., 2012) have not reported the numerical values for the model parameters, nor given reproducible descriptions of the methods used to obtain parameter values. In studies where the aims included generating fully parameterised models and determining numerical values for the model components (Venture et al., 2005, Mohammed et al., 2012), the passive component could not be determined from measurement. However a fully parameterised model is required to generate a realistic prediction of movement.

Hof (Hof, 1998) reported numerical values for one of the passive components: the parallel spring component in a Hill muscle model of the triceps surae muscle, from in vivo experiments. But this work had not progressed to developing predictive models. Differences in the derivations of parameters had caused

incompatibilities between studies; and therefore numerical values reported in the literature cannot be used for parameterising models. For example, the spring constants for the muscle model spring reported by Hof were in Nm/rad (Hof, 1998), which acted around a joint, whereas the traditional approach (including that used in this work) describe the spring components within the muscle model as linear springs, in N/m. There are also inconsistencies in the definitions of some parameters within the models, for example the lengths of the tendons described by An et al. (An et al., 1981) and Winters and Stark (Winters and Stark, 1988) included a portion of the tendon embedded in the bulk of the muscle, measured from excised muscles; whereas free tendon length defined by Hatze (Hatze, 1981) only included the portion of the tendon external to the bulk of the muscle, as the lengths are measured using palpation and surface measurement in vivo, in which the embedded portion cannot be measured.

Mohammed (Mohammed et al., 2012) proceeded to predict movement using passive component values from the literature, however those values were arbitrary numerical assumptions. In a study to determine implanted FES control strategies for arm manoeuvres (Liao et al., 2013), zero values were used for the passive components, and this partly contributed to the inability for the models to correctly predict arm positions and movement. Their stimulation patterns to achieve desired arm positions were identified from a trial and error approach.

The limits on using published values for model parameters, and the need for them led to the primary goal of the work presented in this thesis, which was to identify experimental methods to determine the numerical values for the passive components in the muscle models and the joint models in vivo.

In order to achieve the primary goal of parameterising the passive model components, a musculo-skeletal model must be developed. Although, clinically, it is advantageous for models to reflect the anatomy and physiology as realistically as possible, so that clinicians can understand the changes system parameter has in terms of anatomy and physiology; there is a trade-off between

the level of detail in the description of the anatomy and physiology and the ability to successfully determine the numerical values experimentally; and for obtaining parameters specific to individual patients, measurement must be obtained in vivo. For example, Venture et al. (Venture et al., 2005) developed a model of the arm where muscles were individually modelled; however they have not been able to uniquely identify numerical values of the components of the individual from in vivo measurement of joint movement. Subsequently their joint model was reduced to a simple second order rotational system where the mathematical description of the muscle anatomy was lost (Venture et al., 2006). In this thesis, the development of the musculo-skeletal model focuses on describing the anatomy and physiology of the musculo-skeletal components as realistically as possible, while ensuring that the parameters remain determinable, and particularly, that unique numerical values can be obtained.

1.2 Aims, objectives and the structure of the thesis

The aim of the work described in this thesis was to develop predictive mathematical models of the human musculo-skeletal system, and reproducible methods for experimentally determining the passive model parameter values in vivo. The models and the obtained parameter values would then be used in forward simulation to predict movement.

Chapter 2 summarises the relevant background knowledge for the work described in this thesis, which included the anatomy and physiology of the human musculo-skeletal system, observational and analytical techniques in biomechanics for studying human movement, the theory of multi-segment modelling and models of human skeletal muscle.

The main instrumentation for obtaining measurement for the work described in this thesis is the Gait Laboratory, which combines 3D motion capture, force measurement, electromyogram and allows other study-specific equipment to be integrated into the data set capture. These instrumentations are described in Chapter 3, and are used in the experiments described in Chapter 5 to Chapter 7.

The work in this thesis studied the dynamics of the elbow joint, in which the development of a musculo-skeletal of the human arm is described in Chapter 4. It included two rigid segments representing the upper arm and the forearm and it gives a detailed analysis of the dynamics of the elbow joint. The arm model has only 1 degree of movement (elbow flexion/extension) and this is governed by the muscle activities of the elbow flexor muscle and elbow extensor muscles. From a modelling perspective, selecting a joint with minimum degree of freedom is favourable, as it minimises the complexity in a model that has to be validated against measured data.

The theoretical method that described the dynamics of the skeletal model (the Newton-Euler method) must also be validated; this was done by comparing the simulated movements of single segment, and two segments pendulum against measured data of a physical pendulum developed for this work. This validation work forms the first part of the development process to develop the skeletal model.

The muscles responsible for flexion and extension differ in geometry, points of origin and insertion, and mechanical characteristics. This meant the dynamic characteristics in flexion are different to those in extension and therefore the muscles had to be modelled individually. However the ability to obtain parameter values for those muscles must also be considered, to ensure dynamic characteristics of muscle models could be uniquely determined. In this thesis, muscles were grouped together and modelled as two functional groups: elbow flexor muscles and elbow extensor muscles.

The models and parameters within must be anatomically meaningful. Additionally such models need to be developed to ensure that all model parameters must be determinable from in vivo measurements, either through direct measurement, or through parameter estimation experiments. Structural identifiability was performed for different forms of Hill muscle model to ensure that parameters can be uniquely obtained through measurements in vivo

(section 4.2). This led to developing the muscle models incorporated into the skeletal models to complete the musculo-skeletal of the arm.

Ethically, the experiments and measurements to determine model parameter values must be non-invasive when living subjects are used. Additionally, if such models are to have clinical applications, then subject specific parameter values must be obtained through in vivo measurements.

Irrespective of their purpose, some parameter values in musculo-skeletal models cannot be directly measured in vivo, and these are determined through parameter estimation techniques, where simulated model dynamics are fitted with measured movement or force dynamics to estimate the numerical values for the parameters. Traditionally, measurements from maximum voluntary contraction (MVC) have been used as part of the parameterisation of muscle models, e.g. (Winters and Stark, 1988, Frigo et al., 2000, Muramatsu et al., 2001, Maganaris, 2004, Venture et al., 2005). However, a problem arises if voluntary contraction is not possible, for example when working with spinal cord injury (SCI) subjects who have lost voluntary control of their muscles. In these cases the MVC method cannot be used. As a solution, this study proposes an experimental method using passive movements, in which the muscles are completely relaxed and non-active, to obtain numerical values for the passive mechanical parameters in the muscle model. Measurements of passive elbow flexion and extension were used for model fitting and parameter estimation. This work is presented in Chapter 5.

The goal for this work was for the models to be able to predict movement, and the model developed in this work was used to predict movement in an FES experiment. However prior to performing FES on human subjects, the force generated by FES must be specified. To achieve this, an experimental method of measurement of the isometric MVC elbow flexion and extension for the whole range of elbow angle was developed (Chapter 6). The results allow a target FES force to be specified, but it also allowed the force/length characteristics of the

active components of the muscle models to be identified, which were compared with results reported in the literature.

Finally using the MVC results to specified target force generated, a preliminary experiment was performed to generate forces and movement using FES (Chapter 7). The measured elbow flexion elbow movement generated by FES was compared with simulated movement generated by FES.

1.3 Mathematical notation

This thesis uses the following mathematical notation to describe vectors and time derivative variables.

1.3.1 Time derivative variables

Time derivative of a variable is defined using the notation in Eqn 1.1

$$\dot{x}(t) = \frac{dx(t)}{dt} \text{ and } \ddot{x}(t) = \frac{d^2x(t)}{dt^2} \qquad \text{(Eqn 1.1)}$$

Specific attention should be paid to the notations of geometrically orientated variables. In this thesis, lengths are scalar variables. Positions, linear velocities, linear accelerations, angles, angular velocities, angular accelerations, forces and their derivatives, moments and their derivatives are vector variables. The work described in this thesis uses 2D planar models.

1.3.2 Scalar variables

Lengths are defined as l_{xy}, where l denotes the variable is a scalar length between point x and y.

1.3.3 Vector variables

Vectors are denoted by an arrow above the variable; they are products of their magnitudes multiplied by their unit vector matrix of the vector's reference frame. An example is shown here:

$$\vec{x} = \begin{bmatrix} x_1 & x_2 & x_3 \end{bmatrix} \begin{bmatrix} \hat{a}_1 \\ \hat{a}_2 \\ \hat{a}_3 \end{bmatrix} = x_1\hat{a}_1 + x_2\hat{a}_2 + x_3\hat{a}_3 \qquad \text{(Eqn 1.2)}$$

where x_1, x_2 and x_3 are the magnitudes and $\hat{a}_1$, $\hat{a}_2$ and $\hat{a}_3$ are the unit vectors of the reference frame A, the reference frame is described in section 1.3.4.

Positional vectors are defined as $\vec{p}^{XY}$, where $\vec{p}$ denotes a position vector, and the superscript denotes position of point Y from point X. If the position of such point is computed about the global origin, it will be denoted as $\vec{p}^{Y}$ or Y for example.

The vector notation of the linear velocity, linear acceleration, angle, angular velocity and angular acceleration are $\vec{v}$, $\vec{a}$, $\vec{\omega}$ and $\vec{\alpha}$ respectively. For example $\vec{v}^{Y}$ denotes the velocity of point Y.

1.3.4 Reference frame

When dealing with a system containing multiple objects, each object has its own local axes, and origin, collectively this is known as the reference frame, which defines the local origin and directions of the local axes's unit vectors. When describing vectors in a multi-reference frame system, it is important to specify the reference frame the vector is referring to. If multiple reference frames are present, one reference frame is chosen to be the global reference frame. In this thesis, the global axes and reference frame is N, with unit vectors $\hat{n}_1$, $\hat{n}_2$ and $\hat{n}_3$. The N reference frame is fixed in location and the direction of gravity acts in the $-\hat{n}_2$ direction.

The reference frame notation for vectors is added as a superscript before the vector. For example the linear acceleration of Y computed from the global reference frame N will be denoted as ${}^{N}\vec{a}^{Y}$. The vector $\vec{x}$ in section 1.3.3 has a reference frame of A, and should be correctly written as ${}^{A}\vec{x}$. If a vector is presented without a reference frame, then the global reference frame N applies. Vectors can be transformed between reference frames using the table of direction cosines, e.g. (Yamaguchi, 2001).

Force vectors and their derivatives are denoted as $\vec{F}_{XY}$ and $\dot{\vec{F}}_{XY}$, denoting force and its first derivative acting on object Y from object X. In this case the reference frame is not listed; therefore again the reference frame of the force is in the global reference frame.

1.3.5 Error calculation

Percentage errors of measurements reported in this thesis were calculated by the following method:

$$\text{Error } (\%) = \left| \frac{\text{Expected value} - \text{Measured value}}{\text{Measured value}} \right| (\times 100\%) \qquad \text{(Eqn 1.3)}$$

In this thesis, propagations of error were calculated using the methods described by Hughes and Hase (Hughes and Hase, 2010).

Chapter 2 Background

The knowledge of the anatomy and physiology of the human body forms the foundation of biomechanical modelling. It is necessary to understand the mechanisms that are responsible for human movement in terms of anatomy and physiology. While anatomy and physiology can provide subjective descriptions of the functions of, and relations between, different human body components, objective measurements and analytic descriptions must be present to enable the modelling of biological systems.

This chapter summarises the relevant human anatomy and physiology that are essential to enable the mathematical models of human movement. It also includes summaries and comparisons of modelling and measurement techniques in biomechanics, which provides an insight into the reasons behind the selection of methods for measurement and modelling used in this study.

2.1 Anatomy and physiology of human skeleton and skeletal muscles

To generate anatomically meaningful models to represent the musculo-skeletal system of the human body, requires consideration of the organs responsible for generating the movement, and also the other tissues or components of the human body that affects movement dynamics. These are the skeletal muscles, fat, bones and the soft tissues surrounding joints. The relevant anatomy and physiology of these organs described in this thesis are based on the description in Marieb (Marieb, 2001), which were used to develop the mechanical model of the musculo-skeletal system described in this thesis.

The skeleton provides the function to support our body and allows movement. It is composed mainly of bones, to which are linked to other bones at moveable joints (synovial joints). At the joints, the bones are linked by ligaments; these anatomical structures determined the maximum range of movement for joints within the body.

In this thesis, the term joint will be used to refer to synovial joints.

The anatomy of the bones and connecting ligaments determines the type of movement for the joints. Figure 2.1 shows four examples of movable joints in the human body with their freedom of movement.

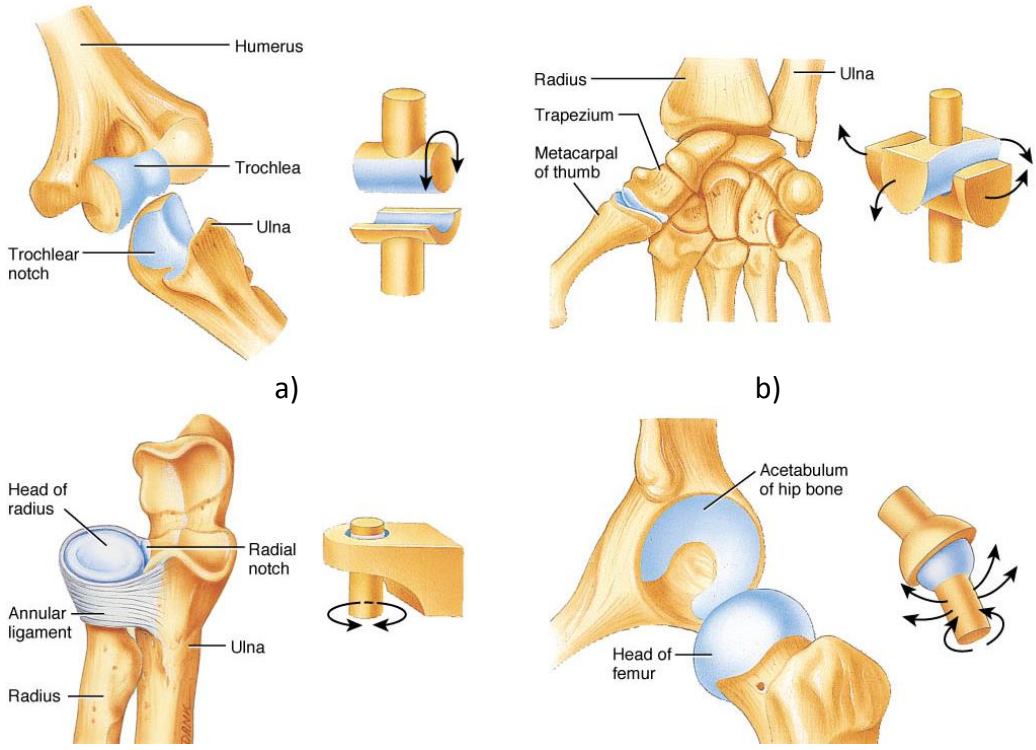

Figure 2.1. Different types of human joint by freedom of motion. A) Hinge joint, e.g. between the humerus and ulna allowing the flexion and extension of the elbow joint. B) Saddle joint, e.g. between the trapezium and 1st metacarpal of the thumb allowing flexion, extension, abduction and adduction of the carpometacarpal of the thumb. C) Pivot joint, e.g. between the radius and ulna allowing the pronation and supination of the forearm. D) Ball joint, e.g. between the hip bone and femur allowing flexion, extension, abduction, adduction, rotation and circumduction at the hip joint. Image taken from (Tortora and Derrickson, 2008).

Skeletal muscles produce the movement of the skeleton, and are connected to bones via tendons. These muscles use the bones as mechanical leverages to stabilise the joints or move the joint in a desired manner.

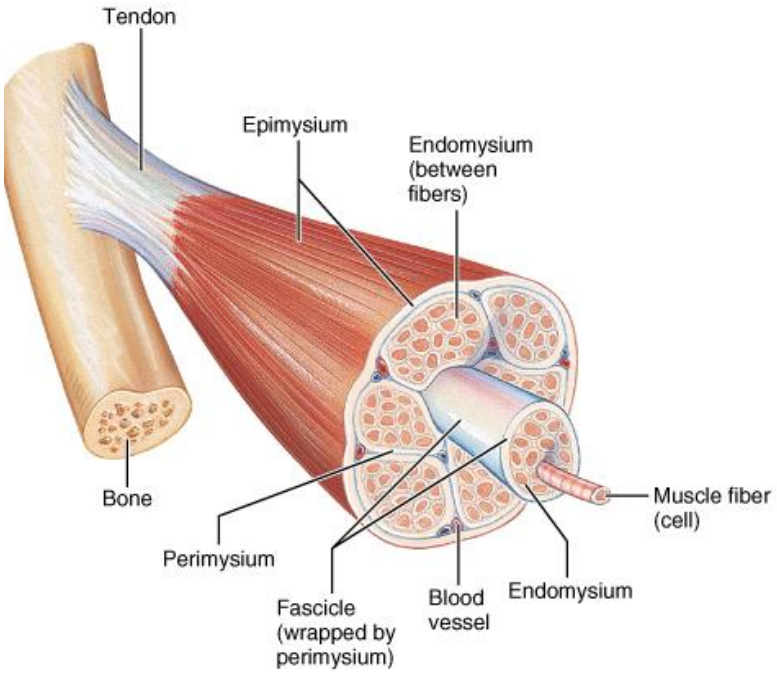

Figure 2.2. Gross anatomy of the skeletal muscle. Showing the bulk of the muscle connected to the bone (beige part on the left) via a free tendon (white part). The bulk of the muscle (red part on the right) is a large group of muscle fibres (contractile part) within connective sheath of endomysium, perimysium and epimysium. Image taken from (Marieb, 2001)

Skeletal muscles wrap around and connect to the skeleton. The gross anatomy of a skeletal muscle is shown in Figure 2.2. Each muscle contains bundles of muscle fibres (cells) which convert chemical energy into mechanical energy, providing the contractile tension to maintain muscle length under load or shorten the muscle. The micro-anatomy of the muscle fibre cell will be described later in this section to further explain the working mechanism of the contractile force mechanism.

The skeletal muscles have natural resting lengths, when they are stretched beyond this length, they produce passive spring force. When released, this force characteristic returns the muscle to its natural resting length.

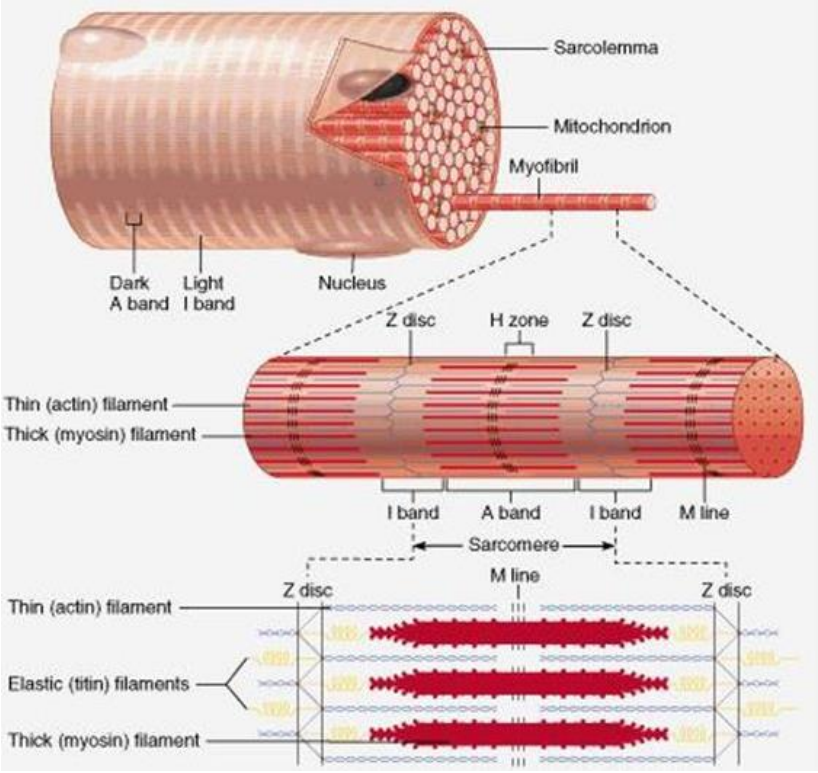

Figure 2.3. Micro anatomy of a muscle fibre. Image taken from (Marieb, 2001)

The component of the muscle that is responsible for producing contractile force is the actin and myosin filaments within muscle fibre cells, shown in an illustration of the micro anatomy of the muscle in Figure 2.3. When the muscle is activated, the bonding and releasing action of the actin and myosin filaments act as a mechanical ratchet system, attempting to shorten the length of the sarcomere. When the muscle length shortens, the portion of the overlap between the actin and myosin filaments increases, providing more bonding sites between the actin and myosin filaments, and allowing a stronger possible contractile force. The maximum possible force drops when the actin filaments are pushed against the Z disc. When the muscle is relaxed, the bonds between the actin and myosin breaks and the filaments are allowed to slide away to a natural resting length.

2.2 Musculo-skeletal modelling

Human movement, such as standing and walking, can be mathematically modelled as mechanical systems, where the anatomy and geometry of the human skeleton are modelled as jointed segments, and the muscles are modelled as force generators. These mathematical models are known as musculo-skeletal models, and these systems are used to describe human movement as one part of a wider discipline called Biomechanics.

2.2.1 Human skeletal system modelling using vector based kinematics

The human skeletal system can be mechanically described and represented as a series of rigid bodies connected together by freely moving joints. In this thesis, systems of mechanically linked rigid bodies are called multi-segment systems. The body segments such as the trunk of the body, upper arm, forearm and hand, are represented by rigid bodies, which are referred to as segments in this thesis. These segments are connected to (an)other segment(s) by synovial joints (freely movable joints), such as the shoulder, elbow and wrist, etc. These anatomical joints can be represented mechanically as ball and socket joints, hinged joints and ellipsoidal joints.

One of the common approaches to model and simulate a multi-segment model is to use the Newton-Euler method to describe the movement and force interactions between segments, using a series of system equations in the form of ordinary differential equations. Forward modelling (integration) techniques can then be used to simulate the movement trajectories. The background theory of vector based kinematics is widely known, e.g. (Yamaguchi, 2001). An example of a multi-segment model is shown in Figure 2.4 and this is used as the basis for modelling the musculo-skeletal systems described in this thesis.

2.2.1.1 Multi-segment pendulum modelling – Newton-Euler's method

Consider 2D planar multi-segment system in Figure 2.4, showing the geometry of three linked rigid segments A, B and C. Segment A is connected to a non-moving ground plane N at A^0; segment B is connected to segment A at B^0 and segment C

is connect to B at C^0. A*, B* and C* are the geometric centres of each segment and they are also the centres of mass of each segment.

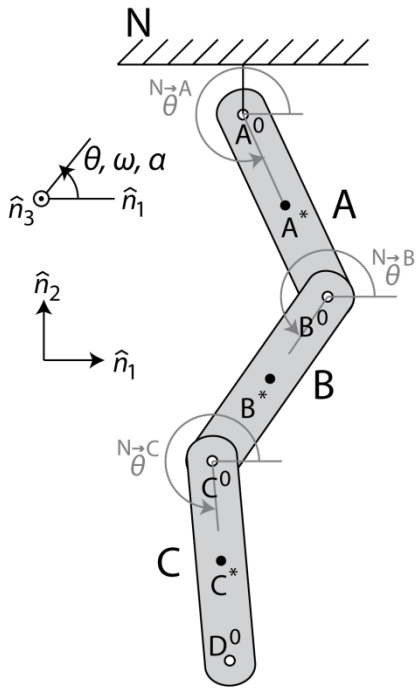

Figure 2.4. A planar chain of three segments, A, B and C, connected to a non-moving ground plane N at the point A^0. A^0, B^0 and C^0 are freely rotating joints connecting the segments (and the ground plane) shown in the figure. A*, B*, C* are the centre point of segment A, B and C respectively and also their respective centres of masses. D^0 is the lower point of segment C where an external force maybe applied. The angle of each segment relation to the global reference frame N is shown in grey.

The global reference frame N's origin is at the fixed point A^0. Eqn 2.1 to Eqn 2.8 describe the positions of point A*, B^0, B*, C^0, C* and D^0, in relation to lengths of the segments and angles of the segments in the N reference frame.

$$A^*(t) \equiv {}^N\vec{p}^{A^0A^*}(t) = A^0 + l_{A^0A^*} \times \left[\cos({}^N\vec{\theta}^A(t)) \quad \sin({}^N\vec{\theta}^A(t))\right]\begin{bmatrix}\hat{n}_1\\ \hat{n}_2\end{bmatrix} \qquad \text{(Eqn 2.1)}$$

$$B^0(t) \equiv {}^N\vec{p}^{A^0B^0}(t) = A^0 + l_{A^0B^0} \times \left[\cos({}^N\vec{\theta}^A(t)) \quad \sin({}^N\vec{\theta}^A(t))\right]\begin{bmatrix}\hat{n}_1\\ \hat{n}_2\end{bmatrix} \qquad \text{(Eqn 2.2)}$$

$$B^*(t) \equiv {}^N\vec{p}^{A^0B^*}(t) = B^0(t) + l_{B^0B^*} \times \left[\cos({}^N\vec{\theta}^B(t)) \quad \sin({}^N\vec{\theta}^B(t))\right]\begin{bmatrix}\hat{n}_1\\ \hat{n}_2\end{bmatrix} \qquad \text{(Eqn 2.3)}$$

$$C^0(t) \equiv {}^N\vec{p}^{A^0C^0}(t) = B^0(t) + l_{B^0C^0} \times \left[\cos({}^N\vec{\theta}^B(t)) \quad \sin({}^N\vec{\theta}^B(t))\right]\begin{bmatrix}\hat{n}_1\\ \hat{n}_2\end{bmatrix} \qquad \text{(Eqn 2.4)}$$

$$C^*(t) \equiv {}^N\vec{p}^{A^0C^*}(t) = C^0(t) + l_{B^0C^0} \times \begin{bmatrix} \cos({}^N\vec{\theta}^C(t)) & \sin({}^N\vec{\theta}^C(t)) \end{bmatrix} \begin{bmatrix} \hat{n}_1 \\ \hat{n}_2 \end{bmatrix} \quad \text{(Eqn 2.5)}$$

$$D^0(t) \equiv {}^N\vec{p}^{A^0D^0}(t) = C^0(t) + l_{C^0D^0} \times \begin{bmatrix} \cos({}^N\vec{\theta}^C(t)) & \sin({}^N\vec{\theta}^C(t)) \end{bmatrix} \begin{bmatrix} \hat{n}_1 \\ \hat{n}_2 \end{bmatrix} \quad \text{(Eqn 2.6)}$$

The segment's linear velocities and accelerations are described at the points of the centre of masses of each segment, A*, B* and C*, they have the following relations.

$${}^N\vec{v}^A(t) \equiv \frac{dA^*(t)}{dt} \quad \text{(Eqn 2.7)}$$

$${}^N\vec{v}^B(t) \equiv \frac{dB^*(t)}{dt} \equiv {}^N\vec{v}^A(t) + {}^A\vec{v}^B(t) \quad \text{(Eqn 2.8)}$$

where ${}^A\vec{v}^B$ is the velocity of segment B relative to segment A and reference frame A, and

$${}^N\vec{v}^C(t) \equiv \frac{dC^*(t)}{dt} \equiv {}^N\vec{v}^A(t) + {}^A\vec{v}^B(t) + {}^B\vec{v}^C(t) \quad \text{(Eqn 2.9)}$$

where ${}^B\vec{v}^C$ is the velocity of segment C relative to segment B and reference frame B.

Similarly the linear accelerations of the segments, computed at the points of the centres of masses of the segments are:

$${}^N\vec{a}^A(t) \equiv \frac{d^2A^*(t)}{dt^2} \equiv \frac{d\,{}^N\vec{v}^A(t)}{dt} \quad \text{(Eqn 2.10)}$$

$${}^N\vec{a}^B(t) \equiv \frac{d^2B^*(t)}{dt^2} \equiv \frac{d\,{}^N\vec{v}^B(t)}{dt} = {}^N\vec{a}^A(t) + {}^A\vec{a}^B(t) \quad \text{(Eqn 2.11)}$$

$${}^N\vec{a}^C(t) \equiv \frac{d^2C^*(t)}{dt^2} \equiv \frac{d\,{}^N\vec{v}^C(t)}{dt} = {}^N\vec{a}^A(t) + {}^A\vec{a}^B(t) + {}^B\vec{a}^C(t) \quad \text{(Eqn 2.12)}$$

The acceleration of each segment is governed by Newton's second law (NIIL) and is the sum of the external forces acting on the segment and gravity, divided by

the segment's mass, shown in Eqn 2.13 to Eqn 2.16. The forces acting on each individual segment are shown in Figure 2.5.

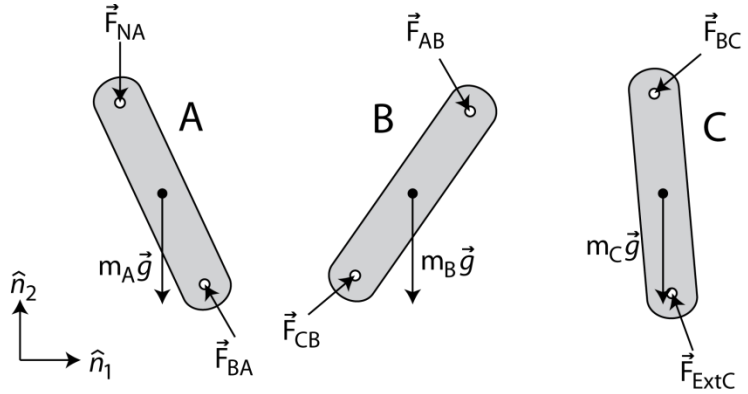

Figure 2.5. Forces acting on individual segments of the three segments pendulum model. Showing the downward force due to gravity acting on the centres of mass, and external forces acting on the pivot joints of each segment.

$$\sum F(t) = ma(t) \quad \text{(NIIL)}$$

$$\vec{F}_{ExtC}(t) + \vec{F}_{BC}(t) + m_C\vec{g} = m_C\vec{a}_C(t) \quad \text{(Eqn 2.13)}$$

$$\vec{F}_{CB}(t) + \vec{F}_{AB}(t) + m_B\vec{g} = m_B\vec{a}_B(t) \quad \text{(Eqn 2.14)}$$

$$\vec{F}_{BA}(t) + \vec{F}_{NA}(t) + m_A\vec{g} = m_A\vec{a}_A(t) \quad \text{(Eqn 2.15)}$$

$$\vec{F}_{AB}(t) = -\vec{F}_{BA}(t) \text{ and } \vec{F}_{BC}(t) = -\vec{F}_{CB}(t) \quad \text{(Eqn 2.16)}$$

The segment's angular acceleration of each segment can be calculated using the Euler's second law of angular motion (EIIL).

$$\alpha(t) = \sum(F(t) \times \text{moment arm } (t)) / I \quad \text{(EIIL)}$$

$${}^N\vec{\alpha}^A(t) = \left(\vec{F}_{NA}(t) \times \vec{p}^{\,A^0A^*}(t) + \vec{F}_{BA}(t) \times \vec{p}^{\,B^0A^*}(t)\right) / I_A \quad \text{(Eqn 2.17)}$$

$${}^N\vec{\alpha}^B(t) = \left(\vec{F}_{AB}(t) \times \vec{p}^{\,B^0B^*}(t) + \vec{F}_{CB}(t) \times \vec{p}^{\,C^0B^*}(t)\right) / I_B \quad \text{(Eqn 2.18)}$$

$${}^N\vec{\alpha}^C(t) = \left(\vec{F}_{BC}(t) \times \vec{p}^{\,C^0C^*}(t) + \vec{F}_{ExtC}(t) \times \vec{p}^{\,D^0C^*}(t)\right) / I_C \quad \text{(Eqn 2.19)}$$

With the assumption that each segment is a rod with uniformly distributed mass along its length, the moment of inertia of A, B and C are given by:

$$I_A = m_A l^2_{A^0 B^0} / 3 \quad \text{(Eqn 2.20)}$$

$$I_B = m_B l^2_{B^0 C^0} / 12 \quad \text{(Eqn 2.21)}$$

$$I_C = m_C l^2_{C^0 D^0} / 12 \quad \text{(Eqn 2.22)}$$

where moment of inertia of A is calculated at one end of the segment A at A^0, and the moment of inertias of B and C are calculated at the point of the centre of mass of the segments.

The above equations summarise the position, velocity, acceleration, angular velocity and angular acceleration of the system. These equations will be used in section 4.1, and rearranged to allow the movement of multi segment pendulums to be simulated.

Two key model components are needed to achieve a musculo-skeletal model: the first is to model the skeletal component; and the second is to model the muscular components. Additionally soft tissues around the joint also modulate the dynamics of the joint, and those are also considered in the models described in this thesis.

2.2.2 Classical Hill muscle model

The classical Hill muscle model shown in Figure 2.2 (Hill, 1938, Yamaguchi, 2001, Winter, 2005) is a mechanical model of the whole of a skeletal muscle based on its anatomy.

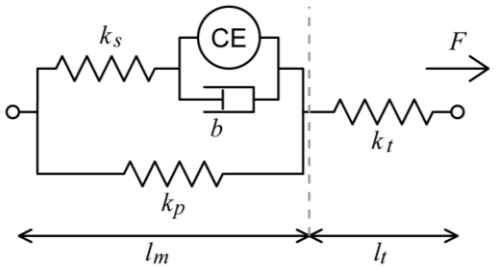

Figure 2.6. Classical Hill muscle model

The classical Hill muscle model is a mechanical model describing the mechanical characteristics of the anatomical components within the bulk of the muscle, which is connected to the free tendon described in section 2.1. The internal components of the muscle are the components included in the l_m portion in Figure 2.6. The contractile element (CE) represents the contractile force generated by the actin-myosin cross bridges (Figure 2.3). In parallel with the CE there is a damping element b, which represents the resistance to movement when fluid is moving in and out between the actin-myosin filaments when the sarcomere lengthens or shortens (Hill, 1938). In series with the CE and damping element, there is a serial spring k_s, which represents elasticity in the Z-disc, titin filaments, actin filaments and myosin filaments. In parallel with all these is a parallel spring component k_p, which represents the elastic properties of the epimysium, perimysium and endomysium that wrap around the muscle fibre fascicles. This elasticity in parallel to the muscle fibres gives the muscle its ability to spring back to a natural resting length once it has been released from a stretched length beyond its natural resting length. In series with the Classical Hill muscle model is a serial spring k_t, included in the l_t portion of the muscle schematic presented in Figure 2.6. This is a combined component encompassing the free tendon at both ends of a muscle. The model is connected to the point of origin and point of insertion at the bones, and exerts tension force at these two points.

2.2.2.1 Force/length characteristics and force/velocity characteristics.

The contractile element in the classical Hill muscle, which is a pure force generator, has two additional characteristics, which are the force/length (F/L) characteristics (Gordon et al., 1966) and force/velocity (F/V) characteristics (Hill, 1938, Bigland and Lippold, 1954).

The force/length characteristics (Gordon et al., 1966) describe the isometric force a muscle fibre can produce at different lengths. A sarcomere has an optimal length where the muscle fibre can produce the maximum force. At longer or shorter lengths, the maximum force that can be produced is reduced, with the characteristics shown in Figure 2.7. Anatomically these characteristics can be explained as follow: at the optimal sarcomere length (see Figure 2.8a), there is a maximum number of actin myosin bonding sites for the muscle fibre to generate contractile force. When the sarcomere is stretched beyond its optimal length (see Figure 2.8b), there are less bonding sites to generate contractile force, and therefore the maximum force of the fibre decreases. When the sarcomere shortens (see Figure 2.8c), the actin filaments begin to overlap, again reducing the available actin myosin bonding sites. When the sarcomere contracts further (see Figure 2.8d), the myosin filaments pushes against the Z disc and the fibre cannot contract any further.

The force/length characteristics obtained by Gordon et al (Gordon et al., 1966) were from the sarcomere level. In term of a muscle as a whole, it consists of many sarcomeres connected in series and parallel, and therefore the shape of the force/length curve from the sarcomere level can be scaled up to describe the force/length characteristic at the whole muscle level. However, muscles are embedded in the skeletal system, and the range of the force/length curve each muscle operates in vivo, is limited by the range of the joint angle. Examples of the force/length curves for the muscles around the elbow joint can be seen in (Murray et al., 2000, Maganaris, 2001, Maganaris, 2004).

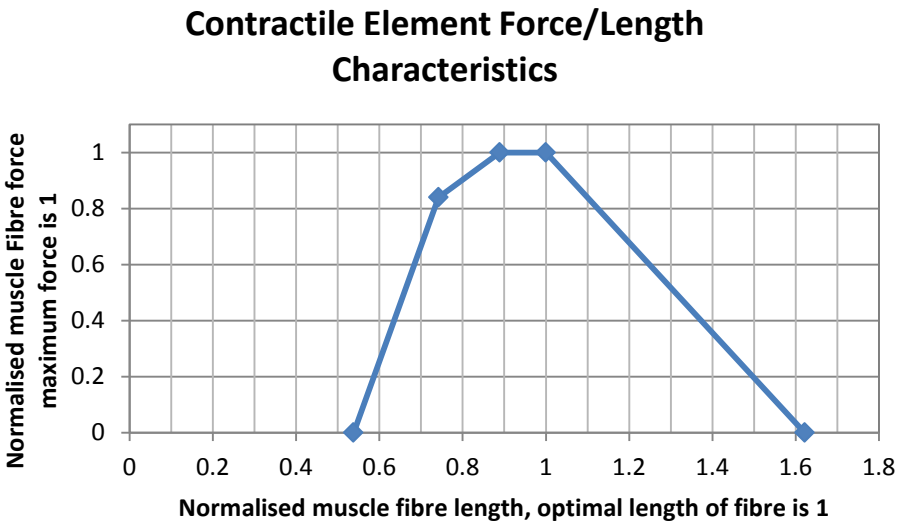

Figure 2.7. Force/length characteristics adapted from measured normalised maximum sarcomere force against sarcomere length (Gordon et al., 1966). The sarcomere length where maximum force was produced has been normalised to 1 to give the optimal contractile element length.

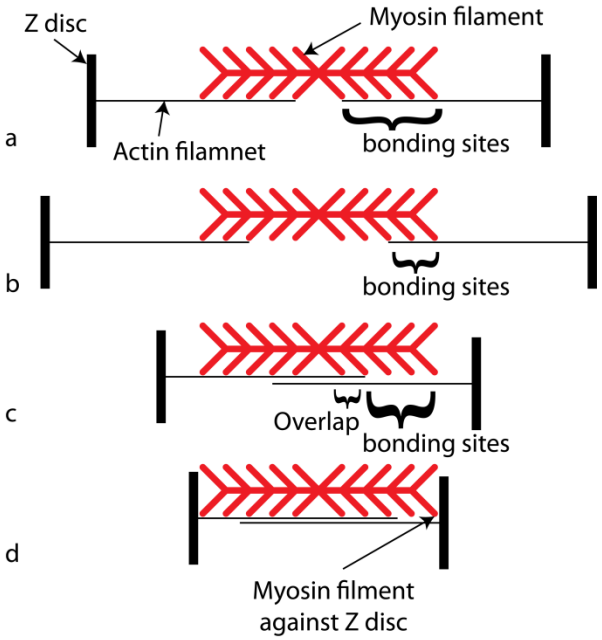

Figure 2.8. Available actin myosin bonding sites for different sarcomere length. a) Optimal sarcomere length where maximum number of bonding sites are available. b) Lengthened sarcomere with reduced number of bonding sites available due to less overlap between the actin filament and myosin filament. c) Shortened sarcomere with reduced number of bonding sites available due to actin filaments overlap. d) Myosin filament pushes against Z-disc.

2.3 Nomenclature and definitions

2.3.1 Hill muscle models and parameter definitions

When describing body organs and tissues as mechanical components, anatomical terms have often been loosely used. The main variation in definition is the use of tendons in the Hill muscle models, e.g. (An et al., 1981, Zajac, 1989, Hof, 1998, John et al., 2012). It is not clear if these tendons are modelled as a separate component within the Hill muscle model or are included as part of the external tendon components to the Hill muscle model. In this thesis, the term “free tendon” will be used to describe the parts of the tendon external to the bulk of the muscle; and “embedded tendon” will be used as a combined term for the epimysium, perimysium and endomysium which are embedded in the bulk of the muscle.

2.3.2 Parameterisation experiments

Hill type muscle models (Hill, 1938) represents the muscle as a combination of mechanical components. Because these mechanical components model properties were derived from the sum of a large number of microscopic components at the sarcomere level, it is not possible to measure the dynamic properties of these components directly in vivo. Therefore, the only approach to obtain parameter values is to use parameter estimation techniques, in which simulated data are fitted to measured data in order to estimate the parameter values, e.g. (Thelen et al., 2003, Venture et al., 2005, John et al., 2012), and this approach is also used in the work described in this thesis

2.3.3 Predictive models

Although prediction of movement dynamics has been difficult due to the unknown values of the passive components, some studies e.g. (Lloyd and Besier, 2003, Maganaris, 2004) have been able to predict the force dynamics of muscles or joint torques generated by voluntary contractions or from FES. Those predicted forces were validated against measured forces or joint torques from measurements of isometric contractions or isokinetic contractions, and good

agreement was seen between measured and simulated force dynamics. In all of those cases, some forms of frame support (e.g. dynamometers in isokinetic measurements) were used to maintain or control the position of the body segments around the joints. In these studies (Lloyd and Besier, 2003, Maganaris, 2004), the mechanical dynamics of the relaxed muscles were first recorded to give “reference measurements”, in order to allow the mechanical properties of the supports to be eliminated from the dynamics of the active muscles. In these approaches, the mechanical dynamics of the passive components are also included in the “reference measurements”, and therefore it is not necessary to identify the passive characteristics of the models. However when one wishes to successfully control movement away from those experimental environments, where the supports are not used, then the passive mechanical dynamics must be known.

Chapter 3 Instrumentation

3.1 Introduction

In this thesis, a Gait Laboratory was used to obtain measurement of human movement dynamics. The laboratory contains a Vicon MX biomedical motion capture system, the key measurement components of which are a 3D motion capture system, a force plate to measure forces during movement and a 16 channel electromyography (EMG) system. The Gait Laboratory provides 8m (length) x 3m (width) x 2m (height) of usable measurement space (Figure 3.1). The data from all the components of the system were collected together in the system's software: Vicon Nexus 1.4, allowing a temporal and cross sectional analysis of the sequences of events to be analysed.

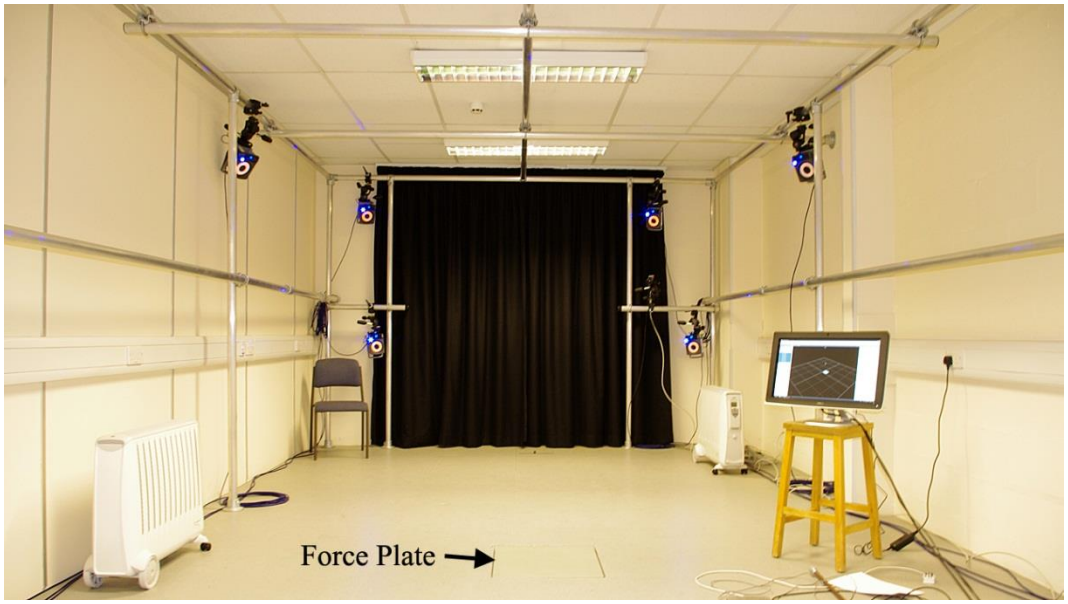

Figure 3.1. Gait Laboratory motion capture area. Showing six infra-red motion capture cameras with blue indicator lights and red/infra-red ring lights. The cameras are mounted to a rigid metal frame. At the centre of the motion capture area, an AMTI force plate is installed into the floor, as labelled in the figure. The monitor on the right shows a live reconstruction of the 3D space, with a 2D grid representing the floor and a grey square representing the force plate.

3.2 3D motion capture

The Vicon MX biomedical 3D motion capture suite was used to measure kinematic data. It is a marker based motion capture system, which uses videos captured from 12 infra-red (IR) cameras (MX cameras, see Figure 3.2) placed at different positions around the room (Figure 3.1) to track positions of spherical reflective markers attached to the skin of human subjects or equipment being studied. The system uses IR for motion capture so that normal room lighting (e.g. the fluorescent tubes in the lab) does not interfere with the MX system. The IR source is provided by a ring of IR LEDs surrounding the lens on each MX camera unit.

Figure 3.2. A Vicon MX infra-red camera used for motion capture. It has a 4 row red/infra-red ring light providing the infra-red light providing the light source for the infra-red camera. at the centre of the ring light is a infra-red pass filter, placed in front of the lens and camera sensor. At the bottom right of the camera is a blue indicator light.

The reflective markers used to track movements were attached onto the surface of the skin of human subjects using medical double sided tape (e.g. 3M 1422), or on the surface of the mechanical rig using double sided tape. Figure 3.3 shows one of the markers used for motion capture.

Figure 3.3. A motion capture marker. A plastic sphere covered in high visibility tape, connected to a black plastic base, providing a flat surface at the bottom to be attached to the subjects using double sided tape. This marker has a diameter of 14mm; the base has a diameter of 16mm and thickness of 2.5mm.

The reflective markers are plastic spheres covered in high visibility tape. The markers reflect the infra-red light from the MX cameras' ring lights to the MX camera sensors. Markers of two different sizes were used in these experiments, 14mm diameter spheres and 9.5mm spheres, both with same sized bases. The larger 14mm markers were used to allow the system to detect the markers from larger distances. Marker model that defined where markers should be placed, were developed and described in section 3.5.2. The marker models were also used in the software to identify individual markers in the measured data. Smaller 9.5mm spheres were attached to the mechanical rigs (IACR) in the experiments described in Chapter 6 and Chapter 7, as they provided higher accuracy than using the 14mm markers, and the MX cameras remained capable of detecting the smaller 9.5mm diameter markers within the Gait Laboratory.

In this thesis, the MX cameras were capturing at 200 frames per second according to Vicon's recommended setting for biomechanical studies. This allowed fast movement (e.g. fast impulse movements) to be recorded without aliasing.

In additional to IR motion capture videos, there are two colour digital video cameras (DV cameras) that recorded footages of the motion capture trials. These allowed inspections after the measurement trials, to verify the computed 3D locations of the markers in the digital reconstructed space. The DV cameras were capturing at 100 frames per second according to Vicon's recommended settings. The recorded files from the DV cameras are much larger than the MX camera

files and require higher transfer and recording bandwidth, therefore the frame rate for DV cameras were lower than the MX motion capture cameras.

The MX cameras and the DV cameras were connected to two Vicon Giganet control boxes and the video data were recorded onto a PC. The system was controlled using the system software Vicon Nexus (version 1.4) on the system's PC. The recorded video footages were analysed and the 3D location of the markers were reconstructed in a digital 3D space using Vicon Nexus. The software and analysis are described in section 3.5.

3.3 Force plate

An AMTI OR6-7 force plate (AMTI, 2013b) is installed in the floor in the centre of the Gait Laboratory's capture room, as shown in Figure 3.1. The force plates uses four strain gauge bridges to measure ground reaction force (AMTI, 2013b) and provides 6 analogue output of the force in the x, y and z directions (Fx, Fy and Fz respectively), and moments in the x, y and z directions (Mx, My and Mz respectively). These are input into the Vicon system software, Vicon Nexus, via an AMTI Miniamp amplifier (AMTI, 2013a) and an analogue to digital converter (ADC) into the Vicon system (Giganet control box). The force plate sampling rate was 1kHz. In additional to the ground reaction force and moment in the x, y and z axes, the ground reaction force's origin, known as the centre of pressure (CoP), is calculated in Vicon Nexus in the x and y direction, and shown in Eqn 3.1 and Eqn 3.2 (AMTI, 1991, AMTI, 2004). The ground reaction force and CoP is commonly used in the analysis of balance during standing (Winter et al., 2001, Morasso and Sanguineti, 2002, Braz et al., 2009) and trajectories in CoP in gait (Romanò et al., 1996, Schmid et al., 2005). In this thesis, the force plate was used with a mechanical rig to measure elbow flexion and extension forces in Chapter 6 and Chapter 7.

$$CoP_x = M_y / F_z \qquad \text{(Eqn 3.1)}$$

$$CoP_y = M_x / F_z \qquad \text{(Eqn 3.2)}$$

3.4 Electromyography

Electromyography data from an Aurion Zero-Wire surface electromyography (sEMG) system is input into Vicon Nexus to record muscle activity. It uses silver/silver chloride (Ag/AgCl) hydrogel electrodes attached to the surface of the skin, (Figure 3.4) and measures the EMG using small amplifiers. There are 16 EMG channels available, each channel is in a self-contained transducer unit, which wirelessly communicates to a central receiver. The EMG central receiver then transmits those analogue signals to the Vicon Giganet box's ADC. Each channel samples at 1000 samples per second. The Zero-Wire sEMG system was chosen over a wired EMG system, as no wired connections are present between the subject and the main system acquisition station and therefore there are no constraints on subject movement. Each wireless transducer is small and light weight and therefore has minimal effect on the subject's movement dynamics.

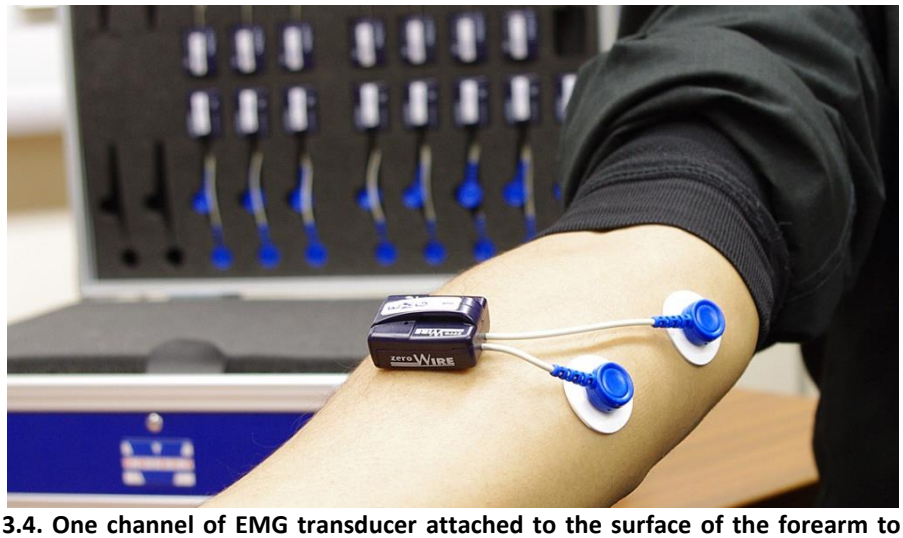

Figure 3.4. One channel of EMG transducer attached to the surface of the forearm to record muscle activity underneath that portion of the skin. Two surface Ag/Cl hydrogel electrodes with adhesive pads are attached to the surface of the skin. These are connected to the transducer leads via pop buttons. The transducer is a small wireless module which transmit analogue signal to the main receiver for the data to be recorded.

3.5 Software and data processing

Data acquisition and data post processing were performed in Vicon Nexus 1.4. The aim of the data post processing was to:

1) Compute the 3D locations of each marker in each time frame using the raw video data from the MX cameras (reconstruction).
2) Label each marker according to the marker model (section 3.5.2).
3) Export the computed locations and trajectories (kinematic data) and other data such as forces and EMG data for further analysis. In this thesis, further analysis of kinematic data was performed in Matlab 2009b (MathWorks®, 2013).

The reconstruction and labelling processes are shown in Figure 3.5 and described in section 3.5.1 and 3.5.2.

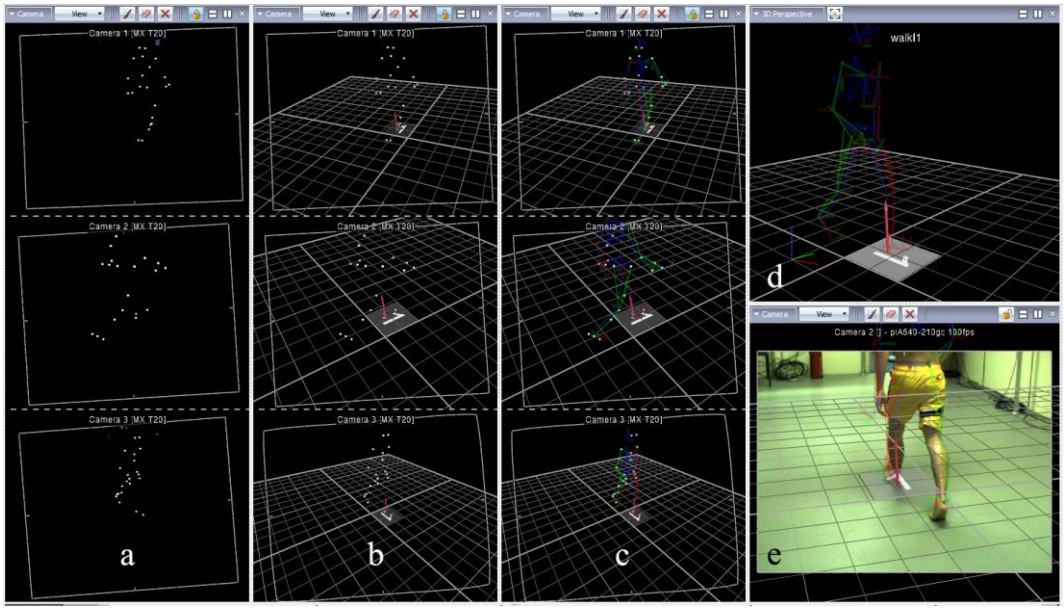

Figure 3.5a. Images from three of the twelve MX cameras after intensity threshold to identify the markers. The frames of the camera sensors are shown by white rectangles; the markers are shown as white dots and dark blue dots are masked area where data are ignored. b. Markers reconstructed into a 3D digital space, calibrated to a floor shown by a white grid. The force plate is shown by a grey square labelled 1. A red arrow shows the ground reaction force at the force plate, representing its origin (CoP), magnitude and direction. The camera frames have been calibrated against lens distortion. c. Each marker is labelled according to the Vicon Plug-in Gait marker model. The markers are linked to other markers according to body segments. d. Shows a 3D perspective view, the ground reaction force is clearly visible against the left foot where the foot is in contact with the floor during walking. e. A DV camera view with an overlay of the 3D space and labelled markers, allowing the quality of the labelling to be verified.

3.5.1 Kinematic data reconstruction

The MX cameras recorded video data from different angles and detected the IR light reflected from the markers; the video footages are thresholded to exclusively detect the markers. To reconstruct the markers' locations in a 3D space, Vicon Nexus applies multiple view geometry computation (Hartley, 1999, Hartley and Zisserman, 2004) to compute and provide the 3D position of each marker from the 2D marker positions in the camera planes. The system was calibrated using the recommended method by Vicon. The Vicon MX system used in this work has a reported precision of 1mm and accuracy of ±0.1mm. The measured linear precision error was 0.4mm and the measured gradient error of the x-y plane in the reconstructed space against the horizontal plane in the measured space was less than ±1°. These errors were obtained by placing 8 markers on the floor distributed evenly on a ring of circle with 1m radius from the origin. Two markers were aligned along the x axis and two markers were aligned along the y axis. Reconstructed locations were compared against measured locations. The markers aligned with the x and y axes were used to compute the angular error and the remaining four markers were used to ensure the reconstructed marker locations were on the same plane.

3.5.2 Marker labelling

The markers in the 3D space were labelled according to a marker model, such as the Plug-In Gait marker model (Vicon®, 2010). An example of a motion capture trial of the walking motion using the Vicon Plug-in Gait model is shown in Figure 3.6. A marker model is the layout of markers used in motion capture, in the Vicon Plug-in Gait and the arm marker model used in this work, the markers are placed in anatomical positions so that the location of body segments or joints can be located. All the defined markers in the marker models have unique names. In most instances, several markers are associated together to form a segment in the marker model. For example, in Figure 3.6, four markers around the head of the subject are associated together to form the head segment of the model, represented by a white block in the 3D reconstruction. Markers can also

be part of more than one segment, for example a marker placed next to the knee can be associated with the segment representing the upper leg and the segment representing the lower leg. The relative orientations between segments can be used to calculate joint angles, for example knee joint angle. A detailed description of the marker model of the arm used in this thesis was developed to measure movement of the arm and is described section 5.3.

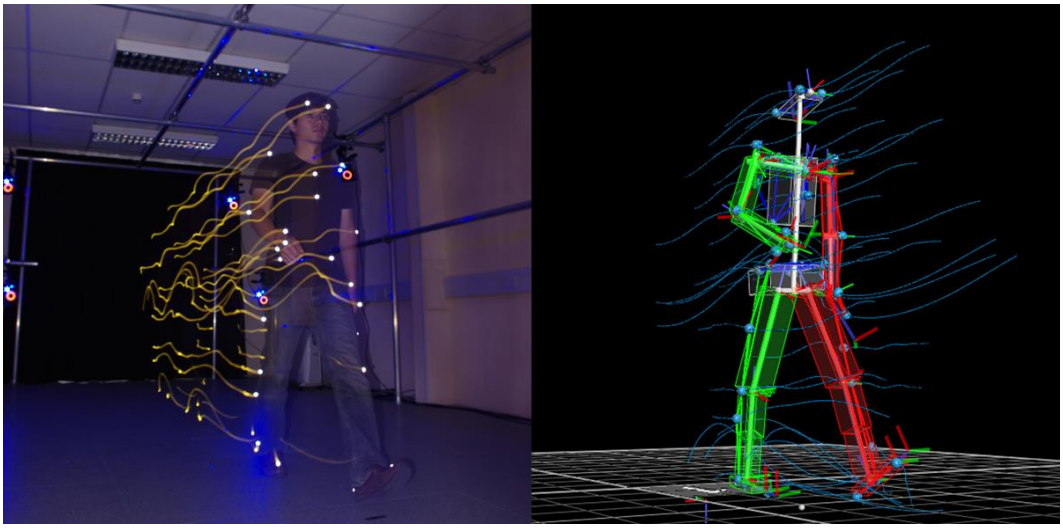

Figure 3.6. The human gait in digital form. Markers are attached to the subjects at different locations, the trajectories of these markers are shown in yellow in the left image and in blue in the right image. The marker location in real space is reconstructed in a 3D space shown in the right image (with perspective), the markers had been associated to body segments such as the upper leg, and form different rigid body segments.

3.5.3 Export data for analysis

After the markers had been reconstructed and labelled, the trajectories of the markers, force data and EMG data were exported in the form of comma separated variables (CSV) files. The CSV files are imported into Matlab® 2009b for further analysis.

3.6 Comparison of kinematic measurement techniques

The three main types of equipment that are used to measure human movement and joint dynamics are goniometers, accelerometers and the use of images or video footage for analysis, in which the most advanced form is video motion capture (e.g. Vicon motion capture and coda motion capture).

Electro-mechanical goniometers such as those available from Biometrics Ltd (Figure 3.7) allow the time history of the angle between two body segments to be measured; it provides instantaneous result of the measured angle. However, the skin surface gradient of human body against the skeletal segment (the bone) is not constant over different joint angles, and can move during joint movement or interactions with other objects. These errors are difficult to quantify. Furthermore, when analysing body segment locations, of which body segments are connected in series, there are accumulated angle errors when multiple body segment locations are derived, for example the location of the foot relative to the trunk of the body has the error accumulated from the ankle joint, knee joint and hip joint.

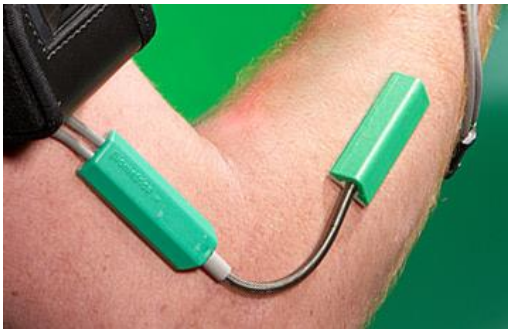

Figure 3.7. A Biometrics Ltd goniometer. Two green sections are attached to the upper arm and forearm with double sided adhesive tape. The flex of the metal braded connection measures the acute angle between the two green sections. Image from www.biometricsltd.com

Accelerometers provide instant results of the acceleration; from which the velocity and position can be calculated or computed through integration of the acceleration signal against time. However the positions of the sensors require known starting positions, which have to be measured using other methods at the beginning of the kinematic measurement.

Motion capture methods are divided into marker based systems and marker-free motion capture. Marker based motion capture systems track special markers attached to anatomical or geometrical locations, while marker free motion capture uses image processing and item recognition to locate desired body segments. Marker based motion capture offers higher accuracy then marker-free motion capture, as the markers to be detected are small, e.g. 14mm diameter, in

comparison to marker-free detection, e.g. detection of a upper arm, approximated to a cylindrical shape, would have a diameter of about 100mm, therefore the derivation of the exact location of a certain point is more accurate for a marker based system than a marker-free system.

In comparison to goniometers, motion capture does not add mechanical components to the joint; therefore there are minimal effects on the mechanical dynamics of body movement. The system measures all markers in a global 3D space; therefore there is no accumulation of errors when deriving locations of multiple linked segments or bodies.

3.7 Consideration for motion capture experiments

To locate the positions of the joints, motion capture markers are placed closed to the centre of the joint, preferably aligned with the axis of rotation. To minimise the movement of the markers against the bones and joints, the markers are placed at the locations where there are minimal soft tissues between the bone and joint and surface of the skin.

The markers' locations cannot be placed at the centre of the rotation of the joints, if the location of the joints are necessary, then these locations can be derived using multiple markers, for example, the centre of the elbow can be calculated by finding the centre location between two markers placed either side of the elbow, which are aligned with the elbow's axis of rotation. Further details of these calculations are shown in section 5.3.4.

Chapter 4 Mathematical Models of the Human Musculo-skeletal System

This chapter describes the development of mathematical models of the human musculo-skeletal system suitable for predictive FES control. As outlined in Chapter 1, model parameters must be anatomically meaningful and obtainable from direct measurements, calculations, or parameter estimation. When parameter values are to be obtained through parameter estimation, they must be unique.

This chapter is divided into three main sections. Section 4.1 describes the work to validate the method to mathematically model the skeletal system as a multi-segment model, based on the Newton-Euler's method of multi-segment dynamics. Comparisons were made between the measured movements of physical multi-segment pendulums and the simulated movements of the models of the same multi-segment pendulums derived from the Newton-Euler method. The model with simulated dynamics that agreed with measured data was then used to model the skeletal system in the musculo-skeletal model developed in section 4.3.

Section 4.2 describes the method to model human skeletal muscle dynamics using the classical Hill muscle model and modified forms of the classical Hill muscle model. The system equations of the muscle models are derived, and assessed to determine whether they can be incorporated as sub-systems into the skeletal models. A suitable form of muscle model was selected to be incorporated into the musculo-skeletal model to form a predictive model. For all biomechanical models of the muscle, some model parameters cannot be directly

measured in vivo; and therefore parameter estimation techniques are required. A mathematical technique called structural identifiability analysis was used to ensure that the parameter values in the muscle models can be uniquely determined from measured data, assuming perfect noise-free data is available.

Section 4.3 describes the development of a musculo-skeletal model of the arm and elbow joint, which used the findings of the analysis of the skeletal modelling method and Hill muscle model to ensure parameter values of the models developed in this work can be obtained experimentally in vivo, and such a model can be used to predict movement. The arm model incorporated two muscle models to represent the elbow flexor muscle and elbow extensor muscles. Through measurement and model fitting, the model parameter values can be estimated. Experiments to obtain measured data and estimate model parameter values are described in Chapter 5 and Chapter 6.

4.1 Skeletal models

As described in section 2.2, the human skeletal system can be modelled as a mechanical system consisting of multiple rigid bodies that represent body segments such as the foot, lower legs, upper legs and trunk, connected with mechanical joints representing the synovial joints such as the ankle, knee and hip. Controlled movement such as standing can be modelled as the control of a multi-segment inverted pendulum. The movement and force dynamics of these models can be described using the Newton-Euler's equations of motion shown in section 2.2.1. Alternatively the skeletal system can also be modelled using the Lagrange-Euler equations, which model the energy and angular movement in the system.

This work selected the Newton-Euler method to describe the dynamics of the model of linked rigid bodies over the Lagrange-Euler method, as forces can be directly measured using force sensors such as load cells and force plates, whereas energy has to be calculated from primary data. Therefore using the Newton-Euler method, model forces predicted by the system equations would

be directly comparable with measured forces and no conversion calculations are necessary.

Before comparing the model of the skeletal model with measured data of human movement, the theory to describe the movement dynamics of multiple linked segments using the Newton-Euler method was validated, to ensure that the theory can reproduce movement dynamics in the physical world. To achieve this, a mechanical multi-segment pendulum was developed, which can be configured as a single segment pendulum, two segments pendulum (double pendulum) or a three segments pendulum. The dynamic movements of the pendulum segments were measured using the Gait Laboratory and compared with the simulated results using forward dynamic simulations derived from the Newton-Euler equations (section 2.2.1.1.).

4.1.1 Multi-segment pendulum design

A three segments aluminium pendulum was designed and manufactured according to the technical drawings shown in Figure 4.1. Aluminium was used as it provides a high stiffness while not being so heavy that a substantial support was required to ensure the pendulum's fixed pivot at location A^0 does not move. Aluminium was also chosen as it has good machining properties. The aluminium segments were cut from readily available aluminium bars, which determined the width and thickness of the segments. All of the segments are identical and are shown in Figure 4.2.

Rotational joints were constructed into both ends of each segment to allow segments to be connected to form multi-segment pendulums. The theory assumes joints connecting segments have no rotational resistance; therefore to reduce rotational friction, the joints consisted of needle roller bearings (IKO Nippon Thompson, RS stock number: 198-9342) press-fitted into holes in the segment. The segments were connected with silver steel axles passed through the roller bearings. The roller bearings and steel axles restricted the oscillation of the segments to one axis (see Figure 4.3). The axles were retained with spring

retainers to prevent the bearings from sliding off the axles. High speed bearing oil was added to the bearings to further minimise rotational friction. Figure 4.1 shows the technical drawing of a single segment of the pendulum, which includes the specification for the physical dimension and material of the segment.

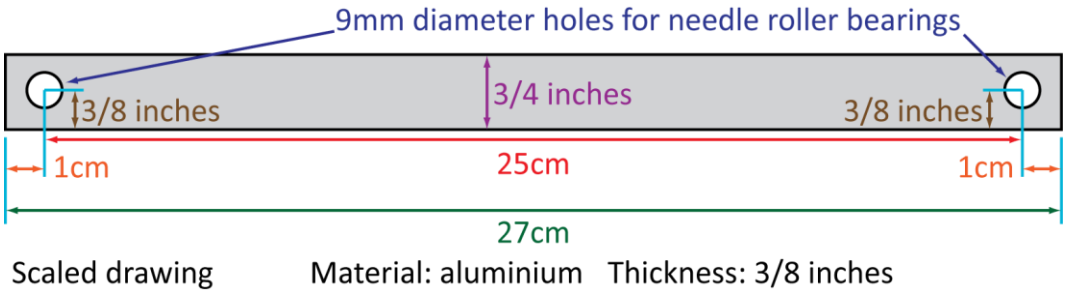

Figure 4.1. Scaled drawing of a single pendulum segment. Total of 3 identical segments are used in this thesis. Two 9mm holes are drilled into each end for needle roller bearings to be press-fitted into the segments.

Figure 4.2. Three pendulum segments and one of the silver steel axle and one axle retaining spring shown at the bottom left. Segments are aluminium with needle bearings press fitted into each end. All segment have identical dimensions. The bottom two segments are shown with motion capture markers attached, which were used for tracking the positions and orientations of the pendulum during measurements.

4.1.2 Multi-segment pendulum experiment protocol

Measurement of the movement of the pendulum was obtained from 3D motion capture in the Gait Laboratory for three physical setups: a single segment pendulum, a two segments pendulum and a three segments pendulum as shown in Figure 4.3. For each physical setup, multiple initial positions of the segments were used. The starting positions were defined by the angles of each segment in relation to the vertical axis (of the global reference frame). These angles were

measured using spirit levels and the live motion capture capability of Vicon Nexus in the Gait Laboratory.

Reflective markers were placed on the pendulum segments, which can be seen in Figure 4.2. These allowed the locations and the angles of each segment to be derived.

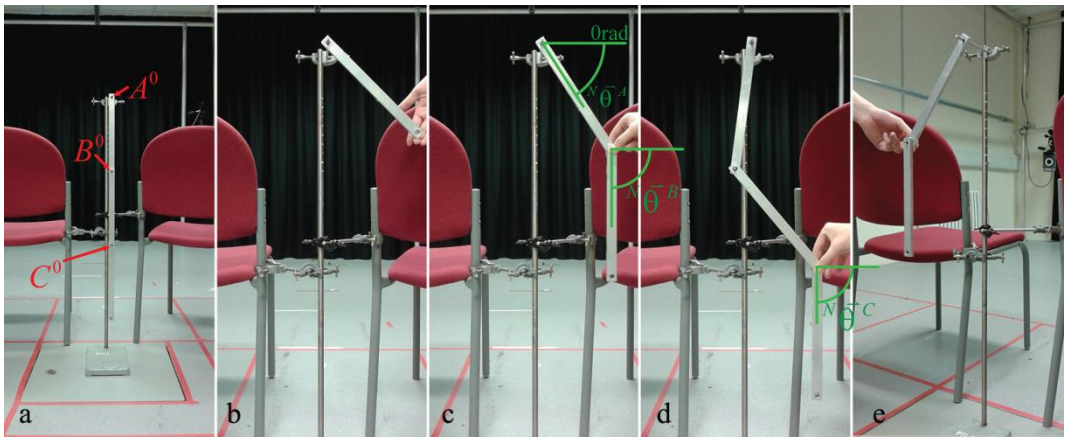

Figure 4.3. Multi-segment pendulum experiment setup. a) Overall setup of a three segments pendulum experiment, showing the support stand fixed to two chairs to reduce stand vibration. The joint pivots are labelled in this figure. b) Setup for one segment pendulum, showing the method to set the initial starting angle. c) Setup for two segments pendulum, the initial position setup shown here is $^N\vec{\theta}^A$ is at about -60° and $^N\vec{\theta}^B$ is at -90°. d) Setup for three segments pendulum, with the angle of segment C labelled. e) View of the two segments pendulum setup from an angled perspective. The motion capture markers are not attached in this figure, but they have been used in the experiments involving motion capture.

In preliminary observation of the single pendulum movement with an initial starting pendulum of 0rad (segment was horizontal), the pendulum oscillated for around 20 minutes before it became stationary due to friction. Preliminary observation recorded the single pendulum to have around 70 periods of swing in 1 minute. From these observations, each motion capture trial recording length was set to 1 minute. Whilst this is much greater than the data required for analysis, this was within the recording and processing capability of the motion capture system (including the 4GB maximum file size limitation of Windows XP 32 bit operating system). An additional assumption was that, if the simulated dynamics did not agree with measured dynamics in the beginning, then the following simulated dynamics later in the time history would not agree with

measured data, therefore the dynamics at the beginning of the measurements and the simulations are the most important.

4.1.3 Single segment pendulum model, system parameters, equations and simulation

The Newton-Euler equations that describe the forces and movement dynamics of the pendulum segment were described in section 2.2.1.1. In order to use the Newton-Euler based model to simulate and predict the movement of a single segment pendulum, the equations describing the model must be reordered and rearranged to allow the forces and movement dynamics to be computed. The model equations that have been reordered into equations for simulation are described in this section. The standard approach to simulate the model is described in Yamaguchi (Yamaguchi, 2001), and forms the basis of the method described in this section.

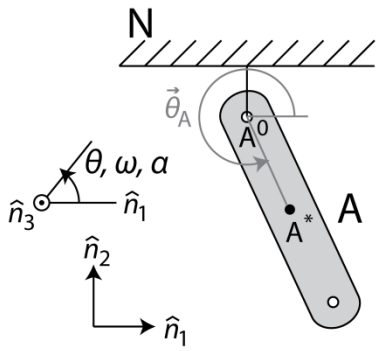

Figure 4.4. Model representation of single segment pendulum shown in Figure 4.3b. Unit vectors of the global reference frame is 1 meter in the horizontal or vertical axes. A^0 is the fixed pivot point, A* is the centre of mass of segment A

This single segment pendulum has the physical properties shown in Table 4.1.

Table 4.1. Mechanical properties of single segment physical pendulum used for modelling

Description	Symbol	Value
Mass of segment A (including markers)	m_A	0.136 kg
Length from pivot A^0 to centre of mass of segment A, A*	l_{A^0A*}	0.125 m
Moment of inertia of segment A	I_A	2.955×10^{-3} kgm^2

In Table 4.1, the mass and length were directly measured. The moment of inertia for segment A, I_A, was calculated at the point of the pivot A^0 (centre of rotation of segment A) using the approximation of the moment of inertia for a rectangle: $\frac{1}{12}m(l^2+w^2)$ and the parallel axis theorem, as shown in Eqn 4.1.

$$I_A = \frac{1}{12}m_A(l^2+w^2) + m_A l_{A^0A^*}^2 \qquad \text{(Eqn 4.1)}$$

where l and w are the length and width of the segment as listed in Figure 4.1, which are 27cm and 1.9cm (3/4 inches) respectively. $l_{A^0A^*}$ is the distance between the centre of mass A* and the pivot point A^0 listed in Table 4.1.

With the physical properties of the pendulum known, the movement of the pendulum model was then predicted using forward simulation, in which model variables at successive points in time (time steps) are calculated by numerical integration. The forward simulation can be separated into two parts: the first part, Part A, was the computation to obtain the segment's angular acceleration $\alpha_A(t)$ and angular velocity $\omega_A(t)$ at a time step t. These were computed using the rearranged forms of the Newton-Euler's equations described in section 2.2.1.1, which are the equations Eqn 4.2 to Eqn 4.5, and computed in the order they are presented. The second part, Part B, involved the numerical integration of $\alpha_A(t)$ and $\omega_A(t)$ from Part A, to obtain the segment's angular velocity and angle for the next time step $t+\delta t$, which are $\omega_A(t+\delta t)$ and $\theta_A(t+\delta t)$ respectively, described by Eqn 4.7. The simulation repeatedly computes Part A and Part B, and advancing a time step after Part B to predict the movement of the pendulum.

To begin the forward simulation of the model, the simulation begins with its initial conditions: angle $\theta_A(t=0)$ and angular velocity $\omega_A(t=0)$. It should also

be noted that the gravity vector $\vec{g} = \begin{bmatrix} 0\hat{n}_1 & -9.81\hat{n}_2 \end{bmatrix}$, where $\hat{n}_1$ and $\hat{n}_1$ are unit vectors in metres shown in the diagrams of the pendulums, e.g. Figure 4.4.

The positional and angular descriptions of all segments in this section and for the two segments pendulum in section 4.1.4 are described in relation to the global space, which is the global space N. Angles are measured counter clockwise from the horizontal, in which zero degree (radian) is in the direction of the unit vector $\hat{n}_1$, as shown in Figure 4.4.

The Newton-Euler equations that describe the model shown in section 2.2.1.1 have been rearranged into the following equations to allow the segment's angular acceleration $\alpha_A(t)$ to be computed from $\theta_A(t)$ and $\omega_A(t)$ for each time step t in the simulation. The derivations of these equations are also described.

First, in order to allow forces and moment of forces to be computed, the locations of the pivot and the centre of mass of segment A have to be derived. Using the segment angle and its length in Table 4.1, and Eqn 2.1, the position of $\vec{A}^0(t)$ and $\vec{A}^*(t)$ can be found using Eqn 4.2.

$$\begin{aligned} \vec{A}^0(t) &= \begin{bmatrix} 0\hat{n}_1 & 0\hat{n}_2 \end{bmatrix} \\ \vec{A}^*(t) &= \vec{A}^0(t) + \begin{bmatrix} l_{A^0A^*}\cos\theta_A(t)\hat{n}_1 & l_{A^0A^*}\sin\theta_A(t)\hat{n}_2 \end{bmatrix} \end{aligned} \qquad \text{(Eqn 4.2)}$$

These locations of $\vec{A}^0(t)$ and $\vec{A}^*(t)$ are then used to derive a vector between these two points to be used in the Newton-Euler equations previously presented in Eqn 2.15 and Eqn 2.17.

$$\vec{\rho}_{A^0A^*}(t) = \vec{A}^*(t) - \vec{A}^0(t) \qquad \text{(Eqn 4.3)}$$

To compute the angular acceleration of segment A, all forces acting on the segment must be known. By rearranging Newton's second law that describes the forces acting on segment A as shown in Eqn 2.15, the force of the fixed pivot N at A^0 acting on A, $\vec{F}_{NA}(t)$, can be calculated:

$$\vec{F}_{NA}(t) = -\left(m_A\vec{g} + m_A\left(\omega_A(t)\right)^2\vec{\rho}_{A^0A^*}(t)\right) \qquad \text{(Eqn 4.4)}$$

In Eqn 4.4, the term $\left(\omega_A(t)\right)^2\vec{\rho}_{A^0A^*}(t)$ is the linear acceleration of segment A, i.e. $\vec{a}_A(t)$, and is the centripetal acceleration of segment A towards A^0 during the swing of the pendulum. It is derived using the centripetal acceleration: $\omega^2 r$ where r is the radius of arc of the trajectory. In this case the radius is $\vec{\rho}_{A^0A^*}(t)$, which is the vector between the pivot A^0 and centre of mass A*. It should be noted that using centripetal acceleration to derive the linear acceleration is additional to the method shown in (Yamaguchi, 2001). Yamaguchi uses $\vec{F}_{NA}(t) = -\left(m_A\vec{g} + m_A\vec{a}_A(t)\right)$ instead of Eqn 4.4, where $\vec{a}_A(t)$ is the linear acceleration of the point A*. However, with the equation in such form, there are two unknown variables in the equation, which are $\vec{F}_{NA}(t)$ and $m_A\vec{a}_A(t)$, for which additional expressions must be obtained.

Finally the angular acceleration of segment A can be computed, by rearranging Euler's second law describing the segment's moment as shown in Eqn 2.17. Summing the products of distances (Eqn 4.3) and perpendicular forces (Eqn 4.4) **from the centre of mass**, gives the angular acceleration of segment A:

$$\alpha_A(t) = \frac{1}{I_A}\left(-\vec{\rho}_{A^0A^*}(t)\times\vec{F}_{NA}(t)\right) \qquad \text{(Eqn 4.5)}$$

For Eqn 4.5, note that gravity acting on segment A is not included, as the moment is computed at the centre of mass, this gives a distance of zero between the averaged point of gravity acting on the mass and the point of moment calculation, therefore the moment due to gravity is eliminated.

When describing vectors as 1x2 matrices as shown in Eqn 4.6, the moment of a force $\vec{\rho}(t)\times\vec{F}(t)$ is calculated using the following operation.

$$\vec{\rho}(t)\times\vec{F}(t)\equiv\begin{bmatrix}\rho_{\hat{n}_1}(t) & \rho_{\hat{n}_2}(t)\end{bmatrix}\begin{bmatrix}0 & 1\\ -1 & 0\end{bmatrix}\begin{bmatrix}F_{\hat{n}_1}(t) & F_{\hat{n}_2}(t)\end{bmatrix}^T \qquad \text{(Eqn 4.6)}$$

It should also be noted that in Eqn 4.5, the moment was calculated at the centre of mass instead of at the point A^0 as shown in (Yamaguchi, 2001). If the moment is summed around the pivot A^0, then it would also need to include the linear acceleration of the segment $\vec{a}_A(t)$, in which case the moment would be $\vec{\rho}_{A^0A^*}(t)\times m_A\vec{a}_A(t)$. However as discussed for Eqn 4.4, if the linear acceleration of the segment is indeterminable or if the centripetal acceleration derivation approach shown in Eqn 4.4 is incorrect, then computing the moment around A^0 would introduce an error.

Eqn 4.2 to Eqn 4.5 complete the computation required for each simulation time step t, and gives the angular velocity $\omega_A(t)$ (directly taken from the input angular velocity for the time step t) and angular velocity $\alpha_A(t)$ from Eqn 4.5. The forward simulation then integrates the angular velocity and angular acceleration, to give the angle and angular velocity for the next time step $t+\delta t$, which are $\theta_A(t+\delta t)$ and $\omega_A(t+\delta t)$ respectively.

$$\begin{aligned}\theta_A(t+\delta t) &= \theta_A(t)+\omega_A(t)\delta t\\ \omega_A(t+\delta t) &= \omega_A(t)+\alpha_A(t)\delta t\end{aligned} \qquad \text{(Eqn 4.7)}$$

Eqn 4.7 is the Euler's method (first order explicit solver), which is the simplest method to solve ordinary differential equation. However when this explicit Euler method was used, the fixed step size causes large numerical error when variables (angle, velocity and acceleration) tends to zero. Therefore an improved ODE solving method was used to simulate this forward dynamic model: ode45 ordinary differential equation solver (MathWorks®, 2009) in MATLAB 2009b, where ode45 performed the integration shown in Eqn 4.7. The time step δt was

variable and determined internally by ode45 using the Runge-Kutta method to reduce accumulated numerical errors (MathWorks®, 2009).

The starting position and angular velocity of the pendulum for the simulations were obtained from measurement of the physical pendulum movement shown in section 4.1.1 and 4.1.2. The simulated trajectory is shown together with the measured data in section 4.1.5.

4.1.4 Two segments pendulum model, system parameters, equations and simulation

In this section, the method used to simulate the movement dynamics of a two segments pendulum is described, which represented the physical two segments pendulum shown in Figure 4.3b. It is an expanded version of the single pendulum method in section 4.1.3, in which the Newton-Euler equations that describe the movement dynamics of the pendulum segments presented in section 2.2.1.1, were rearranged to allow the movement of the two segments pendulum to be predicted through forward dynamic simulation.

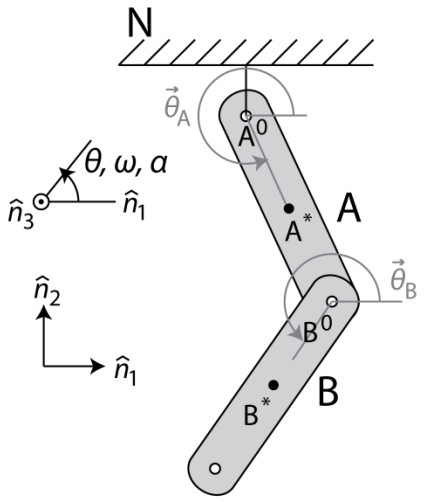

Figure 4.5. Model representation of single segment pendulum shown in Figure 4.3c.

The two segments pendulum has the physical properties described in Table 4.2. The masses and lengths were directly measured. The moment of inertia of segment A was calculated at the point of A^0 using Eqn 4.1. The moment of inertia of segment B, is calculated at the point of centre of mass of B, B* (Yamaguchi, 2001), and uses the moment of inertia approximation of a rectangle, see Eqn 4.8.

Table 4.2. Mechanical properties of two segments physical pendulum used for modelling

Description	Symbol	Value
Mass of segment A (including markers and half of steel axle at B^0)	m_A	0.139 kg
Mass of segment B (including markers and steel axle at B^0)	m_B	0.139 kg
Length from pivot A^0 to centre of mass of segment A, A*	l_{A^0A*}	0.125 m
Length from pivot A^0 to pivot B^0	$l_{A^0B^0}$	0.25 m
Length from pivot B^0 to centre of mass of segment B, B*	l_{B^0B*}	0.125 m
Moment of inertia of segment A	I_A	2.955×10^{-3} kgm^2
Moment of inertia of segment B	I_B	4.182×10^{-6} kgm^2

$$I_B = \frac{1}{12} m_B (l^2 + w^2) \qquad \text{(Eqn 4.8)}$$

l and w have the same meanings as in Eqn 4.1 and are 27cm and 1.9cm (3/4 inches) respectively.

As well as the system constants listed in Table 4.2. The forward simulation required initial conditions, which were the angles and angular velocities of the two segments: $\theta_A(t=0)$, $\omega_A(t=0)$, $\theta_B(t=0)$ and $\omega_B(t=0)$.

The Newton-Euler equations that describe the model shown in section 2.2.1.1 have been rearranged into Eqn 4.9 to Eqn 4.12, which allow the segments' angular accelerations $\alpha_A(t)$ and $\alpha_B(t)$ to be computed from $\theta_A(t)$, $\theta_B(t)$, $\omega_A(t)$ and $\omega_B(t)$ in each successive time step in the forward dynamics simulation.

First, in order to allow forces and moment of forces to be computed, the locations of the pivots and the centres of mass of segment A and B have to be derived. Using the segment angles, their lengths in Table 4.2 and Eqn 2.1 to Eqn 2.3, the position of $\vec{A}^0(t)$, $\vec{A}^*(t)$, $\vec{B}^0(t)$ and $\vec{B}^*(t)$ can be found using Eqn 4.9.

$$\begin{aligned}
\vec{A}^0(t) &= \begin{bmatrix} 0\hat{n}_1 & 0\hat{n}_2 \end{bmatrix} \\
\vec{A}^*(t) &= \vec{A}^0(t) + \begin{bmatrix} l_{A^0A^*}\cos\theta_A(t)\hat{n}_1 & l_{A^0A^*}\sin\theta_A(t)\hat{n}_2 \end{bmatrix} \\
\vec{B}^0(t) &= \vec{A}^0(t) + \begin{bmatrix} l_{A^0B^0}\cos\theta_A(t)\hat{n}_1 & l_{A^0B^0}\sin\theta_A(t)\hat{n}_2 \end{bmatrix} \\
\vec{B}^*(t) &= \vec{B}^0(t) + \begin{bmatrix} l_{B^0B^*}\cos\theta_B(t)\hat{n}_1 & l_{B^0B^*}\sin\theta_B(t)\hat{n}_2 \end{bmatrix}
\end{aligned} \qquad \text{(Eqn 4.9)}$$

These locations are then used to derive the vectors (shown in Eqn 4.10), which are used in the Newton-Euler equations previously presented in Eqn 2.14, Eqn 2.15, Eqn 2.17 and Eqn 2.18.

$$\begin{aligned}
\vec{\rho}_{A^0A^*}(t) &= \vec{A}^*(t) - \vec{A}^0(t) \\
\vec{\rho}_{A^0B^0}(t) &= \vec{B}^0(t) - \vec{A}^0(t) \\
\vec{\rho}_{A^*B^0}(t) &= \vec{B}^0(t) - \vec{A}^*(t) \\
\vec{\rho}_{B^0B^*}(t) &= \vec{B}^*(t) - \vec{B}^0(t)
\end{aligned} \qquad \text{(Eqn 4.10)}$$

To compute the angular acceleration of the two segments A and B, all forces acting on the segments must be known. By rearranging Newton's second law that describes the forces acting on segment A and B as shown in Eqn 2.14 and Eqn 2.15, and starting from the most distal segment and working inwards towards A^0 (Yamaguchi, 2001), the force of segment B acting on segment A, $\vec{F}_{BA}(t)$, and the force of the fixed pivot N at A^0 acting on A, $\vec{F}_{NA}(t)$, can be calculated:

$$\begin{aligned}
\vec{F}_{BA}(t) &= m_B\vec{g} + m_B\left(\left(\omega_A(t)\right)^2\,\vec{p}_{A^0B^0}(t) + \left(\omega_B(t)\right)^2\,\vec{p}_{B^0B^*}(t)\right) \\
\vec{F}_{AN}(t) &\equiv -\vec{F}_{NA}(t) = m_A\vec{g} + m_A\left(\omega_A(t)\right)^2\,\vec{p}_{A^0A^*}(t) + \vec{F}_{BA}(t)
\end{aligned} \qquad \text{(Eqn 4.11)}$$

It should also be noted that from Newton's third law (and Eqn 2.16), that $\vec{F}_{BA}(t) \equiv -\vec{F}_{AB}(t)$.

The terms $(\omega_A(t))^2 \vec{p}_{A^0B^0}(t) + (\omega_B(t))^2 \vec{p}_{B^0B^*}(t)$ in Eqn 4.11 to calculate $\vec{F}_{BA}(t)$ give the linear acceleration of segment B, $\vec{a}_B(t)$, which is the centripetal acceleration of segment B towards the pivot at B^0 plus the centripetal acceleration of B^0 towards A^0. This derivation of linear acceleration uses the same principle as that used to derive the linear acceleration of segment A in section 4.1.3, Eqn 4.5.

Finally the angular acceleration of segment A and B can be computed, by rearranging Euler's second law describing the segment's moment as shown in Eqn 2.17 and Eqn 2.18. Starting from the most inner segment, i.e. segment A, and working outwards, the angular accelerations for segment A and B are calculated. Summing the products of distances and perpendicular forces **around the centre of mass** for each segment, gives the angular accelerations of segment A and B:

$$\alpha_A(t) = \frac{1}{I_A}\left(\vec{\rho}_{A^0A^*}(t) \times \vec{F}_{NA}(t) - \vec{\rho}_{A^*A^0}(t) \times \vec{F}_{BA}(t)\right)$$
$$\alpha_B(t) = \frac{1}{I_B}\left(\vec{\rho}_{B^0B^*}(t) \times \vec{F}_{AB}(t)\right) - \alpha_A(t) \qquad \text{(Eqn 4.12)}$$

In Eqn 4.12, the moments were calculated around the centre of masses of each segment, i.e. at A* for segment A and at B* for segment B, instead of calculated at the pivots A^0 and B^0 in the method described by Yamaguchi (Yamaguchi, 2001). This uses the same principle as that used for deriving Eqn 4.5.

It should be also noted that the function that had been derived to calculate angular acceleration of B in Eqn 4.12 includes the term $-\alpha_A(t)$, which is a subtraction of the angular acceleration of segment A. This is not presented in the Euler's equation (Eqn 2.18). Although this has not been described previously in the literature, preliminary comparison of simulation results with and without the

inclusion of this term (see Figure 4.7 in section 4.1.5), showed that simulation with the inclusion of the $-\alpha_A(t)$ term gave better agreement with measured dynamics, in comparison to the simulated movement without the $-\alpha_A(t)$ term.

Eqn 4.9 to Eqn 4.12 conclude the computation required for each simulation time step t, and give the angular velocities $\omega_A(t)$ and $\omega_B(t)$ (directly taken from the input angular velocities for the time step t) and angular velocity $\alpha_A(t)$ and $\alpha_B(t)$ from Eqn 4.12. The forward simulation then integrates the angular velocities and angular accelerations, to give the angles and angular velocities of segment A and B for the next time step $t+\delta t$, which are $\theta_A(t+\delta t)$, $\omega_A(t+\delta t)$, $\theta_B(t+\delta t)$ and $\omega_B(t+\delta t)$ respectively.

$$\begin{aligned}
\theta_A(t+\delta t) &= \theta_A(t) + \omega_A(t)\delta t \\
\omega_A(t+\delta t) &= \omega_A(t) + \alpha_A(t)\delta t \\
\theta_B(t+\delta t) &= \theta_B(t) + \omega_B(t)\delta t \\
\omega_B(t+\delta t) &= \omega_B(t) + \alpha_B(t)\delta t
\end{aligned} \qquad \text{(Eqn 4.13)}$$

Again, Eqn 4.13 represents the first order explicit Euler method to solve ODE, but this model was simulated using the ode45 solver (Runge-Kutta method) (MathWorks®, 2009) in Matlab to reduce numerical accumulated errors. The starting angles and angular velocities of the two segments pendulum for simulation were obtained from the measurements described in section 4.1.2. The simulated trajectory is shown together with the measured data in section 4.1.5.

4.1.5 Results

4.1.5.1 Single segment pendulum

The measured trajectory of the single segment pendulum from the motion capture experiment was used to compute the angle of segment A over time, in relation to the global frame N. The time history of the pendulum's measured angle from motion capture experiment and simulated angle from the model equations shown in section 4.1.3 are plotted in Figure 4.6.

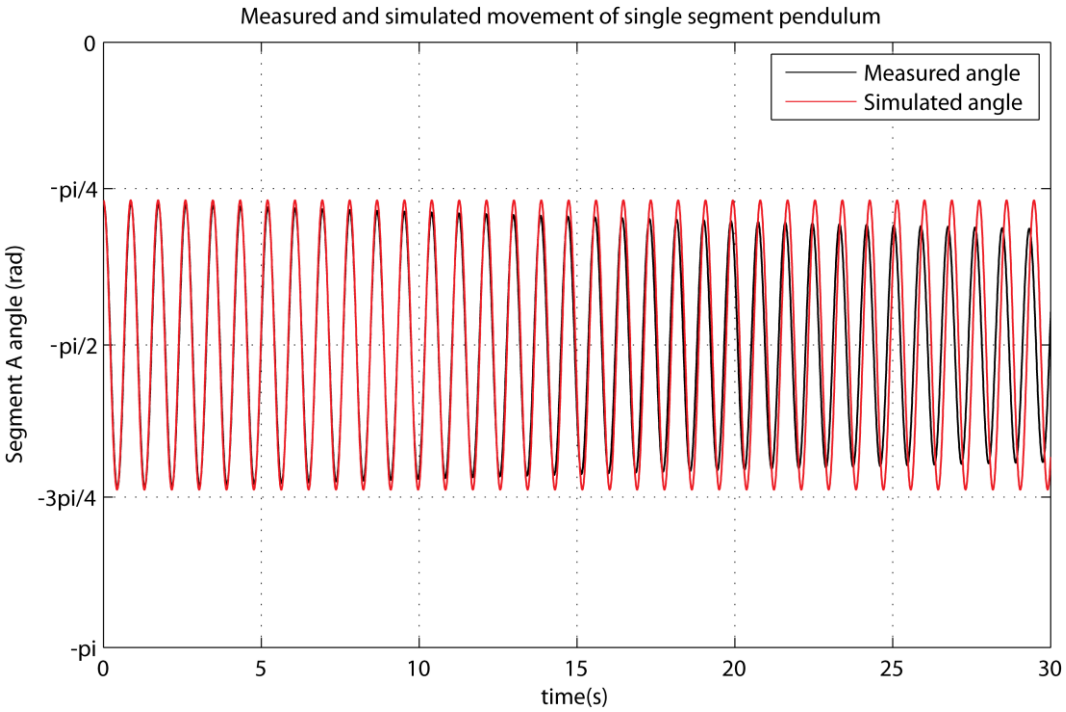

Figure 4.6. Measured and simulated movement trajectory of the single segment pendulum

The pendulum started from a static position, the measured initial starting angle of the pendulum was -0.82rad, which was 0.75rad from the vertical axis. This angle was used as the initial pendulum angle in the simulation. The frequency for the first oscillation period of the pendulum from measured data was 1.149Hz. The frequency of the simulated oscillation was 1.156Hz. The simulation frequency remains the same for the whole time history, as energy lost due to friction was not included in the model. The measured amplitude and frequency at 10s after the start of the experiment were 0.696rad and 1.156Hz respectively. The amplitude was 92% of the starting amplitude and the frequency was 0.6% higher than the measured starting frequency. At 30 second, the measured

amplitude and frequency were 0.608rad and 1.176Hz, which were 81% of the starting amplitude and 2.3% higher than the measured starting frequency respectively. At 30 seconds, the measured oscillation leads the simulation with a phase shift of 1.03rad (59.3°).

4.1.5.2 Two segments pendulum

In section 4.1.4, the calculation to compute the angular acceleration of segment B in Eqn 4.12 included a $-\alpha_A(t)$ term. The preliminary simulated results with and without such term in comparison with measured results are shown in Figure 4.7.

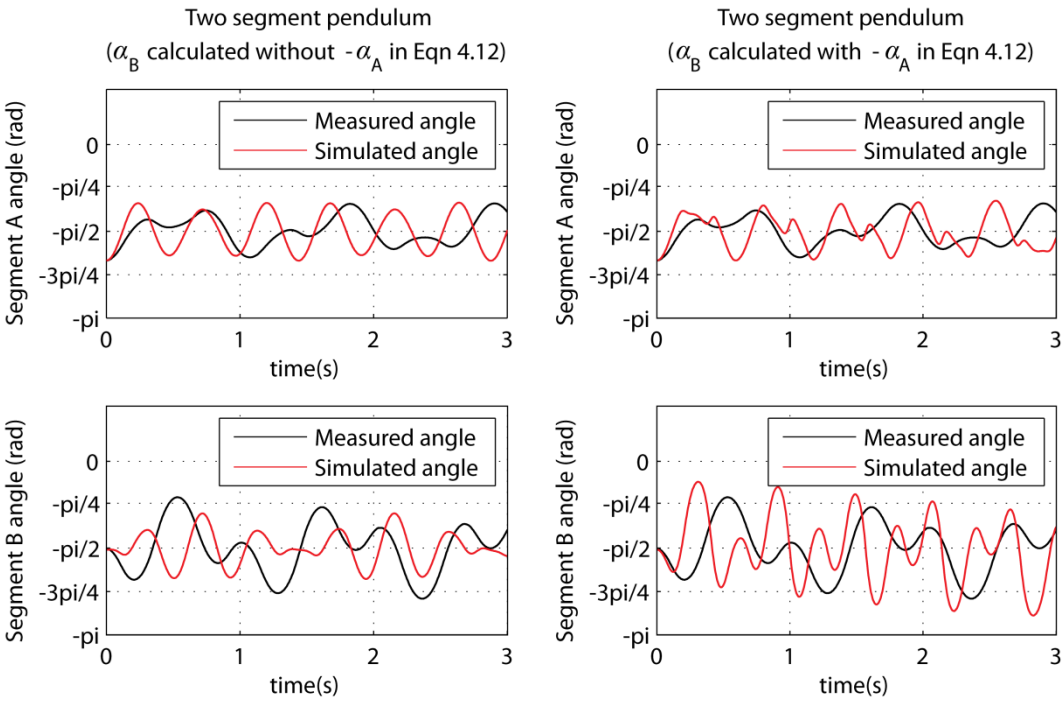

Figure 4.7. Comparison of the simulated dynamics of the two segments pendulum with and without the $-\alpha_A(t)$ term in the calculation of $\alpha_B(t)$ in Eqn 4.12 against measured data. The red lines in the two graphs on the left are simulated segment movement without the $-\alpha_A(t)$ term. The red lines in the two graphs on the right are simulated segment movement with the $-\alpha_A(t)$ term.

The initial starting angle for segment A from measurement was -2.1rad (0.53rad from vertical), and 1.57rad for segment B (vertical). The starting angles were the same for the simulation. The simulated movement of segment A without the $-\alpha_A(t)$ term, shown in the top left graph in Figure 4.7 behaved more similarly to a single segment pendulum in comparison to the simulated result with the

$-\alpha_A(t)$ term, shown in the top right graph in Figure 4.7. This also showed that with the $-\alpha_A(t)$ term, the movement of segment B was more influenced by the addition of segment B in the system, which is more similar to the movement characteristics of segment A in the measured result.

Segment B started from a vertical position, the measured result showed that it swung towards -3π/4 rad after the start of the movement, this characteristic is better reflected in the simulation with the $-\alpha_A(t)$ term in the calculation of $\alpha_B(t)$ in Eqn 4.12.

The measured angles and simulated angles from the model described in section 4.1.4, Eqn 4.9 to Eqn 4.13, are plotted in Figure 4.8.

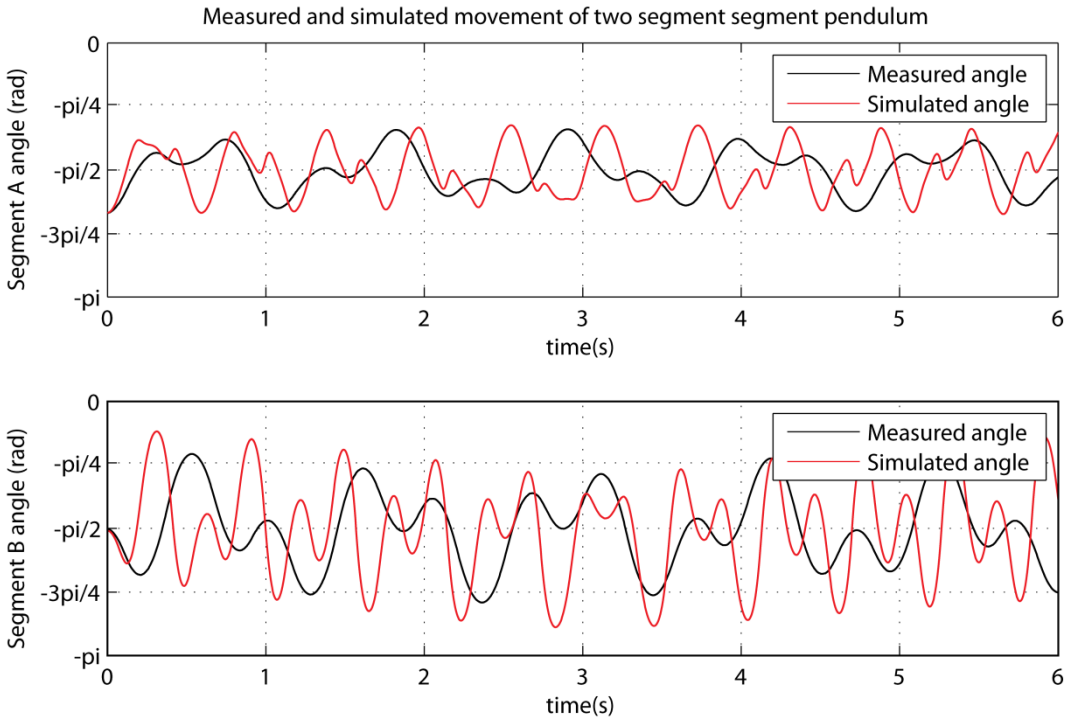

Figure 4.8. Measured and simulated movement trajectory of the two segment pendulum using the simulation method shown in section 4.1.4, using Eqn 4.9 to Eqn 4.12.

The initial angles for segment A are -2.10rad and -1.57rad respectively. Starting velocities of both segments were 0rads^{-1}.

4.1.6 Discussion

It is advantageous to validate the theories of dynamic movement using measurements of mechanical pendulum movements instead of human movements. Physical pendulums can be manufactured to have uniform density and known properties, while it is not possible to specify the physical properties of the human body. The mass and moment of inertia of a mechanical (e.g. metal) segment can also be accurately measured and determined, while the mass of a body segment (in vivo) cannot be directly measured, and the derivations of the centre of mass and moment of inertia required certain assumptions. Using physical pendulums allows for measurements to give minimal error in model parameter values.

4.1.6.1 Pendulum models

In this thesis, three physical pendulum segments were produced and it was possible to analyse the dynamics of a three segments pendulum. However, only the modelling of the single segment pendulum (section 4.1.3) and a two segments pendulum (section 4.1.4) were described. The assumption was that if the model of a two segments pendulum does not produce realistic results, then models and simulations of systems consisting of more segments would not produce realistic results. Therefore this work focused on improving the model of the two segments pendulum.

In section 4.1.3, the method for simulating the movement of the single pendulum can be simplified by computing the moment of segment A in Eqn 4.5 around A^0 instead of A*, then the force of N acting on A in Eqn 4.4 would not need to be considered, and Eqn 4.4 is unnecessary. However the presented method described in section 4.1.3 is scalable to a multiple-segment system, where the equations can be applied to other segments in a multiple segment pendulum, such as the two segments pendulum described in section 4.1.4.

4.1.6.2 Simulated results

The results in Figure 4.6 and Figure 4.8 have shown that the single pendulum model produced results that agree with measured data, while the two segments model did not produce results that agree with measured data.

The measured and simulated movement of the single pendulum in Figure 4.6 show that the measured amplitude at 10s had decreased by about 10% from the original amplitude, due to friction. This was not included in the model, and therefore the measured data after 10s from the start of the experiment was not used for comparison with simulated movement.

A good agreement can be seen between the measured and simulated movement of the single pendulum in Figure 4.6. The model parameter values were measured or calculated and did not have to be obtained through model fitting or parameter estimation. This showed that the Newton-Euler method to model the movement of a single pendulum can provide good agreement with measured data.

Figure 4.7 showed the effect of the simulated movement of the two segments pendulum with and without the term $-\alpha_A(t)$ in the calculation of $\alpha_B(t)$ in Eqn.4.12. It can be seen that the initial measured movement of segment B swings towards $-\frac{3}{4}\pi\ rad$. The simulation with the $-\alpha_A(t)$ term has shown better agreement with this movement characteristic than the simulation without the $-\alpha_A(t)$ term. Furthermore the measured movement of segment A did not resemble a sine wave, however the simulated movement of segment A without the $-\alpha_A(t)$ resembled a sine wave with very small distortion. This suggests the movement dynamics of A is significantly affected by the movement of segment B, which can be seen in the simulated movement of segment A with the $-\alpha_A(t)$ term in the calculation of $\alpha_B(t)$.

Six seconds of simulated and measured data of the two segments pendulum (with the $-\alpha_A(t)$ term in the calculation of $\alpha_B(t)$) are shown in Figure 4.8. The shape of the trajectories of the segments are similar between the measured and simulated result, however there is a noticeable difference in the oscillation frequencies between the measured and simulated data. The oscillation frequency of the simulated data was about twice of the oscillation frequencies of the measured data. From the theory of second order system oscillation (Cartwright, 2001), a second order system of the form as shown in Eqn 4.14, where $x(t)$ is the system variable and $u(t)$ is the system input, has an undamped natural frequency of ω_n for a step input.

$$\frac{1}{\omega_n^2}\frac{dx^2(t)}{dt^2}+\frac{2\zeta}{\omega_n}\frac{dx(t)}{dt}+x(t)=u(t) \qquad \text{(Eqn 4.14)}$$

If Eqn 4.14 is rearranged into

$$\frac{dx^2(t)}{dt^2}=\omega_n^2\left(-\frac{2\zeta}{\omega_n}\frac{dx(t)}{dt}-x(t)+u(t)\right) \qquad \text{(Eqn 4.15)}$$

then this can be compared with Eqn 4.12 where $x(t)$ is equivalent to $\theta(t)$ and ω_n^2 is equivalent to $1/I_A$ and $1/I_B$. This suggests that the mathematical derivations of the moment of inertias for the two segments pendulum may be incorrect and caused the error in oscillation frequency. This suggests that the method to calculate the moment of inertias for the segments should be an area of investigation if the Newton-Euler method is to produce simulated dynamics that agree with measurements for two or more segments pendulums and multi-linked rigid bodies.

In this work, the single pendulum forward simulation has produced results that agreed with measured data, while it has not been the case for the double and triple pendulum. This suggests that accumulated numerical error in the ODE solver is not the cause for the error, but instead additional theory is required to

support the Newton-Euler's equation of dynamics motion to produce realistic results. A suggestion for this is that the calculation of the moment of inertia for segment B and any other distal segments in a multi-segment system should be reassessed.

Several new methods had been used in this work in attempting to identify and rectify the causes of the disagreement in dynamics, including the derivations of linear accelerations using centripetal accelerations in Eqn 4.4 and Eqn 4.11, and the inclusion of the angular acceleration of segment A in the calculation of the angular acceleration of segment B in Eqn 4.12. However the end results were still unsatisfactory.

4.1.6.3 Alternative methods and work by other researchers

The Lagrange-Euler method has not been used in this work. However, the Lagrange-Euler and the Newton-Euler methods have been shown to be equivalent though symbolic analysis (Silver, 1982), therefore if the Newton-Euler method cannot give good agreement between the measured and simulated data, then this implies the Lagrange-Euler method cannot produce good agreement either.

Other researchers in biomechanics (John et al., 2012) have also used the Newton-Euler method in multi-segment musculo-skeletal modelling, for inverse analysis to compute joint forces, and forward simulation to predict movement. John et al has encountered the problem that using the Newton-Euler's equations of motion in inverse dynamics analysis has resulted in residual forces and acceleration in the system. They have used a least square estimation technique to minimise the error, however the error reduction method was not a deterministic and robust approach, and this does not fully solve the problem.

External to biomechanics, the Newton-Euler method is widely used in robotics (Niku, 2001), however hardware feedback implantations have been the norm to correct angular, positional and velocity errors. Subsequently there has not been

a need in the field of automation and robotics to rectify the problem in the Newton-Euler method identified in this work and (John et al., 2012).

Clearly if one wishes to successfully predict multi-segment movement and apply this in biomechanics, further investigations into the multi-segment modelling theory are required.

4.1.7 Conclusion

The validation work in this section has determined that only a single pendulum model can produce simulated results that agree with measured results, and therefore the musculo-skeletal model developed in this thesis will only examine the movement of a single segment, where that moveable segment is connected to a non-moving segment via a pivot that is fixed in position.

4.2 Muscle models

This section describes the work to develop muscle models suitable for incorporating into musculo-skeletal models. Section 4.2.1 derives the model equation for the classical Hill muscle. Section 4.2.2 discusses the feasibility of incorporating the classical Hill muscle model as a sub system into musculo-skeletal models, and subsequently leads to the development of the modified Hill muscle model described in section 4.2.3. This modified Hill muscle model was used for the development of a musculo-skeletal model or the human arm with the elbow joint in section 4.3. The estimation of the parameters values are described in Chapter 5 and Chapter 6.

4.2.1 The classical Hill muscle model (equation derivation)

The classical Hill muscle model (Hill, 1938) and the anatomical meanings of its structure and each of the internal components were introduced in Section 2.2.2. To be able to incorporate this model into a musculo-skeletal model, a model equation must be obtained that describes the muscle force as a function of its internal components.

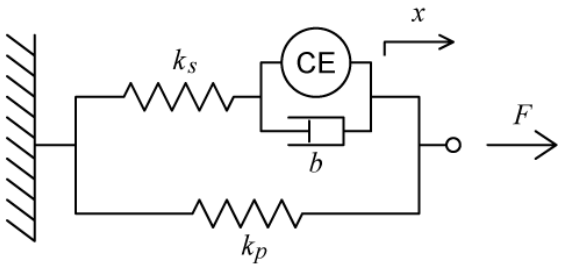

Figure 4.9. Classical Hill muscle model (Hill, 1938)

Figure 4.9 shows the classical Hill muscle model representing the bulk of the muscle, excluding the free tendon(s) external to the bulk of the muscle that connect(s) the muscle to bones. The muscle model has 4 mechanical elements, including a serial elastic element with spring constant k_s and length x_{ks} ; in series with two parallel components: a dashpot element with damping coefficient b and contractile element CE, both with length x_b . These components, excluding CE, are referred to as the passive components in the

model. The contractile element (CE) is the active component of the muscle and is a pure force generator, producing a force $F_{CE}(t)$. These three elements are in parallel with an elastic element (also passive component) with spring constant k_p and length x_{kp}, as shown in Figure 4.9. It should be noted that the sum of the length of the serial spring and the damper is the length of the parallel spring, which is also the length of the muscle (Eqn 4.21).

In this thesis, the spring and damping elements in the muscles are assumed to be linear. From basic mechanics, the relationships between the forces and lengths of the springs and the relationship between force and velocity of the damper are shown in Eqn 4.16 to Eqn 4.18:

The force $\vec{F}_{ks}(t)$ of the serial spring element k_s in the direction shown in Figure 4.9 is given by

$$\vec{F}_{ks}(t) = -k_s(\vec{x}_{ks}(t) - \vec{x}_{ks\_0}) \qquad \text{(Eqn 4.16)}$$

where x_{ks_0} is the natural length of the serial spring element in which no force is generated.

The force $\vec{F}_b(t)$ of the damping element b is given by

$$\vec{F}_b(t) = -b\frac{d\vec{x}_b(t)}{dt} \qquad \text{(Eqn 4.17)}$$

where $\frac{d\vec{x}_b(t)}{dt}$ is the lengthening/shortening velocity of the damping element and the contractile element.

Finally the force $\vec{F}_{kp}(t)$ of the parallel spring element k_p is given by

$$\vec{F}_{kp}(t) = -k_p(\vec{x}_{kp}(t) - \vec{x}_{kp\_0}) \equiv -k_p(\vec{x}(t) - \vec{x}_0) \qquad \text{(Eqn 4.18)}$$

where $\vec{x}_{kp\_0}$ is the natural length of the parallel spring in which no force is generated when the parallel element is at this length. The length of the parallel spring is also the overall length of the muscle $\vec{x}(t)$, and the static length at which the muscle exerts no force is $\vec{x}_0$, which is the same as $\vec{x}_{kp\_0}$.

The forces of k_s, b and CE also have the following relationship:

$$\vec{F}_{ks}(t) = -\vec{F}_b(t) - \vec{F}_{CE}(t) \quad \text{(Eqn 4.19)}$$

The total muscle force $\vec{F}(t)$ is the sum of the serial and parallel spring force:

$$\vec{F}(t) = \vec{F}_{ks}(t) + \vec{F}_{kp}(t) \quad \text{(Eqn 4.20)}$$

The total length of the muscle $\vec{x}(t)$ is:

$$\vec{x}(t) \equiv \vec{x}_{kp}(t) = \vec{x}_{ks}(t) + \vec{x}_b(t) \quad \text{(Eqn 4.21)}$$

Using Eqn 4.16 to Eqn 4.21, the derivation described in Eqn 4.22 to Eqn 4.23 gives a model equation that relates the muscle's total force $F(t)$ to the muscle's total length $\vec{x}(t)$ and their first order derivatives. It should be noted that the aim of this derivation is to produce an equation that describes the model without the inclusion of any internal lengths or velocities of individual components (i.e. $\vec{x}_{ks}(t)$, $\vec{x}_b(t)$ and $d\vec{x}_b(t)/dt$) in the muscle model. Physically these internal lengths are unknown and cannot be measured, as the characteristics of the muscle model components have their origins in the sarcomere level, and their effect on the whole muscle is the sum of the contributions from many sarcomere. Therefore these parameters lengths have no anatomical or physiological meaning at the whole muscle level and are not directly measurable.

Beginning with differentiating Eqn 4.21, this gives:

$$\begin{aligned}
\frac{d\vec{x}(t)}{dt} &= \frac{d\vec{x}_{ks}(t)}{dt} + \frac{d\vec{x}_{b}(t)}{dt} \\
&= -\frac{1}{k_s}\frac{d\vec{F}_{ks}(t)}{dt} - \frac{\vec{F}_{b}(t)}{b} \\
&= -\frac{1}{k_s}\left(\frac{d\vec{F}(t)}{dt} - \frac{d\vec{F}_{kp}(t)}{dt}\right) - \frac{\vec{F}_{b}(t)}{b} \\
&= -\frac{1}{k_s}\left(\frac{d\vec{F}(t)}{dt} - \frac{d\vec{F}_{kp}(t)}{dt}\right) + \frac{\vec{F}_{ks}(t) + \vec{F}_{CE}(t)}{b} \\
&= -\frac{1}{k_s}\left(\frac{d\vec{F}(t)}{dt} + k_p\frac{d\vec{x}(t)}{dt}\right) + \frac{\vec{F}(t) - \vec{F}_{kp}(t) + \vec{F}_{CE}(t)}{b} \\
&= -\frac{1}{k_s}\left(\frac{d\vec{F}(t)}{dt} + k_p\frac{d\vec{x}(t)}{dt}\right) + \frac{\vec{F}(t) + k_p\left(\vec{x}(t) - \vec{x}_0\right) + \vec{F}_{CE}(t)}{b} \\
&= -\frac{1}{k_s}\frac{d\vec{F}(t)}{dt} - \frac{k_p}{k_s}\frac{d\vec{x}(t)}{dt} + \frac{\vec{F}(t)}{b} + \frac{k_p\left(\vec{x}(t) - \vec{x}_0\right)}{b} + \frac{\vec{F}_{CE}(t)}{b}
\end{aligned} \qquad \text{(Eqn 4.22)}$$

Rearranging all force terms on the left and all length terms to the right gives:

$$\frac{\vec{F}(t)}{b} - \frac{1}{k_s}\frac{d\vec{F}(t)}{dt} + \frac{\vec{F}_{CE}(t)}{b} = \frac{k_p}{k_s}\frac{d\vec{x}(t)}{dt} + \frac{d\vec{x}(t)}{dt} - \frac{k_p}{b}\left(\vec{x}(t) - x_0\right) \qquad \text{(Eqn 4.23)}$$

Simplifying the coefficients in Eqn 4.23 gives the model equation for the classical Hill muscle Eqn 4.24.

$$\vec{F}(t) - \frac{b}{k_s}\frac{d\vec{F}(t)}{dt} + \vec{F}_{CE}(t) = b\left(1 + \frac{k_p}{k_s}\right)\frac{d\vec{x}(t)}{dt} - k_p\left(\vec{x}(t) - \vec{x}_0\right) \qquad \text{(Eqn 4.24)}$$

4.2.2 Designing a muscle model to be incorporated into musculo-skeletal models

The classical Hill muscle model has been derived based on the anatomy of skeletal muscle in section 2.2.2 , the model equation derived in section 4.2.1 (Eqn 4.24) includes time derivatives of both the overall muscle force $\vec{F}(t)$ and length $\vec{x}(t)$. However with an equation that includes the time derivatives of both the force and length, it is difficult to incorporate this muscle model into musculo-

skeletal models as a subsystem, as an explicit equation cannot be derived that describes the muscle force as a function of muscle length and lengthening/shortening velocity, due to the $\frac{d\vec{F}(t)}{dt}$ term. Therefore the muscle model cannot be inserted into a joint model such as that developed in section 4.3.3, and alternative Hill type muscle models are required which give the muscle force as a function of lengths and velocities without derivatives of the muscle force in the equation.

To understand the reason that gave the muscle its complex system equation, in this section, simpler forms of muscle models are analysed to assist the design and development of a muscle model that can be incorporated into joint models, while also remaining anatomically meaningful.

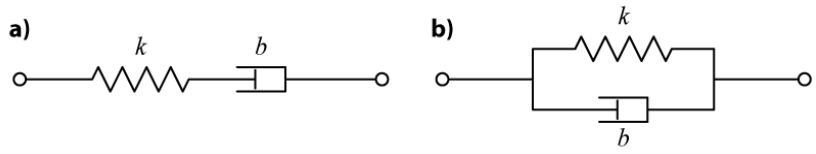

Figure 4.10. Serial and parallel muscle models. a) serial muscle model; b) parallel muscle model

Figure 4.10 are two simpler forms of muscle model. The system equations for each model are derived and shown in section 4.2.2.1 and section 4.2.2.2 .

Each spring has the relationship: $F_k(t) = -k(x_k(t) - x_{k\_0})$, where x_k is the spring's length and x_{k_0} is its natural length; no force is exerted when $x_k(t) = x_{k\_0}$. Each damper has the relationship: $F_b(t) = -b\frac{dx_b(t)}{dt}$, where x_b is the length of the damping element.

4.2.2.1 Serial model (Equation Derivation)

Consider the serial muscle model shown in Figure 4.10a, which consists of a spring and damper in series. Note that the derivation of the model equation for this model is shown in Yamaguchi (Yamaguchi, 2001), however it is included in this thesis for discussion.

From Newton's third law, the force of the muscle $F(t)$ is equal to the force of the spring and the force of the damper:

$$F(t) = F_k(t) = F_b(t) \quad \text{(Eqn 4.25)}$$

The total muscle length is the sum of the length of the spring and length of the damper:

$$x(t) = x_k(t) + x_b(t) \quad \text{(Eqn 4.26)}$$

The shortening/lengthening velocity of the model can be obtained by differentiating Eqn 4.26 with respect to time:

$$\frac{dx(t)}{dt} = \frac{dx_k(t)}{dt} + \frac{dx_b(t)}{dt} \quad \text{(Eqn 4.27)}$$

Substituting the differential of the spring force, i.e. $\frac{dx_k(t)}{dt} = -\frac{1}{k}\frac{dF_k(t)}{dt}$, and the damper force into Eqn 4.27 gives:

$$\frac{dx(t)}{dt} = -\frac{1}{k}\frac{dF_k(t)}{dt} - \frac{1}{b}F_b(t) \quad \text{(Eqn 4.28)}$$

Rearranging Eqn 4.28 and using Eqn 4.25 gives

$$\frac{dF(t)}{dt} + \frac{k}{b}F(t) = -k\frac{dx(t)}{dt} \quad \text{(Eqn 4.29)}$$

4.2.2.2 Parallel model (Equation Derivation)

Consider the serial muscle model shown in Figure 4.10b, which consists of a spring and damper in parallel. The output force is the sum of the force from the spring and the force from the damper. This gives the model equation shown in Eqn 4.30, where $x(t)$ is the length of the muscle.

$$F(t) = F_k(t) + F_b(t)$$
$$F(t) = -kx(t) - b\frac{dx(t)}{dt} \quad \text{(Eqn 4.30)}$$

4.2.2.3 Comparison of the serial and parallel model equations

The model equations of the parallel and serial muscle models derived in section 4.2.2.1 and section 4.2.2.2 have shown that for a model with parallel elements, a model equation for the muscle force can be obtained as a function of muscle length and velocity, see Eqn 4.30. This form of equation can be incorporated into joint model as a sub-system. However, for the serial model, the system equation Eqn 4.29 contains the muscle force and its first order time derivative, and this model equation cannot be incorporated into the joint model developed in section 4.3.

By inspecting the method of equation manipulation to derive the model equation of the serial model, it can be seen that in order to obtain a model equation that does not include internal lengths and velocities of individual components, which cannot be measured; those internal lengths and velocities must be substituted (Eqn 4.27 and Eqn 4.28). This substitution method has also been used in section 4.2.1, Eqn 4.22 to derive the system equation for the classical Hill muscle model. In that case, the model equation presented in Eqn 4.24 contains both the time derivative of the muscle force and muscle length, which cannot be incorporated into the joint model. Therefore a muscle model should only include parallel elements, to allow the model to be incorporated in a musculo-skeletal model as a sub-system.

4.2.3 The modified Hill muscle model

A modified Hill muscle model that only includes parallel components is shown in Figure 4.11, and is in series to a free tendon $k_{t'}$ that represents tendons external to the bulk of the muscle that connect to the bones. This modified form of the Hill muscle model has commonly been used by other researchers to obtain parameter values, e.g. (van Zandwijk et al., 1998, Venture et al., 2005, Scovil and

Ronsky, 2006, Erdemir et al., 2007), over the classical Hill model described in section 2.2.2.

The reasons for selecting the modified Hill muscle model (Figure 4.11) over the classical Hill muscle (section 2.2.2) have not been discussed in any available literature. However the inability to incorporate the classical Hill muscle model equation into musculo-skeletal models, as identified in the last section, may be the reason for which researchers have used modified forms of the Hill muscle model.

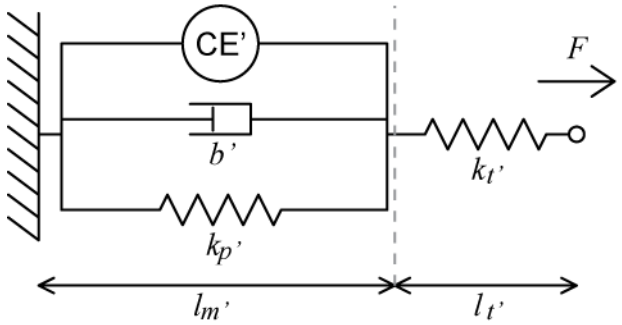

Figure 4.11. Modified Hill muscle model with free tendon. Each component is labelled with a prime symbol as these do not have the same anatomical definition to the classical muscle model in Figure 4.9.

The modified Hill muscle model includes three mechanical components in parallel, which are a spring $k_{p'}$ (passive component), a damper b' (passive component) and a contractile element CE' (active component), which is a pure force generator. The three muscle components and the muscle model itself have the same length $l_{m'}(t)$. A free tendon $k_{t'}$ with length $l_{t'}(t)$ is also included in Figure 4.11. This will be included in the musculo-skeletal model developed in section 4.3 to more accurately describe the anatomy of the musculo-skeletal system.

The structure of the modified Hill muscle model shown in Figure 4.11 only contains parallel components; this matches the criteria from the findings in section 4.2.2, that the muscle model must only include parallel components, so that there are no unknown internal lengths. This ensured that the muscle model

equation does not include the time differential of the output force, and therefore can be incorporated into musculo-skeletal models as a sub-system.

4.2.3.1 Comparison between the Classical Hill muscle model and the Modified Hill muscle model

The structure of this modified form of the muscle model is not the same as the classical Hill model described in section 2.2.2 and section 4.2.1. Therefore it must be analysed to demonstrate that the two models are compatible, and that they have the same dynamic characteristics.

Fung (Fung, 1971) has shown that the two series/parallel models in Figure 4.12 are equivalent.

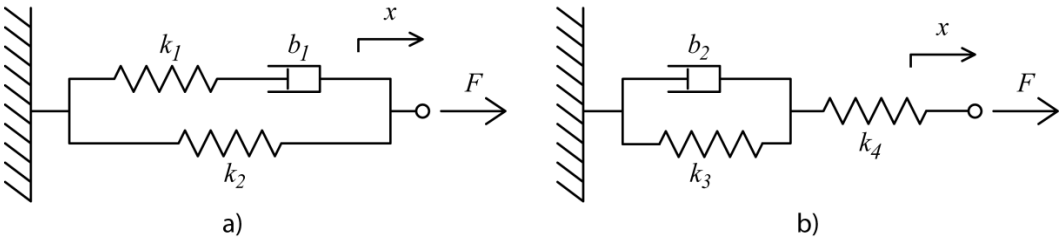

Figure 4.12. Two equivalent mechanical models. a) A spring k_1 in series with a damper b_1, which are both in parallel with spring k_2. b) A parallel spring k_3 and damper b_2 in series with a spring k_4. The two models have the same overall length and output force.

Fung showed that the two models in Figure 4.12 have the same dynamic characteristics if:

$$k_4 = k_1 + k_2 \ , \ \frac{k_3 k_4}{k_3 + k_4} = k_2 \ \text{and} \ \frac{b_2}{k_3 + k_4} = \frac{b_1}{k_1} \qquad \text{(Eqn 4.31)}$$

Using Fung's finding, the modified Hill muscle model in Figure 4.11 can be shown to be equivalent to the classical Hill muscle model described in section 2.2.2, see Figure 4.13 and the following discussion.

It should be noted that in human anatomy of the musculo-skeletal system, muscles are connected to the bones by free tendons. In this thesis, the free tendons are the part of the tendons that are external to the bulk of the muscles, and are modelled by linear springs. In Figure 4.13a, the classical Hill muscle

model is connected to a spring in series that represents the free tendon. The free tendons at both ends of the muscle are lumped into one spring component.

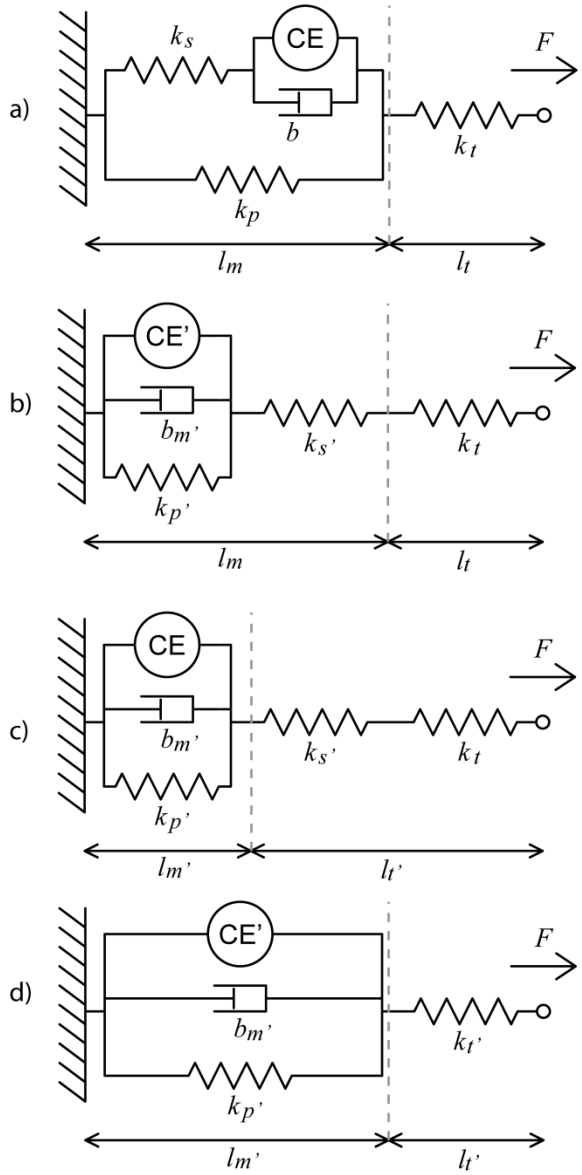

Figure 4.13. Comparison of the Classical Hill model (with free tendon) and the modified Hill muscle model using Fung's method (Fung, 1971) to prove the two muscle models are equivalent. a) The classical Hill muscle model shown in section 2.2.2 with length l_m, in series with a serial free tendon k_t with length l_t. b) An equivalent muscle model that has identical dynamic characteristics in comparison to the classical Hill muscle model using Fung's method of derivation. c) Identical to figure b with new length definitions for the muscle model and free tendon model. d) Identical to figure c with $k_{s'}$ and k_t lumped into one spring $k_{t'}$.

From Figure 4.13a, the classical Hill muscle model has been transformed to an equivalent combination of springs, damper and CE in Figure 4.13b using Fung's method (Fung, 1971). The resulting model in Figure 4.13b gives three parallel

components: CE', b' and $k_{p'}$, in series with a spring $k_{s'}$ and the free tendon spring k_t. From Eqn 4.31, those components in the muscle models in Figure 4.13b are anatomically and therefore numerically different to those in the classical Hill muscle model in Figure 4.13a. and are marked with a prime symbol.

The force of the serial spring $k_{s'}$ and free tendon spring k_t in Figure 4.12b are the same. However if the length of the serial spring cannot be determined, the numerical values of these two spring constants cannot be uniquely identified. Therefore in Figure 4.13c, new muscle model length $l_{m'}$ and free tendon length $l_{t'}$ has been defined for the musculo-tendon combination, where the modified muscle model length contains only the length of the parallel components, and the free tendon length also includes the length of the serial spring $k_{s'}$. Since the serial spring and free tendon spring values cannot be separately determined, they are combined together as one spring component $k_{t'}$, as shown in Figure 4.13d, this gives the modified Hill muscle model with a free tendon shown in Figure 4.11d.

4.2.3.2 Anatomical Meanings of the Modified Hill Muscle Model

With the structure of the modified Hill muscle model derived, these muscle components must still be anatomically meaningful. The CE' is a pure force generator, which represents the force generated by the actin-myosin cross bridges. The damping component b' represents resistance due to fluid moving in and out between the actin myosin cross bridges during shortening and lengthening of the sarcomere (Winter, 2005), and the parallel spring component $k_{p'}$ represents the muscle's ability to return to its natural resting length once it is released from a stretched muscle length. This muscle model is connected to a free tendon $k_{t'}$, which is the part of the tendon external to the bulk of the muscle.

4.2.3.3 Free Tendon Assumption

In Figure 4.11 and Figure 4.12, musculo-tendon models were presented. As free tendons are also part of the musculo-skeletal system in addition to muscles and bones, and musculo-tendon models will be incorporated into the musculo-skeletal model instead of just muscle models. However, the musculo-tendon combination as a whole that incorporates the modified Hill muscle model has components connected in series internally. From the finding in section 4.2.2, this series musculo-tendon structure would give a model equation that includes the time derivative of the muscle force as well as its length, and such model equations would be difficult to incorporate into a musculo-skeletal model as a sub system. Therefore an additional assumption for the free tendon is used.

In this thesis, the free tendon is assumed to be much stiffer than the muscle, the extension of the free tendon external to the bulk of the muscle is considered negligible, and thus the length $l_{t'}$ is fixed. This assumption will be used in the development of the musculo-skeletal model shown in section 4.2.3, so that the muscle (and tendon) force can be described by a function of length and velocity, and which can be incorporated into the musculo-skeletal model as a sub model. Equivalent free tendon spring constants have been reported to lie in the range 60-170kN/m (Maganaris and Paul, 1999). The maximum strain of a tendon before failure is about 10%, and it has been suggested that the nominal strain is about 3.3% (Zajac, 1989). In body movements, the change in the total length of the muscle and free tendon during muscle elongation is much larger than the maximum strain achieved through the free tendon, and therefore the majority of this increase in length comes from the muscle. During passive elongation, i.e. when the muscle is non-active and relaxed, a muscle can be stretched to 1.5 times its resting length with minimal force. Therefore the extensions of the free tendons caused by the passive muscle forces are considered negligible in comparison to the extension of the bulk of the muscle and thus the free tendons are assumed to have fixed lengths. The result of this assumption is that when the contractile element CE is not active, the dynamics of the muscle are completely

determined by the spring and damping elements. This scenario is used experimentally in Chapter 5 to allow the parameter values for the passive elements, i.e. the parallel spring and damper in the muscle model, to be determined.

4.2.3.4 Model equation of the Modified Hill Muscle Model

From Figure 4.11 and the assumption for the free tendon, the muscle force (and tendon force) of the modified Hill muscle model is:

$$\vec{F}(t) = \vec{F}_{CE'}(t) - b'\frac{d\vec{l}_{m'}(t)}{dt} - k_{p'}(\vec{l}_{m'}(t) - l_{m'\_0}) \qquad \text{(Eqn 4.32)}$$

where $l_{m'\_0}$ is the natural length of the muscle in which the parallel spring element $k_{p'}$ exerts no force.

4.2.4 Structural identifiability of muscle models

While the muscle models have been derived from the anatomical structure and mechanical properties of the muscle, and their respective model equations derived, in practice, it is important to determine if unique values of the model parameters can be obtained. Parameters such as body weight, body segment weight, arm length, muscle length and free tendon lengths can be directly measured or calculated. However, other components in the model such as the spring constants, damping constants and CE are embedded in the muscle and cannot be directly measured in vivo. However in vivo measurements are the only possible route for parameterising the models in living subjects, therefore parameter values that cannot be directly measured must be obtained through model fitting and parameter estimation techniques. To determine if unique parameter values can be obtained (at least theoretically) through model fitting and parameter estimation, this thesis uses an analytical method called structural identifiability analysis (Bellman and Åström, 1970, Godfrey and DiStefano, 1987) to examine both the classical Hill muscle model shown in section 2.2.2 and 4.2.1, and the modified Hill muscle model described in section 4.2.3.

The analyses in section 4.2.2 and section 4.2.3 have already determined that the modified Hill muscle model should be selected to be incorporated into musculo-skeletal models. However, for completeness and the possibility of incorporating the classical Hill muscle model in further work, the structural identifiability of the classical Hill model is also analysed in this thesis.

Section 4.2.4.1 to section 4.2.4.4 outlines the basic concept to the method used in this thesis, section 4.2.4.5 and section 4.2.4.6 shows the analyses performed on the two muscle models.

4.2.4.1 Basic concept

To determine whether unique parameter values for an input/output model can be obtained through experiments and parameter estimation, structural identifiability analysis (Bellman and Åström, 1970, Godfrey and DiStefano, 1987) can be performed on the system equations prior to the lengthy processes of parameter estimation. Structural identifiability analysis is a symbolic analysis method that examines the known system equations of an input/output system, to determine whether the parameter values in the system can be uniquely identified through parameter estimation techniques, providing perfect input/output data are available from measurement.

This thesis uses the Laplace transform or transfer function approach (Godfrey and DiStefano, 1987) to analyse the Hill muscle models. This is described in section 4.2.4.4.

The outcome of structural identifiability analysis is to determine whether unique values of model parameters can be obtained (from perfect noise-free data). If a parameter is determined to be ***uniquely identifiable***, then it means a unique solution (value) for the parameter can be obtained, assuming perfect input/output measured data is available. If a parameter is has countable numbers of values that can achieve the same system input/out, then such parameter is ***locally identifiable (or non-uniquely identifiable)***. If a parameter is determined to be ***unidentifiable***, then it means there is an infinite number of

values for such parameter that would achieve the same system input/output characteristics.

4.2.4.2 Structural Identifiability Analysis Example

Consider the follow example of a first order model described in (Godfrey and DiStefano, 1987), Eqn 4.33 to Eqn 4.55:

$$\frac{dx(t)}{dt} = p_1 x(t) + p_2 u(t) \quad \text{(Eqn 4.33)}$$

$$x(0) = 0 \quad \text{(Eqn 4.34)}$$

$$y(t) = p_3(t) x(t) \quad \text{(Eqn 4.35)}$$

Where $x(t)$ is the system's state, $u(t)$ is the system's known input, $y(t)$ is the model's measured output. The system has three constant parameters: p_1, p_2 and p_3, which are unknown and are to be obtained through parameter estimation. The explicit solution for this system (Eqn 4.33 to Eqn 4.35) is:

$$y(t) = p_2 p_3 \int_0^t e^{p_1(t-\tau)} u(\tau) d\tau \quad \text{(Eqn 4.36)}$$

And for an impulsive input, where $u(t) = \delta(t)$, then the output is:

$$y(t) = p_2 p_3 e^{p_1 t} \quad \text{(Eqn 4.37)}$$

The form of Eqn 4.37 resembles an exponential decay:

$$y(t) = Ae^{-\lambda t} \quad \text{(Eqn 4.38)}$$

When comparing Eqn 4.36 and Eqn 4.38, it can be seen that the coefficient $A = p_2 p_3$ and $\lambda = -p_1$. Through model fitting experiments, the value of A and λ can be estimated. This allows the values p_1 and $p_2 p_3$ to be determined. In this case, the parameter p_1 is uniquely identifiable. For p_2 and p_3, only their product is uniquely identifiable, but individually they are unidentifiable, and an

infinite number of solution exist for both p_2 and p_3. Overall this system is unidentifiable. However if either of the value of p_2 or p_3 is known, then the other parameter value can be determined, and all parameter values can only be uniquely determined if the value of p_2 or p_3 is known.

4.2.4.3 Identifiability from additional system information

For physical systems, parameters can be locally identifiable, and those parameters cannot be determined through knowing the values of other system parameters, such as the example of p_2 and p_3 as shown in section 4.2.4.2, however additional physical constrains or boundaries in the model may allow unique values for the structurally unidentifiable parameters to be obtained.

For example, consider the following system with the explicit solution shown in Eqn 4.39, where $y(t)$ is the model output and $u(t)$ is the model input.

$$y(t) = p_4{}^2 u(t) \qquad \text{(Eqn 4.39)}$$

Mathematically there are two solutions for p_4: one being the negative of the other solution. Structurally p_4 is only locally identifiable. However if the model has a constrain that $p_4 \geq 0$, then this rules out the negative value(s) for p_4. Therefore a unique value for p_4 can be obtained through parameter estimation.

4.2.4.4 The Laplace transform / transfer function approach

For linear time derivative models that can be described by linear ordinary differential equations (ODEs), it is more convenient to determine the identifiability of the parameters in the model or system using the Laplace transform/ transfer function approach (Godfrey and DiStefano, 1987). The system is inspected in the form of an output/input transfer function in the Laplace *S* domain. Each of the coefficients of powers of s in the transfer function is a function of the model parameters, by analysing the relationships

between the coefficients and the model parameters, the identifiability of each model parameter can be determined.

The advantage of observing the model's input/output transfer function in the Laplace *S* domain is that it eliminates the need to derive an explicit solution of the model equations as shown in the example in section 4.2.4.1 (Eqn 4.36).

This method considers each time variable in the model (e.g. $x(t)$ and $\frac{d}{dt}x(t)$) as a state variable in the system (e.g. $x_1(t)$ and $x_2(t)$). In this, first rearrang and combine the system equations into a series of first order differential equations as shown in Eqn 4.40. Each first order differential equation describes the differential of each state variable as a function of all other state variables in the system. The number of first order differential equations equals to the number of state variables in the system.

$$\begin{aligned}
\frac{dx_1(t)}{dt} &= f_1\left(x_1, x_2, \ldots x_n, u\right) \\
\frac{dx_2(t)}{dt} &= f_2\left(x_1, x_2, \ldots x_n, u\right) \\
&\vdots \\
\frac{dx_n(t)}{dt} &= f_n\left(x_1, x_2, \ldots x_n, u\right)
\end{aligned} \qquad \text{(Eqn 4.40)}$$

The whole system can then be combined and rearrange into matrices to form one first order state equation, as shown in Eqn 4.41. Here, the differential of each variable is represented by a dot above the variable, e.g. $\frac{dx_1(t)}{dt} \equiv \dot{x}_1(t)$. A matrix is denoted by a bar over the variable.

$$\dot{\bar{x}}(t) \equiv \begin{bmatrix} \dot{x}_1(t) \\ \dot{x}_2(t) \\ \vdots \\ \dot{x}_n(t) \end{bmatrix} = \bar{A}\bar{x}(t) + \bar{B}u(t)$$
$$= \begin{bmatrix} a_{11} & a_{12} & \cdots & a_{1n} \\ a_{21} & a_{22} & \cdots & a_{2n} \\ \vdots & \vdots & \ddots & \vdots \\ a_{n1} & a_{n2} & \cdots & a_{nn} \end{bmatrix} \begin{bmatrix} x_1(t) \\ x_2(t) \\ \vdots \\ x_n(t) \end{bmatrix} + \begin{bmatrix} b_1 \\ b_2 \\ \vdots \\ b_n \end{bmatrix} u(t) \qquad \text{(Eqn 4.41)}$$

Through experiments, system outputs normally measures one of the state in the system:

$$y_1 = c_1 x_1,\ y_2 = c_2 x_2,\ \ldots y_n = c_n x_n \qquad \text{(Eqn 4.42)}$$

The system outputs can be put into a matrix form:

$$\bar{y}(t) = \begin{bmatrix} y_1(t) \\ \vdots \\ y_n(t) \end{bmatrix} = \bar{C}\bar{x}(t) = \begin{bmatrix} c_1 & \cdots & 0 \\ \vdots & \ddots & \vdots \\ 0 & \cdots & c_n \end{bmatrix} \begin{bmatrix} x_1(t) \\ \vdots \\ x_n(t) \end{bmatrix} \qquad \text{(Eqn 4.43)}$$

Taking Laplace transforms of the state equation and output equation, with $\bar{x}(0) = 0$, this gives:

$$s\bar{X}(s) = \bar{A}\bar{X}(s) + \bar{B}U(s)$$
$$\bar{X}(s) = \left(s\bar{I} - \bar{A}\right)^{-1} \bar{B}U(s) \qquad \text{(Eqn 4.44)}$$

$$\bar{Y}(s) = \bar{C}\bar{X}(s) \qquad \text{(Eqn 4.45)}$$

Where $\bar{I}$ is the identity matrix. $\bar{X}(s)$ can then be substituted into Eqn 4.45 to obtain the system's input output transfer function.

$$\bar{Y}(s) = \bar{C}\left(s\bar{I} - \bar{A}\right)^{-1} \bar{B}U(s)$$
$$\bar{Y}(s) = \bar{H}(s)U(s) \qquad \text{(Eqn 4.46)}$$

where

$$\begin{aligned}\bar{H}(s) &= \bar{C}\left(s\bar{I}-\bar{A}\right)^{-1}\bar{B} \\ &= \frac{1}{\Delta(s)}\bar{C}\ adj\left(s\bar{I}-\bar{A}\right)\bar{B}\end{aligned} \qquad \text{(Eqn 4.47)}$$

where $\Delta(s)$ is the determinant of $\left(s\bar{I}-\bar{A}\right)$, and $adj\left(s\bar{I}-\bar{A}\right)$ is the adjoint of $\left(s\bar{I}-\bar{A}\right)$.

By multiplying the constant matrices, transfer functions would be obtainable for each model output, e.g. $Y_1(s)/U(s)$, in the form of Eqn 4.34.

$$\frac{Y_n(s)}{U(s)} = \frac{\beta_n s^{n-1}}{s^n + \alpha_1 s^{n-1} + \ldots + \alpha_{n-2}s + \alpha_{n-1}} \qquad \text{(Eqn 4.48)}$$

where the numerator in Eqn 4.47, $\beta_n s^{n-1}$, is determined by $\bar{C}\ adj\left(s\bar{I}-\bar{A}\right)\bar{B}$ and the denominator is $\Delta(s)$.

The coefficients of the s terms in the numerator and denominator in the transfer functions, i.e. β_1 to β_n and α_1 to α_{n-1} are functions of the parameters in the model, similar to the example of coefficients in the explicit equation in Eqn 4.36 and combinations of model parameters in Eqn 4.37 and Eqn 4.38. Through model fitting using measured input and output data, the transfer function coefficients β_1 to β_n and α_1 to α_{n-1} can be estimated. By algebraic manipulation, if model parameters can be described by a unique function of only the transfer function coefficients β_1 to β_n and α_1 to α_{n-1}, then such a parameter is uniquely identifiable. If model parameters are derived to be functions of other model parameters, then those parameters are unidentifiable, however in such cases, knowing one or more of the value(s) of the parameters may allow all parameter values to be determined. If model parameters cannot be described as functions of the coefficients in the transfer function, i.e. β_1 to β_n

and α_1 to α_{n-1}, then such model parameter is unidentifiable. The structural identifiability of each model parameter is determined in the same manner as shown in section 4.2.4.1.

In practice, e.g. in parameter estimation experiments, the condition for these parameters to be uniquely identifiable is that there must be sufficient measurement of the time history of the input and outputs, so that the coefficients of the s terms in the transfer functions can be determined through model fitting and parameter estimation. This is known as the numerical identifiability of the system.

4.2.4.5 Structural Identifiability of the Classical Hill muscle model

In section 4.2.1, the system equation for the classical Hill model shown in Eqn 4.24 was found to be:

$$F(t) + F_{CE}(t) - \frac{b}{k_s}\frac{dF(t)}{dt} = b\left(1 + \frac{k_p}{k_s}\right)\frac{dx(t)}{dt} - k_p(x(t) - x_0) \qquad \text{(Eqn 4.49)}$$

The muscle length is defined by x and the natural resting length is x_0.

Eqn 4.49 equates the muscle force and its first derivative and muscle length and its first and second derivative. In order to examine the structural identifiability of the model, there must be an additional relationship between the muscle force, length or their time derivatives.

For muscles in vivo, the relationship between lengths and forces are governed by the geometry of the joints and body segments at which the muscles are acting on; for example in the elbow model developed in this thesis (introduced in section 4.3). However in this section, a simple muscle and mass configuration shown in section Figure 4.14 is used. The assumption is that if the muscle model is structurally identifiable in this simple configuration, then the same muscle model incorporated in a joint model may be identifiable. However if the muscle model is not structurally identifiable in the simple configuration, then the overall

identifiability of a joint model that incorporates the unidentifiable muscle model will be unidentifiable.

This simple configuration incorporates a muscle that connects between a fixed point and a freely moving mass, as shown in Figure 4.14. In this case the relationship between force and acceleration is $F(t) = ma(t)$, from Newton's second law. The shortening of the muscle would make the attached mass move along the horizontal direction.

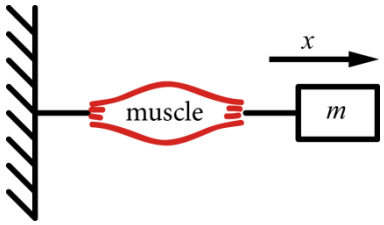

Figure 4.14. Excised muscle. Muscle is attached to a fixed position on the left and a movable mass m on the right.

Taking the assumption from Newton's second law:

$$F(t) = ma(t) \equiv m\frac{d^2x(t)}{dt^2} \qquad \text{(Eqn 4.50)}$$

Eqn 4.50 can be used to derive the following states in the system.

$$x_1(t) = x(t)\ ,\ x_2(t) = \frac{dx(t)}{dt}\ ,\ x_3(t) = \frac{d^2x(t)}{dt^2} = \frac{F(t)}{m}$$
$$\text{and } \dot{x}_3(t) \equiv \frac{dx_3(t)}{dt} = \frac{1}{m}\frac{dF(t)}{dt} \qquad \text{(Eqn 4.51)}$$

Rearranging Eqn 4.49 gives Eqn 4.52, and incorporating Eqn 4.50 and Eqn 4.51 gives Eqn 4.53.

$$\frac{b}{k_s}\frac{dF(t)}{dt} = F(t) + F_{CE}(t) - b\left(1 + \frac{k_p}{k_s}\right)\frac{dx(t)}{dt} + k_p(x(t) - x_0) \qquad \text{(Eqn 4.52)}$$

$$\frac{b}{k_s}m\frac{d^3x(t)}{dt^3} = m\frac{d^2x(t)}{dt^2} + F_{CE}(t) - b\left(1 + \frac{k_p}{k_s}\right)\frac{dx(t)}{dt} + k_p(x(t) - x_0) \qquad \text{(Eqn 4.53)}$$

The system states in Eqn 4.51 and the differential equation shown in Eqn 4.53 can be now used to express the system in state space form in Eqn 4.54. Note that in matrices, the time differential of a time variable is $\frac{dx(t)}{dt} \equiv \dot{x}(t)$.

$$\begin{bmatrix} \dot{x}_1(t) \\ \dot{x}_2(t) \\ \dot{x}_3(t) \end{bmatrix} = \begin{bmatrix} 0 & 1 & 0 \\ 0 & 0 & 1 \\ \frac{k_p k_s}{bm} & -\frac{k_p + k_s}{m} & \frac{k_s}{b} \end{bmatrix} \begin{bmatrix} x_1(t) \\ x_2(t) \\ x_3(t) \end{bmatrix} + \begin{bmatrix} 0 \\ 0 \\ \frac{k_s}{bm} \end{bmatrix} F_{CE}(t) + \begin{bmatrix} 0 \\ 0 \\ -\frac{k_p k_s}{bm} x_0 \end{bmatrix} \quad \text{(Eqn 4.54)}$$

Consider the system input to be $F_{CE}(t)$, equivalent to $u(t)$ in Eqn 4.41. If the measured outputs are length $x(t)$ and force $F(t)$, then output $\bar{y}(t)$ is:

$$\bar{y}(t) = \begin{bmatrix} y_1(t) \\ y_2(t) \end{bmatrix} = \begin{bmatrix} 1 & 0 & 0 \\ 0 & 0 & m \end{bmatrix} \begin{bmatrix} x_1(t) \\ x_2(t) \\ x_3(t) \end{bmatrix} \quad \text{(Eqn 4.55)}$$

Putting Eqn 4.54 and Eqn 4.55 into the form of Eqn 4.41 and Eqn 4.43, then

$$\bar{A} = \begin{bmatrix} a_{11} & a_{12} & a_{13} \\ a_{21} & a_{22} & a_{23} \\ a_{31} & a_{32} & a_{33} \end{bmatrix} = \begin{bmatrix} 0 & 1 & 0 \\ 0 & 0 & 1 \\ \frac{k_p k_s}{bm} & -\frac{k_p + k_s}{m} & \frac{k_s}{b} \end{bmatrix}, \bar{B} = \begin{bmatrix} b_1 \\ b_2 \\ b_3 \end{bmatrix} = \begin{bmatrix} 0 \\ 0 \\ \frac{k_s}{bm} \end{bmatrix},$$

$$\bar{C} = \begin{bmatrix} c_1 & 0 & 0 \\ 0 & 0 & c_2 \end{bmatrix} = \begin{bmatrix} 1 & 0 & 0 \\ 0 & 0 & m \end{bmatrix} \text{ and } \bar{k} = \begin{bmatrix} 0 \\ 0 \\ -\frac{k_p k_s}{bm} x_0 \end{bmatrix} \quad \text{(Eqn 4.56)}$$

Applying Laplace transform to the state equations (Eqn 4.54) and output function (Eqn 4.55) gives:

$$s\bar{X}(s) = \bar{A}\bar{X}(s) + \bar{B}F_{CE}(s) + s^{-1}\bar{k} \quad \text{(Eqn 4.57)}$$

$$\bar{X}(s) = \left(s\bar{I} - \bar{A}\right)^{-1}\left(\bar{B}F_{CE}(s) + s^{-1}\bar{k}\right) \quad \text{(Eqn 4.58)}$$

$$\bar{Y}(s) = \bar{C}\bar{X}(s) \qquad \text{(Eqn 4.59)}$$

The output can be written in the form of:

$$\bar{Y}(s) = \bar{C}\left(s\bar{I} - \bar{A}\right)^{-1}\left(\bar{B}F_{CE}(s) + s^{-1}\bar{k}\right) \qquad \text{(Eqn 4.60)}$$

Note that a transfer function of output /input $(Y(s)/U(s))$ in the format of Eqn 4.48 cannot be obtained from Eqn 4.60 due to the term $s^{-1}\bar{k}$ in the numerator. However if the muscle length is considered to be the difference between the muscle's overall length and its natural length, i.e. $x_0 = 0$; then the matrix $\bar{k}$ in Eqn 4.60 will be eliminated. The input/output transfer function therefore becomes the form in Eqn 4.46. Now the transfer functions in the form of Eqn 4.48 can be obtained.

With the zero and one values of $\bar{A}$ in Eqn 4.56 substituted into the matrix $(s\bar{I} - \bar{A})$, the adjoint $adj(s\bar{I} - \bar{A})$ and determinant $\Delta(s)$ of the inverse matrix $(s\bar{I} - \bar{A})^{-1}$ are:

$$adj(s\bar{I} - \bar{A}) = \begin{bmatrix} (s^2 - a_{33}s - a_{32}) & (s - a_{33}) & 1 \\ a_{31} & (s^2 - a_{33}s) & s \\ a_{31}s & (a_{32}s + a_{31}) & s^2 \end{bmatrix} \qquad \text{(Eqn 4.61)}$$

$$\Delta(s) = s^3 - a_{33}s^2 - a_{32}s - a_{31} \qquad \text{(Eqn 4.62)}$$

This gives the overall system transfer function and individual transfer functions for each output:

$$\bar{H}(s) = \frac{\bar{Y}(s)}{U(s)} = \frac{1}{\Delta(s)}\begin{bmatrix} k_s/bm \\ 0 \\ k_s s^2/bm^2 \end{bmatrix} \qquad \text{(Eqn 4.63)}$$

$$Y_1(s) = \frac{k_s}{bm} \frac{1}{s^3 - \frac{k_s}{b}s^2 + \frac{k_p + k_s}{m}s - \frac{k_p k_s}{bm}} U(s) \quad \text{(Eqn 4.64)}$$

$$Y_2(s) = \frac{k_s}{bm^2} \frac{s^2}{s^3 - \frac{k_s}{b}s^2 + \frac{k_p + k_s}{m}s - \frac{k_p k_s}{bm}} U(s) \quad \text{(Eqn 4.65)}$$

Assuming that from experiments, known input $U(s)$ (CE force) and measured outputs $Y_1(s)$ (muscle length) and $Y_2(s)$ (muscle force) can be obtained. Through model fitting and parameter estimation, the coefficients of powers of s in the numerator and the denominator: β_1, α_1, α_2, α_3 and β_2 in the system transfer functions, Eqn 4.66 and Eqn 4.67, can be determined.

$$Y_1(s) = \beta_1 \frac{1}{s^3 + \alpha_1 s^2 + \alpha_2 s + \alpha_3} U(s) \quad \text{(Eqn 4.66)}$$

$$Y_2(s) = \beta_2 \frac{s^2}{s^3 + \alpha_1 s^2 + \alpha_2 s + \alpha_3} U(s) \quad \text{(Eqn 4.67)}$$

By comparing Eqn 4.64 and Eqn 4.65 with Eqn 4.66 and 4.67, it can be shown that each of the coefficients for the powers of s is a function of the muscle model parameters:

$$\beta_1 = \frac{k_s}{bm}\ ,\ \alpha_1 = -\frac{k_s}{b}\ ,\ \alpha_2 = \frac{k_p + k_s}{m}\ ,\ \alpha_3 = -\frac{k_p k_s}{bm} \text{ and } \beta_2 = \frac{k_s}{bm^2} \quad \text{(Eqn 4.68)}$$

If β_1, α_1, α_2, α_3 and β_2 are known, then each of the muscle model parameters can be determined using the derivations in Eqn 4.68 to Eqn 4.74. Note that the value for the external mass m is also assumed to be known.

Rearranging $\beta_1 = \frac{k_s}{bm}$ to give:

$$bm = \frac{k_s}{\beta_1} \quad \text{(Eqn 4.69)}$$

Substituting Eqn 4.69 into $\alpha_3 = -\frac{k_p k_s}{bm}$ gives:

$$\alpha_3 = -k_p k_s \left(\frac{\beta_1}{k_s} \right) = -k_p \beta_1 \qquad \text{(Eqn 4.70)}$$

Rearranging Eqn 4.70 gives:

$$k_p = -\frac{\alpha_3}{\beta_1} \qquad \text{(Eqn 4.71)}$$

Substituting Eqn 4.71 into $\alpha_2 = \frac{k_p + k_s}{m}$ gives Eqn 4.72, and rearranging gives Eqn 4.73.

$$\alpha_2 = \frac{1}{m}\left(-\frac{\alpha_3}{\beta_1} + k_s \right) \qquad \text{(Eqn 4.72)}$$

$$k_s = \alpha_2 m + \frac{\alpha_3}{\beta_1} \qquad \text{(Eqn 4.73)}$$

Rearranging the combination of $\alpha_1 = -\frac{k_s}{b}$ and Eqn 4.73, gives:

$$b = -\frac{1}{\alpha_1}\left(\alpha_2 m + \frac{\alpha_3}{\beta_1} \right) \qquad \text{(Eqn 4.74)}$$

If m is unknown, or if the value of m is to be verified, then it can be obtained using Eqn 4.75, which is derived from the equations $\beta_1 = \frac{k_s}{bm}$ and $\beta_2 = \frac{k_s}{bm^2}$.

$$m = \frac{\beta_1}{\beta_2} \qquad \text{(Eqn 4.75)}$$

The above method has shown that each of the muscle internal parameters: k_p, k_s and b of the classical Hill muscle model are functions of the coefficients of

the powers of s in the system transfer functions, without the inclusion of other model parameters in the functions (with the exception of known mass m, which can be determined using Eqn 4.75). Therefore each of the parameters in the classical Hill muscle model is uniquely identifiable and therefore the classical Hill muscle model is **structurally globally identifiable**.

4.2.4.6 Structural Identifiability of the Modified Hill Muscle Model

To examine the modified Hill muscle model in section 4.2.3, again consider the case of an excised muscle (Figure 4.14), where one side of the muscle is connected to a fixed point, and a mass is attached to the other end of the muscle (the free tendon is not considered in this analysis, because its length can be directly measured, see section 5.3.2). The muscle is modelled by the modified Hill muscle model in section 4.2.3. Applying $F(t) = ma(t) \equiv m\dfrac{d^2x(t)}{dt^2}$ and the following system states :

$$x_1(t) = x(t)\ ,\ x_2(t) = \frac{dx(t)}{dt} \text{ and } \dot{x}_2(t) = \frac{d^2x(t)}{dt^2} = \frac{F(t)}{m} \qquad \text{(Eqn 4.76)}$$

Together with the system equation of the modified Hill muscle model (Eqn 4.18) with a mass attached can be expressed as the follow state equation:

$$\dot{\bar{x}}(t) = \begin{bmatrix} \dot{x}_1(t) \\ \dot{x}_2(t) \end{bmatrix} = \begin{bmatrix} 0 & 1 \\ -k_{p'}/m & -b'/m \end{bmatrix} \begin{bmatrix} x_1(t) \\ x_2(t) \end{bmatrix} + \begin{bmatrix} 0 \\ \dfrac{1}{m} \end{bmatrix} F_{CE'}(t) + \begin{bmatrix} 0 \\ \dfrac{k_{p'}}{m} x_0 \end{bmatrix} \qquad \text{(Eqn 4.77)}$$

Applying Eqn 4.77 in the form of Eqn 4.27, the coefficient matrices are:

$$\bar{A} = \begin{bmatrix} a_{11} & a_{12} \\ a_{21} & a_{22} \end{bmatrix} = \begin{bmatrix} 0 & 1 \\ -k_{p'}/m & -b'/m \end{bmatrix} \text{ and } \bar{B} = \begin{bmatrix} b_1 \\ b_2 \end{bmatrix} = \begin{bmatrix} 0 \\ \dfrac{1}{m} \end{bmatrix} \qquad \text{(Eqn 4.78)}$$

Again if the measured length of the muscle is to be considered as the difference between whole length and its natural length, i.e. $x_0 = 0$, then the constant term at the end of Eqn 4.68 will be eliminated after Laplace transform.

Take $F_{CE'}(t)$ as the system input and the muscle length $x_1(t)$ as the output, i.e.:

$$y(t) = \bar{C}\bar{x}(t) = \begin{bmatrix} 1 & 0 \end{bmatrix} \bar{x}(t) \quad \text{(Eqn 4.79)}$$

Taking Laplace transform of the state equation and output equation, and applying the method from Eqn 4.41 to 4.47. And with the zero and one values of $\bar{A}$ substituted into the matrix $(s\bar{I} - \bar{A})$, $adj(s\bar{I} - \bar{A})$ and $\Delta(s)$ are:

$$adj(s\bar{I} - \bar{A}) = \begin{bmatrix} s - a_{22} & 1 \\ a_{21} & s \end{bmatrix} \quad \text{(Eqn 4.80)}$$

$$\Delta(s) = s^2 - a_{22}s - a_{21} \quad \text{(Eqn 4.81)}$$

This gives:

$$\frac{Y_1(s)}{U(s)} = \left(\frac{1}{m}\right)\frac{1}{s^2 - a_{22}s - a_{21}} = \left(\frac{1}{m}\right)\frac{1}{s^2 + \left(b'/m\right)s + \left(k_{p'}/m\right)} \quad \text{(Eqn 4.82)}$$

The transfer function is a 2nd order transfer function. From experiment and model fitting, the coefficients of the powers of s terms in the following equation can be obtained.

$$\frac{Y(s)}{U(s)} = \frac{\beta}{s^2 + \alpha_1 s + \alpha_2} \quad \text{(Eqn 4.83)}$$

Comparing the terms β, α_1 and α_2 in Eqn 4.83 and the transfer function in Eqn 4.82, the identifiability of each model parameter can be obtained. The value of external mass m is known, however it can also be obtained from $1/\beta$. The spring constant $k_{p'}$ can be obtained from $\alpha_2\beta$ and the damping coefficient can be obtained from $\alpha_1\beta$. Therefore all parameter values in the modified Hill muscle model are uniquely identifiable and the model is **structurally globally identifiable**.

4.2.5 Discussion

The model equation of the classical Hill muscle model that has been derived in section 4.2.1 gave a model equation that includes the time derivative of both the muscle force and muscle length. This is difficult to be incorporated into a musculo-skeletal model. The modified Hill muscle model described in section 4.2.3 that had been demonstrated to be equivalent to the classical Hill muscle model gave a model equation that equate the muscle force as a function of the internal component values, length and velocity of the muscle. This form of the model will be used to develop a musculo-skeletal model.

As discussed in section 4.2.4, some model parameters can only be obtained through model fitting and parameter estimation for living subjects. The structural identifiability analysis described in section 4.2.4 has showed that, at least theoretically, unique parameter values can be obtained for the modified Hill muscle model from parameter estimation.

4.3 Musculo-skeletal model of the human arm

The movement of a rigid body segment connected to a fixed pivot (joint) can be modelled as a single segment pendulum. And it has been shown in section 4.1 that the Netwon-Euler model for a single segment pendulum gives simulated movement that is in good agreement with measured data. Therefore in this thesis a musculo-skeletal model was developed to model the movement of a single body segment connected to a fixed pivot.

The movement of the forearm is studied in this thesis, in which the human arm and the movement dynamics of the elbow joint is modelled using a two segments skeletal model incorporating the structurally identifiable modified Hill muscle, see Figure 4.15. As described in Figure 2.1a, the elbow is a hinge joint with one degree of freedom, allowing the elbow to flex and extend.

In this thesis, the wrist joint does not move and the forearm and hand are seen a one rigid segment.

The muscles responsible for the movement of the elbow are the flexor muscles, defined as the biceps muscle in this thesis, which anatomically describes the biceps brachii and brachialis acting in parallel; and the extensor muscle, triceps brachii, defined as the triceps muscles in this thesis.

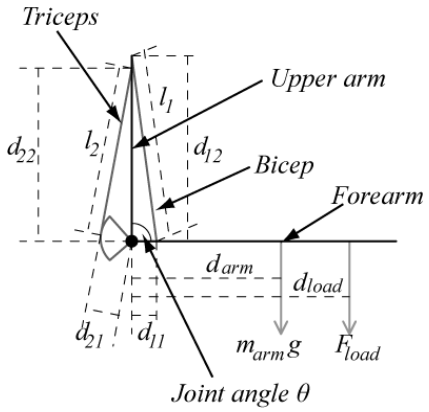

Figure 4.15. Two muscle arm model, showing the flexor biceps muscle and extensor triceps muscle. Elbow angle increases as forearm extends, clockwise direction is positive in this figure. The arm position shown in this figure has an elbow angle of 90°.

4.3.1 Skeletal model of the arm

In the arm model shown in Figure 4.15, the upper arm is designed to be fixed in position thus the location of the elbow joint is fixed. The forearm (and hand) is the only moving segment in the model, which is connected to the upper arm at the elbow. The movement of the forearm around the elbow that is fixed in position resembles the movement of a single segment pendulum. Equations to describe its movement dynamics are shown in section 4.3.3.

The arm model in this thesis only considers the movement of the elbow in the flexion and extension directions, thus the model can be simplified into a 2D planar pendulum model similar to the pendulum model described in section 4.1.3. The movement of the forearm in these two directions are governed by all the muscles that are connected around the elbow joint and surrounding soft tissues.

As shown in Figure 4.15, the arm model includes several geometric parameters, and these are required to compute forces and moments of muscles acting around the elbow joint, shown in section 4.3.3. The lengths d_{11}, d_{12}, d_{21} and d_{22} are the distances from the centre of the joint to the points of origin and insertion of the free tendons. The free tendon is that portion of the tendon which is external to the bulk of the muscle (see section 4.3.2). It should be noted that anatomically the lower free tendon of the triceps brachii has a point of insertion on the forearm, the lower end of the triceps muscle free tendon wraps tightly around the elbow when the arm is flexed. The portion of the free tendon that wraps around the elbow was assumed to follow the shape of an arc with a constant radius equal to d_{21} from the centre of the rotation of the elbow. This is depicted in Figure 4.15 by the triceps muscle tendon wrapping around a sector of a circle, where the lower end of the triceps muscle tendon is attached to the forearm at the bottom corner of the circle sector. This circle sector is part of the forearm segment. When the triceps muscle shortens, this pulls the bottom corner of the circle sector and rotating the circle sector and the forearm

anticlockwise. d_{arm} is the distance between the centre of the elbow joint and the centre of mass of the arm plus hand. d_{load} is the distance from the elbow to the centre of the load force applied to the hand, the latter being the centre of known weights held in the hand during the experiments in Chapter 5. The lengths of the biceps and triceps muscles plus the lengths of the free tendons are defined by $l_1(t)$ and $l_2(t)$ respectively, and these are described in section 4.3.2.

The dynamics of this model are determined by the dynamics of the muscles and the mechanical geometry of the skeletal and soft tissue components, which are described in sections 4.3.2 and 4.3.3.

During the movement of the arm, the flexor muscles and the extensor muscle are slack at different range of angles. And these muscles are different in muscle volume and cross-sectional area, which mean there maybe differences in the muscle model parameter values between the muscles in the model. The differences in muscle characteristics may give different movement dynamics between flexion and extension. Therefore the flexor and extensor muscles were modelled as individual components, to allow the musculo-skeletal model to be able to more realistically represent the movement of the joint.

Although modelling each of the muscles around the joint individually would better describe the anatomy of the joint, the arm model of this work (Figure 4.15) contains only a single flexor muscle. Anatomically, three muscles cause flexion at the elbow: the biceps brachii, brachialis and brachioradialis. Of these, the biceps brachii and brachialis contribute the majority of the force (Murray et al., 2000). These two muscles are of similar length (An et al., 1981, Murray et al., 2000), and anatomically overlay each other and act in the same direction. Therefore they have similar moment arms. By fitting the arm model with only one flexor muscle, the mechanical properties of both the biceps brachii and brachialis have been combined into the model's biceps muscle. In practice it would be impossible to measure the length of the brachialis in vivo using

palpation and surface measurement as it is embedded under the biceps brachii, but palpation and surface measurement have been the method used to obtain bulk muscle lengths in this thesis, and is the only non-invasive method without cross sectional imaging techniques such as X-ray CT and MRI.

Additionally, if the biceps brachii and brachialis are modelled as individual components, structurally the individual muscle forces are not identifiability, i.e. unique force values of the muscle cannot be obtained from parameter estimation experiments, as they effectively act in parallel. This inability to obtain unique parameter values may explain the reason why Venture et. al. were unable to obtain parameter values for the model in their original work (Venture et al., 2005), with the result they subsequently excluded any form of Hill muscle models from their work (Venture et al., 2006). Therefore in this thesis the muscles have been grouped in terms of function, i.e. triceps (extensor) muscle includes the triceps brachii; the biceps (flexor) muscle includes the biceps brachii, brachialis and brachioradialis.

4.3.2 Modified parallel Hill muscle model with exposed free tendon

The mechanical characteristic of the muscles in the model: biceps and triceps muscles are represented by a modified parallel element Hill muscle model (shown in section 4.2.3) in series with an exposed free tendon k_t (Figure 4.16).

It should be noted that from this point onwards in this thesis, the labels of each mechanical component in the modified Hill muscle model are different to the muscle models described and analysed in sections 4.2.1 and 4.2.3, as the parameters here have specific geometric definitions for each muscle in the model (described in section 4.3.3) as well as anatomical definition described in section 2.2.2. The muscle model consists of three parallel components: the contractile element (CE), a spring k_m and a dash-pot damper b_m. The contractile element (CE) represents the force source when the muscle is activated. The damping element b_m represents energy loss within the muscle from mechanical

inefficiency at the actin/myosin level. The parallel spring element k_m represents elasticity of the bulk muscle reflecting its ability to return to its natural length. The length x represents the length of the bulk muscle, and x_t represents the length of exposed free tendon. The lengths of the free tendons at both ends of a muscle are summed together and modelled as one serial spring.

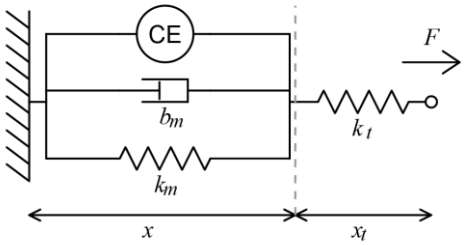

Figure 4.16. Modified parallel Hill muscle model incorporating a free tendon of spring constant k_t, and length x_t. x represents the length of the bulk of the muscle, which has a contractile element CE, damper b_m and spring k_m in parallel.

As discussed in section 4.2.3.3, the free tendon is assumed to be much stiffer than the bulk of the muscle, the extension of the free tendon is considered negligible, and thus have fixed length.

4.3.3 System equations

Euler's second law has been used to derive the system equation for the musculo-skeletal model shown in Figure 4.15. The system equations (Eqn 4.84 to Eqn 4.98) describe the elbow joint dynamics when the arm is in the same orientation as shown in Figure 4.15. The upper arm is fixed in a vertical position and with the muscle not activated, the forearm and hand are allowed to swing, pivoted around the elbow. The wrist is fully extended at all times. Starting with the angular velocity $\dot{\theta}(t)$ and acceleration $\ddot{\theta}(t)$, the equations of motions are Eqn 4.84 and Eqn 4.85:

$$\dot{\theta}(t) \equiv \frac{d\theta(t)}{dt} \qquad \text{(Eqn 4.84)}$$

$$\ddot{\theta}(t) \equiv \frac{d\dot{\theta}(t)}{dt}$$
$$= \left(\tau_{lim1}(t) + \tau_{lim2}(t) + F_1(t)\frac{d_{11}d_{12}\sin\theta(t)}{l_1(t)} - F_2(t)d_{21} + m_{arm}d_{arm}g\sin\theta(t) \right. \quad \text{(Eqn 4.85)}$$
$$\left. + m_{load}d_{load}g\sin\theta(t) - b_{arm}\dot{\theta}(t) \right) / J$$

where the angular acceleration $\ddot{\theta}(t)$ equals to the sum of torques around the elbow joint divided by the moment of inertia of the forearm, hand and any load held in the hand. d_{11}, d_{12}, d_{21}, d_{22}, d_{arm}, d_{load} and $\theta(t)$ are defined in Figure 4.15. A damping factor b_{arm} represents the resistance to movement caused by soft tissues around the elbow joint. $\tau_{\lim 1}(t)$ and $\tau_{\lim 2}(t)$ are the torques at the joint limits and are described at the end of this section and modelled by Eqn 4.96 and Eqn 4.97. The third and fourth terms in Eqn 4.84 (terms containing $F_1(t)$ and $F_2(t)$ respectively) are the torques from the biceps and triceps muscles, which are products of the moment arm and the force of the muscles ($F_1(t)$ and $F_2(t)$) under elongation in the direction perpendicular to the forearm. The biceps muscle moment arm is d_{11}, and the perpendicular force is the biceps force adjusted by the direction of the muscle and angle of the elbow, derived from the geometry in Figure 4.17. The derivation of the torque of the biceps is shown in the derivation from Eqn 4.85 to Eqn 4.91 using the illustration in Figure 4.17. Because the lower triceps free tendon wraps tightly around the elbow (depicted by the sector of the circle described in section 4.3.1), the lower triceps muscle tendon always leaves the outer arc of the circle sector tangentially, and this direction is also perpendicular to the radius of the circle sector. Therefore the moment arm is the radius of the circle sector, equal to d_{21}, and the perpendicular force is the triceps force $F_2(t)$. The two terms following the muscle torques are the torques caused by gravity acting on the mass of the arm and any weights held in the hand. J is the moment of inertia of the forearm

together with any extra weight held in the hand. The approximation for the moment of inertia of the forearm is described in section 5.2.2 and Eqn 5.4.

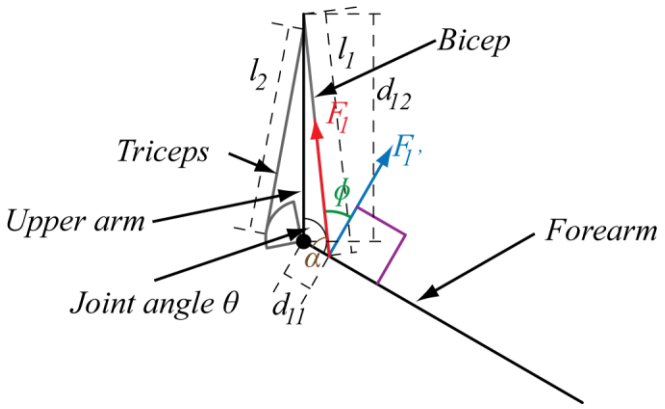

Figure 4.17. Biceps muscle torque calculation. The biceps muscle force perpendicular to the forearm $F_{1'}$ can be calculated using the biceps muscle force F_1 and angle ϕ. The angle α plus ϕ equals 90°.

$$\text{Bicep muscle Torque} = \vec{d}_{11} \times \vec{F}_{1'}(t) = \vec{d}_{11} \times \vec{F}_1(t) \cos\phi(t) \qquad \text{(Eqn 4.86)}$$

Where d_{11} is the moment arm of the biceps muscle acting on the forearm. $\phi(t)$ is the angle between the direction of the biceps force $\vec{F}_1(t)$ and the direction perpendicular to the forearm.

Consider the new angle $\alpha(t)$ shown in Figure 4.17, where:

$$\alpha(t) = 90^\circ - \phi(t) \qquad \text{(Eqn 4.87)}$$

It should be noted that this angle $\alpha(t)$ is not to be confused with the angular acceleration used in other sections in this thesis. It is only used in Eqn 4.87 to 4.91 to describe the derivation of the biceps muscle moment arm shown in Eqn 4.91.

Using the law of sine, the angle $\alpha(t)$ can be obtained from the length of the biceps muscle $l_1(t)$, length d_{12} and the joint angle $\theta(t)$.

$$\frac{\sin\theta(t)}{l_1(t)} = \frac{\sin\alpha(t)}{d_{12}} \qquad \text{(Eqn 4.88)}$$

Rearranging Eqn 4.88 gives

$$\sin\alpha(t) = \frac{d_{12}\sin\theta(t)}{l_1(t)} \qquad \text{(Eqn 4.89)}$$

Using the rules of sine and cosine, and the relationship between $\alpha(t)$ and $\phi(t)$ in Eqn 5.4, gives:

$$\sin\alpha(t) \equiv \cos(90^\circ - \alpha(t)) = \cos\phi(t) \qquad \text{(Eqn 4.90)}$$

Replacing $\cos\phi(t)$ with $\sin\alpha(t)$ in Eqn 4.86 and substituting Eqn 4.89 into the equation gives the term for the torque of the biceps muscle applied to the forearm around the elbow joint in Eqn 4.85, shown below:

$$\begin{aligned} \text{Bicep muscle Torque} &= \vec{d}_{11} \times \vec{F}_1(t)\cos\phi(t) \\ &= \vec{d}_{11} \times \vec{F}_1(t)\sin\alpha(t) \\ &= \vec{d}_{11} \times \vec{F}_1(t)\frac{\vec{d}_{12}\sin\theta(t)}{l_1(t)} \\ &= \vec{F}_1(t)\frac{\vec{d}_{11}\vec{d}_{12}\sin\theta(t)}{l_1(t)} \end{aligned} \qquad \text{(Eqn 4.91)}$$

From Figure 4.16, the biceps muscle force $F_1(t)$ and triceps muscle force $F_2(t)$ are given by:

$$F_i(t) = F_{CEi}(t) + b_{mi}\dot{x}_i(t) + k_{mi}\left(x_i(t) - x_{i\_0}\right), \text{ where } i = 1, 2 \qquad \text{(Eqn 4.92)}$$

where $F_{CEi}(t)$ is the contractile force exerted by the contractile element, $x_1(t)$ and $x_2(t)$ are the lengths of the bulk of the biceps muscle and triceps muscle respectively, $\dot{x}_1(t)$ and $\dot{x}_2(t)$ are the shortening/lengthening velocity of the biceps and triceps muscle respectively, and x_{1_0} and x_{2_0} are the natural lengths of the biceps and triceps muscles, excluding the lengths of the free tendons. As described in section 4.3.2 the free tendons are assumed to have fixed lengths, but when the geometry of the model gives lengths shorter than their fixed

lengths, they become slack. This means the free tendons can only transfer contractile force and therefore if $F_i(t) \leq 0$, then $F_i(t) = 0$ in Eqn 4.92.

The biceps muscle length $x_1(t)$ and velocity of contraction $\dot{x}_1(t)$ and triceps muscle length $x_1(t)$ and velocity of contraction $\dot{x}_2(t)$ in the arm model shown in Figure 4.16 are given by Eqn 4.93 to Eqn 4.96:

$$x_1(t) = l_1(t) - x_{1t} = \sqrt{{d_{11}}^2 + {d_{12}}^2 - 2d_{11}d_{12}\cos\theta(t)} - x_{1t} \quad \text{(Eqn 4.93)}$$

where $\sqrt{{d_{11}}^2 + {d_{12}}^2 - 2d_{11}d_{12}\cos\theta(t)}$ calculates the total length of the biceps bulk muscle and free tendon using the law of cosine, x_{1t} is the biceps free tendon length. The biceps muscle shortening/lengthening velocity $\dot{x}_1(t)$ in Eqn 4.94 is the direct differential of Eqn 4.93.

$$\dot{x}_1(t) \equiv \frac{dx_1(t)}{dt} = \left({d_{11}}^2 - {d_{12}}^2 - 2d_{11}d_{12}\cos\theta(t)\right)^{-0.5} \cdot d_{11}d_{12}(\sin\theta(t))\dot{\theta}(t) \quad \text{(Eqn 4.94)}$$

$$x_2(t) = l_2(t) - x_{2t} = \sqrt{{d_{22}}^2 - {d_{21}}^2} + d_{21}(\pi - \theta(t)) - x_{2t} \quad \text{(Eqn 4.95)}$$

where $\sqrt{{d_{22}}^2 - {d_{21}}^2}$ calculates the total length of the triceps bulk muscle and free tendon using Pythagoras' theorem. The following $d_{21}(\pi - \theta(t))$ term calculates the length of the portion of the triceps tendon that wraps around the elbow joint. x_{2t} is the triceps free tendon length. The triceps muscle shortening/lengthening velocity $\dot{x}_2(t)$ in Eqn 4.96 is the direct differential of Eqn 4.95.

$$\dot{x}_2(t) \equiv \frac{dx_2(t)}{dt} = -d_{21}\dot{\theta}(t) \quad \text{(Eqn 4.96)}$$

Additional torques resulting from soft tissue compression and extension are present near the maximum angle of flexion and extension. $\tau_{\text{lim1}}(t)$ in Eqn 4.85

represents additional torque at maximum extension; and $\tau_{\lim 2}(t)$ represents additional torque at maximum flexion, and are modelled as:

$$\tau_{lim1}(t) = \begin{cases} -k_{lim}(\theta(t) - \theta_{lim1}) - b_{lim}\dot{\theta}(t) & \text{if} \quad \theta(t) > \theta_{lim1} \text{ and } \dot{\theta}(t) > 0 \\ -k_{lim}(\theta(t) - \theta_{lim1}) & \text{if} \quad \theta(t) > \theta_{lim1} \text{ and } \dot{\theta}(t) \le 0 \\ 0 & \text{if} \quad \theta(t) \le \theta_{lim1} \end{cases} \qquad \text{(Eqn 4.97)}$$

$$\tau_{lim2}(t) = \begin{cases} -k_{lim}(\theta(t) - \theta_{lim2}) - b_{lim}\dot{\theta}(t) & \text{if} \quad \theta(t) < \theta_{lim2} \text{ and } \dot{\theta}(t) < 0 \\ -k_{lim}(\theta(t) - \theta_{lim2}) & \text{if} \quad \theta(t) < \theta_{lim2} \text{ and } \dot{\theta}(t) \ge 0 \\ 0 & \text{if} \quad \theta(t) \ge \theta_{lim2} \end{cases} \qquad \text{(Eqn 4.98)}$$

where k_{lim} and b_{lim} represent the effective rotational spring and damping constants of the soft tissue, which were assumed to be the same for both extension and compression in this thesis.

4.4 Discussion

Although some of the internal component lengths (i.e. CE, ks and b) for the classical Hill muscle model were unknown, the method used to derive the system equation still allowed the overall force and length to be equated, by eliminating the internal lengths in the derivation process. This has also been the case for the serial muscle model, where the internal lengths of each component were unknown, but the derivation process can eliminate the need for internal lengths to be known to obtain the model equation. However, the underlying issue with this is that the models include internal lengths that are unknown and cannot be measured, and this has caused the models to be structurally unidentifiable.

There are no available literatures where researchers have used the classical Hill muscle model in parameter estimation experiments; instead the modified version of the Hill muscle model that includes only parallel components was used instead. The reason for this has not been discussed in the available literature. A possible reason for this is that the equation for the classical Hill muscle model, presented in Eqn 4.24 in section 4.2.1, includes the time derivatives of the

muscle force and muscle lengths, this had made it difficult to be incorporated into a musculo-skeletal model as a sub model.

Some researchers included muscle fibre pennation angle in the muscle models e.g. (An et al., 1981, Hoy et al., 1990, Maganaris, 2001, Maganaris, 2004), however this is not included in this thesis. While pennation angle can better describe the anatomical arrangement of muscle fibres in the muscle, such angle is difficult to measure in vivo during dynamic movement. Maganaris (Maganaris, 2001) used ultrasound imaging to obtain cross-sectional image of the internal anatomy during isometric contraction. However such measurement approach is infeasible in dynamic movement. If the pennation angle of a muscle θ_{pin} is assumed to be constant (Maganaris, 2004), then the muscle fibre output force will be multiplied by a constant of $\cos\theta_{pin}$. The muscle force therefore becomes $F(t) = \cos\theta_{pin} \times f(k_p x(t), b\dot{x}(t), F_{CE}(t))$. Without knowing the values of k_p, b and $F_{CE}(t)$, the value of this multiplier $\cos\theta_{pin}$ will not be uniquely identifiable from the internal muscle fibre force. In the thesis, the effect of the pennation angle is already embedded in the values of the passive springs and dampers, as well as the contractile element in the muscle model.

Chapter 5 Passive Movement Method for Parameter Estimation of a Musculo-Skeletal Arm Model Incorporating a Modified Hill Muscle Model

5.1 Introduction

This chapter is the beginning of the parameterisation process of the musculo-skeletal model developed in section 4.3 using measured data, and describes an approach to parameterise the passive components in the arm model from measurement of passive movements.

As discussed in section 1.1, musculo-skeletal diseases differ between patients; to allow clinicians to tailor patient specific rehabilitation strategies, model parameter values must be specific to the individual patient. Therefore in this thesis, the approach was to perform measurements for individual subjects, and the parameter values were obtained on an individual subject basis.

Traditionally measurement of Maximum Voluntary Contraction (MVC) of muscles has been used as the main measurements in parameter estimation process for muscle models in vivo. However when considering the use of the models in FES rehabilitation for patients who have lost the use of their muscles through degenerative diseases or accidents, measurements of MVC, or any measurements requiring voluntary contraction of the muscle will not be possible. Therefore a method of parameterising the muscle model without requiring voluntary contraction by the subject is required. This chapter presents an experimental method of parameterising the passive mechanical characteristics of the biceps and triceps muscles in *vivo*, by fitting the dynamics of the arm and elbow model to measured elbow movements. The movement observed for this

method required the muscles being parameterised to be completely relaxed and non-active. In this thesis, the movement of a freely swinging relaxed body segment (in this case the forearm) is called passive movement.

Another problem associated with attempting to use measurement of MVC or any voluntary control method is that the measured movement or force dynamics, are the sum of the characteristics of both the passive component and the active component. Without knowing one in advance, the other cannot be determined. However the proposed method of analysing passive movement has the advantage that the active components exert zero force, and therefore in passive movements, the characteristics of the active components are eliminated. Therefore this method does not need to consider the force/length and force/velocity characteristics that modulate the active component, CE, of the muscles, of which at this stage of the parameterisation process, are unknown.

Four healthy subjects participated in the experiments described in this chapter, where none of the subjects had any known bone, muscle or nerve disease. Whilst the primary stimulus of this work was FES, Mohammed et. al. (Mohammed et al., 2012) reported that muscle characteristics do not differ between the healthy subjects and SCI subjects when carrying out FES studies, therefore normal healthy subjects with no diagnosed muscle, bone or joint diseases could be used in this study. Height and weight characteristics of the subjects are included in Table 5.2.

5.2 Materials

5.2.1 Musculo-skeletal model of the human arm

The two segments model shown in Figure 5.1 is a representation of the human arm that was introduced in section 4.3. It has one degree of freedom around the elbow joint. The muscles are the flexor muscle, defined as the biceps muscle in this study, which anatomically describes the biceps brachii and brachialis acting in parallel; and the extensor muscle, which is the triceps brachii, and is defined as

the triceps muscle in this study. The descriptions of the geometric parameters in this model are presented in section 4.3.1.

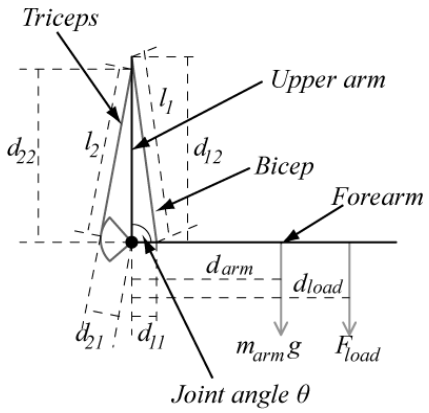

Figure 5.1. Two muscle arm model, showing the flexor biceps muscle and extensor triceps muscle. This arm orientation is the starting arm orientation in experiment 1

In the measurement protocol of this chapter, described in section 5.3, the subjects were required to hold a 1kg or 2kg weight at the centre of the palm during the experiments, and F_{load} shown in Figure 5.1 becomes $m_{load}\vec{g}$, where m_{load} is the mass of the weight held in the hand and $\vec{g}$ is the gravity vector.

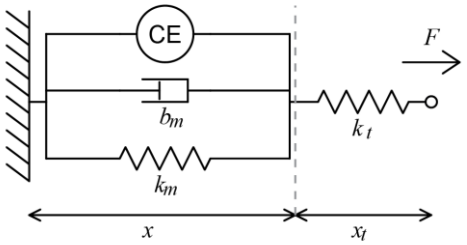

Figure 5.2. Modified parallel Hill muscle model incorporating a free tendon of spring constant k_t, and length x_t. x represents the length of the bulk of the muscle, which has a contractile element CE, damper b_m and spring k_m in parallel.

Figure 5.2 is the modified Hill muscle model in series with a free tendon already introduced in section 4.3.2, with the model equation described in section 4.3.3. As discussed in section 4.2.3.3, the free tendon is much stiffer than the bulk of the muscle, especially true under passive movement, and the extensions of the free tendons are considered negligible and thus the free tendons are assumed to have fixed lengths.

The experiments in this chapter only measured the dynamic movement of the arm when the muscles were completely relaxed, the contractile elements, CE, in the muscle models exert no forces and the CE force are eliminated from the muscle model equation in Eqn 4.92, i.e. in this chapter, the biceps muscle force and triceps muscle forces are:

$$F_i(t) = b_{mi}\dot{x}_i(t) + k_{mi}\left(x_i(t) - x_{i\_0}\right) \text{ , where } i = 1, 2 \qquad \text{(Eqn 5.1)}$$

The arm, positioned as shown in Figure 5.1 with the upper arm placed vertically , has been used to analyse elbow extension in experiment 1 described in section 5.3.3, in which the angular acceleration of the forearm around the elbow, $\ddot{\theta}(t)$ is given by Eqn 4.85. To analyse flexion, described in section 5.3.4 (experiment 2), the upper arm was placed horizontally with the elbow facing upwards. The arm model in Figure 5.1 has now been redrawn as Figure 5.3 to reflect this change in upper arm position. $\ddot{\theta}(t)$ is now given by Eqn 5.2, where the $\sin\theta(t)$ in the terms that include the gravity g in Eqn 4.85 has been changed to $\cos\theta(t)$ to reflect the difference in the direction of gravity with reference to the elbow angle.

$$\begin{aligned}\ddot{\theta}(t) &\equiv \frac{d\dot{\theta}(t)}{dt} \\ &= \left(\tau_{lim1}(t) + \tau_{lim2}(t) + F_1(t)\frac{d_{11}d_{12}\sin\theta(t)}{l_1(t)} - F_2(t)d_{21} + m_{arm}d_{arm}g\cos\theta(t) \right. \\ &\quad \left. + m_{load}d_{load}g\cos\theta(t) - b_{arm}\dot{\theta}(t) \right) / J\end{aligned} \qquad \text{(Eqn 5.2)}$$

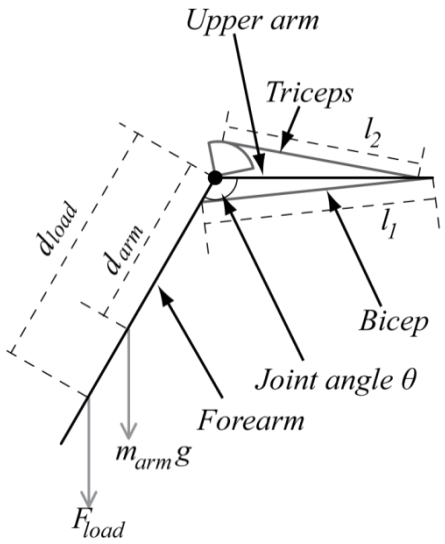

Figure 5.3. Two muscle arm model, showing the arm in the orientation used in experiment 2 to measure elbow flexion. The upper arm is held horizontal and the forearm is allowed to swing. The points of origin and insertion of the muscles are not shown in this figure but are identical to Figure 5.1.

In the preliminary results from the passive movement experiments reported in (Yu and Wilson, 2012a), the arm swing movement in experiment 1 (Figure 5.1), was limited by the maximum elbow extension, which in turn limited the amount of data available for model fitting, (the discussion for this is included in section 5.6). To overcome this, a third experimental setup was used: experiment 3, which is described in section 5.3.5. The upper arm was leaned forward by 45° from vertical, see Figure 5.6c. For this orientation, $\ddot{\theta}(t)$ is given by Eqn 5.3, where the $\sin\theta(t)$ in the terms that include the gravity g in Eqn 4.85 has been changed to $\sin\left(\theta(t)+\pi/4\right)$ to reflect the difference in the direction of gravity with reference to the elbow angle.

$$\ddot{\theta}(t) \equiv \frac{d\dot{\theta}(t)}{dt}$$
$$= \left(\tau_{lim1}(t) + \tau_{lim2}(t) + F_1(t)\frac{d_{11}d_{12}\sin\theta(t)}{l_1(t)} - F_2(t)d_{21} \right. \qquad \text{(Eqn 5.3)}$$
$$\left. + m_{arm}d_{arm}g\sin\left(\theta(t)+\pi/4\right) + m_{load}d_{load}g\sin\left(\theta(t)+\pi/4\right) - b_{arm}\dot{\theta}(t) \right) / J$$

5.2.2 Moment of inertia of the forearm and mass held in hand.

In this thesis, the moment of inertia of the forearm and hand around the elbow joint was calculated by approximating the forearm and hand as a cylinder with the mass uniformly distributed. The mass of the forearm together with the hand, m_{arm}, was measured by supporting the elbow and weighing the arm with the muscles fully relaxed at the 2nd knuckle of the middle finger. From the uniform mass distribution assumption, m_{arm} is twice the mass value obtained from weighing. The moment of inertia of the forearm and hand, J, in Eqn 4.85, Eqn 5.2 and Eqn 5.3 was then calculated by using the following standard approximation for a cylindrical object, plus the moment of inertia of the mass held in the hand m_{load} around the elbow joint calculated using the parallel axis theorem:

$$J = \frac{1}{4} m_{arm} r_{arm}^{\ 2} + \frac{1}{3} m_{arm} l_{arm}^{\ 2} + m_{load} d_{load}^{\ 2} \qquad \text{(Eqn 5.4)}$$

where the length of the cylinder l_{arm} was measured from the centre of the elbow joint to the 2nd knuckle of the middle finger with the hand clenched as a fist. The radius of the arm r_{arm} is approximated as half the diameter of the forearm, measured at 1/3rd of the distance from the elbow to the wrist. The moment of inertia is assumed to be constant over time.

5.3 Experimental design and protocol

The length and mass parameters in the arm model can be directly measured or calculated. The method of measurement is described in section 5.3.2. The arm model contains an antagonist pair of muscles allowing flexion and extension of the forearm. Therefore different types of experimental procedures observing extension (experiment 1 and 3) and flexion (experiment 2) are necessary to determine parameters that are not directly measurable, i.e. the spring and damping constants in the muscle models (Eqn 5.1) and Eqn 4.85, Eqn 5.2 and Eqn 5.3.

These experiments are designed to examine the step response of the elbow joint and determine the system parameters. As described in section 5.1, measuring motion when the muscles are inactive allows the parameter values of the passive components in the arm and the muscles to be determined. To achieve this, free fall motions were used in all experiments. The basic principle was to support the forearm at the wrist initially by a trigger block, where the forearm has potential energy, see Figure 5.6. By quickly (assumed to be instantaneously) removing the trigger block from under the wrist while the muscles are completely relaxed, the elbow joint experiences a step change in net moment, and extends or flexes due to gravity acting on the mass of the forearm, hand and any mass held. The experiments are denoted as experiment 1, 2 and 3, which are described in section 5.3.3 to section 5.3.5 respectively.

5.3.1 Motion capture setup and marker model

The Vicon® biomechanical 3 dimensional (3D) motion capture system described in Chapter 3 was used to measure the trajectories of the arm. The Vicon system captures at 200 frames per second and has a resolution of 0.1mm. An 8 markers configuration (arm marker model) has been developed in this study to locate the 3D position of the shoulder, elbow, wrist and hand. The arm marker model was designed to allow the centres of rotations of the joints (shoulder, elbow and wrist) to be determined, and subsequently allow the elbow angle to be determined from the locations of the joints. Markers were also placed on the trigger block to allow the removal of the block to be captured. The placements of the arm markers are shown in Figure 5.4 and listed in Table 5.1. Figure 5.6 contains images from the experiments showing the locations of the markers. The measured marker positions were used to compute the centre of the joints and elbow angles, these calculations are described in section 5.3.6.

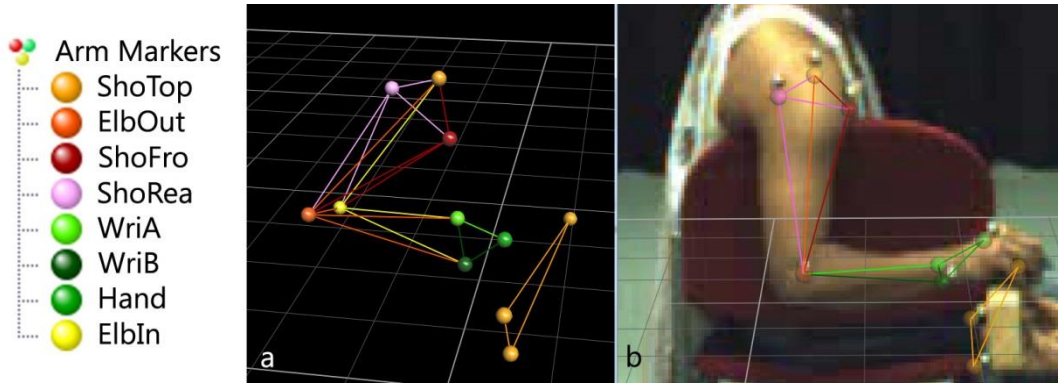

Figure 5.4. Arm and trigger block marker model used in motion capture. The markers in the arm marker model are colour coded and are listed on the left and explained in Table 5.1. a. shows a reconstructed view of the arm markers in the 3D space, as well as the trigger block, marked by 3 markers (yellow). b. shows the markers placed on the subject and trigger block, with the 3D reconstructed markers overlaid on the image.

Table 5.1. Arm markers used in 3D motion capture

Marker name	Description and marker placement
ShoTop	Top of shoulder, placed on top of the highest point of the acromion.
ShoFro	Front of shoulder, place in front of the shoulder; aligns with the anterior-posterior line that passes through the centre of the shoulder joint rotation.
ShoRea	Front of shoulder, place behind the shoulder; aligns with the anterior-posterior line that passes through the centre of the shoulder joint rotation.
ElbOut	Outside of elbow, placed on the lateral side of the elbow aligned with the medial lateral elbow centre of rotation line.
ElbIn	Inside of elbow, placed on the medial side of the elbow aligned with the medial lateral elbow centre of rotation line.
WriA	Wrist marker A, placed on the styloid process of radius.
WriB	Wrist marker B, placed on the styloid process of ulna.
Hand	Hand marker, placed on the back of the hand on top of the head knuckle of the middle finger metacarpal.

5.3.2 Anatomical parameter measurement and calculation

The directly measurable lengths in the arm model (section 4.3) are d_{11}, d_{12}, d_{21}, d_{22}, l_{arm}, r_{arm}, d_{load}, x_{1t}, x_{2t}, x_{1_0} and x_{2_0}. Palpation and surface measurement were used to determine the anatomical lengths; with a resolution of 5mm. Figure 5.5 was used as a guide for measuring free tendon lengths. Average values from five consecutive measurements were used. Distance d_{arm} was derived from l_{arm} using a table of anthropometric data (Winter, 2005). The distance d_{load} was measured from the centre of the elbow joint to the centre of the mass held in the hand.

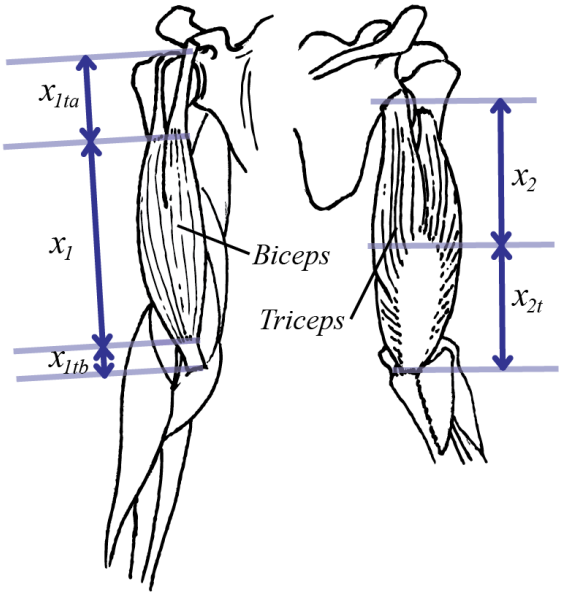

Figure 5.5. Definition of free tendon length and bulk muscle length. Exposed free tendon of the biceps is the sum of x_{1ta} and x_{1tb}. Sum of muscle and free tendon length equals to l_1 and l_2 for the biceps muscle and triceps muscle respectively.

The extensor of the elbow is the triceps muscle. Although there is more than one point of origin and more than one point of insertion for this muscle, the muscle is commonly modelled or measured using average muscle length, e.g. (Murray et al., 2000), and that is the approach used in this work.

The masses in the model, m_{arm} and m_{load}, were also directly measured using the method described in section 5.2.2. The mass held in the hand, m_{load}, was a known weight of 0 kg, 1 kg or 2 kg.

5.3.3 Forearm free fall experiment 1 – elbow extension

This experiment examined the forearm free fall trajectory during arm extension. It began with the subject's right arm positioned in the orientation shown in Figure 5.1 and Figure 5.6a. The upper arm was held vertical at all times and the forearm started from an elbow angle of 90°, which was supported by the trigger block placed under the hand. The orientation of the arm was measured by a spirit level and a set square.

The hand was placed on the trigger block in the orientation as shown in Figure 5.6. This is the neutral pronation/ supination (PS) angle of the forearm and hand when the biceps brachii is relaxed. As the biceps brachii is also involved in the PS rotation of the forearm, wrist and hand; placing the hand in a neutral position minimised any PS rotation of the forearm and hand during the free fall. Therefore the change in length of the biceps brachii was only due to flexion/extension of the elbow and not pronation or supination of the forearm and hand.

When the trigger block was removed, the forearm and hand fell freely under gravity. The arm was expected to reach maximum extension and then rebounded before eventually coming to rest. The length of recorded data for each trial was 10 seconds, where the trigger block was removed after a random time delay of up to 5 seconds after the start of data recording.

Three separate hand loads were used: zero load, 1 kg or 2 kg weights held in the hand. For each subject and experiment, consecutive trials were carried out in the following order: 5 trials with 0 kg added to the hand, 5 trials with 1kg held in the hand, 3 trials with 2 kg held in the hand and 3 trials with 0 kg added to the hand. A smaller number of trials were done with 2 kg to minimise the possibility of fatigue in the hand. The last 3 trials of 0 kg load were carried out to ensure the passive characteristics of the arm and muscle had not changed due to the duration of the experiment and the initial measured trajectories of 0 kg hand load were reproducible.

To ensure the starting position of the arm in repeated measurements (or with different hand load) was the same as the first measurement trial, the starting locations of the arm and trigger block markers in the first measurement trial were recorded and used as a guide for positioning the arm and trigger block in repeated measurements. In this thesis, this method was achieved by attaching a transparent sheet over the computer monitor, and marking the positions of the markers by drawing on the transparent sheet. 3D orthogonal views from the top and right side of the subject were used, and the 3D axis and scale were fixed in relation to the computer screen between different trials.

During the experiments, the subjects were aware of the objective to keep muscle relaxed, and they were asked to report immediately after each measurement if that was not the case. If the subject reported the muscles were not completely relaxed, that measurement was repeated.

5.3.4 Forearm free fall experiment 2 – elbow flexion

Experiment 2 records the subject's forearm free fall trajectory for flexion. The subject's arm starting position in experiment 2 is shown in Figure 5.6b. The upper arm is held horizontal by a strap with elbow facing up at all times and the forearm starts from maximum extension supported by the trigger block placed under the hand. When the trigger block is removed downwards, the elbow joint flexes freely, with the motion being similar to a damped pendulum motion. The recording procedure including the trial length, random delay before removing trigger block, load applied to the hand and the number of measurements taken was identical to the protocol used in experiment 1.

Some form of support to the arm was needed to ensure it was maintained in the correct position and orientation. The movement of the upper arm must be minimised, whilst the elbow and forearm are allowed to swing freely without restriction. Using a strap to position the upper arm was chosen over methods where the elbow joint is held, as any elbow support may restrict motion. The strap has minimal physical volume in comparison to frame based supports and

therefore the elbow angle range was not limited by the support. The width of the strap used in the experiments was a compromise between spreading the load and minimising the peak pressure beneath it and thus the pressure on the biceps muscle. The strap was positioned below the bulk of the biceps muscle as shown in Figure 5.6b and c to minimise pressure from the strap onto the muscle.

5.3.5 Forearm free fall experiment 3 – 45° elbow extension

Experiment 3 measures the forearm free fall trajectory (elbow extension) similar to experiment 1, however in experiment 3 the orientation of the upper arm was at 45° from the vertical position, held by a strap, see Figure 5.6c. The trigger block initially holds the forearm in a horizontal position, where the elbow angle is at 45°, the trigger block was removed downwards in the same fashion as in experiment 1 and 2 to start the experiment. The recording procedure including the trial length, random delay before removing trigger block, load applied to the hand and the number of measurements taken was identical to the protocol used in experiments 1 and 2.

Preliminary results reported in (Yu and Wilson, 2012a), which are also shown in Figure 5.7 to Figure 5.10, experiment 1, and discussed in section 5.6.1 showed the initial elbow extension experiment (denoted experiment 1 in this thesis and described in section 5.3.3) did not adequately describe the trajectory predicted by the model when maximum elbow extension was reached after 90° of movement. This only gave 0.6s of data for parameter estimation; therefore this experiment with a different upper arm orientation was used, providing a larger range of elbow angle movements (135°) for parameter estimation.

To determine the reliability of using subject feedback to monitor if muscles were not relaxed in the measurement. Experiment 3 also measured EMG of the biceps and triceps muscles as an objective measurement to detect muscle activity during the trials, the results and discussions are described in section 5.6.2.

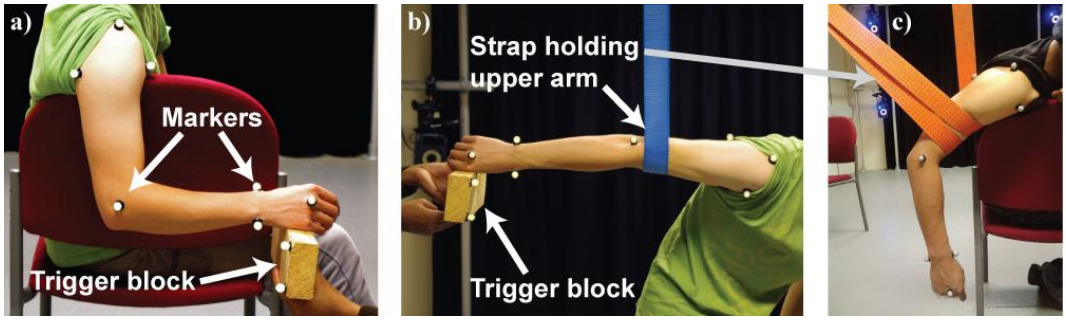

Figure 5.6 a) Experiment 1, 90° elbow extension starting position with trigger block supporting the hand. Some markers and the trigger block are labelled. b) Experiment 2 flexion starting positon with trigger block supporting the hand and strap holding the upper arm. c) Experiment 3, 45° flexion experiment, showing the upper arm fixed by a strap. The ElbIn marker is on the medial side of the elbow and not visible in the images. This is the resting position of the arm at the end of the experiment. The ElbIn marker is on the medial side of the elbow and not visiable in these images.

5.3.6 Motion capture data preparation for parameter estimation

The measured elbow angle was computed on a frame by frame basis using the measured arm marker positions. First the locations at the centres of the shoulder joint (SHO), elbow joint (ELB) and wrist joint (WRI) were calculated using the 3D location of measured markers, which are described in Eqn 5.5 to Eqn 5.7, where the marker names refer to the markers described in Table 5.1.

$$SHO = \left(ShoTop + ShoFro + ShoRea\right)/3 \quad \text{(Eqn 5.5)}$$

$$ELB = \left(ElbOut + ElbIn\right)/2 \quad \text{(Eqn 5.6)}$$

$$WRI = \left(WriA + WriB\right)/2 \quad \text{(Eqn 5.7)}$$

The elbow angle was then calculated as the acute angle between the upper arm vector $\vec{A}$ (Eqn 5.8) and forearm vector $\vec{B}$ (Eqn 5.9), shown in Eqn 5.10.

$$\vec{A} = \overrightarrow{ELB \quad SHO} \quad \text{(Eqn 5.8)}$$

$$\vec{B} = \overrightarrow{ELB \quad WRI} \quad \text{(Eqn 5.9)}$$

$$\theta_{elbow} = \cos^{-1}\left(\frac{\vec{A}\cdot\vec{B}}{\left|\vec{A}\right|\left|\vec{B}\right|}\right) \quad \text{(Eqn 5.10)}$$

Measurements with missing marker data or where the muscles were not fully relaxed were excluded from parameter estimation. The start of each experiment was identified by locating the instant when the trigger block markers moved downward.

5.4 Parameter estimation by forward dynamics simulation

Parameter estimation and optimisation was done on a subject by subject basis, to find a set of fitted parameter values of b_{arm}, k_{m1}, k_{m2}, b_{m1}, b_{m2}, $k_{\lim}$, and $b_{\lim}$ that gave minimum absolute error (MAE), which was the error between measured and simulated elbow angle trajectories.

The protocol for measuring the arm fall movement used a random amount of time between start of data capture and trigger block release, therefore during data processing, each trial was synchronised by observing the fall of the wrist marker WRIA. The moment in the time history when the z component (vertical component) of the WRIA marker fell below 1 standard deviation of its starting position was synchronised as the moment when the arm started to fall (time = 0s), and the simulation starts at this point in time. The starting elbow angles for the simulations were obtained by averaging repeated measurements of the same experiment and the same hand load for each subject, e.g. P3, experiment 2, 1kg. The starting angular velocities were assumed to be zero.

The simulated elbow joint angle and angular velocity time histories for Eqn 4.86, Eqn 5.2 and Eqn 5.3 were obtained by numerically integrating the forward dynamic model using a variable time step Runge-Kutta method ordinary differential equation (ODE) solver. All computational work was carried out in MATLAB® R2009b®.

Preliminary results from experiment 1 (Yu and Wilson, 2012a) concluded that experiment 1 gave limited amount of data for fitting (discussed in section 5.3.5) and therefore were excluded from model fitting. In this thesis, only experiment 2 and 3 were used to calculate the MAE, of which the results are reported in

section 5.5. In each recorded trial the 2 seconds of data following trigger block removal was used to calculate the MAE, see Eqn 5.11. For each subject, repeated trials from each experimental configuration (e.g. exp2 0kg) were averaged to give an average time history to be compared with the corresponding simulated arm fall movement and hand load configuration (e.g. simulated exp2 0kg), this gave 6 averaged measured trajectories and 6 simulated trajectories. The 6 pairs of data were used to calculate 6 MAEs, and these were then averaged to give an overall MAE for the subject (Eqn 5.12).

$$MAE_{Expi,\,jkg} = \frac{\sum_{t=0s}^{2s} \left| \theta_{t,\text{average measured},Expi,\,jkg} - \theta_{t,\text{simulated},Expi,\,jkg} \right|}{t} \quad i = 2,3 \quad j = 0,1,2$$

(Eqn 5.11)

$$\text{Overall } MAE = \frac{\sum_{i=2}^{3} \sum_{j=2}^{2} MAE_{Expi,\,jkg}}{6} \qquad \text{(Eqn 5.12)}$$

Parameter estimation was carried out using a multi-dimensional unconstrained nonlinear optimisation solver (fminsearch, Matlab), which minimised the overall MAE of each subject starting from an initial set of parameter values (the seed).

Free tendon spring constants had been reported to lie in the range 60-170kN/m (Maganaris and Paul, 1999), and the stiffness of the free tendon is considered to be much greater than the stiffness of muscle springs. Therefore, in this thesis, the physiologically realistic values for the spring constants (k_{m1}, k_{m2} and $k_{\lim}$) were assumed to be in the range 0 to 1,000N/m and 0 to 1000Nm/rad. The extreme values for the damping factors (b_{arm}, b_{m1}, b_{m2} and $b_{\lim}$) were assumed to be 0 and 100Ns/m (corresponding to 0 and 100Nms/rad) and values outside this range were rejected.

The parameter estimation for each subject was a two stage process: for the first stage, optimisation was performed for 3 different seeds, to ensure a global minimum MAE was found, these seeds are: fitted values from preliminary results from fitting experiment 1 and experiment 2 that are reported in (Yu and Wilson,

2012a); physiologically realistic values; and all zeros values. For each of these seeds the optimiser was run and the parameter values corresponding to the minimum value of MAE obtained from the 3 seeds was then used as the first seed for the start of the second, iterative stage of the parameter estimation process. In the second stage of the parameter estimation process values of the MAE obtained at the end of each cycle of optimisation were reduced to 3 significant figures (s.f.) and, if different from those obtained from the previous cycle, input as the seed into the next iterative cycle of optimisation. The fitted parameter values were those for which repeated cycles of optimisation produced no change in the 3 s.f. of the MAE values.

5.5 Results

The measured parameters together with the values of moment of inertia derived from the measurements are given in Table 5.2. The optimal parameter values obtained by parameter estimation and optimisation are listed in Table 5.3. In Eqn 4.97 and Eqn 4.98, the boundary angles in this study were established by measuring the range of unrestricted movement on one subject, P1, with a resolution of 10°. The values obtained were: $\theta_{\lim 1} = 2.618 rad(150^{\circ})$ and $\theta_{\lim 2} = 0.873 rad(50^{\circ})$.

The 3 sets of seeds used were the reported fitted values in the preliminary fitted results from experiment 1 and experiment 2; all zero values; and the physiological realistic seed based on the range listed in section 5.4, which was arbitrarily selected as $k_{m1} = k_{m2} = 90N/m$, $k_{\lim} = 0.2Nm/rad$, $b_{m1} = 0.3Nms/rad$, $b_{m2} = 0.5Nms/rad$ and $b_{arm} = b_{\lim} = 0.5Nms/rad$.

With the exception of 1 subject, P4, the 3 seeds gave MAE values that were within 1% for each subject after the initial stage of the parameter estimation process. For P4, using the seed values from previous work and physiologically realistic values yielded MAE values within 1% after the initial stage of parameter estimation. However, the seed with all zero values gave a MAE which converged

to a local minimum. Importantly the initial seeds for all subjects gave MAE values that were taken forward to the second, iterative stage of the parameter estimation process.

Table 5.2. Measured parameters of four subjects

Subject parameters	P1	P2	P3	P4
Height (m)	1.65	1.75	1.80	1.70
Weight (kg)	55	74	75	54
Forearm + hand weight, m_{arm} (kg)	0.92	1.28	1.88	0.96
d_{11} (mm)	45±3.2	50±3.2	37.5±2.5	45±3.2
d_{12} (mm)	269±7.3	285±5.8	250±13.0	275±7.7
d_{21} (mm)	45±4.5	50±3.2	55±3.2	50±0
d_{22} (mm)	240±12.1	255±14.1	248±9.7	248±6.0
x_{1t} (mm)	100±5.5	116±2.0	120±6.3	112±6.2
x_{2t} (mm)	123±8.7	130±4.1	135±7.7	126±7.3
x_{1_0} (mm)	146±4.0	150±6.3	155±4.8	145±4.5
x_{2_0} (mm)	155±6.3	161±16.5	140±13.0	156±8.6
l_{arm} (mm)	340±3.7	370±4.8	380±6.3	340±7.7
d_{arm} (mm)	150	163	168	152
d_{load} (mm)	330±13.6	360±12.6	330±7.7	292±5.1
r_{arm} (mm)	35±2.4	39±2.0	40±3.2	35±3.2
J (kg m^2), 0kg in hand	0.0279	0.0589	0.0912	0.0373
J (kg m^2), 1kg in hand	0.133	0.168	0.200	0.137
J (kg m^2), 2kg in hand	0.246	0.277	0.309	0.235

Note: Measurement errors (± 1 standard deviation) are reported for the directly measured lengths.

Table 5.3. Fitted muscle parameter values using experiment 2 and 3

	P1	P2	P3	P4
b_{arm} (Nms/rad)	0.221	0.285	0.114	0.126
k_{m1} (N/m)	207	218	21.4*	41.4*
b_{m1} (Ns/m)	0.0395	0.188	0.920	0.110
k_{m2} (N/m)	126	148	389*	0.419*
b_{m2} (Ns/m)	1.99	0.192	5.88	4.57
$k_{\lim}$ (Nm/rad)	0.0361	0.0436	2.33	1.13×10^{-6}
$b_{\lim}$ (Nms/rad)	6.00×10^{-3}	0.306	0.0733	0.0106
MAE (rad)	0.185	0.174	0.186	0.254

* See discussion in section 5.6.4

Simulated elbow angles using values in Table 5.3 together with measured elbow angle data are plotted in Figure 5.7 to Figure 5.10.

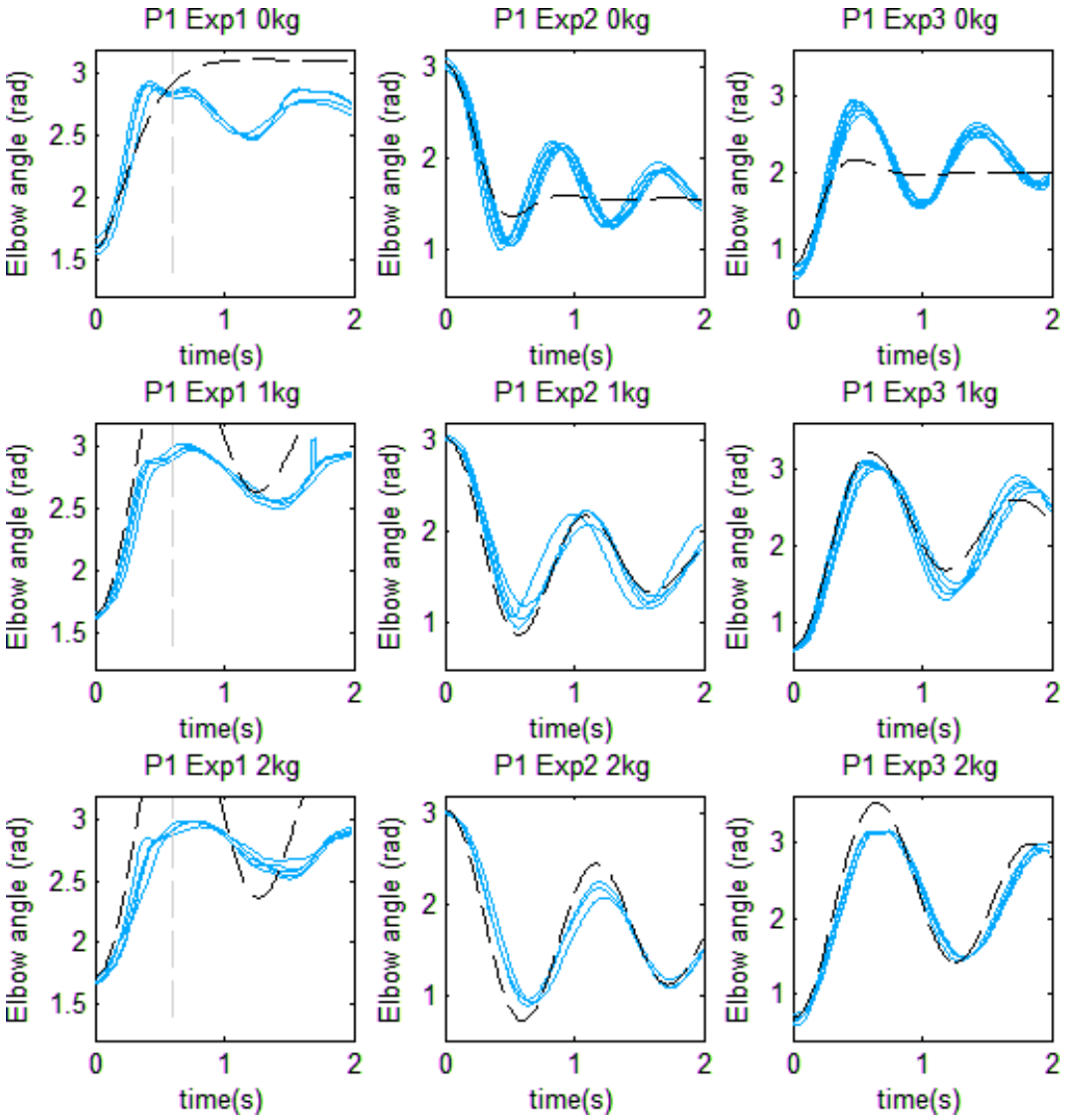

Figure 5.7. Forearm free fall trajectory of subject P1. Blue solid lines: measured joint trajectories. Black dashed line: simulated joint trajectory using values from Table 5.2 and Table 5.3.

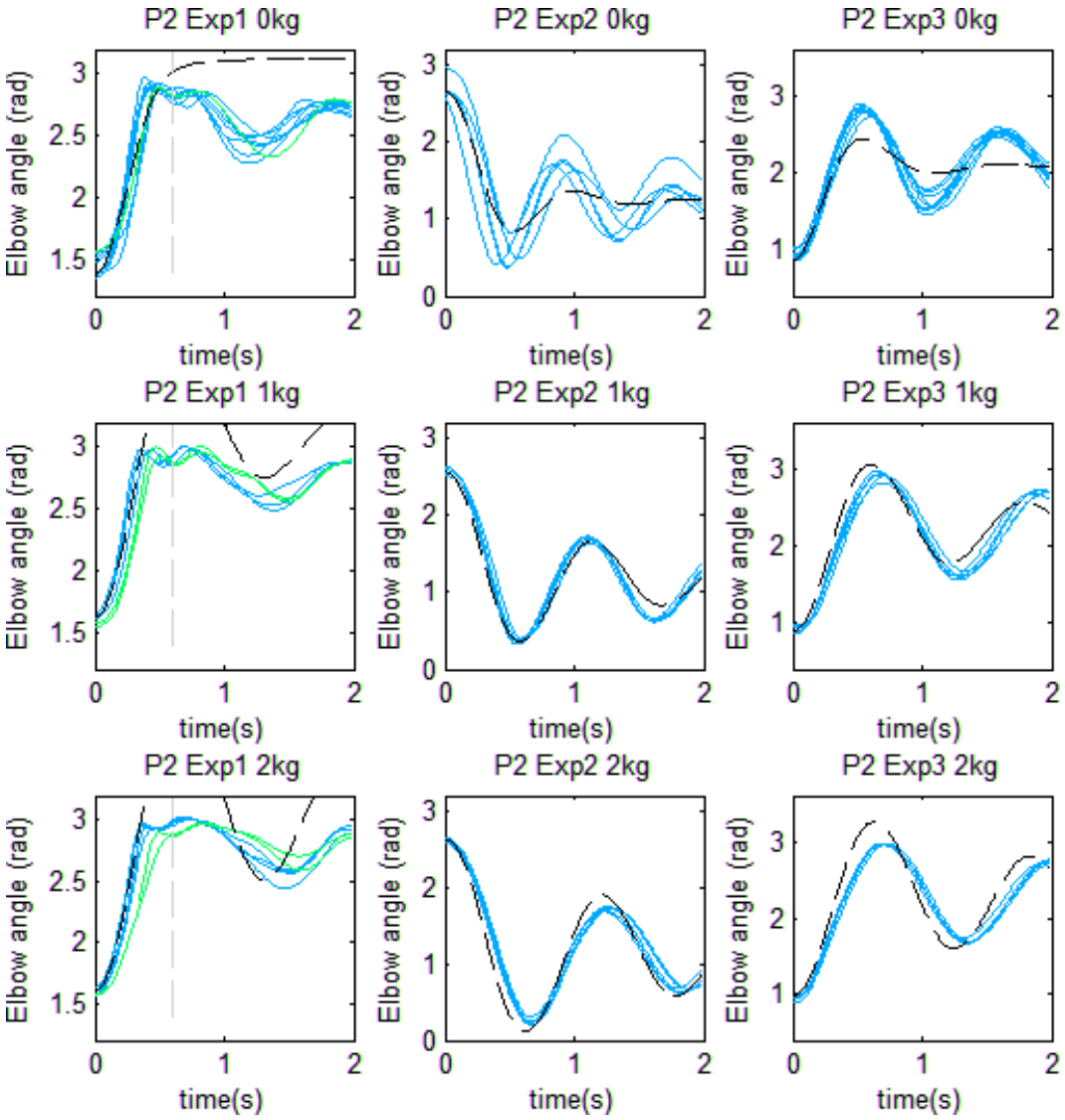

Figure 5.8. Forearm free fall trajectory of subject P2. Blue and green solid lines: measured joint trajectories from different days. Black dashed line: simulated joint trajectory using values from Table 5.2 and Table 5.3.

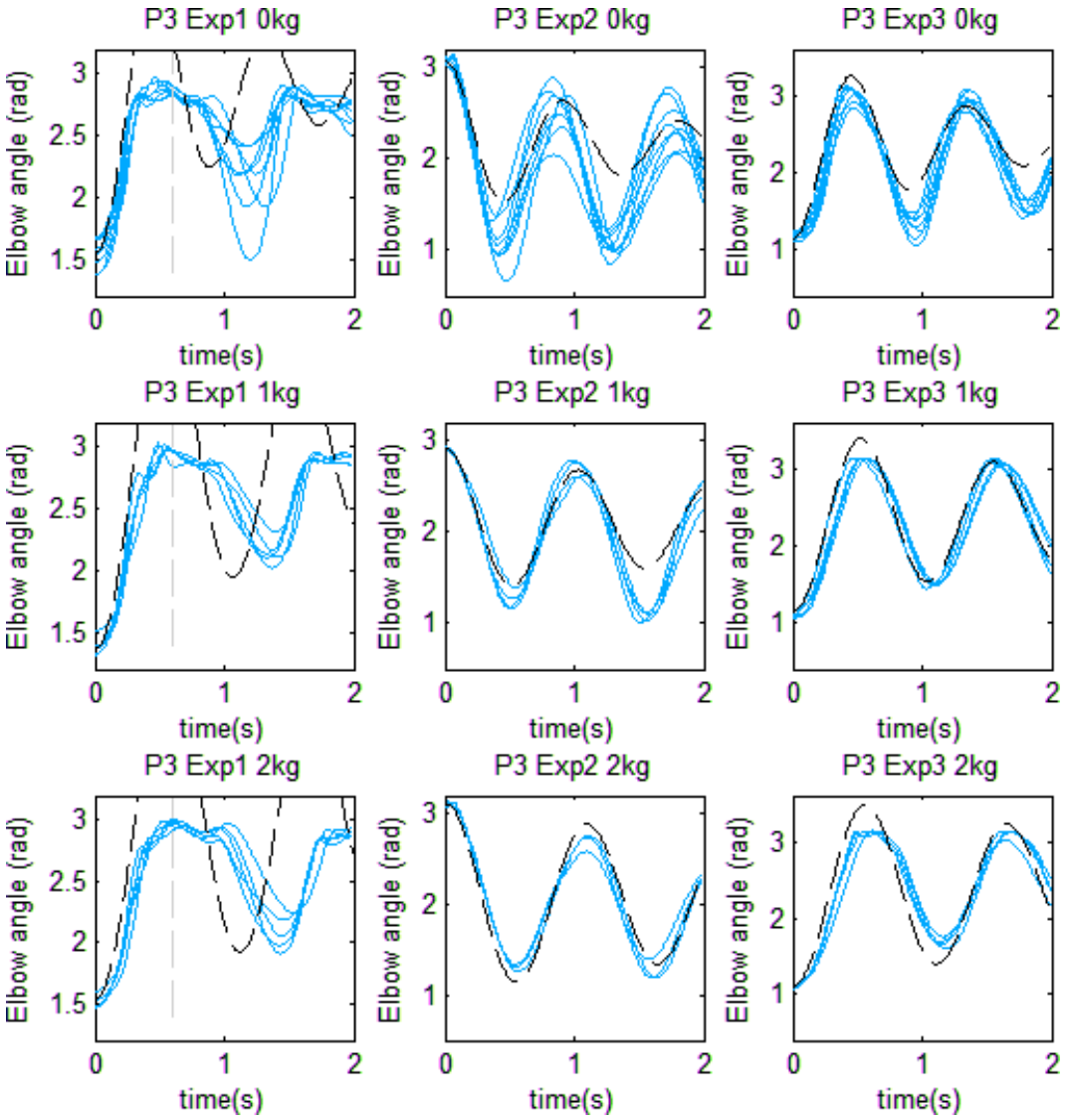

Figure 5.9. Forearm free fall trajectory of subject P3. Blue solid lines: measured joint trajectories. Black dashed line: simulated joint trajectory using values from Table 5.2 and Table 5.3.

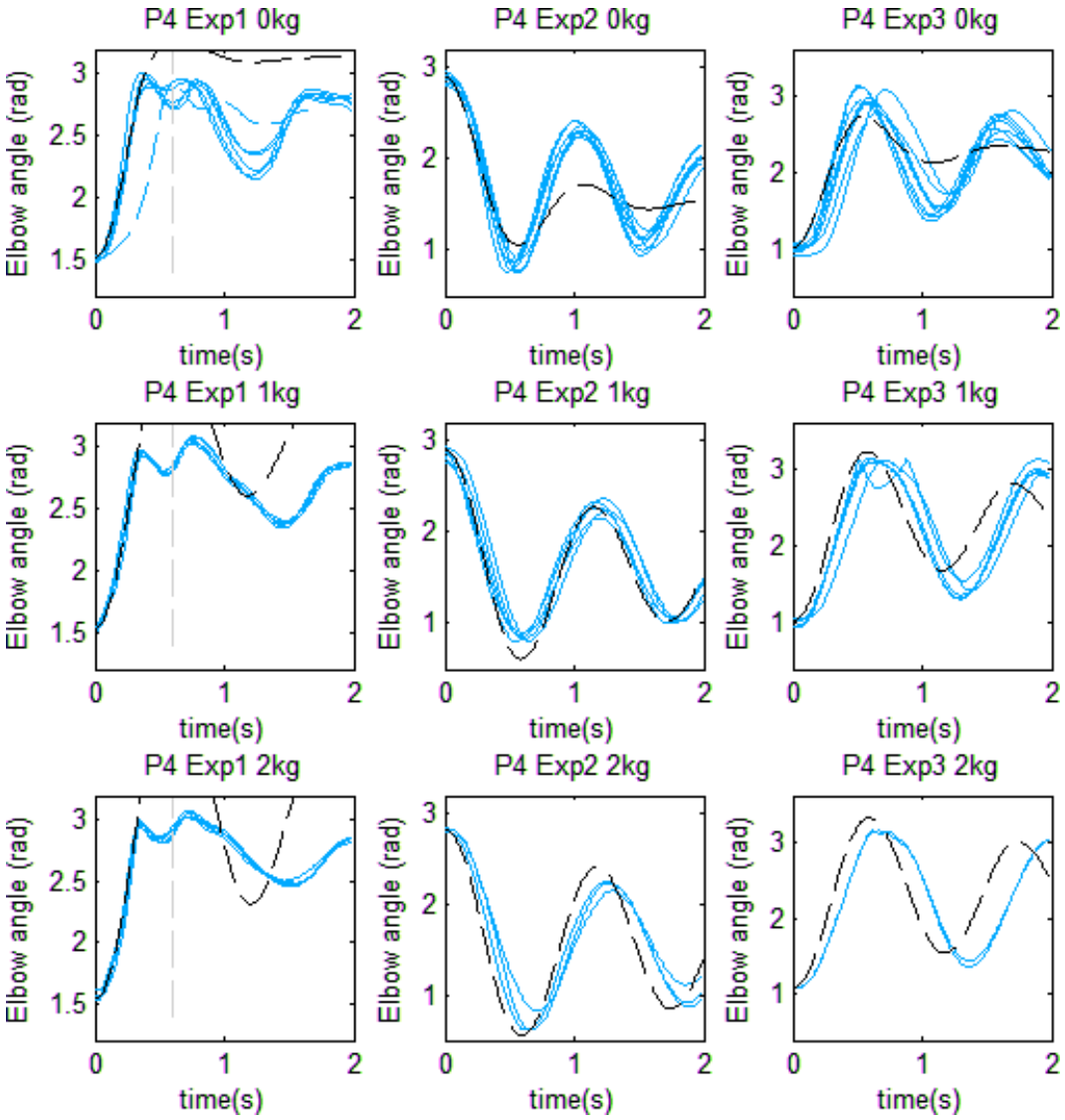

Figure 5.10. Forearm free fall trajectory of subject P4. Blue solid lines: measured joint trajectories. Blue dashed line: measured joint trajectory with muscles not fully relaxed. Black dashed line: simulated joint trajectory using values from Table 5.2 and Table 5.3.

5.6 Discussion

This study has covered a number of aspects of the problem in obtaining parameter values for individual muscles controlling movement of a single joint. Overall the work reported produced unique numerical values for the passive parameters, and the discussion will be organised to highlight different parts of the process.

5.6.1 Experiment design

The experiments described in this chapter required each subject to perform all experiments in one session, i.e. the motion capture marker set was not removed

and replaced between capture trials. Markers were always applied to subjects by the author of this thesis. However to assess the reproducibility of the result obtained across sessions, where the markers would be removed and replaced between sessions, an experiment was performed to obtain an error in computed elbow angle between trials, when markers were removed and replaced. This error in marker placement can also be used to assess how precise the markers can be put on to different subjects at the anatomical features defined in Table 5.1. Using the Isometric Arm Contraction Rig (IACR) described in Chapter 6, a single subject (subject P2) participated where a static elbow angle of about 90°, fixed by the IACR, was used. 10 repeated trials were measured where the markers were not removed and replaced between trials, but the subject removed the arm from the IACR and had it repositioned between trials. The error measured by this protocol was denoted $\delta movement$, and is a measurement of the error caused by repositioning the arm in the IACR. Five more trials were then performed where the marker set was removed and replied between each trial; the error in the computed elbow angles between these five trials, denoted $\delta total$, would include the error from the subject removing the arm from the IACR, $\delta movement$, and also error from replacement of the motion capture markers, $\delta marker\_placement$.

The mean computed elbow angle from the marker reproducibility experiment was 88.2°. $\delta movement$ was obtained by computing the standard deviation of the elbow angles from the ten trials; and was found to be 0.900° (3 s.f.). The total error of the five trials where the marker set had been removed and replaced, $\delta total$, was found to be 2.69°. Assuming $\delta movement$ is the same in the five trials where the marker set was removed and replaced between trials and the original ten trials where the marker set was not changed, then using Eqn 5.13 (Hughes and Hase, 2010), the error in the computed motion capture elbow angle from removing and replacing marker set, $\delta marker\_placement$, can be computed, which was found to be 2.54° (2.88% of 88.2°). These error were

assumed to be normally distributed; $\delta movement$ and $\delta marker\_placement$ were assumed to be cumulative.

$$\delta total = \sqrt{\delta movement^2 + \delta marker\_placement^2}$$
$$\delta marker\_placement = \sqrt{\delta total^2 - \delta movement^2} \quad \text{(Eqn 5.13)}$$

The addition of a 1kg or 2kg hand load in the experiments greatly reduced the uncertainty in the estimated moment of inertia of the forearm and hand (Table 5.2). For 1kg and 2kg hand load, the estimated moment of inertia values of the forearm and hand, calculated using a cylindrical assumption, were of about 11% to 45% of the total moment of inertia, and the uncertainty of the moment of inertia of the hand load around the elbow joint was reduced, as the weight and distance between the weight and centre of elbow were directly measured. Therefore it was expected that the simulated trajectory became more accurate as the hand load increased, potentially giving better agreement between the model and measured data. This can be seen in Figure 5.7 to Figure 5.10 where 1kg and 2kg hand load showed better agreement between measured and simulated results than 0kg hand load. This method provided an alternative to the method of adjusting moment of inertia used by Hof (Hof, 1997), which involved using the recorded moment and angular acceleration to correct the moment of inertia.

From the preliminary results of model fitting using only experiment 1 and experiment 2 reported in (Yu and Wilson, 2012a), it was found that the system equations Eqn 5.14 and Eqn 5.15 cannot adequately describe elbow angle trajectory when maximum extension was reached at about 0.4 seconds (see Figure 5.7 to Figure 5.10, experiment 1), giving only 0.6s of data for parameter estimation (see section 5.6.3). The problem caused by the joint reaching maximum extension or flexion was also experienced by Hof (Hof, 1998), who limited the period over which they could analyse data to 60ms. Using a modified form of the passive extension experiment (experiment 3), where the upper arm

was leant forward by 45° from the vertical, allowed the forearm to swing further backwards, this gave a larger range of elbow angle for parameter estimation (about 135° whereas 90° was seen in experiment 1). The measured trajectories from experiment 3 (Figure 5.7 to Figure 5.10) showed the maximum extension was not reached in any of the trials, and therefore this did not limit the duration of data available for MAE calculation and parameter estimation.

5.6.2 Measured results

Surface palpation was used to determine the free tendon and muscle resting length parameters in this study. In future work, medical imaging technique such as ultrasound or magnetic resonance imaging (MRI) could potentially improve the accuracy of these parameters. A study of this type together with a formal sensitivity analysis of the model would allow the validity of the palpation method to be further assessed.

The measured parameter values (Table 5.2) demonstrated good consistency between subjects. The reproducibility of the calculated elbow angles from the measured data (Figure 5.7 to Figure 5.10) for repeated experiments was good. There was also good reproducibility between experiments performed on the same subjects but on different days. An example is shown in blue and green lines for P2 experiment 1 in Figure 5.8. The pattern of elbow angle movement from different trials also showed good consistency between subjects.

In the course of the experiment, a number of measurements were taken where the muscle was not fully relaxed and the trajectory of the forearm was clearly different from that when the muscle was fully relaxed. These measurements were not used in the parameter estimation process to obtain results presented in Table 5.3. The effect of the muscle not being fully relaxed can be seen in the dashed blue line of Figure 5.10 (subject P4, Exp 1 0kg hand load). The initial rate of change is less steep as a result of the active contractile element exerting a resistive force. Importantly, this is clearly distinguishable from the movement of a completely relaxed arm.

Whilst the effect of muscle tension was obvious, for experiment 3, EMG of the biceps and triceps muscles were recorded as an objective measure of muscle activation. Two typical examples of biceps muscle EMG for completely relaxed arm movement and one that was not completely relaxed are shown in Figure 5.11.

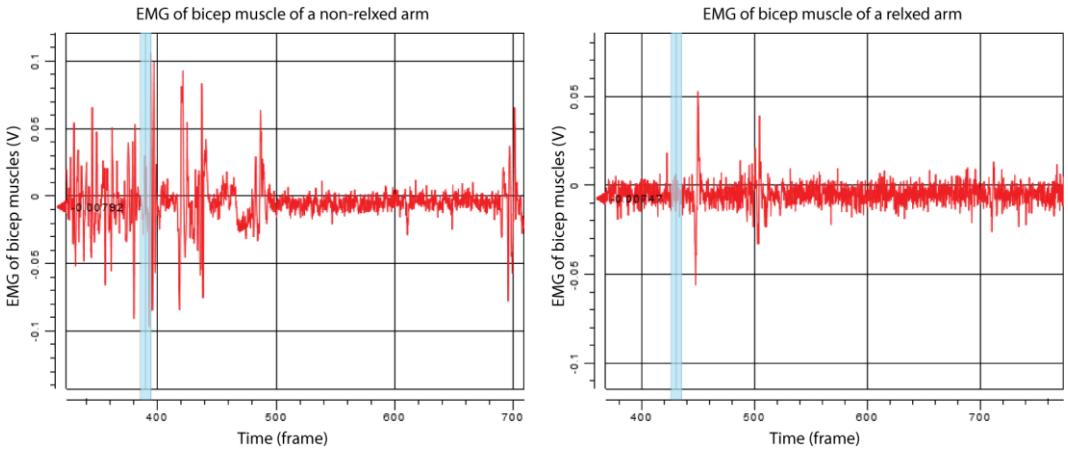

Figure 5.11. Recorded EMG signals of the biceps muscle from a measurement with a non-fully relaxed arm (left) and from a measurement with a fully relaxed arm. The blue lines indicate the moment the trigger block was moved away from the hand. Time unit is in frames of the 3D capture data, at 200 frames per second. EMG was recorded at 1000Hz per second; therefore there are 5 EMG samples per frame.

The EMG signals shown in Figure 5.11 had been amplified but unfiltered. It can be seen that in the first 100 frames after the removal of the trigger block, there was still significant activity in the measured EMG in the non-relaxed arm, while the activity in the relaxed arm was much less significant. In the relaxed arm example, it can be seen that there are spikes of activities at frame 450 and 500 in the relaxed arm example. The origin of these spikes were unclear, however these small spikes were present in all trials when the arm was fully relaxed, and it was concluded that these small spikes were not caused by voluntary contractions. However this added difficulties in determining if there was any voluntary contraction, as subjective judgement was required to identify these EMG spikes from voluntary muscle tension.

Comparison of subject feedback to the EMG or elbow angle time history found that subjects' feedback on whether the muscles were fully relaxed was reliable. Furthermore, subject feedback was immediately available after each

measurement, whilst inspection of the elbow angle time history or EMG can only be carried out after analysis of the data. Therefore subject feedback was the approach to monitor muscle relaxation in this thesis, which was reliable and immediately detected when measurements had to be repeated due to the muscles being not completely relaxed. This ensured enough data of passive movement was available for analysis and prevented the requirement for the subjects to attend further measurement days to obtain results to replace those rejected measurements.

5.6.3 Parameter estimation

The root mean square error (RMSE) is a widely used factor to minimise in parameter optimisation, and this was used in the original optimisation process using experiment 1 to obtain the preliminary fitted parameters (Yu and Wilson, 2012b). However it was found that the standard RMSE calculation did not give equally weighted values if trial lengths were different, and therefore MAE was used instead and carried into the optimisation process using experiment 2 and 3 to allow comparison between results from fitting experiments 1 and 2 and fitting experiments 2 and 3.

The duration of data taken for the MAE calculation in both experiment 2 and 3 was 2 seconds. This was chosen as it included several cycles of oscillation, but was not so long that movement had ceased at the end of the period, as introducing a large number of near zero error values during a period of low amplitude movement would reduce the sensitivity of the MAE to differences in the movement dynamics, which was the important factor in the fitting process.

In the preliminary work (Yu and Wilson, 2012a), experiment 1 was used to parameterise the model, where the maximum elbow extension was reached at about 0.4s and the data up to 0.6s (grey dashed line, Figure 5.7 to Figure 5.10) was included so a decrease in elbow angular velocity was present for the parameter estimation and optimisation. However, when experiment 3 was used in the fitting process and compared with the results previously obtained using

data from experiment 1, it was found that the difference in elbow angle trajectory characteristics between measured and simulated data at maximum elbow extension in experiment 1 caused the parameter estimation process to result in an unsatisfactory prediction of the elbow angle overall. Therefore in the final parameter estimation process, the MAE was calculated using only measured and simulated data from experiment 2 and 3, and excluded data from experiment 1. This resulted in better model fit and lower MAE values were obtained.

The use of different seeds in the optimisation process was to help ensure that global minima were found, by ensuring that starting different initial seeds gave the same final values. For subject P4, when the parameter estimation was started with all zero values in the seed, fminsearch reached a local minimum, where the MAE was not as small as those obtained using the other initial seeds. This result was ignored and the global MAE from the other seeds was used. MAE values obtained from the two remaining initial seeds were within 1%, suggesting the fminsearch optimisation process had found global minima. It also suggested that using a physiologically meaningful seed has a higher chance of finding global minima than starting with all zero values.

In the model fitting, fminsearch effectively performed a 7 dimensional grid search to obtain the seven parameter values. In order to visualise the form of the error surfaces, the MAEs for pairs of variables were plotted. The error surfaces had steep sides with a shallow bowl region around the minimum MAE. An example of one of these error surfaces are shown in Figure 5.12, which shows the MAE surface for subject P2 where the muscle model springs k_{m1} and k_{m2} are varied, other parameter values in the model uses those presented in Table 5.2 and Table 5.3. These plots confirmed that the estimated parameter values were at the global minimum of the MAE. The shape of these plots also suggested that the model had a low sensitivity to the values.

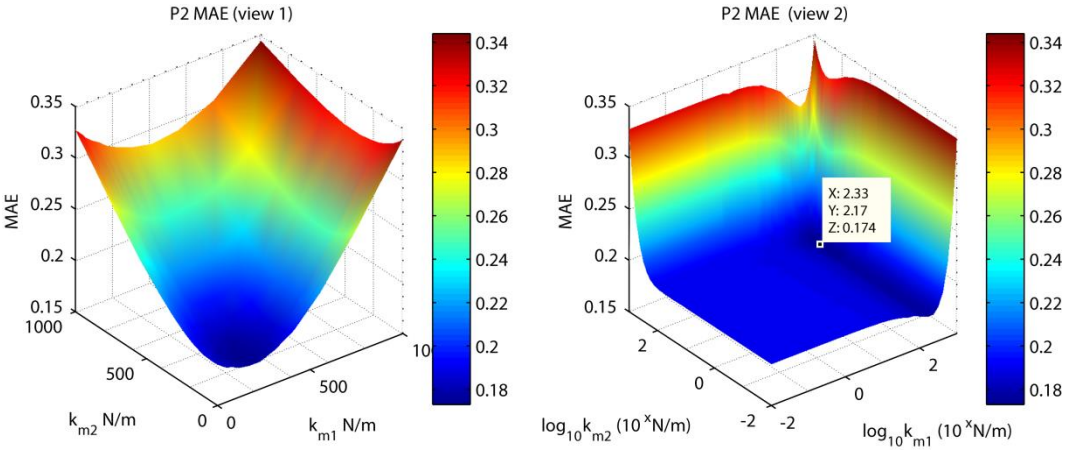

Figure 5.12. Error surfaces of the MAE between measured and simulated elbow angle trajectories by varying the values of the muscle model springs k_{m1} and k_{m2}. The left plot shows normal scales for the parameter values, the right plot shows log scales for the parameter values, where a global minima for k_{m1} can be seen clearly. The global minimum MAE is marked on the graph.

5.6.4 Fitted results

It can been seen in Figure 5.7 to Figure 5.10 that the simulated trajectories using the fitted parameter values when maximum elbow angle was not reached, show good agreement with measured elbow angle trajectories. The values in Table 5.3 obtained by only using experiment 2 and 3 for parameter estimation values also gave predicted elbow angle trajectories that agree with the initial 0.4s of measured elbow angle trajectories obtained in experiment 1. This suggests that the fitted values were appropriate for predicting elbow angle for different arm orientations.

The fitted spring and damper values (Table 5.3) were within the predicted range of values. The fitted values of b_{arm} showed good agreement between all subjects. The muscle spring constants k_{m1} and k_{m2} showed good agreement between subjects P1 and P2; however the same values for P3 and P4 showed large variation. This could be due to uncertainty in the measurement of the muscle and tendon length. In subject P1 and P2, it was easier to identify the bulk of the muscle by palpation in comparison to P3 and P4, and therefore the error in length determination in P3 and P4 were expected to be greater than in P1 and P2. In Eqn 4.92 the force generated by muscle spring k_m is dependent on the

muscle extension, which is in turn dependent on the measured lengths x_{1_0}, x_{2_0}, x_{1t} and x_{2t}, therefore any error in those measured lengths will have a corresponding error in the force generated which will affect the parameter optimisation process.

As already discussed in section 5.6.1, the model cannot adequately describe the dynamic characteristics of the joint when maximum extension angle is reached, this suggests further investigation is required to improve the modelling of the joint when maximum extension is reached. Furthermore, the joint model in this thesis uses the same functions to describe joint limit at maximum extension and maximum flexion, however, anatomically the flexion limit comes from compression of soft tissues including the muscles; whereas the extension limit comes from the shape of the bones held by stiff ligaments. The mechanical properties of these different types of tissue would give different dynamics at the two joint limits. In future work, modelling the limits separately with separate parameter values would improve the joint model.

5.6.5 Comparison with other Work

It was difficult to compare measured length values between this study and studies reported in the literature because of differences in the definition of the model parameters. For example, the tendon length defined by Winters (Winters and Stark, 1988) includes sheet tendons embedded in the bulk muscle. Hatze's model (Hatze, 1981) was similar to the one used in this study, and reported average triceps muscle length of 0.1125m, which was shorter than all the triceps muscle lengths (x_{2_0}) measured in this study. However the lengths for Hatze's model were obtained through parameter estimation, where the muscle lengths determined were the lengths at which the muscles produced maximum force and not the resting length of the muscles.

No previous studies were identified in which numerical values of the elbow joint passive spring and damping for the modified Hill muscle model were reported,

and therefore, no direct comparison of values between studies could be made. Hof's study (Hof, 1997) on the human triceps surae muscle included a parallel elastic component (PEC) in the muscle model, equivalent to the spring component k_m of the muscle model in this thesis. However the reported values were in $Nrad^{-1}$, which represents effects on the joint, and the muscle length was not calculated. His model parameter is anatomically incompatible with the spring constants reported in this thesis, which are in Nm^{-1}, and specifically the biceps muscle length had a non-linear relationship with elbow angle, therefore the values could not be compared. Furthermore, Hof's fitted values were derived from joint moment against joint angle. While it gave a detailed analysis of the spring components, the muscle's dynamics over time were not analysed, and therefore the damping components were not included. It is unsure if those springs constants obtained by Hof can be used in forward dynamics simulations to predict dynamic joint movement.

Mohammed et al. (Mohammed et al., 2012) had attempted to develop a predictive FES controller to stimulate knee extension. Their muscle model also included the passive components in the knee joint and muscles, and that a similar experiment that involved passive movement of the knee joint was also presented. They have fitted the model movement to measured data and obtained numerical values for the knee joint spring and damping constants, however they failed to experimentally identify numerical values for the muscle passive components, and had taken values from the literature, although no justification was provided by Mohammed et al. for the use of these values.

5.7 Conclusion and future Work

In this study, the CE was considered a pure force generator. Since the muscles were completely relaxed in the passive movements, no forces were generated by the CE. In MVC studies and other parameter estimation experiments where the muscle is active, the CE force is modulated by the force-length and/or the force-velocity characteristic (Hill, 1938), and therefore parameters for the CE and the spring and damping constants cannot be uniquely determined. Measurements from passive movement allowed the effect of the spring and damping components to be observed separately from the characteristics of the active components (contractile elements) and therefore the passive parameter values can be exclusively and successfully determined.

Overall, parameter estimation of the musculo-skeletal model from passive movement measurement was successful. By adapting the skeletal model to other joints in the body, such as the knee joint or ankle joint, other muscle groups in the body could be parameterised in a similar manner. In order to develop better models and more robust parameter estimation techniques, more numerical values need to be reported in the literature.

The passive movement method described in this chapter can also be used for parameterisation of muscle models in healthy subjects. To achieve this, the passive components are first parameterised using the method described in this chapter, and then the active components (CEs) are parameterised. The advantage of beginning with parameterising only the passive component of the model is that the time history of the force from the CE (active part of the model) is unknown and cannot be measured uniquely, therefore the dynamic characteristics of the CE and the dynamic characteristics of the passive components are not separable from MVC measurement. However a healthy subject is capable of relaxing the muscle around a joint, and therefore the joint's dynamic characteristics from passive movement only consist of the dynamic characteristics of the passive components. The work in this thesis therefore first

parameterises the passive components exclusively using measurement of passive movement, then the active components (CEs) could then be parameterised using measurement of joint dynamics when the muscles are active. The procedure to experimentally determine the force/length characteristics of the muscle active component, the contractile element, is described in the next chapter, to 1) provide a more complete muscle model, and 2) provide numerical values of possible forces for the preliminary FES experiment described in Chapter 7.

Chapter 6 Voluntary Contraction Method for Determining the Force/Length Characteristics of the Biceps and Triceps Muscles

6.1 Introduction

In this chapter, the force/joint angle characteristics of the arm model and the force/length characteristics of the contractile elements (CEs) in the muscle models are determined from measurements of isometric maximum voluntary contractions (MVC).

The work described in this chapter allows a more complete muscle model to be obtained, in which the force/length relationship in the CEs were also characterised as well as the passive parameter values obtained from the passive movement experiments. Furthermore, the purpose of this experiment was to identify the maximum force output of the muscles in healthy subjects, to give an upper limit in the expected force for the preliminary experiments to predict movement generated by FES (Chapter 7).

When a joint is flexed or extended, the change in joint geometry causes a change in the lengths of the muscles. Additionally, the angles of muscle forces acting on the body segments change when joint angle changes, therefore the MVC moment around a joint is not constant for all joint angles. The maximum voluntary muscle force varies with the length of the muscle, this is described by the force/length characteristics (Gordon et al., 1966) in the CE of the muscle model as introduced in section 2.2.2.1. Thus muscle force characteristic from the force/length relationship and the musculo-skeletal geometry must be considered

and included in muscle and musculo-skeletal modelling. To achieve this, the isometric MVC force must be measured for different joint angles.

Using a rig developed for this work, termed the Isometric Arm Contraction Rig (IACR), the MVC force from elbow flexion and extension were measured at a range of different elbow angles. The results allowed the maximum forces of the muscles in the arm model to be determined as functions of muscle length, and in turn were used to obtain the CEs' force/length characteristics.

Five healthy subjects participated in the MVC experiment described in this chapter, of which 3 had participated in the passive movement experiments described in Chapter 5.

6.2 Materials

6.2.1 Muscle force in the musculo-skeletal model during isometric muscle contraction

The experiment described in this chapter measured isometric joint moment under MVC in elbow flexion and extension, i.e. $\dot{\theta}(t) = 0 rads^{-1}$ and $\ddot{\theta}(t) = 0 rads^{-2}$. The net moment around the joint equalled 0Nm where the moments generated by the muscles were balanced by the weight of the forearm and hand, and the force exerted at the hand. The equation that describes the moment around the elbow joint given in Eqn 4.85 can be rearranged to be:

$$\text{Total elbow moment} = F_1(\theta)\frac{d_{11}d_{12}\sin\theta}{l_1} - F_2(\theta)d_{21} + m_{arm}d_{arm}g\sin\theta + F_{load}d_{load} \qquad \text{(Eqn 6.1)}$$

Since the total elbow moment in this experiment is zero:

$$F_1(\theta)\frac{d_{11}d_{12}\sin\theta}{l_1} - F_2(\theta)d_{21} = -\left(m_{arm}d_{arm}g\sin\theta + F_{load}d_{load}\right) \qquad \text{(Eqn 6.2)}$$

As $\dot{\theta}(t) = 0$, the $b_{arm}\dot{\theta}(t)$ term in Eqn 4.85 is eliminated in Eqn 6.1 and 6.2. As discussed in section 5.6.1, the model cannot adequately describe the dynamic

characteristics of the joint when maximum extension angle is reached, therefore the effect of joint torques at maximum flexion and extension, described as τ_{lim1} and τ_{lim2} in Eqn 4.85, were not included in the models in this chapter.

It should be noted that the variables F_1, F_2, θ and l_1 in Eqn 6.1 and 6.2 that were previously described as functions of time (t) in Eqn 4.85 are constant over time during isometric MVC, and therefore, (t) is not used here. Additionally as these variables in the arm model are constant over time, they can be determined directly (inverse technique) without using a numerical solver and model fitting techniques. It should further be noted that the muscle forces F_1 and F_2 have been described as functions of elbow angle (θ), to denote that these forces are not constant over elbow angle. As the lengths of the muscles in the model are also functions of elbow angle θ, using Eqn 4.93 and Eqn 4.95, MVC muscle forces can be expressed as functions of muscle length, $F_1(x_1)$ and $F_2(x_2)$, which in turn can be used to compute the MVC force of the CEs as a function of muscle lengths and elbow angle (section 6.3.2 and section 6.3.3).

6.2.2 Contractile element force in the musculo-skeletal model during isometric muscle contraction

During isometric contraction of the muscle, the lengths of muscle models are fixed thus the damping element b in each of the muscle model exerts no force. Therefore the force of the modified Hill muscle model described in Eqn 4.92 that represents the biceps and triceps muscles becomes:

$$F_i\left(x_i\right) = F_{CEi}\left(x_i\right) + k_{mi}\left(x_i - x_{i\_0}\right) \text{ , where } i = 1,2 \qquad \text{(Eqn 6.3)}$$

It should be noted that the forces in Eqn 6.3 are described as functions of the length of the muscles $\left(x_i\right)$; this is used in this chapter to denote the force/length relationship.

During MVC under flexion, only the flexor muscles contracts, the CE of the triceps muscle (extensor) exerts no force, i.e. $F_{CE2} = 0N$. However the passive spring components still exert a moment around the joint if the muscles (and free tendons) are not slack, and therefore during flexion, the triceps muscle force is still considered. The forces of the muscles during MVC under flexion are therefore:

$$\text{Flexion MVC: } \begin{cases} F_1(x_1) = F_{CE1}(x_1) + k_{m1}(x_1 - x_{1\_0}) \\ F_2(x_2) = k_{m2}(x_2 - x_{2\_0}) \end{cases} \quad \text{(Eqn 6.4)}$$

The same principle applies for MVC under extension of the elbow. The CE of the biceps muscle (flexor) exerts no force, i.e. $F_{CE1} = 0N$, and therefore the forces of the muscles are:

$$\text{Extension MVC: } \begin{cases} F_1(x_1) = k_{m1}(x_1 - x_{1\_0}) \\ F_2(x_2) = F_{CE2}(x_2) + k_{m2}(x_2 - x_{2\_0}) \end{cases} \quad \text{(Eqn 6.5)}$$

By combining Eqn 6.2 with Eqn 6.4, the force/length characteristics of the biceps muscle under MVC, $F_{CE1}(x_1)$ can be obtained. Similarly, by combining 6.2 with Eqn 6.5, the force/length characteristics of the triceps muscle under MVC, $F_{CE2}(x_2)$ can be obtained.

It should be noted that in this chapter, the extensions of the free tendons of the muscle model are also considered negligible following the free tendon assumption described in section 4.2.3.3.

6.2.3 Isometric arm contraction measurement rig (IACR)

To allow the MVC to be measured for a range of elbow angle from full abduction to full extension, an adjustable mechanical rig was developed, known as the Isometric Arm Contraction Rig (IACR), see Figure 6.1.

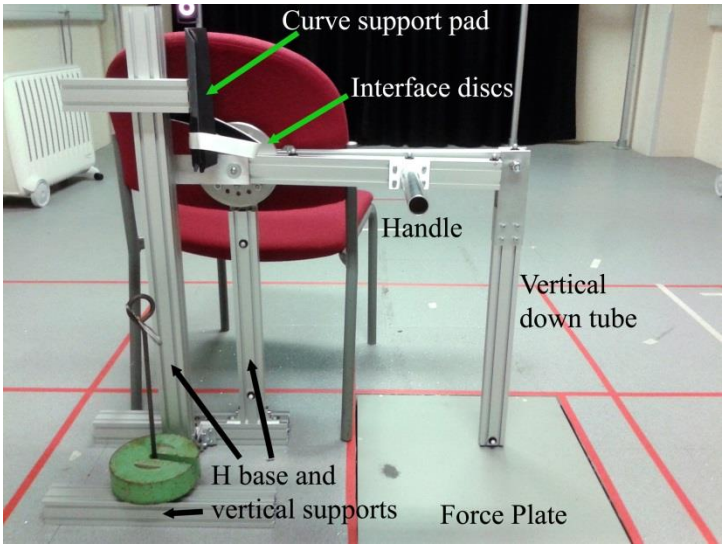

Figure 6.1 Isometric Arm Contraction Rig (IACR), in the orientation to measure elbow extension force when the elbow is at 90°.

The rig was designed to measure isometric elbow force of the right arm using the force plate within the Gait Laboratory, so that the positional information and force could be correlated using a single measurement system (Vicon Nexus). The elbow moment was measured by the subject exerting force onto a round handle. The detailed operation of the IACR is described in section 6.3.

The IACR is constructed primarily using off-the-shelf aluminium profile tubes, the components are labelled in Figure 6.1 and Figure 6.2. The rig consists of a non-moving support frame, which includes an H-shape base, two vertical supports with arms that hold the axle that is connected to the movable parts. The support frame also has a short horizontal cross arm with a curved pad to support the back of the upper arm. The movable parts include a cross arm (cross arm A) that is connected to a round tube (handle) which the hand exerts force on. This cross arm is fixed to an interface disc, which is connected to another round interface disc that is connected to a second cross arm (cross arm B). At the centre of the two interface discs is the axle that connects these to the support frame. Cross arm B is always horizontal, and is connected to a vertical down tube that transfers the force to the force plate in the Gait Laboratory. The two interface discs have a series of holes so that they can be fixed together at different angles using a set of bolts and nuts; this allows different angles to be set between the

two movable cross arms. The subject's upper arm is placed against the curved pad. The elbow's axis of rotation is aligned with the axle of the two round interface discs. The hand rests against the round tube. Cross arm B always remains static as the vertical down tube is rested on the force plate. Changing the angle between the two interface discs and effectively between the two cross arms allows the elbow's isometric MVC moment to be measured at different angles. The round tube (handle) position is adjustable and can be slid along cross arm A to accommodate the difference in forearm length between subjects.

The axle is connected to the interface discs using a bearing block with needle bearings, and therefore there is minimal rotational friction between the static support frame and movable cross arms. This ensured that all moments from the handle and cross arm A is transferred to cross arm B and to the force plate.

To ensure the IACR does not slip against the floor during the experiments, 40kg of weights were placed on the H shape base. This was adequate to keep the IACR static during all measurements.

In Figure 6.1, the IACR is in the extension setup to measure elbow extension force at elbow angle of 90°. The hand is placed above the handle. When the elbow exerts torque in the extension direction, this generates a moment around the axle at the interface discs. This moment is transferred to the force plate via cross arm B and the vertical down tube. By using the force measured on the force plate, together with the geometry of the IACR and the arm, the moment around the elbow and the muscle force can be calculated.

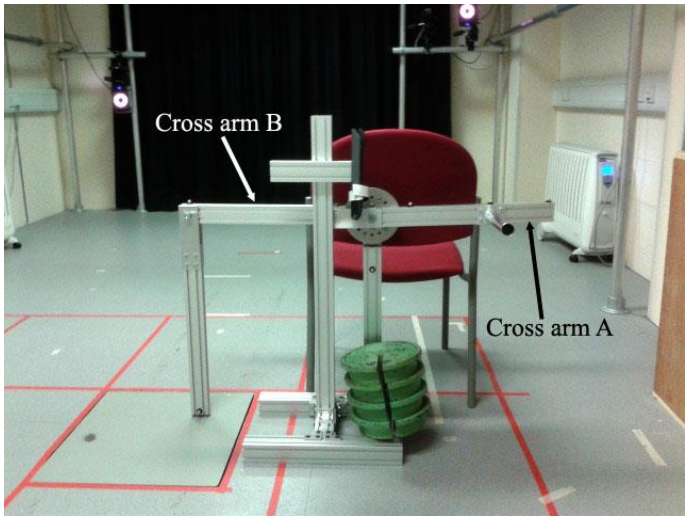

Figure 6.2. Isometric Arm Contraction Rig (IACR), in the orientation to measure elbow flexion force when the elbow is at 90°.

To measure elbow flexion force, cross arm B of the rig is placed in the position shown in Figure 6.2. When the hand pulls the handle upwards, the moment is transferred through the axle at the interface plates and transferred to the force plate via cross arm B and the down tube. The orientation of the arm on the rig remains similar between the flexion and extension experiment where the back of the upper arm rests against the curved pad and the elbow is aligned with the interface discs. The hand exerts force on the handle when the elbow joint extends or flexes.

The angle of cross arm A can be set to the following angles: 22.5°, 45°, 67.5°, 90°, 112.5°, 135°, 157.5° and 180°, where the angle is 0° when cross arm A is vertical with the handle above the axle. This allows a maximum of eight different elbow angles to be measured. These eight angles are incrementally labelled as angle 1 to angle 8, e.g. angle 2 is 45°. These angles are similar to the elbow angle being measured. Due to the position of the hand and arm that was placed above or below the handle, and to a lesser extent, the mechanical tolerance of the IACR, the true elbow angle was measured using motion capture.

The IACR has a non-moving curve pad where the upper arm rested against, and the upper arm was kept vertical in all experiments described in this chapter in the orientation shown in Figure 4.15. The elbow was aligned with the axis of

rotation of the IACR interface discs, and the angle of the forearm and the angle of cross arm A were always similar, therefore the direction of force exerted from the hand, F_{load} , which is perpendicular from the forearm and in the flexion and extension direction, was assumed to be the same as the perpendicular force of the handle, F_{handle} , acting around the IACR rotating axle, i.e. $\vec{F}_{\text{handle}} = \vec{F}_{load}$. F_{handle} can be calculated from the moments around the IACR axle, in which moment of the force measured on the force plate equals to moment of the force at exerted on the handle:

$$F_{\text{force plate}} \times d_{\text{cross arm B}} = F_{\text{handle}} \times d_{\text{cross arm A}}$$

$$F_{load} = F_{\text{handle}} = \frac{F_{\text{force plate}} d_{\text{cross arm B}}}{d_{\text{cross arm A}}} \qquad \text{(Eqn 6.6)}$$

$d_{\text{cross arm B}}$ was constant at 495±1.7mm.

6.2.3.1 IACR marker model for motion capture

Figure 6.1 and Figure 6.2 shows motion capture markers attached to the IACR using double sided tape. One pair of markers are attached to the vertical down tube. One marker is placed at the top of the down tube and one is placed at the bottom. The 3D locations of these two markers recorded and visualised using the Vicon motion capture system ensure the down tube is vertical. On cross arm A there are five markers, four along the top side of cross arm A, where the one furthest to the left in Figure 6.2 is attached to the bearing block fixed to the interface discs, in which the fifth marker on cross arm A is placed below and on the bottom side of the bearing block, these two markers allow the centre of the axle to be located on the motion capture system. The remaining three markers on cross arm A are used to compute the angle of cross arm A against the global axis. One of these markers is aligned with the handle to allow the motion capture system to record the distance between the handle and the axle at the interface discs.

6.2.3.2 IACR measurement validation

To ensure the force measured by the IACR and force plate was accurate, the performance of the force plate and the IACR was validated using a set of known weights. The centre of the force plate was loaded with no load, 1kg, 2kg, 5kg and 10kg certified weights. These weights were chosen from the assumption that the maximum weight a normal subject can lift in an elbow flexor curl movement (or commonly described as biceps curls) was about 15kg to 25kg, and the chosen certified weights were of similar value. The force plate was calibrated to 0N when there was no load on the force plate. The errors between the measured weights from the force plate against the known weights were 1.5%, 0.5%, 1.4% and 0.7% for the 1kg, 2kg, 5kg and 10kg known weights respectively. This gives a maximum error of 1.5%.

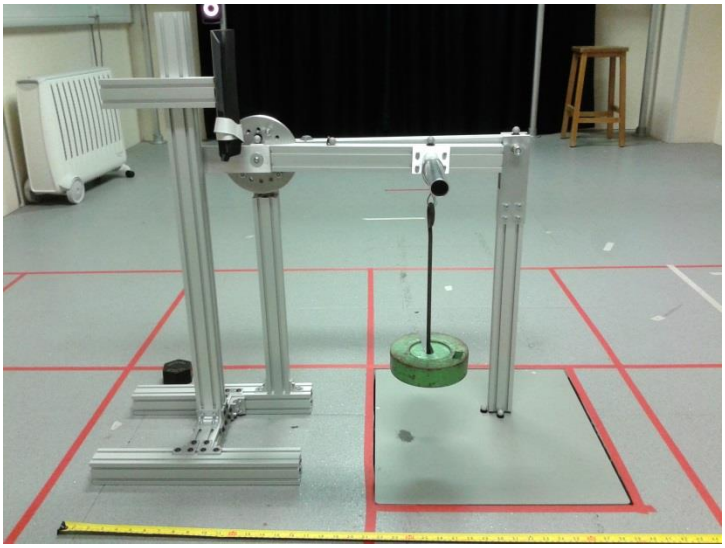

Figure 6.3. IACR validation with a known weight of 5kg loaded to the handle via a weight hanger (0.826kg).

The down tube of the IACR was then placed on the force plate with the orientation shown in Figure 6.3. Different known weights were then loaded on the handle of the IACR via a weight hanger (0.826kg), placed on the round handle tube at the point closest to cross arm A, see Figure 6.3. In this figure, the IACR was setup in the extension experiment position with cross arm A being horizontal. Using the known weights and the geometry of the IACR, the expected forces exerted on to the force place were calculated and compared with the

measured forces on the force plate. An expected force of 36.7N was calculated based on a load weight of 5kg plus the hook platform (5.862kg total) in combination of the geometry of the IACR. The measured force from the force plate was 37.33N. Therefore the IACR measurement error was 1.7%.

It was observed that due to mechanical tolerance of the interface discs and the connecting bolts and nuts that fastens the two discs together, cross arm A was not exactly horizontal, therefore in the MVC experiments described in section 6.3.2 and section 6.3.3, the true angle of cross arm A was measured using motion capture, and was used as part of the geometry calculation to compute muscle forces.

The point at which the force was applied to the handle was also varied to test the rigidity of the rig. This was tested by sliding the weight hanger along the handle. Beginning by the hanger being placed closest to cross arm A (0cm); the hanger was then moved along the handle away from cross arm A at 1cm intervals and the force measured. The forces at twenty one locations on the handle were measured. These are shown in Figure 6.4. The weight used was 5.862kg (5kg weight plus hanger). The average of the twenty one measured forces was -57.1N with standard deviation of 0.274N. The linear line fitted to the measured forces gives force difference of 0.46N between 0cm and 20cm. This is 0.8% of the averaged measured force (-57.1N).

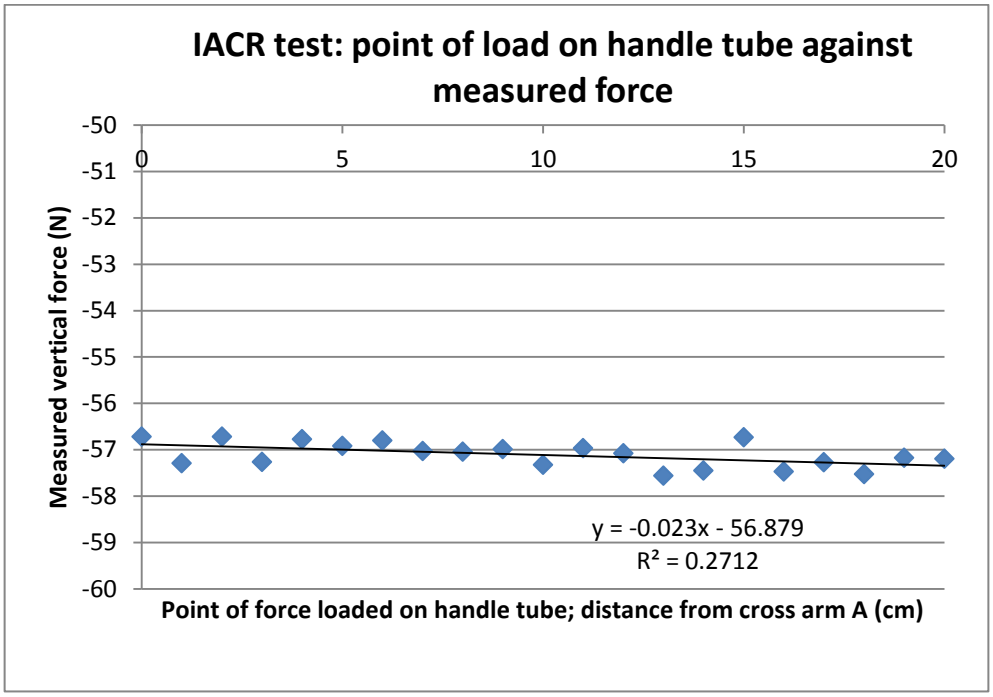

Figure 6.4. Measured vertical force on force plate on the IACR handle against position of the weight hanger on the handle. The geometry of the IACR is shown in Figure 6.3. The x axis denotes the distance along the handle from cross arm A at which the point of force was applied.

The measured forces of the IACR showed good agreement with the expected forces, therefore the IACR was suitable for measuring the elbow moment under MVC of the arm muscles.

6.3 Experimental design and protocol

The isometric MVC experiments were performed for two actions, elbow flexion and extension, which separately measured the force produced by the biceps and triceps muscles in the arm model.

The arm marker model (section 5.3.1) used in the passive movement experiments was also used in the MVC experiments to measure elbow angle through motion capture. The motion capture settings, e.g. frame rate and camera settings were identical to those used in the passive movement experiment, and are described in section 3.2.

The experimental protocols for measuring MVC were designed to minimise muscle fatigue, as the physiological effect of muscle fatigue was not included in

the muscle models in this thesis. If the MVC is to be measured for the 7 or 8 angles for both elbow flexion and extension, as described in section 6.3.2 and section 6.3.3, then subjects were required to perform MVC for a significant period of time (around 10 minutes in total). The experiment protocols had to allow a steady state of muscle contraction to be measured, and sufficient period of contraction should be measured to allow averaging, in order to obtain a good estimate of the MVC. However MVC causes muscle fatigue, and therefore the period of contraction must not be too long so that the strength of contraction decreases during the period of measurement from muscle fatigue. For example, Chesler and Durfee found that joint torque during maximum isometric contraction decreased by 50% after 20 seconds for both healthy subjects and paraplegic subjects (Chesler and Durfee, 1997). Based on this, a measurement period of 10 seconds of MVC was used to measure the MVC force. To increase the data available and to assess the reproducibility of the measured MVC, three periods of 10 second contraction were used in each measurement trial. Between each contraction period, a suitable resting period of 20s between periods of MVC was included so that the muscles could recover from any on-set of muscle fatigue during the muscle contraction period. This resting period was defined after the preliminary MVC experiments described in section 6.3.1.1.

The finalised recording sequences for the flexion and extension MVC experiments are listed in Figure 6.5 and Figure 6.6.

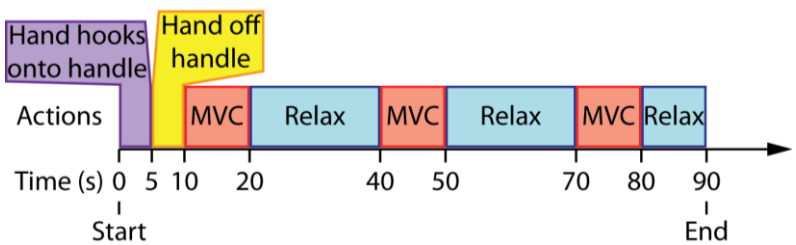

Figure 6.5. Action over time of the elbow flexion MVC measurement protocol. The flexor muscles contract during the MVC periods.

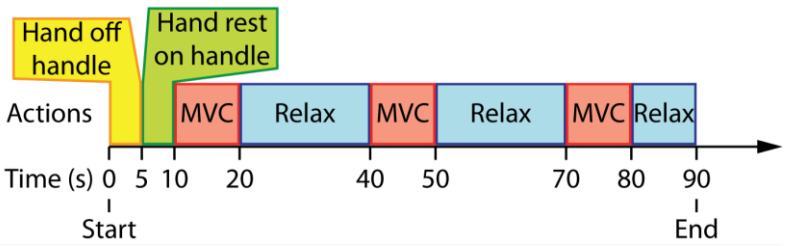

Figure 6.6. Action over time of the elbow extension MVC measurement protocol. The extensor muscle contracts during the MVC periods.

During the measurements, the time stamp in Vicon Nexus software during data recording was observed, and verbal instructions were given to the subject of the actions shown in Figure 6.5 and Figure 6.6. For each of the beginnings of the MVC action, the assistant gave the subject a 3 seconds countdown, whilst the end of the MVC periods were instructed without count down at the time shown in Figure 6.5 and Figure 6.6. Early measured results showed that if the relax command is given with a countdown, the subject can become distracted and the maximum level of elbow force exerted could not be sustained, therefore in the final protocol, the relax command was given at the moment when 10s of MVC was up.

The hand hooking onto the handle during the first 5s in the flexion experiment and the hand resting on the handle during the second 5s in the extension experiment allow the reference force to be measured, and these are described in detail in section 6.3.2 and section 6.3.3.

In the experiments described in section 6.3.2 and section 6.3.3, three sequences of recordings were used for each angle; the orders of angles measured are described in section 6.3.2 and section 6.3.3.

6.3.1 Preliminary fixed angle flexion and extension MVC experiment

To ensure the measurement protocol does not cause muscle fatigue as the experiment progresses, a set of preliminary MVC experiments were carried out on 1 subject (S3) for elbow flexion and extension at a fixed elbow angle of 90°. Five recording sequences (three contraction periods of 10 seconds with resting

periods in between) were performed for the flexion experiment and five recording sequences for the extension measurement.

6.3.1.1 Fixed angle MVC results and discussion

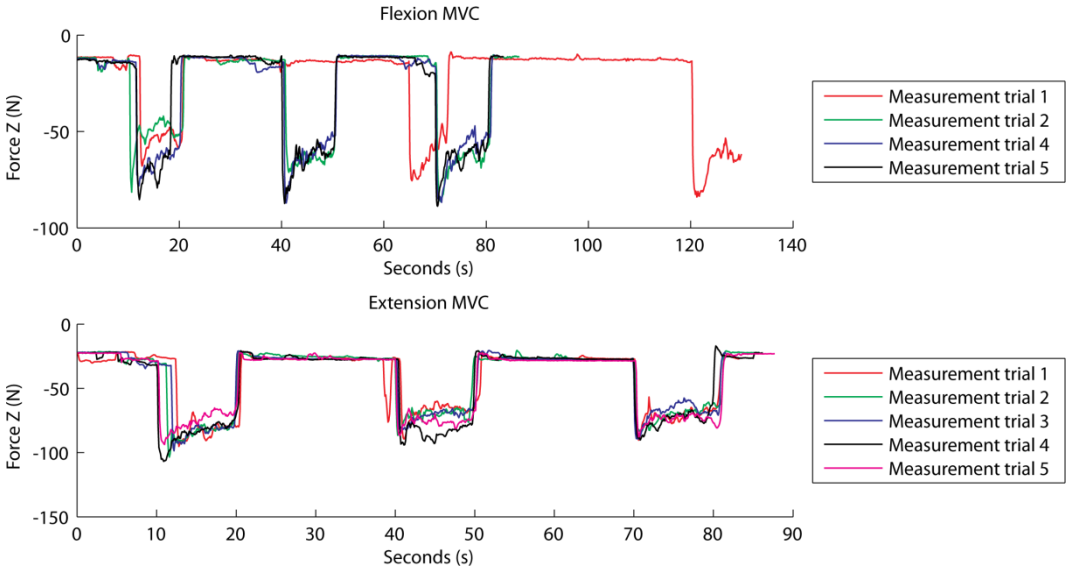

Figure 6.7. Preliminary measured force for isometric MVC with elbow angle at 90°. Flexion experiment trial 1 uses a longer resting period (45s) between MVC periods instead of 20s resting period for future trials. The force measured is the vertical force exerted from the IACR's vertical down tube measured by the force plate.

The preliminary measurement results are shown in Figure 6.7, the use of three separate 10s period of MVC had successfully provided nearly 30s of data from each measurement trial for analysis.

The first flexion MVC trial in the preliminary experiment (Figure 6.1, flexion MVC, trial 1) uses 45s of resting time between periods of MVC. Through subject feedback, it was found that 45s of resting period between MVCs was too long, and the subject could lose concentration and not promptly follow the remaining instructions. For the rest of the measurements, a resting periods of 20s was used. Through subject feedback, it was also determined that 20s was sufficient for the arm muscles to rest.

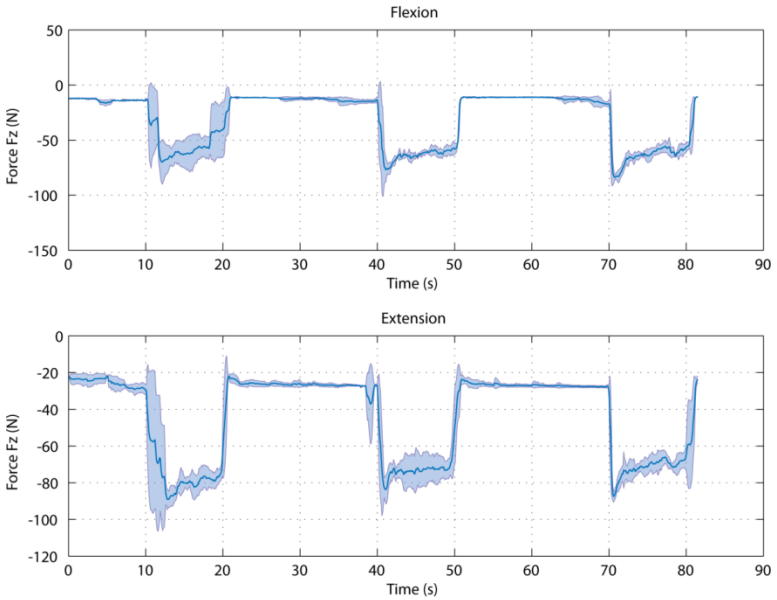

Figure 6.8. Averaged measured force of flexion MVC and extension MVC trails with elbow angle at 90°. The flexion plot is the average of trials 2, 4 and 5 in Figure 6.7 and the extension plot is the average of extension MVC trials 1 to 5. The mean force is plotted with the centre blue solid line; ±1 s.d. is plotted as shaded area above and below the mean forces.

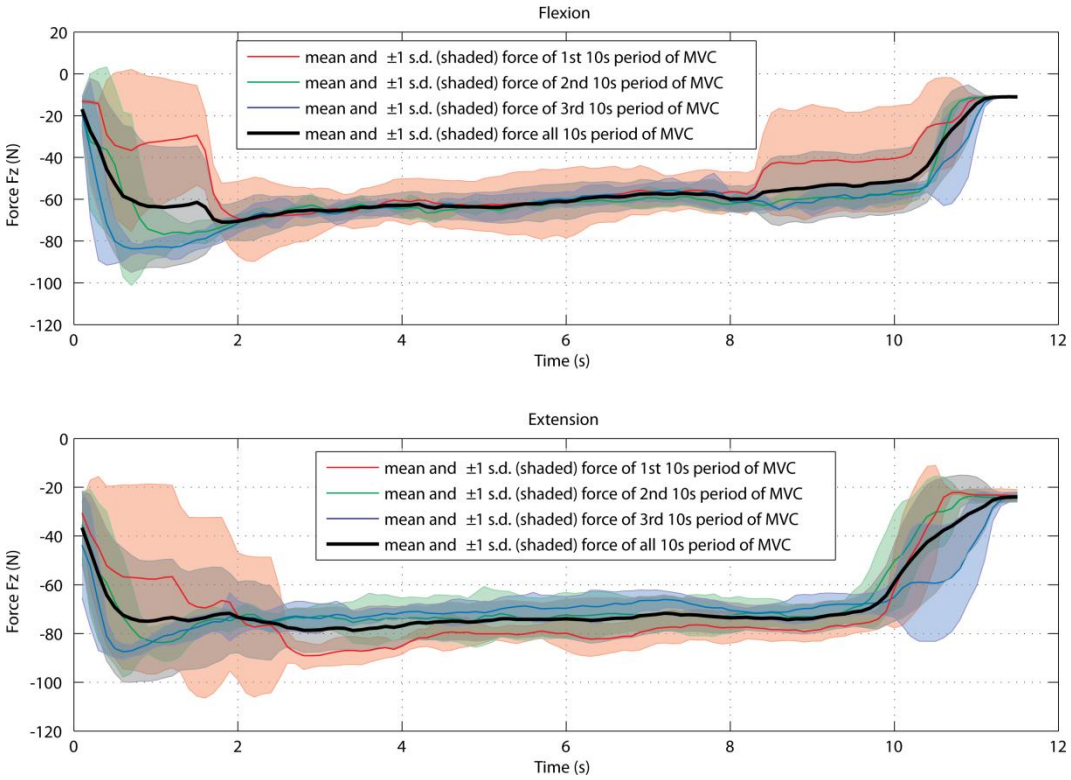

Figure 6.9. Averaged MVC contraction of preliminary MVC experiments

Figure 6.8 shows the averaged measured forces from the preliminary measurement trails. There is good reproducibility in the MVC forces between different trials. Figure 6.9 shows the averaged measured forces for the first 10s

MVC period between different trials, and this has been repeated for the second and third periods of MVC. The black lines are the averaged measured force for all MVC periods.

The results showed good reproducibility in the level of force measured between different measurement trials (Figure 6.8) and different periods of MVC (Figure 6.9). This demonstrated that the results of the MVC force measurements are reproducible, and the protocol avoided any on-set of muscle fatigue that could cause a decrease in the MVC force as the measurement progresses.

The protocol allowed adequate amount of data for the MVC forces to be estimated. The results showed that the time required for the joint force to reach an acceptable steady level was 2 seconds. In some instances, the subject may lose concentration before completing the full 10s of MVC. Therefore, in this thesis, the MVC force was estimated by averaging the measured force from all MVC periods, using the data beginning from 2 seconds after the start of the MVC period, up to 8 seconds from the start of the MVC period, i.e. the plateau period in Figure 6.9. This gives 18 seconds (3x6s) of measured force data to be averaged to derive the MVC force for each measurement trial.

6.3.2 Isometric maximum voluntary contraction experiments – elbow flexion

For the flexion MVC experiment, each subject performed a series of trials with the elbow at different angles. For each subject, the sitting height was adjusted so that the centre of the elbow was aligned with the centre of rotation of the interface discs. The upper arm was vertical and rested against the curved pad. The hand was placed below the handle, therefore when the subject exerted force in the flexion direction; this force was exerted on the handle. Positioning the hand under the handle meant that the true elbow angle will be greater than the IACR angle, e.g. elbow angle was slightly above 90° when the IACR was at angle 4. Motion capture was used to determine the true angle of the elbow joint. The location of the handle along cross arm A was adjusted to be in line with the

subject's wrist, so that the point of contact to the handle was at the base of the palm. For each subject, this handle position on cross arm A was fixed for all angles in the flexion MVC experiment. The base of the palm was selected as the point of force transfer instead of using the centre of the palm. If the centre of the palm was used to exert force to the handle, then the force measured would be the maximum force in which the subject can keep the wrist angle constant (straight), instead of measurement of the maximum elbow torque under arm muscle MVC. An image of the flexion MVC experiment is shown in Figure 6.10.

Figure 6.10. Isometric flexion MVC experiment. Cross arm A of the IACR was at angle 4 (90°). A moment in the anti-clockwise direction in this view was exerted to the IACR when the arm flexed. Cross arm B transferred the force to the down tube and the force plate, which is marked by red tape on the ground.

For each subject, six or seven different elbow angles were measured depending on the achievable elbow angle at maximum extension. Each angle referred to the angle orientation on the IACR: angle 2 to 8. None of the subjects could flex the elbow to perform flexion at angle 1 (22.5°). Due to the subject's hand being placed below or behind the handle, one of the subjects was not able to hyper extend their elbow to place their hand behind the handle when the IACR's angle was at angle 8 (180°, vertically point downwards).

The order of measured angles were as follow: angle 4 (~90°), minimum (angle 2), maximum (angle 7 or 8), then a random order of elbow angles (3, 5, 6 and 7, or 3, 5 and 6 if maximum possible angle was angle 7), followed by a random order of angles 2, 4 and 8 (or 2, 4 and 7 if angle 7 was maximum possible angle).

Beginning with angle 4 (~90°) allowed the subjects to familiarise themselves with the experiment, as well as allowing the handle position along cross arm A on the IACR to be set. Following this with trials of minimum and maximum angles ensured the subject was comfortable with the positions and actions during the measurements. The use of random order of elbow angle was to avoid any psychological or physiological effects that could affect the level of force exerted if the angles were measured in an ascending or a descending order. The final three measurements at angle 4, maximum and minimum were to ensure the results were reproducible and there was no effect of decrease in MVC force due to muscle fatigue during the entire duration of measurement trials. An example order of angle measured was: 4, 2, 8, 5, 3, 7, 6, 2, 8, 4; for a subject who can perform MVC at IACR angle 8.

Figure 6.5 shows the action protocol for the flexion MVC experiment. For the first five seconds, the subject hooks the hand onto the handle. At this point the elbow muscles were completely relaxed. This measured a force defined as the "reference force", $F_{\text{force plate (reference)}}$, in this thesis that included the weight of the IACR on the force plate, and the moment exerted onto the rig due to gravity acting on the weight of the forearm and hand. From 5 to 10 seconds the subject then prepares for the MVC action by positioning the base of the palm in contact with the handle. During MVC, the elbow moment generated by the flexor muscle effectively lifted the weight of the forearm, and the remaining moment was exerted to the handle as a force and transferred through the IACR to the force plate.

The reference force measured from 0 to 5 seconds included the weight of the IACR exerted onto the force plate, as well as all passive components that exerted moment around the elbow, which are the gravity weight for the forearm and hand, and the passive components of the muscles that exerts passive forces to return the elbow to a resting angle. Therefore the difference in the force measured during MVC and the reference force, consisted only of the elbow

moment generated by the CE of the biceps muscle. In this thesis, this differential force measured at the force plate is denoted as $F_{measured}$ (see Eqn 6.7).

$$F_{measured}(\theta) = F_{\text{force plate (during MVC)}}(\theta) - F_{\text{force plate (reference)}} \quad \text{(Eqn 6.7)}$$

This measured force $F_{measured}$ can be used to derive the load exerted by the wrist to the handle during MVC, $F_{load\ (\text{during MVC})}$, by rearranging Eqn 6.6 that equated the moment around the IACR:

$$F_{load\ (\text{during MVC})}(\theta) = \frac{F_{\text{measured}}(\theta) d_{\text{cross arm B}}}{d_{\text{cross arm A}}} \quad \text{(Eqn 6.8)}$$

As already discussed, this force exerted from the arm only consisted of the CE force from the flexor muscle, where the moment of this force around the elbow equals to the moment of the force exerted by the CE, Eqn 4.85 becomes:

$$F_{load}(\theta) d_{load} = F_{1\ (\text{CE only})}(\theta) \frac{d_{11} d_{12} \sin\theta}{l_1} \quad \text{(Eqn 6.9)}$$

Rearranging Eqn 6.9 gives:

$$F_{1\ (\text{CE only})}(\theta) = F_{load}(\theta) d_{load} \frac{l_1}{d_{11} d_{12} \sin\theta} \quad \text{(Eqn 6.10)}$$

Knowing that $F_{1\ (\text{CE only})}(\theta)$ only includes the tension generated by the CE, then $F_{CE1}(\theta) = F_{1\ (\text{CE only})}(\theta)$.

$F_{CE1}(\theta)$ was transformed from a function of elbow angle to a function of the muscle model length, i.e. $F_{CE1}(x_1)$, using Eqn 4.93, to give the force/length characteristics of the biceps muscle CE.

6.3.3 Isometric maximum voluntary contraction experiments – elbow extension

To measure the MVC of the extensor muscle, the IACR was configured to the extension experiment position as described in section 6.2.3. As shown in Figure 6.3, the subject's upper arm and elbow's position was identical to the flexion experiment. The subject placed the hand above the handle bar. The point of force transfer from the arm to the IACR handle was again at the base of the palm. When the elbow attempted to extend, a force was exerted to the handle, which was transferred to the force plate. For each subject, the position of the handle along cross arm A was set with the IACR at angle 4. Positioning the hand above the handle bar meant that the true elbow angle was less than the IACR angle, e.g. elbow angle was slightly below 90° when the IACR was at angle 4. Therefore the elbow angle was determined using motion capture during measurement. An image of this experiment is shown in Figure 6.11.

For this experiment, the placement of the hand meant that the elbow did not have to be super extended for angle 8 on the IACR; therefore all subjects can perform MVC in the extension direction for all seven IACR angles.

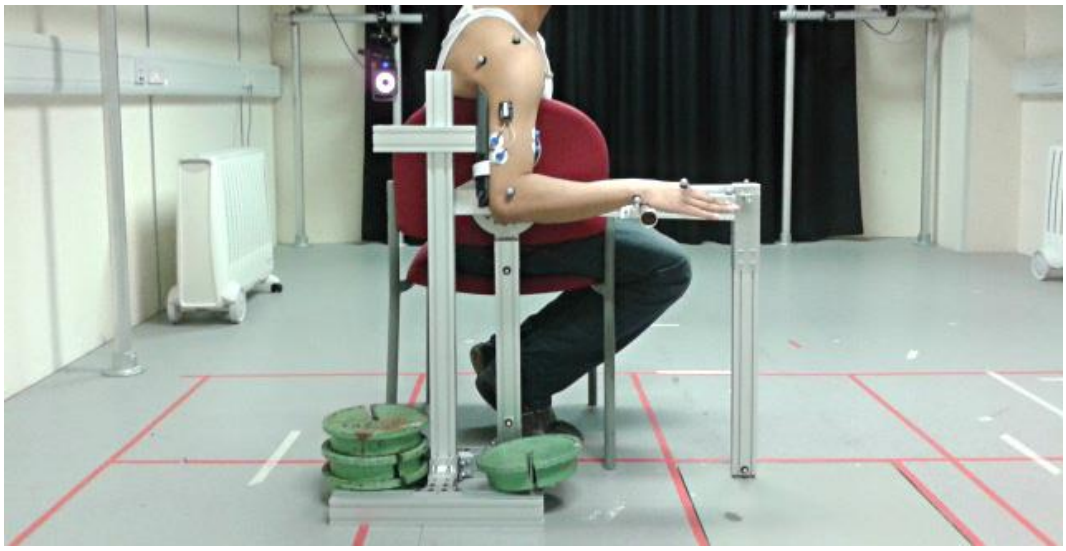

Figure 6.11. Extension MVC experiment setup. The right upper arm is rested against the support pad. The elbow is aligned with the axle of the IACR interface discs. The wrist is above the handle in which the position of the handle along cross arm A is adjusted to the position of the base of the palm when the IACR is at angle 4, as shown in the figure. The IACR is fixed with weight at the H shape base. The subject extends the elbow during MVC of the extensor muscles.

The order of forces measured at different elbow angles for each subject was generated in the same manner as the flexion experiment in section 6.3.2.

The actions for each measurement trial during extension MVC are shown in Figure 6.6. For this experiment, a reference force, $F_{\text{force plate (reference)}}$, was also measured, which was performed at 5 to 10s from the start of the measurement, with the subject's hand rested on the handle and the arm muscles completely relaxed. Again, this measured reference force from the force plate included the weight of the IACR, and the elbow moment due to gravity acting on the forearm arm and hand, and the moment generated by the passive components in the muscles. Eqn 6.7 and Eqn 6.8 from the flexion MVC experiment also applies in the calculation of the extensor CE force. However, in this experiment, the moment of the force $F_{load\ \text{(during MVC)}}$ around the elbow joint equals to the moment of the CE force of the triceps muscle around the elbow joint:

$$F_{load}(\theta)d_{load} = F_{2\ \text{(CE only)}}(\theta)d_{21} \qquad \text{(Eqn 6.11)}$$

Also, knowing that $F_{2\ \text{(CE only)}}$ only includes the tension generated by the CE, i.e. $F_{2\ \text{(CE only)}} = F_{CE2}$, then:

$$F_{CE2}(\theta) = F_{2\ \text{(CE only)}}(\theta) = \frac{F_{load}(\theta)d_{load}}{d_{21}} \qquad \text{(Eqn 6.12)}$$

Using Eqn 4.95, $F_{CE2}(\theta)$ can be transformed from a function of elbow angle to function of the length of the muscle model, $F_{CE2}(x_2)$, giving the force/length characteristics of the triceps muscle CE.

It should be noted that because the passive forces in the muscles and the arm were already included in the reference forces, by subtracting the reference forces, those passive forces were eliminated in the calculation of the force/length characteristic. Therefore this experimental design exclusively

allowed the force/length characteristics of the CEs to be characterised without the need for the values of the passive components.

6.4 Results

Five subjects participated in the isometric MVC experiments, who are identified as P1, P2, P3, P6 and P7. Subjects P1, P2 and P3 participated in the previous passive experiments where their subject number remained the same. Subject P4 in the passive experiments was not available to participate in this experiment. Two new subjects, P6 and P7 participated in this experiment to give a total of 5 subjects.

The measured length parameters, d_{load} and $d_{\text{cross arm A}}$ for each subject in the flexion and extension experiments described in section 6.3.2 and 6.3.3 are shown in Table 6.1. It should be noted that d_{load} for the flexion experiment and extension experiment were measured separately.

Table 6.1. Measured geometry for the calculation of the elbow moment and muscle forces

Subject parameters (all lengths in mm)	P1	P2	P3	P6	P7
Flexion MVC d_{load}, centre of elbow to heel of palm	255	277.5	260	240	270
Flexion MVC $d_{\text{cross arm A}}$, centre of axle to centre of handle	242.5	280	275	2325	265
Flexion MVC max IACR angle	8	7	8	8	8
Extension MVC d_{load}, centre of elbow to heel of palm	255	263	260	235	260
Extension MVC $d_{\text{cross arm A}}$, centre of axle to centre of handle	242.5	270	275	235	262
Extension MVC max IACR angle	8	8	8	8	8

For subjects P1, P2 and P3, the anatomical lengths d_{11}, d_{12}, x_{1t}, d_{21}, d_{22} and x_{2t} that were used for analysis in Eqn 6.9 to Eqn 6.12 were taken from the measured values in the passive movement experiments, shown in Table 5.2. For subjects P6 and P7, who had not participated in the passive movement experiments, those anatomical lengths were obtained using the palpation and surface measurement method described in section 5.3.2, and are shown in Table 6.2.

Table 6.2. Measured parameters for subjects P6 and P7 for the isometric MVC experiments

Subject parameters	P6	P7
d_{11} (mm)	40±2.5	42±3.2
d_{12} (mm)	224±5.8	285±7.1
d_{21} (mm)	45±2.5	50±3.2
d_{22} (mm)	232±8.7	237±9.2
x_{1t} (mm)	116±8.0	105±7.7
x_{2t} (mm)	123±6.8	133±8.7

Note: Measurement errors (± 1 standard deviation) are reported for the directly measured lengths.

The raw measured forces on the force plate over time for subject P6, shown in Figure 6.12, are examples of the measured forces, where the actions followed the action protocol described in Figure 6.5 and Figure 6.6. These forces are the $F_{\text{force plate}}$ in Eqn 6.6. It should be noted that these measured forces are negative as the IACR exerted force downward to the force plate.

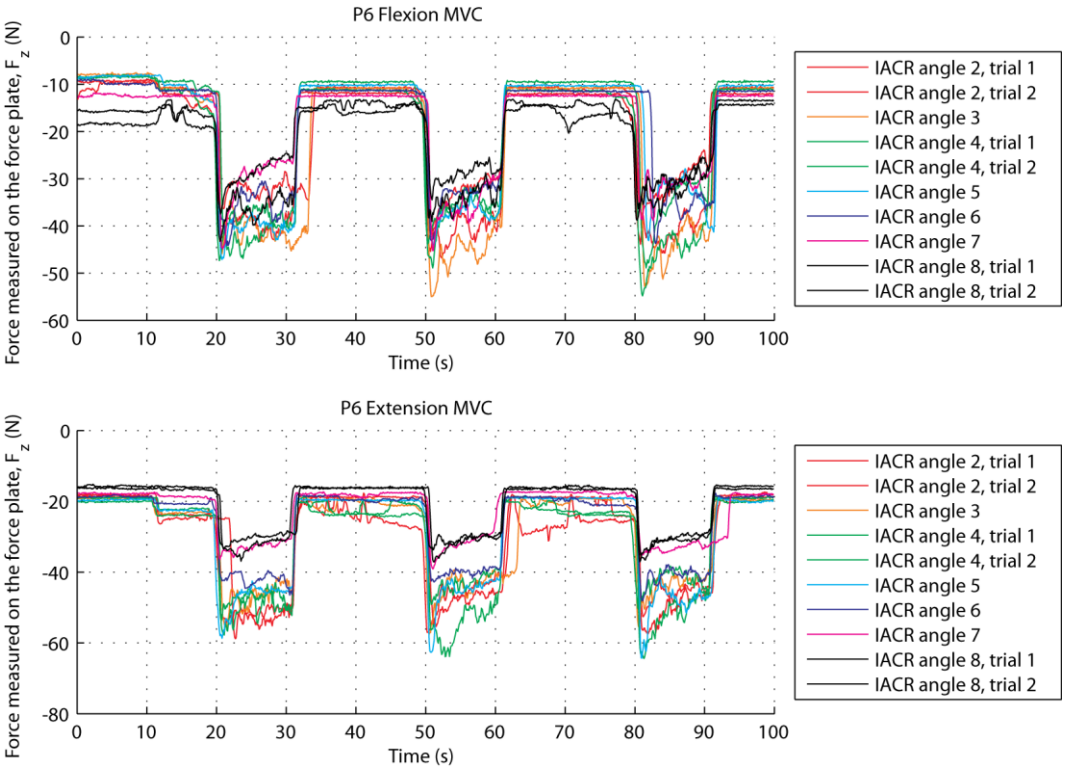

Figure 6.12. Raw force measured from the force plate over time for subject S6. The measured flexion MVC forces for different IACR angles are shown in the top graph; the measured extension MVC force for different IACR angles are shown in the bottom graph.

For each angle in the flexion and extension experiments, the three periods of 10s MVC were averaged together, giving an averaged 10s of MVC for each angle in the flexion and extension experiment. Those averaged MVC period for subject P6 are shown in Figure 6.13.

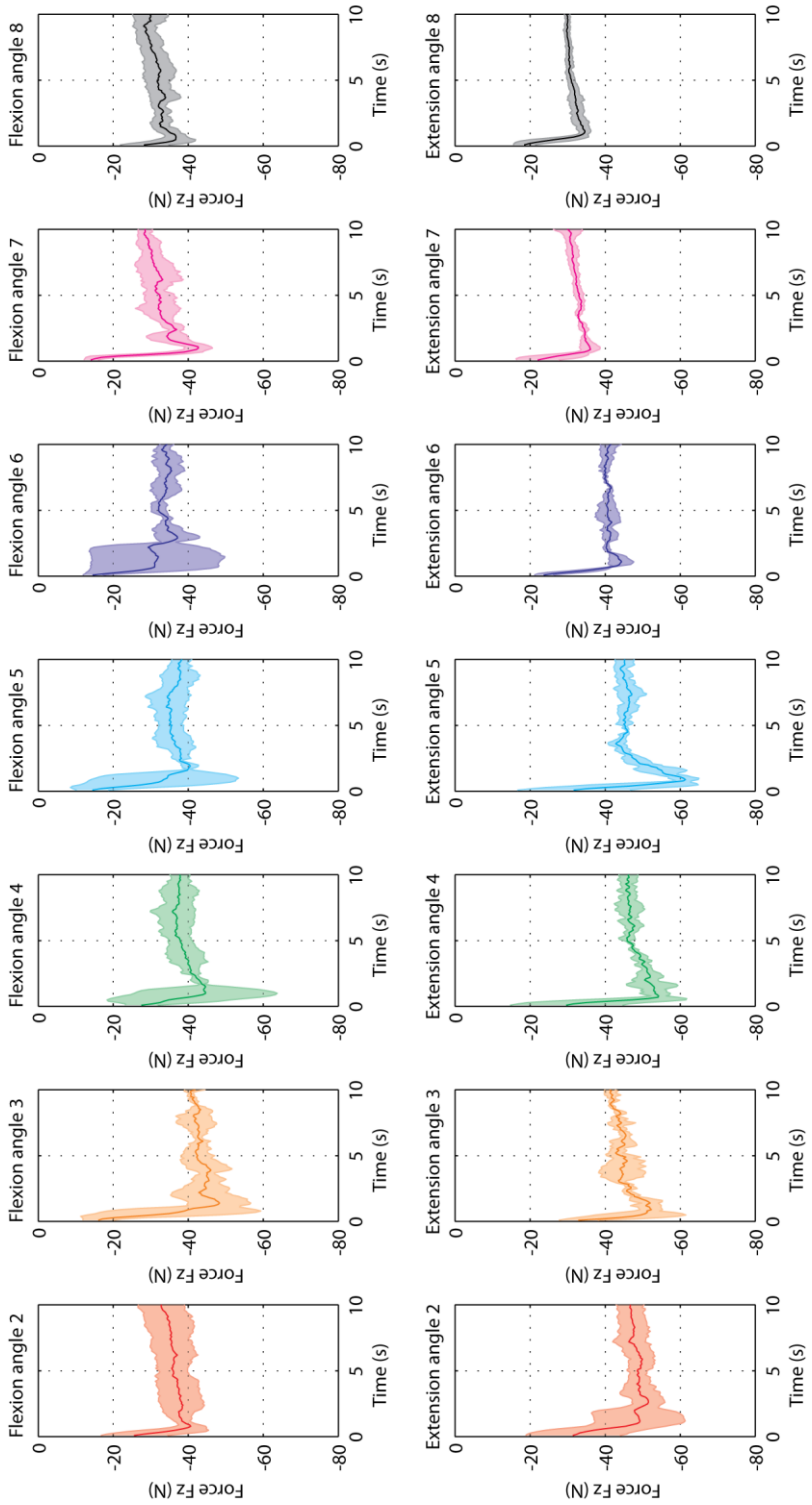

Figure 6.13. Averaged 10s periods of the measured MVC forces for subject S6. The averaged forces are shown in the solid line with the shaded areas showing ± 1 standard deviation. Angles 2, 4 and 8 were averaged of six 10s periods of MVC each, as two measurement trials were performed foe these angles. Angles 3, 5, 6 and 7 were averaged from the three 10s periods from their respective trials.

The average forces from 2 seconds to 8 seconds from the beginning of the 10s MVC period were averaged to give the overall MVC force for each angle, giving $F_{\text{force plate (during MVC)}}(\theta)$ for Eqn 6.7. The reference forces ($F_{\text{force plate (ref)}}(\theta)$ in Eqn 6.7) for each angle in the flexion experiment were obtained by averaging the measured force between the start of the measurement trials and 5s after the beginning of the trials. The reference forces for each angle in the extension experiment were obtained by averaging the measured force between 5s from the start of the measurement trials and 10s after the beginning of the trials.

The overall MVC forces for each angle in each flexion and extension experiment, $F_{measured}(\theta)$ were obtained using Eqn 6.7. Measured elbow angles were derived from the locations of the motion capture markers using the method described in section 5.3.6. The averaged measured elbow angles of different IACR angles for the flexion and extension experiments were averaged from the periods of MVC contractions, i.e. between 10s and 20s, 40s and 50s, and 70s to 80s from the start of each measurement trial. The MVC forces $F_{measured}(\theta)$ against elbow angle for all subjects are shown in Table 6.3 and Table 6.7. The angles, forces and force errors are reported to 3 significant figures.

Individual standard deviation values in the elbow angle for each angle in each experiment are not shown in the tables. The standard deviation values ranged from 0.624° to 3.66°. The average of these standard deviations was 1.87°.

The results shown in Table 6.3 and Table 6.7 are also plotted in Figure 6.14 and Figure 6.15.

Table 6.3. Measured MVC force on the force plate at different elbow angles for subject P1

P1 Flexion MVC			P1 Extension MVC		
Elbow angle (°)	MVC force at force plate (N)	Force error (1 s.d., N)	Elbow angle (°)	MVC force at force plate (N)	Force error (1s.d., N)
57.2	-34.8	0.651	42.8	-34.6	2.55
74.7	-63.7	3.48	61.3	-37.3	1.39
89.0	-78.3	3.10	81.2	-34.8	2.39
107	-72.0	3.40	107	-34.1	2.29
121	-60.0	3.77	124	-31.0	2.37
144	-40.9	2.86	144	-22.0	1.10
153	-33.3	3.15	164	-14.9	0.678

Table 6.4. Measured MVC force on the force plate at different elbow angles for subject P2

P2 Flexion MVC			P2 Extension MVC		
Elbow angle (°)	MVC force at force plate (N)	Force error (1 s.d., N)	Elbow angle (°)	MVC force at force plate (N)	Force error (1s.d., N)
56.5	-44.6	2.25	41.5	-34.5	2.38
74.5	-69.3	2.23	61.1	-27.5	0.910
94.0	-77.6	2.03	83.0	-30.6	1.16
107	-79.5	2.17	118	-27.36	1.50
128	-71.1	3.17	127	-24.7	0.893
139	-59.0	3.57	159	-18.2	1.48
*	*	*	167	-20.9**	0.804

*Subject P2 could not perform flexion MVC at IACR angle 8 due to maximum elbow angle limit.

**See discussion in section 6.5.4.

Table 6.5. Measured MVC force on the force plate at different elbow angles for subject P3

P3 Flexion MVC			P3 Extension MVC		
Elbow angle (°)	MVC force at force plate (N)	Force error (1 s.d., N)	Elbow angle (°)	MVC force at force plate (N)	Force error (1s.d., N)
56.1	-37.6	1.48	38.8	-35.1	2.21
84.2	-54.5	4.22	56.2	-39.3	1.43
93.5	-47.1	3.52	67.0	-45.4	2.97
122	-44.0	2.13	107	-29.4	1.63
131	-31.7	4.84	140	-27.0	1.49
146	-29.2	1.33	152	-19.4	2.00
157	-20.3	2.12	164	-23.5	1.27

Table 6.6. Measured MVC force on the force plate at different elbow angles for subject P6

P6 Flexion MVC			P6 Extension MVC		
Elbow angle (°)	MVC force at force plate (N)	Force error (1 s.d., N)	Elbow angle (°)	MVC force at force plate (N)	Force error (1s.d., N)
58.2	-26.9	1.15	33.1	-24.6	1.33
75.5	-35.5	1.26	55.5	-21.4	1.04
88.0	-30.0	1.74	73.2	-25.0	2.13
110	-28.0	1.28	109	-23.2	1.27
130	-24.1	1.65	121	-20.1	0.491
142	-20.3	1.60	149	-14.1	0.931
162	-15.0	1.73	171	-15.0**	0.985

**See discussion in section 6.5.4.

Table 6.7. Measured MVC force on the force plate at different elbow angles for subject P7

P7 Flexion MVC		
Elbow angle (°)	MVC force at force plate (N)	Force error (1 s.d., N)
61.4	-24.7	2.23
86.0	-25.6	2.32
105	-25.2	2.30
126	-22.4	1.95
139	-20.4	1.67
156	-14.9	1.46
172	-13.7	1.24

P7 Extension MVC		
Elbow angle (°)	MVC force at force plate (N)	Force error (1s.d., N)
43.3	-23.5	1.09
58.5	-27.3	2.24
89.9	-23.5	1.75
119	-23.0	0.876
129	-20.5	1.34
148	-18.1	1.19
176	-12.3	0.781

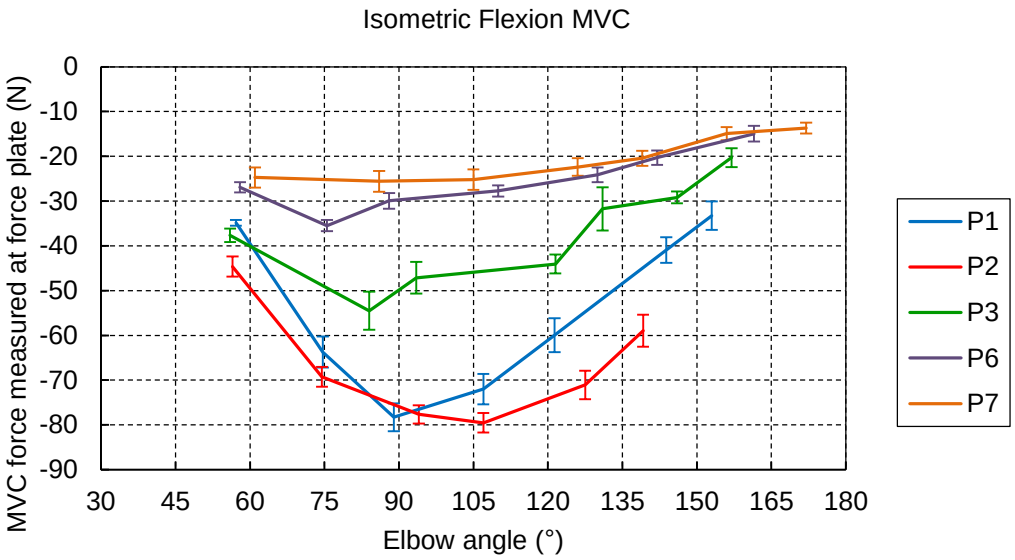

Figure 6.14. Isometric flexion MVC force measured from the force plate over different elbow angles for the five subjects. Vertical error bars represent ±1 s.d. of the averaged forces.

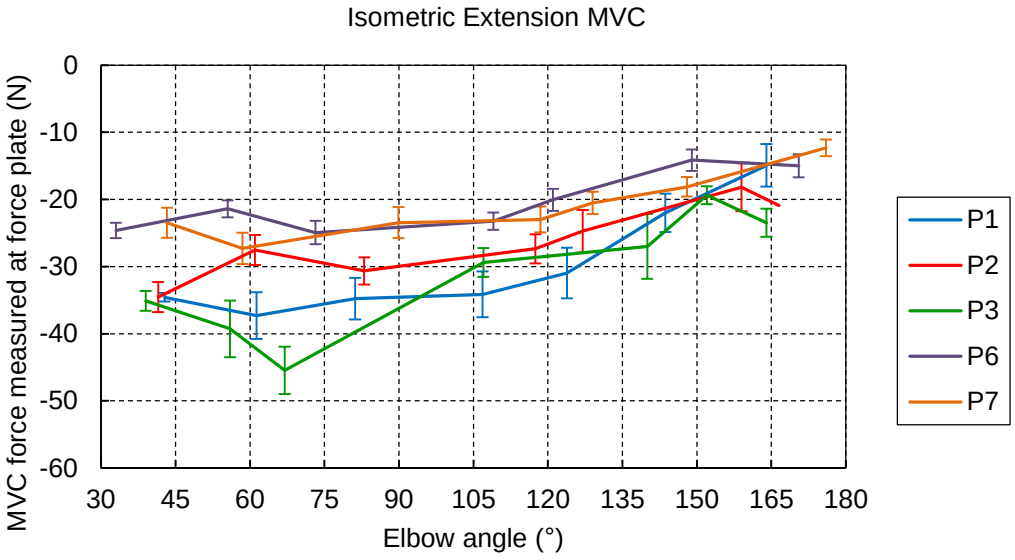

Figure 6.15. Isometric extension MVC force measured from the force plate over different elbow angles for the five subjects. Vertical error bars represent ±1 s.d. of the averaged forces.

Applying the measured forces $F_{\text{measured}}(\theta)$ in Table 6.3 and Table 6.7, the values of anatomical lengths in Table 5.2 and Table 6.2 and the geometries of the IACR and the arm in the experiment listed in Table 6.1 to Eqn 6.8 to Eqn 6.12. The force/length characteristics of the biceps muscle CE and the triceps muscle CE were calculated. The biceps muscle CE force/length characteristic for each subject was calculated using the flexion MVC forces and the triceps muscle CE force/length characteristic was calculated using the extension MVC forces. These are listed in Table 6.9 to Table 6.12.

Table 6.8. Force/length characteristics of the contractile element in the biceps muscle and triceps muscle for subject P1

P1 biceps CE force/length characteristic			P1 triceps CE force/length characteristic		
Elbow angle θ (°)	Biceps muscle length x_1 (m)	$F_{CE1}(\theta, x_1)$ (N)	Elbow angle θ (°)	Triceps muscle length x_2 (m)	$F_{CE2}(\theta, x_2)$ (N)
57.2	0.148	442	42.8	0.221	400
74.7	0.161	741	61.3	0.206	432
89.0	0.172	916	81.2	0.190	402
107	0.185	924	107	0.170	395
121	0.195	890	124	0.157	358
144	0.207	914	144	0.141	254
153	0.210	976	164	0.125	173

Table 6.9. Force/length characteristics of the contractile element in the biceps muscle and triceps muscle for subject P2

P2 biceps CE force/length characteristic			P2 triceps CE force/length characteristic		
Elbow angle θ (°)	Biceps muscle length x_1 (m)	$F_{CE1}(\theta, x_1)$ (N)	Elbow angle θ (°)	Triceps muscle length x_2 (m)	$F_{CE2}(\theta, x_2)$ (N)
56.5	0.145	480	41.5	0.241	333
74.5	0.160	683	61.1	0.224	266
94.0	0.177	784	83.0	0.205	296
107	0.187	867	118	0.175	264
128	0.202	980	127	0.166	239
139	0.208	1.01 x10^3	159	0.138	176
			167	0.132	202

Table 6.10. Force/length characteristics of the contractile element in the biceps muscle and triceps muscle for subject P3

P3 biceps CE force/length characteristic			P3 triceps CE force/length characteristic		
Elbow angle θ (°)	Biceps muscle length x_1 (m)	$F_{CE1}(\theta, x_1)$ (N)	Elbow angle θ (°)	Triceps muscle length x_2 (m)	$F_{CE2}(\theta, x_2)$ (N)
56.1	0.111	524	38.8	0.242	299
84.2	0.129	681	56.2	0.226	334
93.5	0.135	601	67.0	0.215	387
122	0.151	700	107	0.177	250
131	0.156	580	140	0.145	230
146	0.162	735	152	0.134	165
157	0.165	739	164	0.122	200

Table 6.11. Force/length characteristics of the contractile element in the biceps muscle and triceps muscle for subject P6

P1 biceps CE force/length characteristic			P1 triceps CE force/length characteristic		
Elbow angle θ (°)	Biceps muscle length x_1 (m)	$F_{CE1}(\theta, x_1)$ (N)	Elbow angle θ (°)	Triceps muscle length x_2 (m)	$F_{CE2}(\theta, x_2)$ (N)
58.2	0.0916	372	33.1	0.221	271
75.5	0.103	455	55.5	0.203	235
88.0	0.112	386	73.2	0.189	274
110	0.127	405	109	0.161	256
130	0.138	451	121	0.152	221
142	0.143	482	149	0.130	156
162	0.148	704	171	0.113	165

Table 6.12. Force/length characteristics of the contractile element in the biceps muscle and triceps muscle for subject P7

P1 biceps CE force/length characteristic			P1 triceps CE force/length characteristic		
Elbow angle θ (°)	Biceps muscle length x_1 (m)	$F_{CE1}(\theta, x_1)$ (N)	Elbow angle θ (°)	Triceps muscle length x_2 (m)	$F_{CE2}(\theta, x_2)$ (N)
61.4	0.162	318	43.3	0.214	231
86.0	0.180	308	58.5	0.201	268
105	0.194	328	89.9	0.173	230
126	0.206	363	119	0.148	226
139	0.213	417	129	0.139	202
156	0.219	501	148	0.123	178
172	0.222	1.35×10^3	176	0.0981	121

It should be noted that the results for the CE forces, F_{CE} reported in this chapter are positive. But in the muscle models, the CEs produce contractile forces only, and are therefore negative of those values shown here.

The angles, muscle lengths and computed muscle CE forces for the biceps muscle are plotted in Figure 6.16. The bottom graphs show normalised CE forces where the forces were divided by the maximum forces of all angles for individual subject and muscles. It should be noted that the maximum biceps force for subject P7 was taken from elbow angle of 156°, as the maximum value of 1.35 $x10^3$N measured at 172° was presumed to be unrealistic. This is discussed in section 6.5.

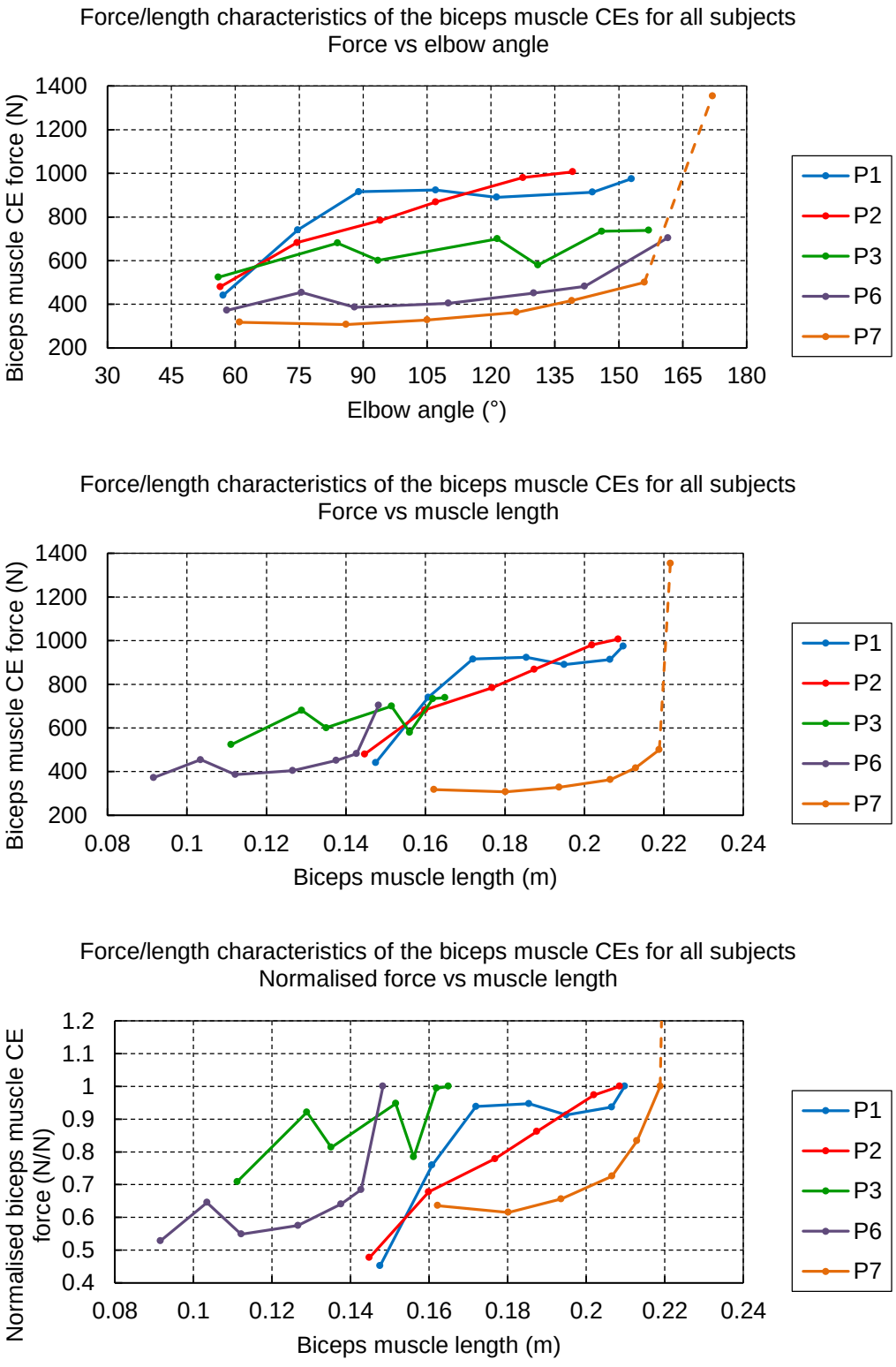

Figure 6.16. Force/length characteristics of the biceps muscle CE for all subjects. The top graph shows the CE force against elbow angle. The middle graph shows the CE force against the biceps muscle length. The bottom graph shows a normalised force against the biceps muscle length.

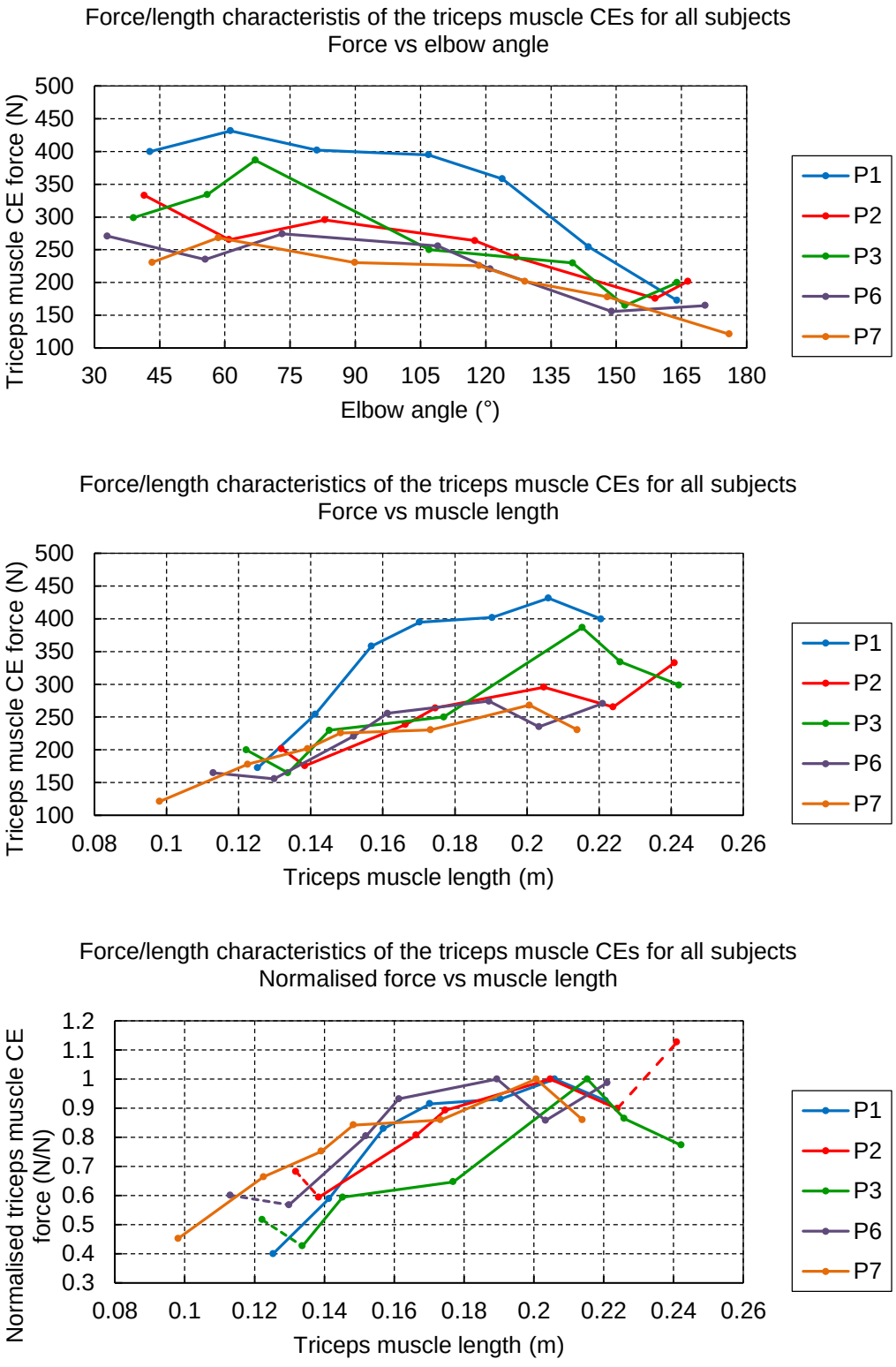

Figure 6.17. Force/length characteristics of the triceps muscle CE for all subjects. The top graph shows the CE force against elbow angle. The middle graph shows the CE force against the triceps muscle length. The bottom graph shows a normalised force against the triceps muscle length.

6.5 Discussion

The work in this chapter obtained the force/length characteristics of the contractile elements of the biceps muscle and triceps muscle in vivo for individual subjects. The discussion is grouped into three sections: experiment method, arm model and calculations, and measured results.

6.5.1 Experiment design

The IACR was developed for the work described in this chapter to transfer elbow moment to the force plate and allowed the elbow moment to be measured. This method was used as the force plate was integrated into the Vicon 3D motion capture system, allowing the force data and positional data to be measured in one system. Furthermore the IACR could be configured to measure elbow extension or flexion by changing the orientation of cross arm B. The elbow angles were adjustable by changing the angle of cross arm A and the rig was adjustable to suit difference in arm length between subjects by moving the position of the handle along cross arm A. This design meant only one rig was required to obtain measurements for both flexion and extension as different elbow angles for all subjects.

The measurements of the reference forces allowed the force/length characteristics of the CEs to be exclusively determined, and therefore the parameter values for the passive components in the model were not necessary in the derivation of the force/length characteristics. This capability had been important for the work in this thesis, as subjects P6 and P7 did not participate in the previous passive experiments described in Chapter 5. If the reference force approach was not used, then those passive parameters would be required prior to deriving the force/length characteristics of the muscles.

The pronation/supination (P/S) angle of the wrist in this experiment was not specified to the natural position during the measurements. Subjects were instructed to produce maximum force in the flexion or extension direction. Subjects naturally pronated the hand in the extension experiment so that the

base of the palm was flat against the handle, instead of contacting the handle at the area around the pisiform, ulnar collateral ligament and styloid process of ulna. This was more comfortable as the large force exerted during MVC was distributed to a wider area. By the same principle, subjects supinated the wrist during the flexion experiments to put the handle contact at the base of the palm instead of applying force at the area around the styloid process of radius. This causes a problem in that the difference in wrist P/S causes a change in the length of the biceps brachii muscle, which is not accounted for in the arm model in this thesis. In the flexion MVC experiments, the biceps brachii contracts, and therefore the change in biceps brachii length from wrist supination modulated the force characteristics in relation to the elbow angle, which may therefore introduce an error in the calculated muscle length for the biceps brachii in the arm model biceps muscle. In the extension experiments, the pronated hand did not affect the result as the triceps brachii is not responsible for wrist P/S rotation, and that the flexor muscles are relaxed of which the passive forces were included in the reference forces, therefore any effects of P/S rotation in the extension experiments were eliminated from the measured results.

6.5.2 Arm model and calculations

The work in this chapter continued to assume that the extensions of the free tendons were negligible. However it has been suggested that the maximum strain of free tendon under MVC is about 3.3% (Zajac, 1989). Maganaris and Paul (Maganaris and Paul, 1999) reported maximum tibialis anterior strain of about 2.5% where the MVC force was about 600N, from MRI measurements in vivo. This meant that the fixed free tendon length assumption could have introduced about 3.3% error in the length of the free tendon during MVC, thus also adding an error into the length of the muscle models. For the average measured free tendon lengths in this thesis of about 150mm, this would equate to about 5mm of tendon extension. This meant there may be a 5mm error in the calculated muscle lengths. For the minimum calculated muscle length (P6 biceps muscle), this gave the maximum error, of about 5.5%. However this change in length

cannot be measured in vivo from palpation and surface measurement, furthermore section 4.2.2 concluded that models with serial elements that can be stretched cannot be incorporated into musculo-skeletal models. Therefore the approach of assuming fixed tendon length has been used in this study. The conclusion was that the maximum possible error of 5% due to this assumption was not significant in the model.

6.5.3 Results of flexion MVC experiment and biceps muscle force/length characteristics

The measurements were successful and produced reproducible estimates of the MVC forces. Figure 6.12 showed the raw measured forces over the time histories of the measured trials for subject P6 as an example. The subject was able to promptly produce MVC forces at the correct time. Both the reference force and MVC forces were obtained successfully by averaging the corresponding forces in the time histories. There were good reproducibility in the repeated measurements in angles 4, 2 and 8, additionally this reproducibility showed there was no detectable decrease in contraction force due to muscle fatigue between measurement trials. There was also good agreement between MVC periods in each trial, again showing there was no muscle fatigue which could have reduced the level of force exerted.

It can be seen in Figure 6.13 that the force exerted was greatest at around 1s after the start of each 10s MVC period, and that the force level was either maintained (e.g. extension angle 6) or slowly decreased (e.g. extension angle 7) over time. Although the true maximum force was at around 1s, in order to give good estimates, the forces were averaged between 2s to 8s from the start of the MVC periods. The maximum 1 standard deviation around the averaged force was 4.84N, at 32N for subject S3, i.e. 15% error. The average 1s.d. for all measured MVC was 6.2%. In comparison to results in the literature, the measured forces in this work are more precise than those reported by Leedham and Dowling (Leedham and Dowling, 1995), where their measured isometric MVC force errors were between about 10% to 35%.

Due to the geometry of the bones, muscle points of origin and insertion and moment arms, the flexor muscles had the best mechanical leverage at an elbow angle of about 90°, and the flexion MVC force was expected to be greatest around this angle. This expected characteristic was seen in the measured forces (hence elbow moments) over elbow angle for all subjects. It can be seen in Figure 6.14 that the flexion MVC forces were significantly greater between 75° to 120° in comparison to a flexed or extended arm. These elbow moment against elbow angle results of the elbow flexor muscle showed good agreement with those reported in the literature (Leedham and Dowling, 1995).

For the measured extension MVC force (hence elbow moment) shown in Figure 6.15. There was good agreement of force characteristics over elbow angle between subjects. Anatomically the lower free tendon of the triceps brachii wraps around the trochlea and joint capsule, there are small variations in triceps brachii moment arm over elbow angle as the trochlea and joint capsule are not perfectly circular, but overall the moment arm is similar over all elbow angles. The expected characteristic of this is a similar maximum extension moment over elbow angle, and this can be seen in the measured results in Figure 6.15.

With a near constant triceps muscle moment arm across all elbow angles, this suggests the force/length characteristic of the triceps muscle plays a more significant role in modulating the maximum extension force at different elbow angles.

The computed force characteristics of the biceps muscle against elbow (top graph in Figure 6.16) shows a similar trend between all subjects; the biceps muscle MVC force increases as elbow angle/muscle length increases.

The biceps muscle lengths calculated from the elbow angle and geometry of the arm model (see Figure 6.16, middle graph) showed significant differences in muscle lengths between subjects. While the range of muscle lengths for all subjects were similar, subject P7 has biceps muscle length range from 0.16m to 0.22m while subject P6 has biceps muscle length range from 0.09m to 0.15m,

which was about 30% difference in the average range values. This suggested that there may be errors in the measured anatomical lengths, which could be due to the inability to accurately pinpoint anatomical features to measure the muscle lengths and free tendon lengths from palpation and surface measurement.

In the normalised force against muscle length results for the biceps muscle, shown in the bottom graph of Figure 6.16, which is the force/length characteristic of the biceps muscle contractile element, subjects P1 and P2 showed expected force/length curves, which agreed with those measured by Leedham and Dowling (Leedham and Dowling, 1995). It should be noted that their length definition for the flexor muscle also included the lengths of the free tendon and are therefore longer than those reported in this thesis.

The range of muscle length achievable in vivo was limited by joint angle range. The computed muscle length range for subjects P1 and P2 corresponded to the normalised muscle length range between 0.5 to 1 unit as shown in Figure 2.7. These agreed with the findings of Murray et al. (Murray et al., 2000), who reported muscle force capacity against muscle length by analysing muscle cross sectional area. These curve characteristics were less prominent in the biceps muscle force/length curves for subject P3, P6 and P7. Subject P3 may not be as familiar with the experiment in comparison to other subjects, and therefore the level of voluntary contraction may not be the same in all experiments, and caused significant non-linearity in the measured force/length relationship. For subjects P6 and P7, the force/length curves had the shapes of exponential growth, which were not expected. The measured force against elbow angle shown in Figure 6.14 were good; these suggested the measured anatomical lengths may have large error, or the geometry that compute the biceps muscle moment arm in the model may need to be improved. The computed muscle force of about 1350N at 172° for subject P7 was likely to be overestimated by an underestimated value of the biceps muscle moment arm. Anatomically the point of origin and insertion of the flexor muscles are at the surface of the bones

instead of along the centre line of the body segment (arm), and that when the elbow is fully extended, the muscle also wraps round the elbow joint capsule, and therefore the moment arm would be greater than the modelled biceps muscle moment arm. These differences in geometry between the arm anatomy and arm model may have caused significant error in the length and force calculations for P6 and P7.

The arm model in this thesis had grouped the biceps brachii, brachialis and brachioradialis as one muscle, therefore the force/length curves of the biceps muscle would in fact be the superposition of the force/length curves of the three muscles. If flexion MVC were measured at different wrist P/S angle, it would be possible that the calculated force/length characteristics of the biceps muscle would be different, as the biceps brachii changes due to wrist P/S rotation and the biceps brachii force/length curve would have shifted in the length axis in relation to the force/length curve of the brachialis and brachioradialis.

Overall from the flexion MVC experiment, it suggested the biceps muscle optimum force where MVC force was maximum was at muscle length that corresponded to maximum elbow extension.

6.5.4 Results of extension MVC experiment and triceps muscle force/length characteristics

The measured MVC forces in the extension experiments showed good agreement between subjects, which are also true for the computed triceps muscle forces shown in the top graph in Figure 6.17. Similar triceps muscle force versus elbow angle characteristics were seen between all subjects.

The computed triceps muscle lengths for all subjects were similar; this showed that the arm model allowed a good estimate of the triceps muscle length to be calculated.

The computed force/length characteristics of the triceps muscle shown in the bottom graph in Figure 6.17 show good agreement between subjects, and the

optimal length when the muscle can produce maximum force was between about 0.19m to 0.21m. There was also a good agreement between the force/length characteristics of the triceps muscle between the results obtained in this study and results reported in the literature (Hatze, 1981).

The measured triceps muscle force/length curve for the full elbow angle range (bottom graph in Figure 6.17) fitted in the range of about 0.7 unit to 1.1 unit of the force/length characteristics with normalised muscle fibre length shown in Figure 2.7. This is in agreement with the results reported by Murray et al. (Murray et al., 2000), who derived the force capacity from muscle cross sectional area over elbow angle.

The force/length characteristics of the triceps muscle for subject P2 shown in the bottom graph in Figure 6.17 had an unexpected large force at maximum muscle length (0.24m). This force was measured at the smallest elbow angle, i.e. producing elbow extension force when the arm was fully flexed. From inspection of the video footages from that trial, it was found that the subject also forced the weight of the trunk forward. Thus the force from the weight of the trunk was transferred from the compressed tissue of the fully flexed arm towards the handle, and therefore that measured force had force applied to the trunk added to the extension of the arm. While the IACR had a curve pad to support the arm, the subjects would still need to actively maintain the posture of the trunk and shoulder angle to ensure the upper arm was vertical and the elbow was in the correct position. For subjects to concentrate on producing maximum force and maintaining posture, subject P2 may have focused on producing maximum force but neglected the source of this force.

For subjects P2, P3 and P6, the calculated force/length characteristics of the triceps muscle at 0.13m (P2), 0.12m (P3) and 0.11m (P6) were higher than expected. An inspection of the motion capture data showed that at IACR angle 8 where the extended was fully extended, their elbow also rotated in the medial direction (i.e. rotated humerus). This allowed the subjects to push backwards

with greater force as the elbow no longer has freedom of movement in that direction.

6.6 Conclusion and future work

The experimental protocols successfully gave reproducible estimates of the MVC forces of the muscles. There was good agreement in the measured values between subjects. The force/length characteristics of the muscle in the arm model were successfully determined from measurement in vivo, and the results in this work showed good agreement to data in the literature.

The results from this chapter demonstrated that isometric muscle forces are not constant for the whole range of joint angle, and are heavily modulated by the geometry of the muscles and bones and well as the CE force/length characteristics. If models are developed to accurately predict forces and moment around a joint, then it is essential that the anatomy of the muscles and bones and the force/length characteristics of muscles are incorporated into the models.

Pronation and supination of the wrist changes the length of the biceps brachii, this was a factor that was not accounted for in the arm model described in this thesis, and therefore there was an unknown error in the biceps brachii length. In future work, the anatomy of wrist P/S rotation can be included in the model so that the change in biceps brachii length due to wrist P/S rotation can be determined.

Chapter 7 Muscle Contraction Using Surface Functional Electrical Stimulation

7.1 Introduction

One of the stimuli for this work was FES. This chapter is a preliminary study into the use of the musculo-skeletal model developed in this thesis to predict movement generated by FES. The example is based on a simple on/off surface Functional Electrical Stimulation of the elbow flexor muscle to generate force and movement in elbow flexion.

The experiments described in this chapter first identified the electrical current required to generate a target isometric elbow flexion force (section 7.2.2), then the current was applied when the arm was allowed to swing and the change in elbow angle resulting from the stimulation was measured (section 7.2.4). The measured and simulated changes in elbow angle under FES were compared.

A major problem faced by any surface FES experiment is the complex relationship between the injected electrical stimulus and force generated by the muscle, which is determined by internal tissue geometry and current flow, and is difficult to model (Nitsche et al., 2003, Bajd, 2006). In surface FES, a muscle contracts by the external electrical stimulus depolarising the transmembrane potential in the muscle fibre, which causes the fibre to contract (fibre recruitment). The strength of the contraction is a function of the number of contracting fibres. For a specific level of electrical stimulation and electrode positions, the current path within the body and the locations of the muscle fibres determine which and how many fibres are recruited, and hence the total force. The internal body geometry and the locations where the current are applied (i.e.

electrode positions, inter-electrode spacing) become critical factors in determining the force generated. Furthermore the internal soft tissue geometry changes during movement, and this causes extra difficulty in determining the force generated (Hausdorff and Durfee, 1991, Mulder et al., 1992). In this thesis, to minimise the change in contractile force for a fixed stimulus caused by unpredictable changes in the internal body geometry during movement, the experiments described in this chapter used low level of stimulation to generate a small muscle force and small movements.

7.2 Method

7.2.1 Instrumentation, electrode positions and current stimulation waveform

The FES experiments described in this thesis were given ethics approval on the basis that:

i. The participants in the FES experiments were limited to those who had previous experience and were familiar with electrical stimulation. Subjects P1 and P3 were the only participants from the previous experiments who fulfilled these criteria.
ii. Experiments must be non-invasive; therefore surface electrodes were used to deliver the electrical stimulus.
iii. Medical electrical equipment designed for use in the clinical environment was used to provide the stimulus to minimise the risks associated with equipment failure. The electrical stimulus was generated by an Excel Tech Ltd NeuroMax (Figure 7.1), which was a clinical EMG and nerve conduction study equipment, certified to EN 60601-1. Stimulation was current controlled and delivered as a pair of balanced current drive. A ground electrode (round, 1.25inch diameter) was used close to the stimulation electrodes to minimise current flow through the remainder of the body in case of a failure in one of the current sources or electrode disconnection.

Subjects' perception of electrical stimulation ranges from slight discomfort to sensation of pain, therefore the stimulation current was limited to maximum of 50mA. The stimulator had a hand held remote control (see Figure 7.1) that could toggle the current on and off and also increase and decrease the current stimulation in 1mA increments. Subjects held this remote control in the hand of the non-stimulated arm and applied the stimulus when instructed. This approach allowed the subject to stop the stimulation at any time.

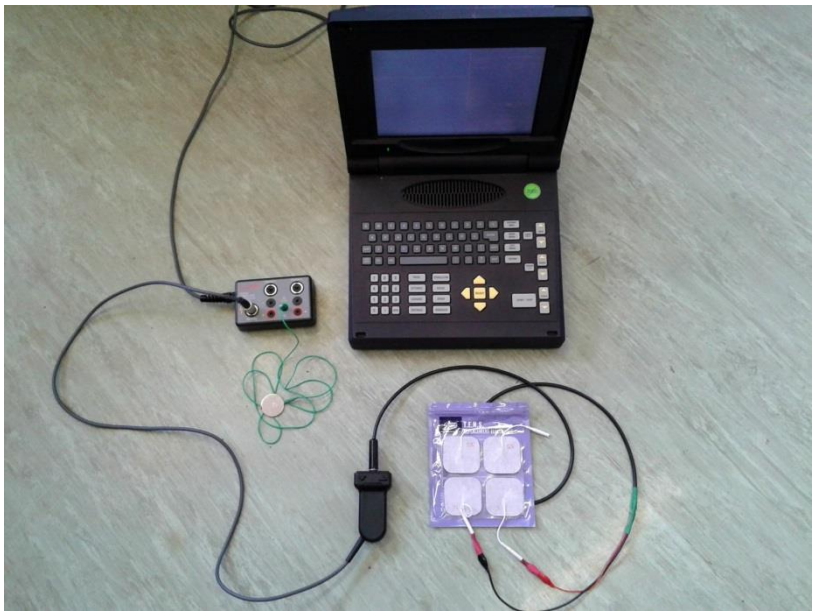

Figure 7.1. Excel Tech Ltd NeuroMax neuro-stimulator and EMG. Main laptop style console allowed current waveform programming. Break out box (left) connects the main control to the hand held remote control and the ground electrode (stainless steel plate connected to green lead). The hand held control (bottom of the image) is between the breakout box and the stimulation electrodes (white pads at the bottom right). The hand held control has three buttons, one to toggle the current on and off, and two to increase and decrease the current.

The surface electrodes used to inject stimulus current were pre-gelled carbon rubber electrodes, 5cm^2 squares with rounded corners (The Boots Company PLC, England). These electrodes are sold for use in transcutaneous electrical nerve stimulation (TENS) for pain relief therapy. The electrodes are flexible with a cotton backing that prevented large stretches in the electrode. The gels self-adhere to the skin.

Electrode positions are critical in determining which muscle or muscles are stimulated (Frigo et al., 2000, Nitsche et al., 2003, Bajd, 2006, Malesevic et al.,

2012). The FES experiments described in this chapter aimed to stimulate the biceps flexor muscles, specifically the biceps brachii and the brachialis, and the electrode configuration concentrated the current flow to these target muscles. During stimulation, positive ions external and close to the surface of the muscle fibre membrane are drawn away from the membrane to the cathode, this inverts the transmembrane potential of the muscle fibres (depolarisation) from the resting potential (external +ve, internal –ve) to the activation potential (external –ve, internal +ve). Therefore muscle fibre depolarisation and recruitment occurs beneath the cathode electrode. To stimulate the bulk of the biceps (flexor), the cathode was placed at the lower centre of the bulk of the biceps brachii as shown in Figure 7.2. The distal edge of the cathode (bottom edge in Figure 7.2) was 2cm proximal to the point where the biceps brachii connects to its free tendon. This cathode position was also close to the brachialis (but separated by the distal end of the biceps brachii). The anode was placed proximal to the cathode (above the cathode in Figure 7.2) with 2cm electrode edge-to-edge spacing. This configuration allowed both the electrodes to be placed on the bulk of the biceps brachii to allow maximum current flow to the elbow flexor muscles in the upper arm. The ground electrode was strapped to the wrist, see Figure 7.3.

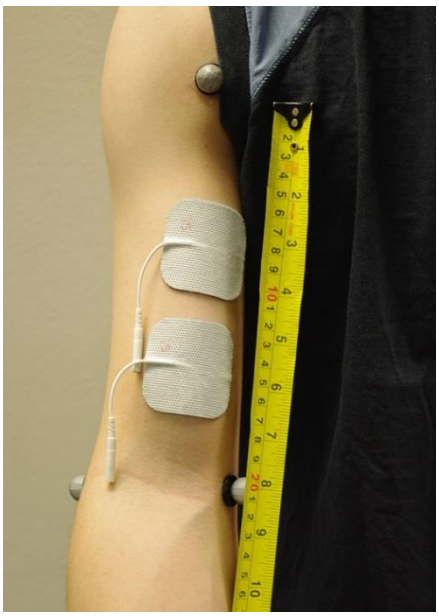

Figure 7.2. FES electrode placement on the bulk of the biceps brachii, the top electrode pad is the anode and the bottom electrode is the cathode. Reflective markers (arm marker model, section 5.3.1) are attached to the arm to measure the movement trajectory of the arm

Stimulation current is normally delivered as pulses with varying frequency and amplitude. Table 7.1 lists examples of stimulation waveform used by other researchers who have used FES for laboratory experiments (all human subjects). Based on these values in the literature (Table 7.1) and the available settings of the stimulator, the injected current used in this study had a fixed rate of 25 pulses per second (25Hz) and 0.3ms pulse durations. The intensity of the stimulus was controlled by varying the amplitude of the stimulus current.

The electrode stimulus was current controlled instead of voltage controlled, the charge delivered through this method is constant regardless of the electrical impedance of the electrodes (Webster, 2009).

Table 7.1. FES stimulation waveform characteristics from literature

	Subjects	Pulse rate and amplitude	Pulse width	Other comments
Frigo C (Frigo et al., 2000)	Healthy subjects rectus femoris	16.67Hz 60mA 40%MVC	0.3ms	5x9cm electrodes
		25Hz 50mA 40% MVC	0.3ms	16cm inter electrode distance
Sharma N (Sharma et al., 2012)	Healthy subjects quadriceps femoris	30Hz	0.4ms	Voltage controlled
Braz at al. (Braz et al., 2009)	4 SCI subjects quadriceps femoris	33Hz	0.15ms	7x13mm oval electrodes
Chesler and Durfee (Chesler and Durfee, 1997)	20 healthy subjects 3 SCI subjects	30Hz 0-150mA	0.3ms	Carbon rubber electrodes 3in x 5in

7.2.2 Preliminary FES experiment

In a preliminary experiment, FES was applied to the biceps muscle to observe the physiological effects and allow the subject to become familiar with the FES setup. The subject's right arm was rested on a table, with the palm facing upwards and the elbow remained on the table. The upper arm was positioned so that the elbow angle was at 135° and the electrode positions for the biceps were described in the previous section and shown in Figure 7.2. The stimulation began with small current amplitude of 0.1mA, 25 pulses per second, 0.3ms pulses. The stimulation was started and stopped by the subject using the hand held remote control in the hand of the non-stimulated arm (left hand). The 50mA maximum current was set at the laptop unit and cannot be exceeded using the hand held remote control. The stimulation was given for a short period of time of 2 to 3 seconds for the physiological effects and movements to be observed. The current was increased during the experiment as the subject became familiar to the sensation. Subject P1 participated in this experiment. Subject P3 did not participate in this experiment as subject P3 was already familiar with experiments using the NeuroMax stimulator.

Table 7.2. Physiological effect of surface FES in a preliminary experiment

Current amplitude	Observation	Other comments
Below 5mA	No observable physiological effects. No stimulation sensation felt by the subject.	
5mA to 10mA	No observable physiological effects. Subject felt slight 'buzzing' sensation from stimulation	
10mA	Visible muscle twitching but no elbow movement. Subject felt twitching in the muscle	
25mA	Caused elbow flexion from 135° to 90◦. Subject felt fast pulses of strong twitches, similar to sensation of pain from muscle cramps at the beginning.	As current increased from 10mA to 25mA, the intensity of the twitches caused pain sensation. The onset of pain sensation was faster than onset of elbow movement.
50mA	Caused elbow to flex from 135° to 45°. Subject felt similar pain sensation from muscle twitch. Subject felt muscle fatigue. When reduced back to 25mA after 15 mins of stimulation, the amount of arm lift was less in comparison to 25mA after 5 mins of stimulation	Subject's pain sensation became less intense over time. It required 15 mins of stimulation training for the subject to accept sensation from 50mA stimulation.
After experiment	No sensation of discomfort or twitch remains. Sensation of muscle fatigue disappeared within 1 hour.	

7.2.3 Isometric FES elbow flexion experiment

The relationship between injected current and muscle contraction force is determined by the stimulus, body geometry, and electrode positions. Without dynamic 3D modelling of the muscle fibre geometry and current paths distributed in the body, it is impossible to predict the stimulus to force relationship (Davoodi et al., 2003). Therefore, prior to predicting the movement from FES, the first stage of the FES experiment aimed at identifying the amount of current required for the flexor CE to exert a target isometric force.

As discussed in the design of the passive movement experiment and voluntary isometric contraction experiment, it is not possible to directly measure the force of the contractile element of the muscle during voluntary or stimulated movement, as passive component forces and CE forces cannot be separately determined from movement dynamics of an activated arm, therefore the isometric force measurement method using the IACR described in Chapter 6, was used to exclusively measure the isometric muscle CE force during FES.

The elbow angles studied were limited to a small range to minimise changes in tissue/current path geometry. The isometric force was measured at IACR angle 6, where the elbow angle was at about 135°. This angle was selected as later in the free movement experiment described in section 7.3.4, the elbow angle allowed a large degree of flexion before maximum flexion was reached. Additionally, the subject would not have to super extend the arm when using the IACR.

In order to minimise the period of discomfort during stimulation for subjects, only one target isometric force was specified. This minimised the number of measurement trials required. Additionally the sensation of discomfort increases with increasing injected current, therefore these experiments only used low level of stimulation.

The set target force was 10% of the flexion MVC elbow moment generated by the subjects at IACR angle 6 measured in Chapter 6. In which equivalently the target force to be measured on the force plate was also 10% of the force

measured during isometric elbow flexion MVC. This force was specified as a compromise between minimising changes in tissue/current path geometry, minimising discomfort from the stimulation and the minimum change in the measured force that can be detected and estimated.

The 1 standard deviation of the measurement noise error for the force plate was 0.91N when forces were averaged for a 5 second period. The target force should therefore be above this standard deviation error. However possible noise from physiological effects should also be accounted for, such as increase or decrease in force during isotonic contraction, and the standard deviation error from averaging 6 seconds of measured MVC forces shown in section 6.4, Table 6.3 to Table 6.7 (force errors column), was an average of 6.2% (defined and reported in section 6.5.3), therefore a target change in force should be above 6.2% of the MVC force if the same level of noise is to be expected from physiological effects. In this thesis, this target force measured at the force plate was rounded up to 10% of the MVC force measured at the force plate.

Figure 7.3 shows the experimental setup to measure the FES isometric force. The position of the handle along cross arm A was set to that measured in the MVC experiment in Chapter 6 (Flexion $d_{\text{cross arm A}}$, Table 6.1). The wrist was strapped to the handle with the wrist and hand in the neutral position, as shown in Figure 7.3. In this experiment, a reference force was also measured, when the arm was completely relaxed and the wrist was strapped to the handle, this reference force measured the passive force of the arm, weight of the arm and force of the IACR acting on the force plate. The target force was the reference force adding 10% of the MVC force measured at the force plate from the isometric MVC experiment. The elbow angle was measured using 3D motion capture with the arm marker model described in section 5.3.1 and computation method described in section 5.3.6.

In this isometric FES flexion experiment, the wrist was strapped to the handle of the IACR for the reference force to be measured, this was different to the

method used in the isometric MVC flexion experiment described in section 6.3.2, in which the hand was closed and the fingers hooked onto the handle. In this FES experiment, the arm muscles had to be completely relaxed, however in order for the hand to hook onto the handle, the wrist must supinate for the palm to face upwards to allow the fingers to hook onto the handle. This meant the biceps brachii must be voluntarily contracted to achieve wrist supination, thus in such case electrically stimulated force cannot be separately determined from voluntarily contraction force. Therefore a strap was used to hold the wrist to the handle.

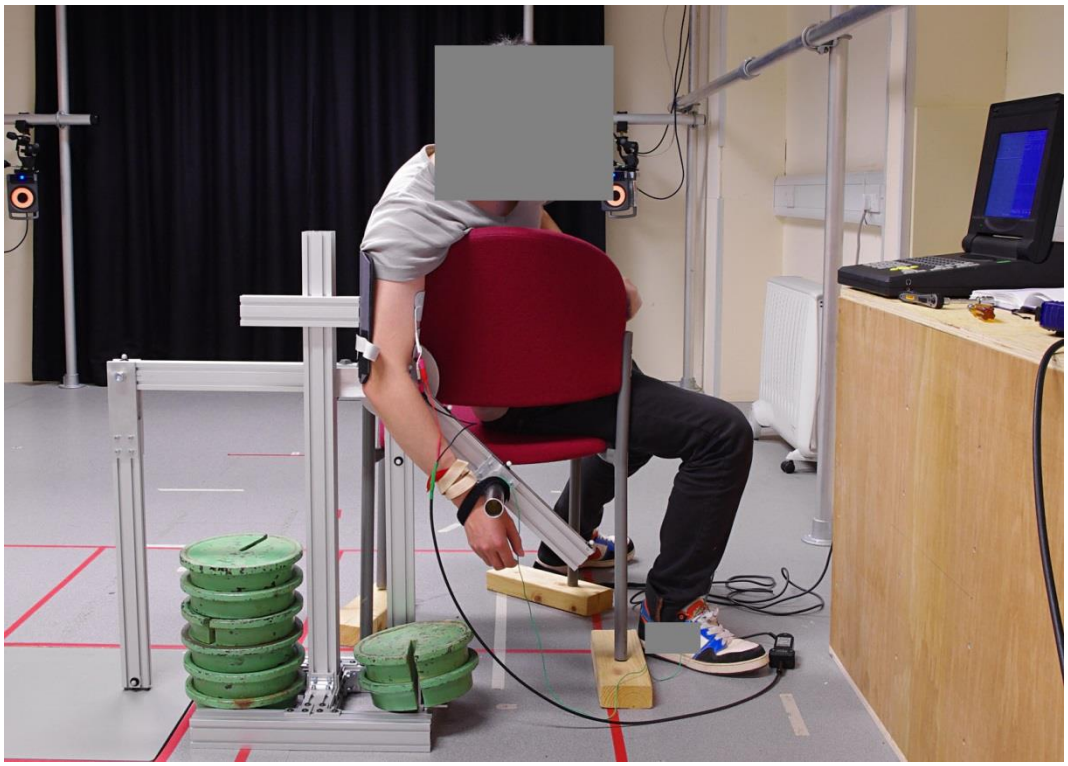

Figure 7.3. FES isometric elbow flexion experiment using the IACR. The electrodes were attached to the surface of the biceps brachii. The ground electrode was strapped to the forearm near the wrist with the beige strap. The wrist was strapped to the handle by the black strap (non-stretchable). The motion capture markers for the arm were not attached in this image.

The subject's arm muscles were relaxed during the experiment (i.e. no voluntary contractions), the subject controlled the application of the stimulus and its amplitude via the hand held remote control.

The stimulation began with 5mA current, in which the stimulus was maintained for 5 seconds to allow a steady force to be measured and estimated from the force plate data. The 5 seconds period allowed enough time for the measured force to be averaged over time, but not too long to cause muscle fatigue and a decrease in muscle tension. The 5 seconds period was also not so long that the subjects would have to endure long period of discomfort when higher current stimuli were used. If the measured force did not reach the target force, the current was incremented by 5mA and the isometric force from the new stimulus was measured. The current increased until the target force was reached. At which point, 5 repeated measurements of 10s period of stimulation that generated the target force were obtained to allow the reproducibility to be analysed.

During the 5 repeated measurements, the subjects were given 5 seconds countdown to apply the stimulus, and the turn off command was given at the moment when the 10s of stimulation was reached.

As subject P3 did not participate in the preliminary FES experiment described in section 7.2.1, subject P3 was allowed to familiarise with the sensation of the stimulation and the experiment protocol before the measurements.

7.2.4 FES elbow flexion movement experiment

The target FES current identified from the isometric FES contraction experiment described in the previous section was then applied to the arm when it was in the same position and setup as in the passive moment experiment, experiment 3 (Chapter 5, Figure 5.6c). Images from this FES arm swing experiment are shown in Figure 7.4. This experiment was performed immediately after the FES isometric flexion experiment and the positions of the electrodes were not changed, in order to minimise changes in the force/stimulation characteristics from possible differences in current path/tissue geometry.

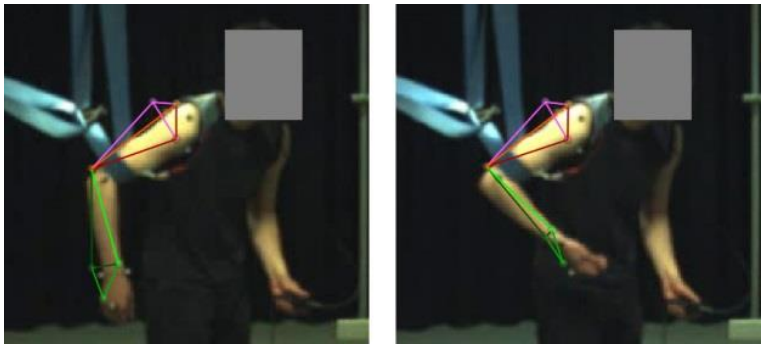

Figure 7.4. FES elbow flexion movement experiment. The upper arm was held by a strap. Left image shows the arm with no stimulation applied and the forearm hangs downwards. The right image shows the arm flexed when a stimulation current of 30mA was applied. Both images show the 3D overlay of the arm markers from 3D motion capture, and lines connecting the marker to show the shape of the arm model. The subject turned the stimulation on and off via the hand held remote control in the left hand. The position of the shoulder was measured prior to the experiment to set the elbow angle to about 135° (5° precision). The upper arm position was maintained throughout the measurement.

The arm was relaxed at all times (no voluntary contraction) and the forearm hung freely downwards at the beginning of the measurement trials. The upper arm was held by a strap as shown in Figure 7.4, the position of the body was placed so that the upper arm was at about 45° from vertical and the elbow angle was at about 135° (precision of 5°). The position was measured using a large protractor and a spirit level before the start of each measurement trial. The body and upper arm positions were maintained throughout the measurements. Five repeated trials each involving 10s of stimulation were measured to allow the repeatability to be assessed. Again the subject turned on and off the stimulus using the hand held control in the left hand; a 5 seconds countdown was given to apply the stimulation and “turn off” command was given when 10s of stimulation was applied. The measured elbow angle trajectories were derived from 3D motion capture, and the changes in elbow angle during the current stimulation were obtained by subtracting the elbow angle during stimulation from the elbow angle when no stimulus was applied.

7.2.5 Simulated FES elbow flexion movement

In this experiment the force generated by the flexor muscle during the arm swing under stimulation, was assumed to be the same as the isometric force measured from the isometric FES experiment. In the arm model, the muscle force from FES

can be modelled by the measured isometric FES force exerted by the biceps muscle CE. The dynamics of the arm during the FES arm swing experiments can be described by a modified version of Eqn 5.3, where the upper arm angle was corrected. In Eqn 5.3 the upper arm was 45° from vertical, the moments from gravity terms were functions of $g\sin(\theta+45°)$, where the 45° represented the upper arm angle from vertical. In the simulation for the FES flexion moment, that angle was changed to the mean measured upper arm angle from vertical (obtained from 3D motion capture).

Forward dynamics simulation approach was used to predict the change in elbow angle when the measured isometric FES force was applied as the CE force of the biceps muscle: F_{CE1}. The simulation method used to simulate the elbow movement trajectory under FES flexor contraction was the same as that used in the passive movement experiment (section 5.4), by numerically integrating the forward dynamic model using ODE45 in Matlab 2009b. The biceps muscle CE force, F_{CE1}, which was zero in the passive movement experiment, is now non-zero and a contractile force is applied. The contractile forces used in the simulations are described in section 7.2.5.1 and section 7.2.5.2. The starting elbow angle for the simulation was obtained from the overall averaged starting angle of the five measurement trials (Table 7.5), the method for calculating this angle is described in detail in p.192 of section 7.3.3.

7.2.5.1 Expected simulated flexion movement generated from FES

The simulated elbow movement when the CE force (from the measured isometric FES force) was applied is referred to as the expected simulated movement in the results. This was compared with the measured change in elbow angle in the FES flexion movement experiment.

7.2.5.2 Fitted simulated flexion movement generated from FES

A separate set of forward simulated elbow trajectory under biceps muscle contraction was simulated for which the value of the biceps muscle CE force,

F_{CE1}, was fitted so that it gave a simulated change in elbow angle under flexor contraction in agreement with the measured result. These simulated elbow movement with a fitted F_{CE1} value are referred to as the fitted simulated movement.

The fitted force for F_{CE1} was obtained by multiplying the measured isometric FES force by a fitted constant, and this constant was obtained by identifying its value where it gave an elbow angle under stimulation that agreed with the measured change in elbow angle. The methods are further described after the measured results of the FES flexion movement experiment in section 7.3.3.

To simulate the movement of the elbow under FES, the remaining arm model parameters were also required. As this experiment was performed about 12 months after the passive experiment for subject P1 and P3 were obtained, the weights of the forearm and hand were re-measured using the method described in section 5.2.2 of the passive movement experiment. The moment of inertia for the forearm and hand were recalculated using the new measured arm weight (Eqn 5.4). The remaining model parameter values for each subject were assumed to remain unchanged and were those obtained in the passive movement experiment. The measured distances were taken from Table 5.2 and the fitted passive component parameters were taken from Table 5.3.

It should be noted that the force/length characteristics of the CE obtained in Chapter 6 were not used, as the measured biceps muscle's force/length characteristic for subject P1 shown in Figure 6.16 varied by less than 5% between elbow angles of 90° to 145°, and the MVC force variation for subject P3 was more non-linear than expected. In this chapter the CE force was assumed to be unaffected by the length of the muscle.

7.3 Results

7.3.1 Re-measured mass of forearm and hand and moment of inertia

The re-measured mass of the arm, m_{arm}, for subject P1 and P3, together with the recalculated moment of inertia of the forearm and hand around the elbow joint, J, are listed in Table 7.3. These values were used to simulate the elbow movement generated by FES described in section 7.2.5, the simulated elbow movements are presented in section 7.3.4.

Table 7.3. Re-measured mass of the forearm and hand and recalculated values of the moment of inertia during the FES experiments

Subject parameters	Subject P1	Subject P3
Mass of forearm and hand m_{arm} (kg)	0.88	1.48
Moment of inertia J (kg m^2)	0.0266	0.0718

7.3.2 Isometric FES elbow flexion experiment

The target forces measured at the force plate in the isometric FES flexion experiment were 6N for subject P1 and about 4.5N for subject P3. These were derived from 10% of MVC force measured at the force plate in Table 6.3: P1, IACR angle 6, elbow angle at 121°, and Table 6.5: P3, IACR angle 6, elbow angle at 131°. It should be noted that the 10% MVC force for subject P3 should be 3N, however this small difference in measured force was difficult to identify from the noise in the raw measured force from the force plate, and therefore the target force for subject P3 was raised to about 4.5N (15% of MVC at 131°, Table 6.5).

The current that generated the target elbow moment (more correctly the target measured force at the force plate) was 30mA for both subjects.

The five repeated measurements of 10s of isometric FES flexion contraction (30mA) are shown in Figure 7.5. The elbow angles during the FES isometric experiments derived from 3D motion capture was 141° for subject P1 and 144° for subject P3.

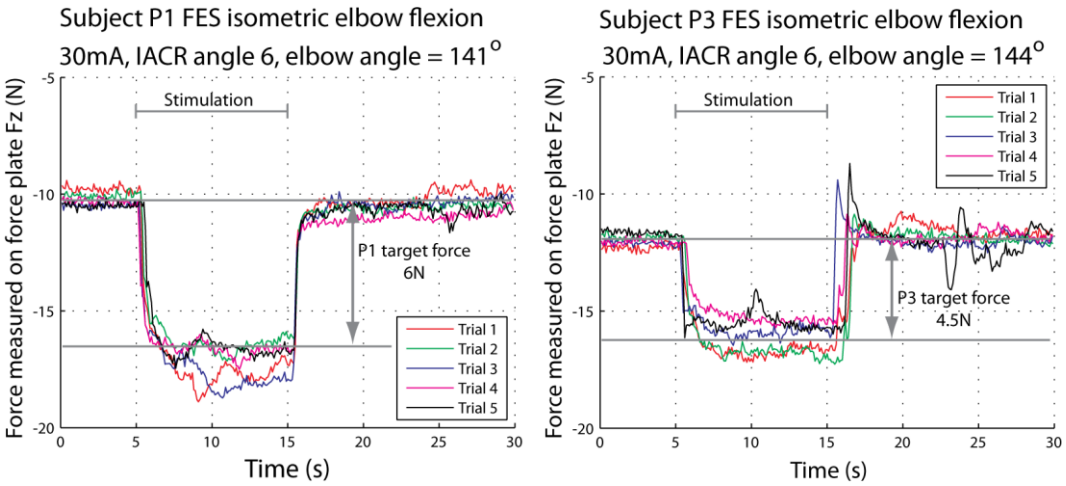

Figure 7.5. Five repeated measurement of isometric elbow flexion by FES. Stimulation was applied between 5s and 15s from the start of each measurement trial. The target force achieved by subject P1 was 7N and the target force achieved by P3 was 4.5N. Both subjects used 30mA stimulation current pulses (25 pulses per second, 0.3ms pulse width).

The reference force (with no stimulation applied) was determined by averaging the measured force in the time history between the start of each measurement to 5s after the start of each measurement trial. The exerted force under stimulation was estimated by averaging the measured force (at the force plate) in the time history of each trial (Figure 7.5) between 7s and 14s from the start of each measurement, from which the reference force was subtracted.

The averaged flexion force achieved by subject P1 with 30mA of stimulation was -8.03±0.453N (measured at the force plate). The averaged flexion force achieved by subject P3 with 30mA of stimulation was -4.49±0.216N (measured at the force plate). The force errors were 1 standard deviation of the measured force from 7s to 14s of the five repeated measurement trials.

Using the equations to derive the force exerted by the biceps muscle's CE as described in section 6.3.2, the measured forces from 30mA stimulus can be used to compute the force exerted from the wrist to the IACR handle and the force exerted by the biceps muscle CE. These values are shown in Table 7.4.

Table 7.4. Force exerted at wrist and biceps muscle CE force in the isometric FES elbow flexion experiment

Parameters	Subject P1	Subject P3
Elbow angle	141°	144°
Measured FES isometric flexion force: $F_{measured}$	-8.03N	-4.49N
Force exerted at the wrist F_{load} using Eqn 6.8	-16.4N	-8.08N
Biceps muscle CE force $F_{1\,(\text{CE only})}$ using Eqn 6.10	(-)102N	(-)62.5N

7.3.3 FES elbow flexion movement experiment

Figure 7.4 shows images from the video footage of the FES flexion movement experiment when the stimulator was off and on. The 5 trials of measured elbow angle trajectories for subject P1 and P3 are shown in Figure 7.6 and Figure 7.7 respectively.

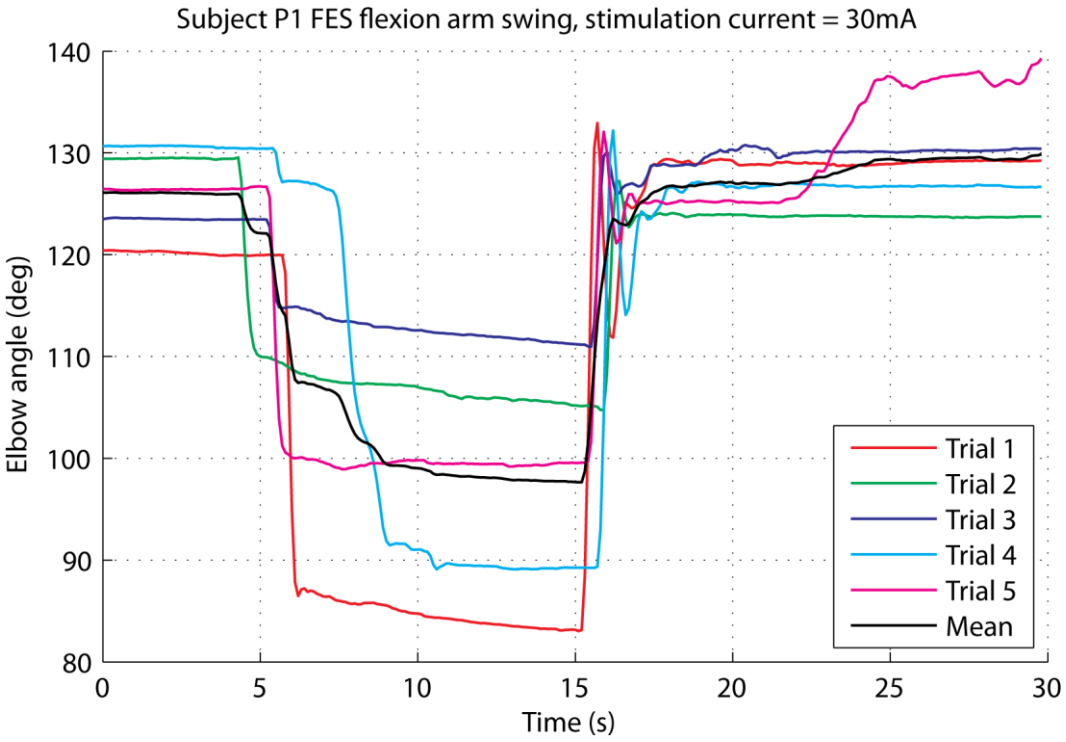

Figure 7.6. Elbow angle trajectory in the FES flexion arm swing experiment for subject P1. Current stimulation applied between 5s and 15s from the start of each measurement trial.

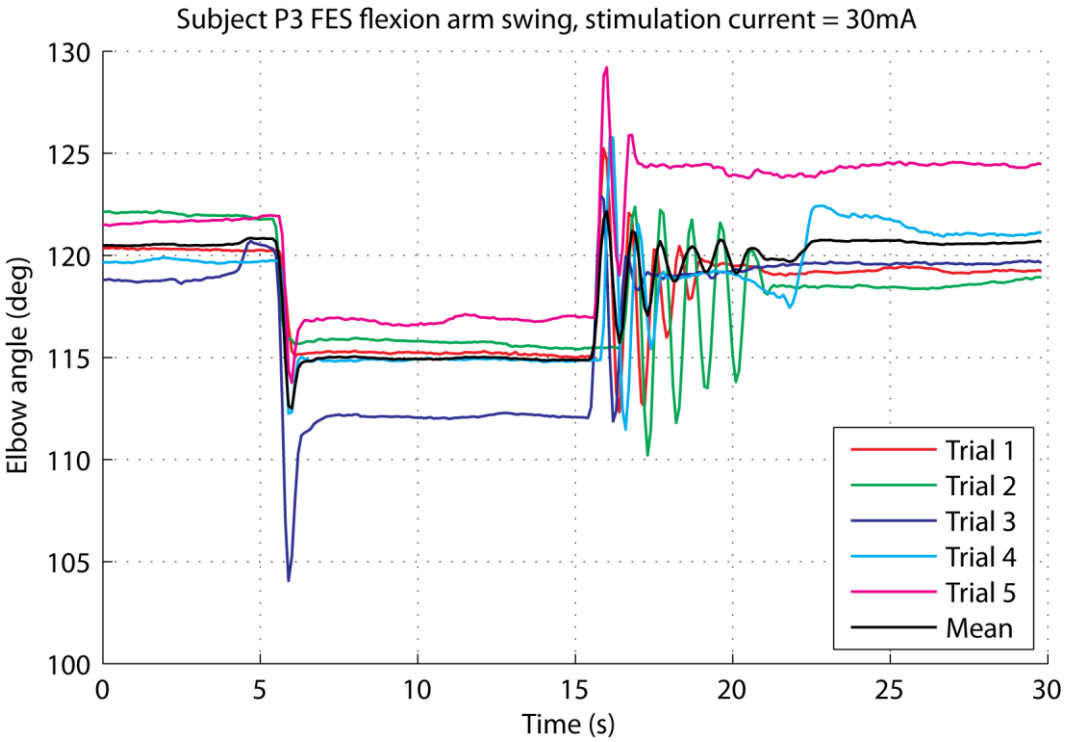

Figure 7.7. Elbow angle trajectory in the FES flexion arm swing experiment for subject P3. Current stimulation applied between 5s and 15s from the start of each measurement trial.

The overall average starting angle between the five repeated trials was the average elbow angle between the start and 4s from the start of each experiment for all measurement trials. As it can be seen in Figure 7.7 that for subject P1, the mean elbow angle trajectory when the stimulation was applied did not become stable until at about 11s from the start of the trials, therefore for subject P1 the overall average elbow angle during current stimulation was the averaged elbow angle between 11s and 15s from the start of the measurement. For subject P3, the overall averaged elbow angle during stimulation was averaged between 7s and 15s from the start of the measurement when the mean elbow angle reached a stable angle. These derived angles are listed in Table 7.5.

Table 7.5. Averaged starting angles and elbow angles under FES in the FES flexion arm swing experiment.

	Subject P1	Subject P3
Overall averaged starting angle	126°±3.83°	120°±1.21°
Overall averaged angle under stimulation	97.9°±10.9°	115°±1.57°
FES induced elbow flexion angle	28.1°	5.00°

7.3.4 Simulated FES elbow flexion movement

The overall averaged starting angles presented in Table 7.5 were used as the starting elbow angles of the forward simulations. The mean upper arm angles from vertical for the 5 measurement trials were obtained from 3D motion capture and were 54° for subject P1 and 60° for subject P3. To correct the upper arm orientation in the equation to describe the dynamics of the arm, Eqn 5.3 was modified to give Eqn 7.1 for subject P1 and Eqn 7.2 for subject P3:

$$\ddot{\theta}_{P1}(t) \equiv \frac{d\dot{\theta}(t)}{dt}$$
$$= \left(\tau_{lim1}(t) + \tau_{lim2}(t) + F_1(t)\frac{d_{11}d_{12}\sin\theta(t)}{l_1(t)} - F_2(t)d_{21} \right. \quad \text{(Eqn 7.1)}$$
$$\left. + m_{arm}d_{arm}g\sin\left(\theta(t)+54°\right) + m_{load}d_{load}g\sin\left(\theta(t)+54°\right) - b_{arm}\dot{\theta}(t) \right) / J$$

$$\ddot{\theta}_{P3}(t) \equiv \frac{d\dot{\theta}(t)}{dt}$$
$$= \left(\tau_{lim1}(t) + \tau_{lim2}(t) + F_1(t)\frac{d_{11}d_{12}\sin\theta(t)}{l_1(t)} - F_2(t)d_{21} \right. \quad \text{(Eqn 7.2)}$$
$$\left. + m_{arm}d_{arm}g\sin\left(\theta(t)+60°\right) + m_{load}d_{load}g\sin\left(\theta(t)+60°\right) - b_{arm}\dot{\theta}(t) \right) / J$$

where the 54° for subject P1 in Eqn 7.1 and 60° for subject P3 in Eqn 7.2 replaced 45° in Eqn 5.3 in the terms to calculate the moment from gravity.

Figure 7.8 shows the simulated and measured FES elbow trajectories for subject P1. The expected simulated movement (solid black line) was generated with the biceps muscle contractile force $F_{CE1} = -102N$, which was the expected isometric force derived from the measurement of the isometric FES flexion experiment, presented in Table 7.4.

The fitted forward simulation (dashed black line) that gave a steady elbow angle under FES of 97.9° (measured at 8s), the biceps muscle contractile force, F_{CE1}, was $-102 \times .066 = -6.732N$, nearly a twentieth of the expected force generated.

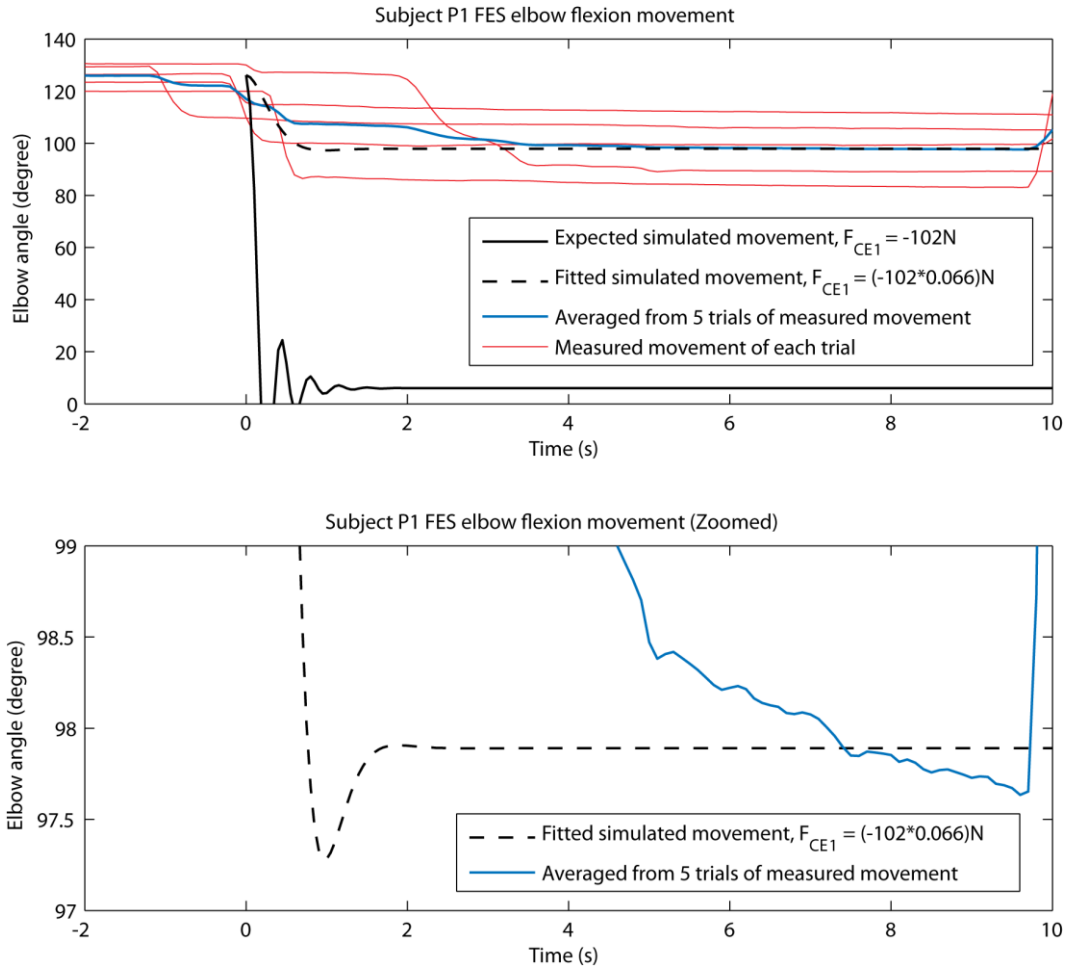

Figure 7.8. Measured and simulated elbow angle trajectory under FES for subject P1. Top graph shows full elbow angle range and bottom graph showed zoomed in y axis to show the fitted simulation and averaged measured results. Subject was instructed to apply the simulation at time 0s shown in the graphs. The simulated elbow angle trajectories started at time zero from the starting angle of 126°. The stable elbow angle for the expected simulated movement was 7.15° (at 8s) and the stable elbow angle for the fitted simulated movement was 97.9° (at 8s).

Figure 7.9 shows the simulated and measured FES elbow trajectories for subject P3. The expected simulated movement (solid black line) was generated with the biceps muscle contractile force $F_{CE1} = -62.5N$, which was the expected isometric force derived from the measurement of the isometric FES flexion experiment, presented in Table 7.4.

The fitted forward simulation (dashed black line) that gave an steady elbow angle under FES of 115° (measured at 8s), the biceps muscle contractile force, F_{CE1}, was $-62.5 \times 0.12 = -7.5N$, about one tenth of the expected force generated.

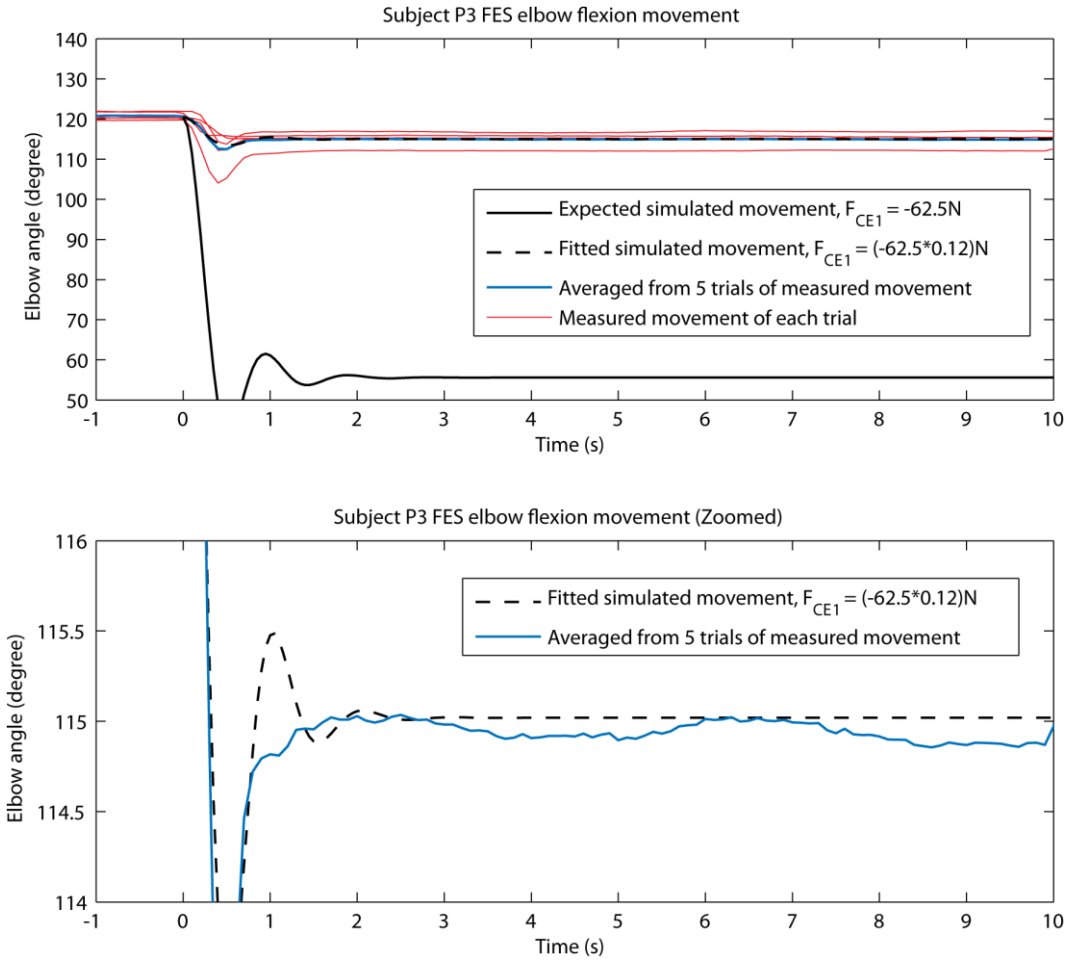

Figure 7.9. Measured and simulated elbow angle trajectory under FES for subject P3. Top graph shows full elbow angle range and bottom graph showed zoomed in y axis to show the fitted simulation and averaged measured results. Subject was instructed to apply the simulation at time 0s shown in the graphs. The simulated elbow angle trajectories started at time zero from the starting angle of 126°. The stable elbow angle for the expected simulated movement was 7.15° at 8s and the stable elbow angle for the fitted simulated movement was 97.9°.

7.4 Discussion

A characteristic of the force generated by the contractile element that had not been included in the model described in this thesis is the onset of the contraction force over time at the whole muscle level. Buchthal and Schmalbruch (Buchthal and Schmalbruch, 1970) described that the speeds of the on-set of contraction are different in different muscles in the body. Furthermore, if the use of this muscle model is in maintaining postures, such controlled movements would only include small perturbations. Therefore the analysis in this chapter focused on the static force and the change in joint angle generated by FES.

*It should be noted that the two experiments described in this chapter share similar name, and can be easily confused. Please pay specific attention to the headings where they specify: the **isometric** FES experiment, or the FES **movement** experiment. Also pay specific attention to the source references (tables and figures) of the numerical results that are discussed.*

7.4.1 Isometric FES elbow flexion experiment

The electrical currents that were identified to generate the target force of 6N for subject P1 and 4.5N for subject P3 were both at 30mA. Although this may suggest that this FES configuration (electrode positions, etc) generated about 10 to 15% of the MVC force from 30mA of stimulus, in this work, only two subjects participated in this experiment.

The electrode positions were unchanged between measurement trials, and the 1 standard deviation error of the measured force between 7s and 14s from the beginning of the measurements for the five trials (Figure 7.5) were 0.453N and 0.216N, which was 5% of the averaged measured force. This suggested the use of fixed arm position and electrode positions gave good reproducibility in the measured isometric force generated by FES, and allowed good estimates of the force to be obtained.

This experiment used a contraction force that was much less than the maximum achievable under MVC, this approach of using small target force eliminated the problem of decrease in contractile force that is associated with muscle fatigue. The resulting measured elbow moments (proportional to the forces measured at the force plate) were reasonably constant between 7s and 14s from the beginning of the trials, and showed no evidence of a decrease in force that could have resulted from muscle fatigue during the period of stimulation or between trials.

The step response of the increase in contraction force when stimulation was applied at 5s after the beginning of the measurement trials had a force/time characteristic similar to a critically damped 2^{nd} order system. This is in agreement with the characteristics of muscle fibre recruitment (hence tension) over time reported in the literature (Buchthal and Schmalbruch, 1970, Winter, 2005), and also reported results of the in vivo measurement of knee movement under FES (Hausdorff and Durfee, 1991).

The actual measured elbow angles of the arm when using the IACR (measured using 3D motion capture) were 141° (P1) and 144° (P3), these were about 10° higher than the predicted 135° and were also different to those in the isometric flexion MVC experiments described in Chapter 6, which were 121° for subject P1 (Table 6.3) and 131° for subject P3 (Table 6.5). From the inspection of the 3D motion capture data, it was found that during the MVC measurements, maximum voluntary flexion caused the shoulder to shift forward slightly, which decreased the expected elbow angle during the MVC experiments. Furthermore, during flexion MVC, the subjects' wrists were supinated. But in the FES isometric flexion, the wrists were in the neutral position, this meant the centre of the wrist joint was closer to the handle in the MVC experiment than the isometric FES experiment, and therefore the elbow angles in the FES experiment were slightly greater.

7.4.2 FES elbow flexion movement experiment

The flexion movement experiments were conducted immediately after the isometric FES experiments. The measured elbow flexion movements of the five repeated trials for subject P1 showed poor reproducibility in the steady elbow angles and also the response times when the stimulation was applied (Figure 7.8); while for subject P3, the result showed good reproducibility between the five repeated trials (Figure 7.9). It can also be seen that the starting elbow angles for subject P3 were much more consistent in comparison to the results of subject P1.

For subject P1, the starting elbow angle and arm position were measured using a spirit level and large protractor before each measurement, while for subject P3, position measurements of the upper arm were not made between repeated trials, and the decision was to quickly repeat the five trials, where subject P3 maintained the body and upper arm position throughout. This change was made as the slouched standing position was tiring and subject P3 requested to repeat the trials quickly. The original method of measuring elbow angle before each trial aimed to provide a more accurate starting elbow angle, however the result shows this method produced worst results in comparison to allowing the subject to maintain body position.

The reason for the inconsistencies in the FES generated change in elbow angle was believed to be caused by the position of the strap interfering with the position of the cathode electrode. Some form of support to the arm was required, and using the strap was the method in which there were minimal restriction to arm movement, as discussed previously in the passive movement experiment (section 5.3.4). However in this experiment the strap also overlapped the cathode electrode. For subject P1 the re-measurement of elbow angle and arm position between trials also included small changes in the position of the straps, and therefore changing the amount of movement the strap had on the cathode electrode, and this had caused changes in the position of the electrode,

electrode spacing, relative position to the muscle fibre, internal current path and thus the force generated. This had showed that the use of the strap had a major effect on force generated, and that consistent electrode position is critical to obtaining reproducible results.

Another unexpected characteristic in the change in elbow angle can be seen in the results of subject P1, trial 4 (Figure 7.6). It can be seen that the stimulation was in two “steps”, between 6s to 7.5s, the FES generated movement was small (about 3°) and a second large increase in flexion was seen at 7.5s. An inspection of the 3D motion data showed that at the first instant that current was produced, it caused the wrist and hand to supinate, and so the position of the geometry of the biceps brachii was changed in relation to the cathode electrode. The second larger increase of change in elbow angle was believed to be the contraction of the biceps brachii, where previously the distal end of the bulk of the biceps brachii separated the cathode and the brachialis, for the contracted biceps brachii, only the free tendon of the biceps brachii separated the cathode and the brachialis. This decreased the distance between the cathode and the brachialis, and the recruitment of the fibres in the brachialis caused the second observed movement of a larger elbow flexion.

These unexpected inconstancies in the results highlighted and confirmed the problems associated with surface FES, in that it is difficult to stimulate individual muscles to produce specific movement, in this case the stimulation of the biceps brachii caused an unwanted wrist supination movement. It also highlights that even though a careful method of fixing the electrodes to the skin was employed, small changes in external factors, in this case the strap, would affect the generated movement. Predictive models for such movement generated under surface FES are unlikely to be robust. Additionally, the movement in the muscle itself caused changes in body tissue/ current path geometry, and the stimulation patterns were different at different stages in the movement.

7.4.3 Simulated FES elbow flexion movement

The electrical current used in both the isometric FES experiment and FES movement experiment were identical, and in this thesis the force generated by the flexor muscle was assumed to be the same. Therefore if the force measured from the isometric experiment was applied as the biceps muscle CE force in the simulated FES movements, the simulated change in elbow angle was expected to be the same as the measured change in the elbow angle of the FES movement experiment.

The expected simulated movements for both subjects P1 and P3 (shown in Figure 7.8 and Figure 7.9) that incorporated biceps muscle CE forces calculated from the isometric FES contraction experiment (shown in Table 7.4) did not produce steady levels of elbow flexion that agreed with the measured elbow flexion.

For subject P1, the expected elbow angle under FES was 7.15°. However from earlier measurements of passive movement (Chapter 5, experiment 1) and the design process of the MVC experiment described in Chapter 6, the minimum achievable elbow angle was about 35°. This meant that if the elbow flexor muscle generated 102N for subject P1, the elbow would flex and reach maximum flexion. Further experiments would be required to model the movement dynamics of the joint when it is fully flexed.

In the fitted simulation results, for the change in simulated elbow angles under FES to be the same as the averaged measured elbow angle under FES (Table 7.5), the biceps muscle CE forces were about a twentieth of the expected force for P1 and about one tenth of the expected force for subject P3. These forces were much less than the expected values. A major cause for this was likely to be the method of using the strap to hold the upper arm. Firstly as already described in section 7.4.2, the strap had to have some overlap onto the cathode electrode, due to the width of the strap. An inspection of the setup showed that the strap also pushed the cathode electrode towards the anode electrode, as the skin was stretched. This reduced the inter-electrode distance and was believed to have

shortened the current path in the muscle, reduced the number of fibres recruited and hence reduced the total contraction force of the muscle. Separately, while attempting to reduce the amount of overlay where the strap was in contact with the cathode electrode, the strap was placed as low as possible, however this was too close to the elbow, and the strap may have added extra resistance to movement of the elbow in the flexion direction. Therefore the unexpectedly small change in elbow angle was believed to be a combination of change in electrode/tissue/current path geometry and additional resistance force from the support (strap).

A factor that was not quantitatively recorded was subject feedback. Subjects reported the sensation of muscle contraction from stimulation was less intense in the FES movement experiment in comparison to the isometric experiment. This supported the claim that there was a decrease in force generated by the muscle from the same stimulus when the arm was placed in the strap.

In Hausdorff and Durfee's FES study (Hausdorff and Durfee, 1991), knee torque and flexion/extension movement generated by stimulating the quadriceps femoris were measured. The subjects were seated with the back of the upper leg supported. This method of support was not changed between the isometric torque experiment and free movement experiment. Hausdorff and Durfee reported there was good agreement in the flexion force generated by the quadriceps femoris between the isometric FES experiment and FES movement experiment. This suggested further attention can be paid in the design of the arm support to minimise differences between the two FES experiments in the elbow flexion force generated by FES.

Another key factor in the accuracy of the simulated elbow angle was the accuracy of the (re-)measured values of the mass of the forearm and hand, an analysis of the equations that determined the dynamics of the joint, Eqn 7.1 and Eqn 7.2, showed that the steady angle was an equilibrium where the flexion moment balances the moment of gravity acting on the weight of the forearm,

therefore a difference in the weight also affects the equilibrium elbow angle. Other factors in the model that affect this equilibrium included the passive spring constants. To fully understand the effect of changes in parameter values have on the simulated elbow angle, a formal sensitivity analysis should be performed to assess these effects.

Analysis of the system equations, Eqn 7.1 and Eqn 7.2 also showed that the recalculated moment of inertia does not play a part in determining the equilibrium elbow angle under FES, as the moment of inertia was a multiplier of the angular acceleration. During equilibrium, the elbow angle is static and the angular acceleration is zero, this eliminated the effect from the value of the moment of inertia.

7.5 Conclusion

Whilst measurements of small perturbations were attractive from a modelling and measurement perspective, as this approach can minimise or eliminate unknown characteristics such as change in force from changes in tissue/current geometries, one of the problems in modelling FES, is determining the relationship between the injected current and the force generated by the muscle. Small changes in the arm support introduced large changes in the force generated by FES, and the results in this chapter have shown that the approach used in this work is unlikely to produce robust FES stimulation, and the model cannot correctly predict the force generated when a change in body support was introduced.

While the absolute force predicted to be generated by the muscle in the FES movement experiment was incorrect and the simulated static change in elbow angle did not agree with the measured change in elbow angle. In the simulations where the contraction forces were fitted, the shape of the dynamic response of the simulated movement generated from FES showed good agreement with the measured movement generated by FES.

7.6 Recommended improvements

A key problem in this FES experiment was the unexpected change in the contractile force generated by the same stimulus, which appeared to be caused by the strap supporting the arm around the flexor muscle in the FES movement experiment. The work described in this thesis only observed the flexion movement, however observing extension movement by stimulating the triceps brachii, where the arm positions remains the same as the protocol described in this thesis, may produce more consistent results. For such movement, the triceps brachii was not in contact with the strap in the FES movement experiment, and the force generated by FES between an isometric contraction and a free movement experiment may be more consistent.

Chapter 8 Summary of Discussions, Conclusions and Recommendations for Further Work

The main aim of the work described in this thesis was to develop predictive models of the musculo-skeletal system. Such models can be used to examine the effect of changes in the dynamics of individual components in the anatomy and physiology on the whole system dynamics, and allow a better understanding of disease progression. Predictive models can also be used to support the development of computational/mathematical model based control strategies for prostheses or orthoses used as part of movement rehabilitation, e.g. in functional electrical stimulation (FES).

Muscle diseases differ between patients, and there may be differences in the dynamics of components within the musculo-skeletal system (Shields and Dudley-Javoroski, 2003). For the development of patient specific rehabilitation strategies that adopt musculo-skeletal models to predict movements and forces, the parameter values in the models must be specific to the individual patients to enable accurate predictions of the dynamics. Therefore, part of the development of the models described in this thesis was to identify the methods required to fully parameterise the models from in vivo measurements on an individual subject basis.

8.1 Musculo-skeletal model of the human arm

The musculo-skeletal models (section 4.3) developed in this work were anatomically meaningful, and focused on describing the anatomy and physiology of body components as realistically as possible, while ensuring that parameter values not directly measurable, were uniquely identifiable through parameter estimation experiments.

Part of the development of the musculo-skeletal models had been to validate the approach of using the Newton-Euler method to describe the dynamics of body segment movement. In this, the body segments are modelled as multiple linked rigid bodies (section 4.1). Within the work presented in this thesis, the Newton-Euler modelling approach was evaluated to determine whether it could produce realistic predictions of movement dynamics. The movement dynamics of physical pendulums developed in this work were measured. Using physical pendulums rather than using human movements to validate pendulum dynamics allowed freedom in the specification of materials, and the physical properties of the segments of the pendulum could be predefined. Metals (mainly aluminium) were selected as they had high stiffness and uniform density distribution. The mass of the segment can be directly measured whereas body segment mass in the human body has to be derived from measurement and calculations (section 5.2.2). Overall the geometric design of the physical pendulum provided more accurate physical properties for modelling in comparison to body segment movements (of organic shapes and nonhomogeneous density). The results showed that the model of a single pendulum derived from the Newton-Euler equations gave accurate prediction of movement in comparison to measured movement dynamics. The measured results of the two segments pendulum were reproducible. However the simulated movement of the two segments pendulum model did not agree with the measured movement. From this, the modelling of the musculo-skeletal system described in this thesis was limited to the analysis of a single joint. One of the differences was in the oscillation frequencies between the simulated results and the measured results, where the frequencies in the simulated results were much higher than the frequencies in the measured results.

The muscles in the body were modelled using a modified form of Hill muscle model over the classical Hill muscle model. Analysis of the derivations of the two variations of Hill muscle model showed that the classical Hill muscle model included the time differential of the force of the muscle, and this was difficult to

be incorporated into musculo-skeletal models as sub-models. The modified Hill muscle model only included parallel components and total muscle force was the sum of the force by the passive muscle spring, passive muscle damper and the parallel active component: the contractile element (CE). Muscles are connected to the bones by tendons, in this thesis, and these were defined as free tendons and assumed to have fixed lengths.

The musculo-skeletal model of the human arm was developed to give a detailed analysis of the motion of the elbow joint. The model has two rigid segments: the upper arm and the forearm, connected by the elbow joint. The hand is also included but is included in the forearm segment, and the wrist joint is assumed to be rigid. Two instances of the modified Hill muscle models (section 4.3.2), representing the elbow flexor muscle and the elbow extensor muscle (and their free tendons) were incorporated, into the geometry of the arm, where the points of origin and insertion were included in the model. The model also incorporated soft tissue around the joint, modelled as a rotational damping component that acts at all angles, as well as limits of full elbow flexion and extension.

As the internal components in the muscle models are not directly measureable, a model fitting and parameter estimation technique was necessary. To ensure that unique values could be obtained through parameter estimation experiments, a structural identifiability analysis was performed on the classical Hill muscle model and the modified Hill muscle model in scenarios of excised muscles. The analysis showed that all the internal passive parameters, are uniquely identifiable, and unique solutions of those values can be obtained through parameter estimation experiments (at least theoretically).

8.2 Parameterising the passive components of the arm model using passive movement measurement in vivo

Recent studies (Venture et al., 2005, Mohammed et al., 2012) that have attempted to obtain numerical values for the musculo-skeletal models through in vivo experiments, have not been able to obtain numerical values for the passive

components in the muscle models and joint models. In order to be able to fully parameterise subject specific predictive models, methods to obtain the numerical values for the passive model components through in vivo experiments were needed, and this forms one of the main advances reported in this thesis.

Traditionally measurements of maximum voluntary contraction were used to characterise the active components of Hill muscle models (the contractile element), including the force/length characteristics (Gordon et al., 1966), e.g. (Hatze, 1981, Durfee and Palmer, 1994, Leedham and Dowling, 1995) and the force/velocity characteristics, e.g. (Hof and Van den Berg, 1981a, Durfee and Palmer, 1994). However the work described in this thesis identified two reasons why the MVC approach was not suitable for parameterising the passive components in the models. Firstly, voluntary contraction includes the sum of both the dynamics of the passive components and active components; at the beginning of the parameterisation process, neither the passive dynamics nor the active dynamics are known and therefore the other cannot be identified. Secondly, if predictive models are to be parameterised through in vivo experiments for individual patients who have lost control of their muscles (e.g. after SCI), then voluntary contraction is not possible. In this thesis an experimental approach was developed to determine the numerical values for the passive components in the model, using measurements of passive movement where the muscles around the joint were completely relaxed.

In the passive movement experiments, 3D motion capture (Vicon motion capture suite) was used to obtain kinematic data. Separate passive movements of elbow flexion and extension were measured, where the position of the upper arm was fixed and the forearm and hand swung freely under gravity. Different upper arm positions were used to allow a larger elbow angle range for the arm swing movement before reaching maximum elbow flexion or extension. Movements with separate loads in the hand were measured, where either no load was added to the hand, or a 1kg or 2kg weight was added to the hand. Good reproducibility

was seen in repeated measurements, and similar dynamics trajectory characteristics were seen between the four healthy subjects. Length parameters such as free tendon lengths were directly measured using palpation and surface measurements. Forearm, hand weight and moment of inertia were calculated from weight measurements. Arm model movement was simulated using forward simulation and the model dynamics were fitted to the measured dynamics by minimising error in the elbow angle. There was good agreement in the arm swing movement between the fitted simulation result and the measured results. However the model was not adequate to describe or produce realistic dynamics of the "rebound" when maximum elbow angle was reached. The process of model fitting successfully gave numerical values of the passive components for the flexor and extensor muscle models and also around the joint. An analysis of the error surfaces against varying passive component values showed that the numerical values obtained were unique.

8.3 Obtaining the force/length characteristics of the active component of the muscle models in vivo

One of the stimuli for this work was to predict movement in FES, and the work described in this thesis included a preliminary experiment to predict the elbow flexion movement generated by FES. Prior to performing the FES experiment, the target force to be generated by FES had to be identified. To do so, measurements of the maximum voluntary contraction (MVC) were performed to identify the maximum force capacity for specifying target forces generated by FES. In addition, to support the design of the FES experiment, the MVC measurements were also used to obtain the force/length characteristics of the flexor and extensor muscle. The results obtained using the musculo-skeletal model developed in this work can then be compared with the results reported in the literature.

A special rig, the IACR, was developed in this work to measure the isometric elbow flexion and extension force at 7 (or 6 depending on maximum elbow angle

of subject) elbow angles distributed over the whole elbow angle range. Joint moment generated from elbow flexion or extension MVC at different angles were measured for five healthy subjects, three of which performed the passive experiments. Reference forces were measured when the arm was supported with the IACR so that the mechanical characteristics of the IACR and the passive components in the muscles and joint could be eliminated from the measurements under MVC. This method also allowed the force/length characteristics to be determined exclusively from the dynamics of the passive components, therefore the passive components for the two new subjects were not required to determine the force/length characteristics of the active component: the contractile element (CE).

The measured results showed good reproducibility in repeated measurements. The approach of using multiple 10 seconds periods of contraction separated by resting periods, and averaging the MVC forces allowed a good estimate of the MVC force to be obtained. Short periods of contraction minimised muscle fatigue and there was no evidence of decreasing contraction force over repeated measurements. Similar joint moment over elbow angle characteristics were seen in the measured data between the subjects, and also showed good agreement with results of arm muscles reported in the literature (Hatze, 1981, Leedham and Dowling, 1995).

The muscle's force/length characteristics were determined using the geometry of the musculo-skeletal model. Similar force/length characteristics were seen between the subject, but there was a higher than expected variation in the biceps muscle length derived from the model. A suggested further investigation should be made in the method to measure the internal lengths. Alternative methods to palpation and surface measurement may give improvements.

8.4 Predicting movement generated by FES

The final experiment was a preliminary investigation to predict elbow flexion movement generated by FES. Two healthy subjects who participated in both of the passive and MVC experiments participated in the FES experiment. Surface FES was used and carbon rubber electrode pads were used to provide the electrical stimulus. The electrodes were attached to the bulk of the biceps muscle to stimulate the elbow flexor muscles in the upper arm.

The first part of the experiment was to identify the electrical stimulus required to generate an isometric elbow flexion joint moment at an elbow angle of about 135° equal to 10% of the MVC elbow flexion measured in the previous experiment. The experiment was performed using the IACR to measure the flexion moment generated. The target force measured at the force plate of the Gait Laboratory was 6N for subject P1 and 4.5N for subject P3. From the isometric FES experiment, the identified stimulus for both subjects was 30mA, 25 pulses per second, 0.3ms per pulse.

The second part of the experiment places the arm where the forearm hung downward from gravity and the upper arm was placed so the elbow angle was similar to the isometric MVC experiment (135°). The electrode positions remained unchanged between the isometric FES experiment and the FES movement experiment. The same electrical stimulus was applied in the FES movement experiment, and the change in elbow angle from flexion generated by FES was recorded.

The force generated in the isometric FES experiment was assumed to be reproduced in the FES movement experiment, as the position of the electrodes remained unchanged and the elbow angles were similar between the two experimental setups.

Simulated elbow flexion movements of the FES movement experiment were generated using the arm model and the passive component values obtained in

the passive movement experiments. The measured biceps muscle force generated by FES in the isometric FES experiment was incorporated into the arm model and simulation as the contractile force of the biceps muscle. The simulated change in elbow angle from the flexion movement did not agree with the measured flexion movement in the FES movement experiment. The main reason for this disagreement was that the force generated by the electrical stimulus in the FES movement experiment was smaller than expected, as the strap support in the FES movement experiment introduced small changes in the electrode/tissue/current path geometry, causing a change in the force generated. Subjects reported the sensation of stimulation was less intense when the strap was used in the FES movement experiment. Furthermore the strap was too close to the pit of the elbow, which added resistance to flexion movement. A separate set of fitted simulated flexion movement was generated where the change in elbow angle agreed with measured movement. The fitted biceps muscle force required to generate such movement in the simulation was about 10% of the force measured in the isometric FES experiment. The dynamics trajectory after the moment when the biceps muscle was stimulated showed good agreement between the measured dynamics and the fitted simulated dynamics. This showed that even minimal changes in the electrode/tissue geometry, caused large changes in the force generated. This suggests that using the FES method described in this thesis is unlikely to give reproducible and robust results. However with the arm model and specifically the numerical values of the model parameters, the dynamic characteristics of the joint can be predicted.

8.5 Force/velocity characteristics

The force/velocity (F/V) characteristics of the Hill muscle model had not been characterised in the work described in this thesis. Measurements of isokinetic movements are often used to obtain the F/V characteristics in vivo, which required specific equipment, known as dynamometers. A dynamometer simultaneously allows a joint to move at a fixed velocity while measuring the

joint torque. Human joint angle ranges are limited, and in Hof's studies (Hof and Van den Berg, 1981a, Hof and Van den Berg, 1981b, Hof and Van den Berg, 1981c, Hof and Van den Berg, 1981d), the time of movements are short and the high speed of movement provides only small amount of data for analysis, and this had been a challenge to estimate the force/velocity characteristics from short periods of movements.

The approach taken in experimental design in this work was to separate the dynamics of the active and passive dynamics in the experiments: the passive movements had no active component dynamics, and the isometric MVC experiments use measurements of reference forces to eliminate the dynamics of the passive components. In measuring the force/velocity characteristics, it is difficult to design an experiment where the active dynamics can be exclusively separated from the passive components dynamics. Further work can be done to design such an experiment.

Currently most non foot-drop FES controllers are being developed to maintain a certain posture, such as unsupported standing where the position of joints are maintained, then the movement speeds are minimal and therefore the force/velocity characteristics have minimal effect. However for dynamic controls, such as walking or moving from sitting to standing, then such characteristics in the model would be required to predict movements.

8.6 Recommended future work

8.6.1 Multi-segment modelling

An interesting finding from this work is that modelling multi-segment dynamics using the widely accepted Newton-Euler method cannot product realistic predictions of multi-segment movement, as demonstrated in the measured and simulated results of the two segments pendulum segment in section 4.1. Other researchers had encountered a similar problem (John et al., 2012).

However there are examples (Thelen et al., 2003, John et al., 2012) where forces determined from inverse dynamics analysis can accurately predict movement by forward simulation using the Newton-Euler equations. A possible explanation for this is that systematic errors introduced in the inverse dynamics process, are eliminated in the forward simulation, as the forward technique is an inverse function of the inverse dynamic technique. Performing a forward simulation after an inverse dynamics analysis may cancel the systematic errors caused by using the current free body movement techniques.

Some studies (Davoodi and Andrews, 1999, Esfanjani and Towhidkhah, 2005) had used predictive models to develop FES control strategies, where genetic algorithms (GA) were used to optimise PID or fuzzy logic control strategies. Further GA optimisation would be required empirically. In those cases, errors in the Newton-Euler method can be compensated by the controller during in vivo GA optimisation, and therefore the problem identified in this thesis may not have been observed. However the sources of the error from the multi-segment modelling or inaccuracy in model parameter values cannot be uniquely separated and investigated.

Outside the field of biomechanics, the other main application of the Newton-Euler method is in robotics (Niku, 2001), e.g. (Boston Dynamcis, 2013), but often positional and velocity based close-loop feedback control are employed and subsequently work had not focused on correcting errors in the forward dynamics (open-loop). Evidently if one wishes to successfully predict the dynamics of a multi-joint or a full body musculo-skeletal model in an open-loop scenario, such as movement of free fall or a step response to a muscle stimulus, further investigation into the Newton-Euler method is required. In particular, the areas for improvement identified by the work described in thesis include the approximation of the moment of inertias, and the correct method for incorporating linear acceleration in the computation loops. Such investigation can be performed using the equipment involved in the validation of the Newton-

Euler method in this work, where the detailed dynamics of physical multi-segment pendulums with known physical properties can be observed using the 3D motion capture. Such measured results can be compared with theoretical dynamics.

The inability to generate accurate predictions of multi-segment movement had limited the analysis of musculo-skeletal movement to an individual joint level. But to be able to predict movement of more than a single joint is important in musculo-skeletal modelling, such as full body modelling for the control of gait, clearly further investigation must be carried out on the theoretic description of multi-segment dynamics.

8.7 Muscle and tendon length measurement

Medical imaging techniques such as computed tomography X-ray imaging, magnetic resonance imaging (MRI) and ultrasound imaging can be used to improve the accuracy of the measured internal body component length, i.e. the muscle and free tendon lengths in the models, over the method of surface measurement and palpation used in this thesis. Figure 8.1 and Figure 8.2 show an example of using ultrasound imaging to locate the end of the biceps brachii muscle and the beginning of the free tendon defined in the model. The boundaries between muscle tissues and tendon tissues can be used to determine the internal component lengths. These imaging techniques may be an improvement over palpation and surface measurement if the subject has large amounts of subcutaneous fat and/or low muscle volume where the muscle tone is not well defined.

Figure 8.1. Using ultrasound imaging to locate muscle/tendon boundaries. Ultrasound transducer placed in line with the biceps brachii muscle and tendon.

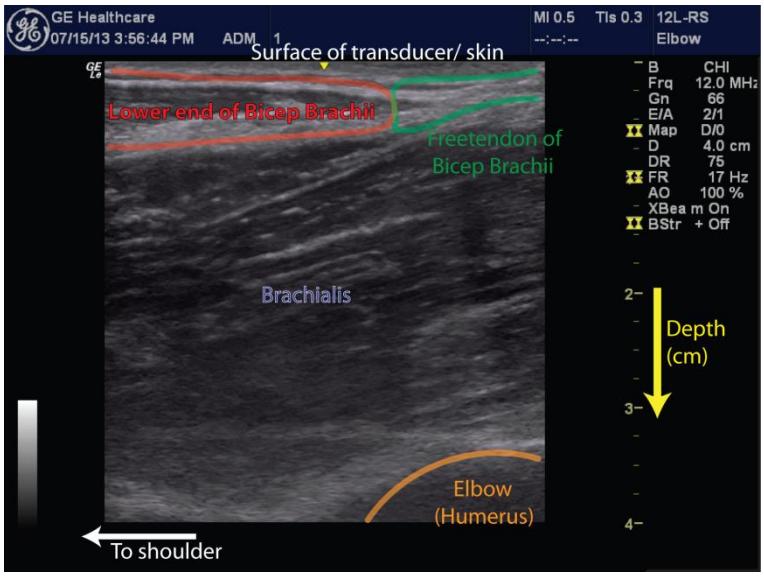

Figure 8.2. An ultrasound image of the elbow flexor muscles. The transducer is placed at the location shown in Figure 8.1. The yellow arrow at the top of the ultrasound image is at the location of the arrow marked on the transducer in Figure 8.1. The biceps brachii muscle and tendon are shown at the top just below the skin. The brachialis is below the biceps brachii and above the humerus.

8.7.1 Modelling the joint dynamics at maximum and minimum joint angles

Results of the passive movement showed that the model cannot predict the dynamic movement when maximum elbow joint extension was reached. Further work can be done to improve the description of dynamics near maximum joint extension or flexion. With the passive components of the muscle models already obtained, future model fitting experiments can be performed to exclusively estimate the parameters that determine the dynamics at maximum elbow extension.

8.7.2 Sensitivity analysis of passive components in the musculo-skeletal models

A recent study (Liao et al., 2013) had used a musculo-skeletal model to predict movement generated by implanted FES, but have used zero values for the passive components. The predicted movement was not in agreement with measured movements during in vivo experiments. But the work in this study has identified that these passive components are important for generating accurate prediction of movement. As a demonstration, simulated elbow trajectories of the passive movement for subject P1, where the passive components are all zero, are shown in Figure 8.3. The fitted simulation that estimated the passive component values were able to predict movement that are more realistic than the simulated movement were zero values were used for the passive component.

The work described in this thesis obtained numerical values for the passive components and demonstrated those values to be unique. A sensitivity analysis investigates the effect of changes in the whole system from changes in the parameter values. Scovil and Ronsky (Scovil and Ronsky, 2006) have performed sensitivity analysis of the Hill muscle model incorporated in a musculo-skeletal model of the lower body. However numerical values used by Scovil and Ronsky were obtained from other studies, where some of the definitions of the

parameters had inconsistencies between studies, and some of these values used were not from human subjects.

The problem with uncertainty in the accuracy of parameter values is that the model output is dependent on more than two parameters. The error surface shown in Figure 5.12 can be used to determine the sensitivity of the model from the two muscle springs. However the whole error surface changes when the other parameter values change, and it is difficult to examine the sensitivity of more than 2 parameters at any one time. Therefore to correctly determine the sensitivity, the remaining fixed values should be correct. This study only examined the sensitivity of the fitted values, mainly to ensure the uniqueness of those values (e.g. Figure 5.12). Scovil and Ronsky had reported high sensitivities in the length parameters. Length parameters were directly measured in the work described in this thesis. However a sensitivity analysis of all parameters included the length parameters, using the correct values such as those reported in this thesis, can allow the examination of the level of changes in the anatomy and physiology has on the overall dynamics.

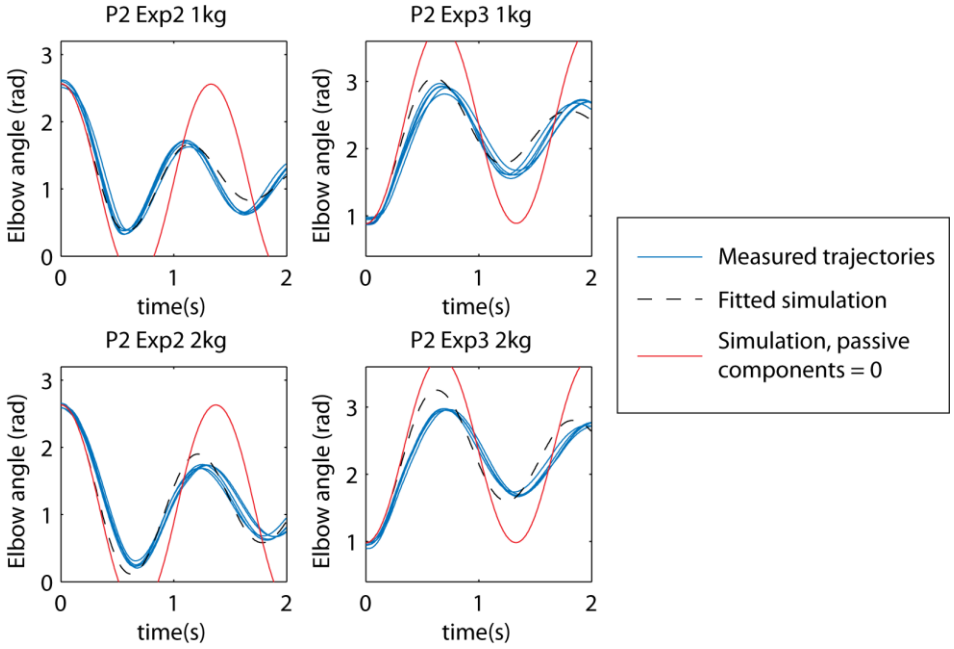

Figure 8.3. Simulated passive elbow movement for subject P2, demonstrating the effect of changes in passive components values. Measured trajectories and fitted simulations were from the passive movement experiment shown in Figure 5.8. The red curves are the simulated trajectories where the passive components values were zero.

8.7.3 A fully parameterised model

The most important results from this work were the development of the passive movement experiments to obtain numerical values of the passive components in the model. The isometric MVC experiment and the FES experiment had also partially obtained the active characteristics of the active component and also an estimate of the relationship between force generated and electrical current injected.

The method developed to obtain the passive component values in the musculo-skeletal model experimentally in vivo formed an important step in being able to fully parameterise musculo-skeletal model through in vivo measurements and parameter estimation. The method to obtain the remaining characteristics, including the force/length, force/velocity and activation characteristics are already widely reported, e.g. (Hatze, 1981, Hof and Van den Berg, 1981a, Durfee and Palmer, 1994, Leedham and Dowling, 1995). By combining all these methods, the musculo-skeletal models can be fully parameterised to form predictive models.

In terms of the predictive model's application in FES control, the relationship of muscle force and stimulation method are widely investigated, e.g. electrode placements. By incorporating more robust FES to muscle force characteristics with the predictive musculo-skeletal models, this would allow more robust predictions of movement generated by FES.

References

AMTI 1991. AMTI FORCE PLATFORM CALCULATIONS.

AMTI 2004. AMTI Biomechanics Platform Instructional Manual.

AMTI 2013a. MINIAMP. http://www.amti.biz/AMTIpibrowser.aspx?__VIEWSTATE=%2FwEPDwULLTE0NzQ1NDQ3OTNkZA%3D%3D&iListbox1=197&iListbox2=198&iListbox3=MSA-6.

AMTI 2013b. OR6-7-1000 specifications. http://www.amti.biz/AMTIpibrowser.aspx?__VIEWSTATE=%2FwEPDwULLTE0NzQ1NDQ3OTNkZA%3D%3D&iListbox1=350&iListbox2=378&iListbox3=OR6-7.

AN, K. N., HUI, F. C., MORREY, B. F., LINSCHEID, R. L. & CHAO, E. Y. 1981. Muscles across the elbow joint: A biomechanical analysis. *Journal of Biomechanics,* 14**,** 659-669.

BAJD, T. 2006. *Surface electrostimulation electrodes*, Wiley Online Library.

BAJD, T., MUNIH, M. & KRALJ, A. 1999. Problems associated with FES-standing in paraplegia. *Technol Health Care,* 7**,** 301-8.

BELLMAN, R. & ÅSTRÖM, K. J. 1970. On structural identifiability. *Mathematical Biosciences,* 7**,** 329-339.

BIGLAND, B. & LIPPOLD, O. 1954. The relation between force, velocity and integrated electrical activity in human muscles. *The Journal of Physiology,* 123**,** 214-224.

BOSTON DYNAMCIS 2013. Atlas - The Agile Anthropomorphic Robot. http://www.bostondynamics.com/robot_Atlas.html.

BRAZ, G. P., RUSSOLD, M., SMITH, R. M. & DAVIS, G. M. 2009. Efficacy and stability performance of traditional versus motion sensor-assisted strategies for FES standing. *Journal of Biomechanics,* 42**,** 1332-1338.

BRAZ, G. P., SMITH, R. M. & DAVIS, G. M. 2007. Designing an FES Control Algorithm: Important Considerations. *World Congress on Medical Physics and Biomedical Engineering 2006, Vol 14, Pts 1-6,* 14**,** 2848-2851.

BUCHTHAL, F. & SCHMALBRUCH, H. 1970. Contraction times and fibre types in intact human muscle. *Acta Physiologica Scandinavica,* 79**,** 435-452.

CARTWRIGHT, A. J. 2001. *Engineering Data Book*, University of Warwick.

CHESLER, N. C. & DURFEE, W. K. 1997. Surface EMG as a fatigue indicator during FES-induced isometric muscle contractions. *Journal of Electromyography and Kinesiology,* 7**,** 27-37.

DAVOODI, R. & ANDREWS, B. J. 1999. Optimal control of FES-assisted standing up in paraplegia using genetic algorithms. *Medical Engineering & Physics,* 21**,** 609-617.

DAVOODI, R., BROWN, I. E. & LOEB, G. E. 2003. Advanced modeling environment for developing and testing FES control systems. *Medical Engineering & Physics,* 25**,** 3-9.

DELP, S. L., ANDERSON, F. C., ARNOLD, A. S., LOAN, P., HABIB, A., JOHN, C. T., GUENDELMAN, E. & THELEN, D. G. 2007. OpenSim: open-source software

to create and analyze dynamic simulations of movement. *IEEE Trans Biomed Eng,* 54**,** 1940-50.

DURFEE, W. K. & PALMER, K. I. 1994. Estimation of force-activation, force-length, and force-velocity properties in isolated, electrically stimulated muscle. *Biomedical Engineering, IEEE Transactions on,* 41**,** 205-216.

ERDEMIR, A., MCLEAN, S., HERZOG, W. & VAN DEN BOGERT, A. J. 2007. Model-based estimation of muscle forces exerted during movements. *Clinical Biomechanics,* 22**,** 131-154.

ESFANJANI, R. M. & TOWHIDKHAH, F. 2005. Application of nonlinear model predictive controller for FES-assisted standing up in paraplegia. *2005 27th Annual International Conference of the IEEE Engineering in Medicine and Biology Society, Vols 1-7***,** 6210-6213.

FRIGO, C., FERRARIN, M., FRASSON, W., PAVAN, E. & THORSEN, R. 2000. EMG signals detection and processing for on-line control of functional electrical stimulation. *Journal of Electromyography and Kinesiology,* 10**,** 351-360.

FUNG, Y. C. 1971. Comparison of different models of the heart muscle. *Journal of Biomechanics,* 4**,** 289-295.

GODFREY, K. R. & DISTEFANO, I., J. J. 1987. Chapter 1: Identifiability of Model Parameters. *Identifiability of Parametric Models***,** 1-20.

GORDON, A. M., HUXLEY, A. F. & JULIAN, F. J. 1966. The variation in isometric tension with sarcomere length in vertebrate muscle fibres. *The Journal of Physiology,* 184**,** 170-192.

HARTLEY, R. & ZISSERMAN, A. 2004. *Multi View Geometry in Computer Vision*, Cambridge University Press.

HARTLEY, R. Z., A. 1999. Multi View Geometry. *users.rsise.anu.edu.au/~hartley/Papers/CVPR99-tutorial/tutorial.pdf*.

HATZE, H. 1981. Estimation of Myodynamic Parameter Values from Observations on Isometrically Contracting Muscle Groups. *European Journal of Applied Physiology and Occupational Physiology,* 46**,** 325-338.

HAUSDORFF, J. & DURFEE, W. 1991. Open-loop position control of the knee joint using electrical stimulation of the quadriceps and hamstrings. *Medical and Biological Engineering and Computing,* 29**,** 269-280.

HILL, A. V. 1938. The Heat of Shortening and the Dynamic Constants of Muscle. *Proceedings of the Royal Society B: Biological Sciences,* 126**,** 136-195.

HOF, A. L. 1997. Correcting for limb inertia and compliance in fast ergometers. *Journal of Biomechanics,* 30**,** 295-297.

HOF, A. L. 1998. In vivo measurement of the series elasticity release curve of human triceps surae muscle. *Journal of Biomechanics,* 31**,** 793-800.

HOF, A. L. & VAN DEN BERG, J. 1981a. EMG to force processing I: An electrical analogue of the Hill muscle model. *J Biomech,* 14**,** 747-58.

HOF, A. L. & VAN DEN BERG, J. 1981b. EMG to force processing II: Estimation of parameters of the Hill muscle model for the human triceps surae by means of a calfergometer. *Journal of Biomechanics,* 14**,** 759-70.

HOF, A. L. & VAN DEN BERG, J. 1981c. EMG to force processing III: Estimation of model parameters for the human triceps surae muscle and assessment of the accuracy by means of a torque plate. *Journal of Biomechanics,* 14**,** 771-85.

HOF, A. L. & VAN DEN BERG, J. 1981d. EMG to force processing IV: Eccentric-concentric contractions on a spring-flywheel set up. *Journal of Biomechanics,* 14**,** 787-92.

HOY, M. G., ZAJAC, F. E. & GORDON, M. E. 1990. A musculoskeletal model of the human lower extremity: the effect of muscle, tendon, and moment arm on the moment-angle relationship of musculotendon actuators at the hip, knee, and ankle. *Journal of Biomechanics,* 23**,** 157-69.

HUGHES, I. & HASE, T. 2010. *Measurements and their uncertainties: a practical guide to modern error analysis*, Oxford University Press.

JOHN, C. T., ANDERSON, F. C., HIGGINSON, J. S. & DELP, S. L. 2012. Stabilisation of walking by intrinsic muscle properties revealed in a three-dimensional muscle-driven simulation. *Computer Methods in Biomechanics and Biomedical Engineering,* 16**,** 451-462.

LEEDHAM, J. & DOWLING, J. 1995. Force-length, torque-angle and EMG-joint angle relationships of the human in vivo biceps brachii. *European Journal of Applied Physiology and Occupational Physiology,* 70**,** 421-426.

LIAO, Y.-W., SCHEARER, E. M., HU, X., PERREAULT, E. J., TRESCH, M. C. & LYNCH, K. M. 2013. Modeling Open-Loop Stability of a Human Arm Driven by a Functional Electrical Stimulation Neuroprosthesis. *In: 35th Annual International Conference of the IEEE Engineering in Medicine and Biology Society (EMBC)*.

LLOYD, D. G. & BESIER, T. F. 2003. An EMG-driven musculoskeletal model to estimate muscle forces and knee joint moments in vivo. *Journal of Biomechanics,* 36**,** 765-776.

MAGANARIS, C. N. 2001. Force–length characteristics of in vivo human skeletal muscle. *Acta Physiologica Scandinavica,* 172**,** 279-285.

MAGANARIS, C. N. 2004. A predictive model of moment–angle characteristics in human skeletal muscle: Application and validation in muscles across the ankle joint. *Journal of Theoretical Biology,* 230**,** 89-98.

MAGANARIS, C. N. & PAUL, J. P. 1999. In vivo human tendon mechanical properties. *Journal of Physiology-London,* 521**,** 307-313.

MALESEVIC, N., MANESKI, L. Z., ILIC, V., JORGOVANOVIC, N., BIJELIC, G., KELLER, T. & POPOVIC, D. 2012. A multi-pad electrode based functional electrical stimulation system for restoration of grasp. *Journal of Neuroengineering and Rehabilitation,* 9**,** 66.

MARIEB, E. N. 2001. *Human Anatomy & Physiology*, Benjamin Cummings.

MATHWORKS®. 2009. *ode45* [Online]. Available: http://www.mathworks.co.uk/help/matlab/ref/ode45.html 2013].

MATHWORKS® 2013. MATLAB®. *http://www.mathworks.co.uk/products/matlab/*.

MOHAMMED, S., POIGNET, P., FRAISSE, P. & GUIRAUD, D. 2012. Toward lower limbs movement restoration with input–output feedback linearization and model predictive control through functional electrical stimulation. *Control Engineering Practice,* 20**,** 182-195.

MORASSO, P. G. & SANGUINETI, V. 2002. Ankle muscle stiffness alone cannot stabilize balance during quiet standing. *Journal of Neurophysiology,* 88**,** 2157-2162.

MULDER, A. J., VELTINK, P. H. & BOOM, H. B. 1992. On/off control in FES-induced standing up: a model study and experiments. *Medical & Biological Engineering & Computing,* 30**,** 205-12.

MURAMATSU, T., MURAOKA, T., TAKESHITA, D., KAWAKAMI, Y., HIRANO, Y. & FUKUNAGA, T. 2001. Mechanical properties of tendon and aponeurosis of human gastrocnemius muscle in vivo. *Journal of Applied Physiology,* 90**,** 1671-1678.

MURRAY, W. M., BUCHANAN, T. S. & DELP, S. L. 2000. The isometric functional capacity of muscles that cross the elbow. *Journal of Biomechanics,* 33**,** 943-952.

NAGANO, A., KOMURA, T., HIMENO, R. & FUKASHIRO, S. 2004. A procedure for adjustment of body segmental parameter values to individual subjects in inverse dynamics. *International Journal of Sport and Health Science,* 2**,** 156-162.

NARICI, M. V. & MAGANARIS, C. N. 2007. Plasticity of the muscle-tendon complex with disuse and aging. *Exercise and sport sciences reviews,* 35**,** 126-134.

NIKU, S. B. 2001. *Introduction to robotics: analysis, systems, applications*, Prentice Hall New Jersey.

NITSCHE, M. A., LIEBETANZ, D., ANTAL, A., LANG, N., TERGAU, F. & PAULUS, W. 2003. Modulation of cortical excitability by weak direct current stimulation–technical, safety and functional aspects. *Supplements to Clinical neurophysiology,* 56**,** 255-276.

PECKHAM, P. H. & KNUTSON, J. S. 2005. Functional electrical stimulation for neuromuscular applications. *Annual Review of Biomedical Engineering,* 7**,** 327-360.

PIAZZA, S. J. & DELP, S. L. 2001. Three-dimensional dynamic simulation of total knee replacement motion during a step-up task. *ASME Journal of Biomechanical Engineering,* 123**,** 599-606.

ROMANÒ, C. L., FRIGO, C., RANDELLI, G. & PEDOTTI, A. 1996. Analysis of the Gait of Adults Who Had Residua of Congenital Dysplasia of the Hip*. *The Journal of Bone & Joint Surgery,* 78**,** 1468-79.

RUSHTON, D. 1997. Functional electrical stimulation. *Physiological measurement,* 18**,** 241.

SCHMID, M., BELTRAMI, G., ZAMBARBIERI, D. & VERNI, G. 2005. Centre of pressure displacements in trans-femoral amputees during gait. *Gait & Posture,* 21**,** 255-262.

SCOVIL, C. Y. & RONSKY, J. L. 2006. Sensitivity of a Hill-based muscle model to perturbations in model parameters. *J Biomech,* 39**,** 2055-63.

SHARMA, N., GREGORY, C. M., JOHNSON, M. & DIXON, W. E. 2012. Closed-Loop Neural Network-Based NMES Control for Human Limb Tracking. *Control Systems Technology, IEEE Transactions on,* 20**,** 712-725.

SHIELDS, R. K. & DUDLEY-JAVOROSKI, S. 2003. Musculoskeletal Deterioration and Hemicorporectomy After Spinal Cord Injury. *Physical Therapy,* 83**,** 263-275.

SILVER, W. M. 1982. On the Equivalence of Lagrangian and Newton-Euler Dynamics for Manipulators. *The International Journal of Robotics Research,* 1**,** 60-70.

THELEN, D. G., ANDERSON, F. C. & DELP, S. L. 2003. Generating dynamic simulations of movement using computed muscle control. *Journal of Biomechanics,* 36**,** 321-328.

TORTORA, G. J. & DERRICKSON, B. H. 2008. *Principles of anatomy and physiology*, Wiley. com.

VAN ZANDWIJK, J. P., BOBBERT, M. F., HARLAAR, J. & HOF, A. 1998. From twitch to tetanus for human muscle: experimental data and model predictions for m. triceps surae. *Biological cybernetics,* 79**,** 121-130.

VENTURE, G., YAMANE, K. & NAKAMURA, Y. 2005. Identifying musculo-tendon parameters of human body based on the musculo-skeletal dynamics computation and Hill-Stroeve muscle model. *2005 5th IEEE-RAS International Conference on Humanoid Robots***,** 351-356.

VENTURE, G., YAMANE, K. & NAKAMURA, Y. 2006. In-vivo estimation of the human elbow joint dynamics during passive movements based on the musculo-skeletal kinematics computation. *2006 Ieee International Conference on Robotics and Automation (Icra), Vols 1-10***,** 2960-2965.

VICON® 2010. Plug-in Gait: Product Guide - Foundation Note. *Vicon Motion Systems, Oxford. UK*.

WEBSTER, J. 2009. *Medical instrumentation: application and design*, Wiley. com.

WINTER, D. A. 2005. *Biomechanics and Motor Control of Human Movement,* Hoboken, New Jersey, Wiley.

WINTER, D. A., PATLA, A. E., RIETDYK, S. & ISHAC, M. G. 2001. Ankle muscle stiffness in the control of balance during quiet standing. *Journal of Neurophysiology,* 85**,** 2630-2633.

WINTERS, J. M. & STARK, L. 1988. Estimated Mechanical-Properties of Synergistic Muscles Involved in Movements of a Variety of Human Joints. *Journal of Biomechanics,* 21**,** 1027-1041.

YAMAGUCHI, G. T. 2001. *Dynamic Modeling of Musculoskeletal Motion: A Vectorized Approach for Biomechanical Analysis in Three Dimensions*, Kluwer Academic Publishers.

YAMAGUCHI, G. T. & ZAJAC, F. E. 1990. Restoring unassisted natural gait to paraplegics via functional neuromuscular stimulation: a computer simulation study. *Biomedical Engineering, IEEE Transactions on,* 37**,** 886-902.

YU, T. F. & WILSON, A. J. 2012a. A Novel Passive Movement Method for Parameter Estimation of a Musculo-Skeletal Arm Model Incorporating a

Modified Hill Muscle Model. *in: Proc. 8th IFAC Symposium on Biological and Medical Systems (IFAC BMS'12),* 8**,** 166-171.

YU, T. F. & WILSON, A. J. 2012b. Structural Identifiability Analysis and Preliminary Parameter Estimation for an Arm Model Incorporating the Hill Muscle Model. *in: 5th European Conference of the International Federation for Medical and Biological Engineering,* 37**,** 864-867.

ZAJAC, F. E. 1989. Muscle and Tendon - Properties, Models, Scaling, and Application to Biomechanics and Motor Control. *Critical Reviews in Biomedical Engineering,* 17**,** 359-411.

ZHANG, D. & ZHU, K. 2004. Simulation study of FES-assisted standing up with neural network control. *Conf Proc IEEE Eng Med Biol Soc,* 7**,** 4877-80.